



**University of
Leicester**

An XMM-Newton View of Normal Galaxies

Yueheng Xu

Supervisors:

Mike Watson
Robert Warwick

Thesis to be submitted for the degree of
Doctor of Philosophy
at the University of Leicester.

X-ray & Observational Astronomy Group
Department of Physics and Astronomy
University of Leicester

January 30, 2009

©Yueheng Xu 2009

This thesis is copyright material and no quotation from it may be published without proper acknowledgement.

Declaration

I hereby declare that no part of this thesis has been previously submitted to this or any other University as part of the requirement for a higher degree. The work described herein was conducted by the undersigned, except for contributions from colleagues as acknowledged in the text.

Yueheng Xu

January 2009

An *XMM-Newton* View of Normal Galaxies

Yueheng Xu

Abstract

Normal galaxies are galaxies whose emission is not dominated by active galactic nuclei (AGN). Current X-ray observatories allow X-ray studies of normal galaxies beyond the local group ($\gtrsim 1$ Mpc). This thesis presents a study of normal galaxy samples drawn from serendipitous sources detected by the *XMM-Newton* Observatory up to a few hundred Mpc.

The work begins with a pilot study in which a sample of 72 normal galaxy candidates is selected from the *XMM-Newton/2dF* Wide Angle Serendipitous Survey using X-ray-to-optical flux ratios, X-ray luminosities and the *2dF* optical spectra. This sample is classified, based on optical emission lines, into five subsamples: AGN, star-forming (SF) galaxies, composite galaxies, unclassified narrow-emission-line galaxies (NELGs) and absorption-line galaxies (ALGs). The X-ray properties of these subsamples, shown by X-ray spectra and hardness ratios, are broadly consistent with the optical classifications.

The Second *XMM-Newton* Serendipitous Catalogue (*2XMM*) is then used to cross-correlate with *Sloan Digital Sky Survey* (*SDSS*) and yields a sample 463 normal galaxy candidates (the *XS* sample) using the same selection criteria as in the pilot study. Using the continuum-subtracted optical emission line measurements from the Max-Planck-Institute for Astrophysics/Johns Hopkins University catalogues (the *MPA/JHU* catalogues), a complete subset of the *XS* sample is separated into five subsamples: AGN, SF galaxies, composite galaxies, unclassified NELGs and ALGs. The X-ray properties, on the basis of the X-ray spectra and hardness ratios, are largely consistent with expectations from their optical classifications. Additional parameters from the *MPA/JHU* catalogues, such as star-formation rates (SFRs) and stellar masses, are used for further investigation of the nature and properties of individual subsamples. The effectiveness of the normal galaxy selection criteria is investigated to show how efficient the X-ray-to-optical flux ratios are on separating AGN from truly normal galaxies.

Acknowledgements

I would like to thank everyone who helped me throughout my time working on this thesis. Firstly, I would like to thank my supervisor Mike Watson for the consistent help and guidance during all these years of my study, without which this thesis would not have become a reality. I would also like to thank the financial support from *Dorothy Hodgkin Postgraduate Awards*. I would also wish to thank my work/office/flat/house/gym-mates, you have make my time in Leicester so wonderful. A great thank you must go to my parents; without your never-ending love, support and encouragement, I would not have got this far.

Dedication

For Mum and Dad.

CONTENTS

1	Introduction	1
1.1	Brief History of X-ray Astronomy	1
1.2	Important Processes in X-ray Astronomy	3
1.2.1	Radiation Mechanisms	3
1.2.2	Accretion	5
1.3	X-ray Components in Galaxies	6
1.3.1	X-ray Binaries	7
1.3.2	Active Galactic Nuclei	8
1.3.3	Ultraluminous X-ray Sources	11
1.3.4	Supernova Remnants	11
1.3.5	Hot ISM in Spiral Galaxies	12
1.3.6	Hot ISM in Elliptical Galaxies	13
1.4	X-ray Studies of Normal Galaxies	13

1.4.1	General Results	14
1.4.2	Normal Galaxies from X-ray Surveys	15
1.4.3	Diagnostic Methods	21
1.5	Aims and Outline of This Thesis	23
2	Instrumentation and Data Analysis	25
2.1	The <i>XMM-Newton</i> Observatory	25
2.2	Data Reduction	28
2.3	Source Detection Algorithm	30
2.4	Data Analysis	32
2.4.1	X-ray Spectral Product Extraction	32
2.4.2	X-ray Spectral Models	33
2.4.3	X-ray Spectral Analysis	33
2.4.4	X-ray Hardness Ratios	34
3	Normal Galaxies in The XWAS	37
3.1	XWAS	37
3.2	Sample Selection	38
3.3	Classification Based on Narrow Emission Line Ratios	40
3.4	X-ray Spectral Properties	41
3.4.1	X-ray Spectra	41

3.4.2	X-ray Hardness Ratios	45
3.5	Chapter Summary	47
4	Normal Galaxies in The XSSS (I)	49
4.1	X-ray Data: <i>2XMM</i>	49
4.2	Optical Data: <i>SDSS</i>	51
4.3	Normal Galaxy Sample	54
4.3.1	Cross-correlation between <i>2XMM</i> and <i>SDSS</i> DR6	54
4.3.2	Sample Selection	55
4.4	Sample Summary	56
4.4.1	Optical Properties	56
4.4.2	X-ray Properties	59
5	Normal Galaxies in The XSSS (II)	66
5.1	Classification for NELGs	66
5.1.1	Classification Based on Narrow Emission Line Ratios	67
5.1.2	Summary of The Subsamples	69
5.2	AGN	73
5.2.1	Overall Properties	73
5.2.2	X-ray Hardness Ratios and Spectra	76
5.2.3	X-ray and Optical Emission Line Luminosities	82

5.3	SF Galaxies	87
5.3.1	Overall Properties	87
5.3.2	SF Galaxies with $L_X > 10^{42}$ erg s ⁻¹	89
5.3.3	X-ray Hardness Ratios	92
5.3.4	X-ray Luminosities and SFRs	93
5.3.5	X-ray and Optical Emission Line Luminosities	96
5.4	Composite Galaxies	96
5.5	Unclassified NELGs	98
5.5.1	Overall Properties and X-ray Hardness Ratios	98
5.5.2	Double-Lobed Radio Galaxies	100
5.6	ALGs	103
5.6.1	Overall Properties	103
5.6.2	X-ray Hardness Ratios	105
5.6.3	X-ray Luminosities and Stellar Masses	107
5.7	Discussion	107
5.7.1	AGN in The <i>MJ</i> Sample	107
5.7.2	Mean X-ray Hardness Ratios	111
5.7.3	Comparison with Normal Galaxies from XWAS	114
5.7.4	Comparison with Normal Galaxies from Other Surveys	114

5.8 Chapter Summary	116
6 Summary and Future Directions	120
6.1 Summary	120
6.2 Future Prospects	122
A The $2dF$ Sample	124
B The MJ Sample	127
C Additional Figures	135
References	140
Acronyms	152

LIST OF FIGURES

1.1	An illustration of a black hole accreting from a star via an accretion disc in an X-ray binary system (credit: <i>ESA</i> , <i>NASA</i> , and Felix Mirabel; taken from http://chandra.harvard.edu/press/07_releases/press_010307.html).	6
1.2	A mosaic and a zoom-in image (red: 0.2-1.0 keV; green: 1.0-2.0 keV; blue: 2.0-12.0 keV; white ellipse: the optical extent of the galaxy) from <i>XMM-Newton</i> observations covering the Andromeda galaxy (M31), the nearest massive spiral galaxy, in which X-ray binaries (point sources) are clearly seen (image courtesy of W. Pietsch, MPE Garching and <i>ESA</i> ; taken from http://xmm.esac.esa.int/external/xmm/_science/gallery/images/1990f4.jpg).	8
1.3	<i>Chandra</i> image ($4' \times 4'$) of the elliptical galaxy NGC 4697 in which X-ray binaries are clearly seen as point sources along with the diffuse emission (credit: <i>NASA</i> , CXC, UVa and C.Sarazin et al. ; taken from http://chandra.harvard.edu/photo/2002/1140/).	9
1.4	<i>Chandra</i> image (purple: 0.45–1 keV; blue: 1–2 keV; $16.8' \times 16.8'$) of spiral galaxy M101, in which the X-ray emission loosely shows the spiral structures (taken from http://chandra.harvard.edu/photo/2008/m101/ ; credit: <i>NASA</i> , CXC, JHU and K.Kuntz et al.).	12

- 1.5 Shown here are examples of superwinds from starburst galaxies (a) M82, (b) NGC 1482 and (c) NGC 253 (reproduced by permission of the AAS from Figure 2 (a), (b) and (c) of *A High Spatial Resolution X-Ray and H α Study of Hot Gas in the Halos of Star-forming Disk Galaxies. II. Quantifying Supernova Feedback*, Strickland et al. 2004b, *ApJ*, Volume 606, Issue 2, pp. 836). The 0.3–2 keV X-ray emission is shown in blue, H α emission in red and the optical R band emission in green. 13
- 1.6 Plots of the soft band (0.5–2 keV) number counts for CDFs sources (top panel) and the fractions of these sources that belong to different subsamples (bottom panel) (reproduced by permission of the AAS from Figure 4 of *The Fall of Active Galactic Nuclei and the Rise of Star-forming Galaxies: A Close Look at the Chandra Deep Field X-Ray Number Counts*, Bauer et al. 2004, *AJ*, Volume 128, Issue 5, pp. 2052). The soft band (0.5–2 keV) number counts are shown for all sources in the CDFs (jagged black curves) and three subsamples: shown: AGN (solid and dashed gray curves), galaxies (solid and dashed dark gray curves), and stars (thick solid black curves). The results from the 1Ms CDF-N fluctuation analysis (Miyaji & Griffiths 2002) are marked as gray shaded areas. The thin solid black line marks the fitting from Moretti et al. (2003). The SF galaxy number counts (Ranalli et al. 2003) predicted from radio band (Richards 2000) are marked by the dotted line. At the top of the panels the fractions of the X-ray background resolved into discrete sources at a given flux calculated from the models in (Moretti et al. 2003) are shown. Extrapolations of these number counts suggest that galaxies will likely outnumber AGN at $\lesssim 5 \times 10^{-18} \text{ erg s}^{-1} \text{ cm}^{-2}$ 20
- 1.7 The Kewley et al. (2006) classification scheme uses three BPT plots (Figure 4 of *The host galaxies and classification of active galactic nuclei*, Kewley et al. 2006, *MNRAS*, Volume 372, Issue 3, pp. 964) to separate galaxies into SF galaxies (the region marked as ‘HII’ in the plots), AGN (further split into Seyfert 2 galaxies and LINER 2s) and composite galaxies (region marked as ‘Comp’ in [a]). 21
- 2.1 The *XMM-Newton* observatory is shown as an artist’s impression (image courtesy of C. Carreau and *ESA*; taken from http://xmm.esac.esa.int/external/xmm_science/gallery/images/AI03_02me.jpg). 26

2.2	The payload of <i>XMM-Newton</i> , adapted from http://xmm.esac.esa.int/external/xmm_science/gallery/images/xmm_pay1.gif (image courtesy of Dornier Satellitensysteme GmbH and ESA).	27
2.3	The light path in <i>XMM-Newton</i> (credit: ESA; taken from the <i>XMM-Newton</i> Users Handbook (Issue 2.6), Figure 2 and Figure 3).	28
2.4	X-ray hardness ratio grids from single component models.	35
2.5	X-ray hardness ratio grids from two-component models.	36
3.1	The SSS <i>R</i> band magnitudes are shown against 0.2–12 keV fluxes of XWAS sources with both X-ray flux measurements and optical magnitudes, including NELGs (squares), ALGs (triangles), broad line AGN (crosses), and stars (asterisks). The circles mark the sources in the <i>2dF</i> sample. The slanted lines indicate constant X-ray to optical flux ratios of $\log(f_X/f_O) = -1, 0, 1$, marked by solid, dashed and dotted lines, respectively, from bottom to top.	39
3.2	Shown here are two examples from the <i>2dF</i> sample, one being an ALG (a) and the other being a NELG (b). The SSS <i>R</i> band image (taken by the UK Schmidt Telescope) is shown on the left with the <i>2dF</i> spectrum on the right. The solid regions are centred at the positions of the X-ray sources and have radii of 1σ X-ray positional uncertainties. The dashed regions have $5''$ radii.	40
3.3	Shown here is the BPT [N II] plot used to classified NELGs in the <i>2dF</i> sample. Galaxies lying above the ‘maximum starburst line’ (yellow solid line; Equation 1.8) are classified as AGN (red dots). SF galaxies (green squares) are those lying below the pure SF line (black dashed line; Equation 1.7). Galaxies lying between these two lines (Equation 1.9 and 1.10) are composite galaxies (blue diamonds).	42
3.4	The SSS <i>R</i> band images from the UK Schmidt Telescope of the four sources whose X-ray spectra are presented here. The solid regions are centred at the positions of the X-ray sources and have radii of 1σ X-ray positional uncertainties. The dashed regions have $5''$ radii.	43

3.5	<i>XMM-Newton</i> spectra of sources with sufficient counts for spectral analysis. The spectra from the pn camera for objects 861 (a) and 2683 (c) were fitted with single APEC models. For object 2677 (b) spectra from both pn (black) and MOS2 (red) cameras were fitted and the best-fit model was a two-component model (APEC plus <code>zpower1w</code>). The pn spectrum of object 2730 (d) was fitted with a single power-law model.	43
3.6	Hardness ratios (HR2 versus HR3) for <i>2dF</i> subsamples. Counts from all three EPIC cameras were used to calculate the hardness ratios. Values from spectral models described in § 2.4.4 are also shown.	46
4.1	(a) The positional uncertainties (column SC_POSERR in <i>2XMM</i>) of all the X-ray sources which have <i>SDSS</i> matches (truncated at 10"). (b) The separations between the X-ray positions and optical positions for all <i>SDSS</i> matches.	54
4.2	All 23265 X-ray sources with <i>SDSS</i> matches are shown as pink dots in this <i>SDSS</i> <i>r</i> band Petrosian magnitude versus 0.2–12 keV X-ray flux plot. Green circles are <i>SDSS</i> spectroscopically classified galaxies, with the filled ones representing the <i>XS</i> sample. The red circles mark the <i>SDSS</i> spectroscopically classified QSOs. The slanted lines indicate constant X-ray-to-optical flux ratios of $\log(f_X/f_O) = 0, -1, \text{ and } -2$, marked by pink dashed line, black solid line and light blue dashed-dotted line, respectively, from top to bottom. The horizontal line indicates the approximate magnitude limit of the <i>SDSS</i> Main Galaxy Sample ($r \approx 17.77$; Strauss et al. 2002).	57
4.3	All 1556 X-ray sources with <i>SDSS</i> spectra are shown here. $\log(f_X/f_O)$ was calculated using Equation 4.1. The 0.2–12 keV luminosity was calculated using the flux from <i>2XMM</i> (column SC_EP_8_FLUX) and redshift from <i>SDSS</i> . Green circles are <i>SDSS</i> spectroscopically classified galaxies, with the filled ones denote the <i>XS</i> sample. The red circles represent the <i>SDSS</i> spectroscopically classified QSOs. The horizontal and vertical lines indicate the values used to selected the <i>XS</i> sample.	58
4.4	Flow chart to summarize the procedures used to select the <i>XS</i> sample.	59

4.5	Distributions of <i>SDSS</i> <i>r</i> band Petrosian magnitudes and redshifts are shown in (a) and (b) respectively. The <i>XS</i> sample, its NELG subsample and ALG subsample are marked with filled (pink), solid (black) and dashed (blue) histograms respectively.	60
4.6	The $u - r$ colours are shown against the concentration index $C_{90/50}$ (the ratio of the radii defined as containing 90% and 50% of the galaxy light using a Petrosian profile). Nineteen galaxies which have <i>u</i> band magnitude fainter than the magnitude limit (~ 22 ; Adelman-McCarthy et al. 2008) are excluded. $u - r = 2.22$ is shown as the dashed-dotted vertical line. $C_{90/50} = 2.6$ is indicated by the dotted horizontal line. Strateva et al. (2001) found that early-type (E, S0 and Sa) galaxies tend to have $u - r > 2.22$ and $C_{90/50} > 2.6$ while late-type (Sb, Sc and Irr) galaxies are likely to have $u - r \leq 2.22$ and $C_{90/50} \leq 2.6$. NELGs are shown with pink circles while ALGs are marked with blue squares. The median of the errors of $C_{90/50}$ is 0.09 and is shown as the black bar. For $\sim 2\%$ of the sources the $C_{90/50}$ is not well constrained.	61
4.7	Distributions of 0.2–12 keV fluxes, the X-ray-to-optical flux ratios and 0.2–12 keV luminosities are shown in (a), (b) and (c) respectively. The <i>XS</i> sample, its NELG subsample and ALG subsample are marked with filled (pink), solid (black) and dashed (blue) histograms respectively.	62
4.8	Distributions of 0.2–12 keV photon counts from the pn camera. The <i>XS</i> sample, its NELG subsample and ALG subsample are marked with filled (pink), solid (black) and dashed (blue) histograms respectively.	63
4.9	The smoothed X-ray hardness ratio (HR2 against HR3) density plots for NELGs and ALGs. Spectral models defined in § 2.4.4 are overlaid in each plot. Contours at 68% and 90% levels are also shown.	63
4.10	The smoothed X-ray hardness ratio (HR2 versus HR3) density plots for <i>XS</i> sources with $\log(f_X/f_O) \leq -2$ and $-2 < \log(f_X/f_O) \leq -1$ respectively. Spectral models defined in § 2.4.4 are overlaid in each plot. Contours at 68% and 90% levels are also shown.	64

4.11	The smoothed X-ray hardness ratio (HR2 versus HR3) density plots for XS sources in three X-ray luminosity bins: $L_X \leq 10^{41}$ erg s ⁻¹ , $10^{41} < L_X \leq 10^{42}$ erg s ⁻¹ , and $10^{42} < L_X \leq 10^{43}$ erg s ⁻¹ . Spectral models defined in § 2.4.4 are overlaid in each plot. Contours at 68% and 90% levels are also shown.	65
5.1	The BPT [N II] plot and the classification scheme from Kewley et al. (2006). Galaxies lying above the yellow solid line (Equation 1.8) are classified as AGN and marked with red dots. Galaxies lying below the black dashed line (Equation 1.7) are classified as SF galaxies and marked with green squares. Galaxies lying between these two lines (Equation 1.9 and Equation 1.10) are referred to as composite galaxies and marked with blue diamonds.	68
5.2	The BPT [S II] plot (a) and the BPT [O I] plot (b) for the AGN classified in Figure 5.1. Also shown is the classification scheme from Kewley et al. (2006). AGN (Equation 1.12 and 1.16) are split into Seyfert 2 galaxies (Equation 1.13 and 1.17; red diamonds) and LINER 2s (Equation 1.14 and 1.18; green triangles).	69
5.3	The $u - r$ colours are shown against concentration index $C_{90/50}$ (the ratio of the radii defined as containing 90% and 50% of the galaxy light using a Petrosian profile). Six galaxies which have u band magnitude fainter than the magnitude limit (~ 22 ; Adelman-McCarthy et al. 2006) are excluded. $u - r = 2.22$ is shown as the solid vertical line. $C_{90/50} = 2.6$ is indicated by the dashed horizontal line. Strateva et al. (2001) found that early-type (E, S0 and Sa) galaxies tend to have $u - r > 2.22$ and $C_{90/50} > 2.6$ while late-type (Sb, Sc and Irr) galaxies are likely to have $u - r \leq 2.22$ and $C_{90/50} \leq 2.6$. AGN, SF galaxies, composite galaxies and the unclassified NELGs are marked as red dots, green squares, blue diamonds and light blue crosses, respectively. The median of the errors of $C_{90/50}$ is 0.08 and is shown as the black bar. For $\sim 1.7\%$ of the sources the $C_{90/50}$ is not well constrained.	70
5.4	Redshifts from <i>SDSS</i> are shown against 0.2–12 keV X-ray luminosities. AGN, SF galaxies, composite galaxies and the unclassified NELGs are marked as red dots, green squares, blue diamonds and light blue crosses, respectively.	71

5.5	The 0.2–12 keV fluxes are shown against the <i>SDSS</i> <i>r</i> band magnitudes. The solid and dashed lines indicate $\log(f_X/f_O) = -1$ and -2 , respectively. The horizontal dashed-dotted line indicates the approximate magnitude limit of the <i>SDSS</i> Main Galaxy Sample ($r \approx 17.77$; Strauss et al. 2002). The <i>2XMM</i> catalogue has the flux limits of $\sim 10^{-14}$ erg s $^{-1}$ cm $^{-2}$ in the soft band (0.5–2 keV) and $\sim 9 \times 10^{-14}$ erg s $^{-1}$ cm $^{-2}$ in the hard band (2–12 keV) at $\sim 90\%$ of its sky coverage (Watson et al. 2009). AGN, SF galaxies, composite galaxies and unclassified NELGs are marked as red dots, green squares, blue diamonds and light blue crosses, respectively.	72
5.6	The distributions of the X-ray-to-optical flux ratios. In all four plots, the <i>MJ</i> sample and its NELG subsample are marked with black solid histograms and pink filled histograms respectively. The classifiable NELGs are marked with black dashed histograms in (a), (b), and (c). AGN, SF galaxies and composite galaxies are marked with red histogram in (a), green histogram in (b) and blue histogram in (c), respectively. The unclassified NELGs are marked with the magenta histogram in (d).	73
5.7	Velocity dispersions (σ of the Gaussian fit to the lines) of Balmer lines are shown against those of the forbidden lines, both from the <i>MPA/JHU</i> catalogue.	75
5.8	The smoothed pn hardness ratio density plots (HR2 versus HR3) for (a) the AGN subsample, (b) AGN with $\log(f_X/f_O) \leq -2$, and (c) AGN with $-2 < \log(f_X/f_O) \leq -1$. Two sources were excluded due to undefined pn hardness ratios. Spectral models defined in § 2.4.4 are overlaid in each plot. Contours at 68% and 90% levels are also shown.	77
5.9	The smoothed pn hardness ratio (HR2 versus HR3) density plots for (a) AGN with $L_X \leq 10^{41}$ erg s $^{-1}$, (b) AGN with $10^{41} < L_X \leq 10^{42}$ erg s $^{-1}$, and (c) AGN with $L_X > 10^{42}$ erg s $^{-1}$. Two sources were excluded due to undefined pn hardness ratios. Spectral models defined in § 2.4.4 are overlaid in each plot. Contours at 68% and 90% levels are also shown.	77

5.10	The smoothed pn hardness ratio (HR2 versus HR3) density plots for Seyfert 2 galaxies and LINER 2s. Two sources were excluded due to undefined pn hardness ratios. Spectral models defined in § 2.4.4 are overlaid in each plot. Contours at 68% and 90% levels are also shown.	78
5.11	The <i>2XMM</i> automatically extracted spectrum from the pn camera for 2XMM J083139.1+524205 (SRCID: 67895) fitted with a two-power-law model: an unabsorbed power-law model (green) with $\Gamma = 1.91_{-0.46}^{+0.47}$ and an absorbed power-law model (red) with $\Gamma = 1.80_{-0.88}^{+0.70}$ associated with an absorption of $2.18_{-0.64}^{+0.49} \times 10^{23}$ atoms cm^{-2} . The pink dotted line shows the Gaussian fit to the emission line at ~ 6.4 keV.	79
5.12	The <i>2XMM</i> automatically extracted pn spectrum for 2XMM J113446.6+485722 (SRCID: 96740) fitted by a two-component model: a power-law model with $\Gamma = 2.19_{-0.34}^{+0.30}$ (red) and an <i>APEC</i> model with $kT = 0.42_{-0.12}^{+0.21}$ keV (green).	80
5.13	The <i>2XMM</i> automatically extracted pn spectrum for 2XMM J160534.5+323941 (SRCID: 143634) fitted by a power-law model with $\Gamma = 1.95_{-0.08}^{+0.09}$	81
5.14	The <i>2XMM</i> automatically extracted spectrum from EPIC for 2XMM J212926.2+000524 (SRCID: 178535) fitted by an <i>APEC</i> model with $kT = 0.65_{-0.06}^{+0.08}$ keV.	82
5.15	Distributions of $\log (f_{2-12\text{keV}}/f_{\text{H}\alpha})$ and $\log (f_{2-12\text{keV}}/f_{[\text{OIII}]})$ for the 46 AGN with $\text{H}\alpha/\text{H}\beta > 3.1$	83
5.16	The extinction corrected $L_{\text{H}\alpha}$ and $L_{[\text{OIII}]}$ are shown against the observed $L_{2-12\text{keV}}$ for the AGN subsample. The black solid lines are the results of least-square (bisector) fits of the AGN with $\text{H}\alpha/\text{H}\beta > 3.1$ (filled circles). AGN with $\text{H}\alpha/\text{H}\beta < 3.1$ are marked by open circles; they were not included in the fit. The blue solid lines are the correlations from Panessa et al. (2006) converted to the 2–12 keV band (assuming a power-law with $\Gamma = 1.7$ and a Galactic absorption of $N_{\text{H}} = 3 \times 10^{20}$ atoms cm^{-2}). The same correlations are also shown with factors of 0.32, 0.07 and 0.01 applied to the $L_{2-12\text{keV}}$ values to represent the effects of intrinsic absorption of 5×10^{23} atoms cm^{-2} , 2×10^{24} atoms cm^{-2} and 5×10^{24} atoms cm^{-2} respectively (shown as grey dashed-dashed lines).	84

5.17	Histograms of $\log(f_{2-12\text{keV}}/f_{\text{H}\alpha})$ and $\log(f_{2-12\text{keV}}/f_{[\text{OIII}]})$ are shown for the 46 AGN with $\text{H}\alpha/\text{H}\beta > 3.1$ (pink dashed histograms). On average Seyfert 2 galaxies (red filled histograms) have lower $f_{2-12\text{keV}}/f_{\text{H}\alpha}$ and $f_{2-12\text{keV}}/f_{[\text{OIII}]}$ than LINER 2s (black histograms).	85
5.18	The extinction corrected $L_{\text{H}\alpha}$ and $L_{[\text{OIII}]}$ are shown against the observed $L_{2-12\text{keV}}$ for the 46 AGN with $\text{H}\alpha/\text{H}\beta > 3.1$. The Seyfert 2 galaxies are marked with red triangles. The LINER 2s are marked with blue squares. The least-square (bisector) fits to the Seyfert 2 galaxies and the LINER 2s are shown as the green dashed-dashed lines and the black solid lines, respectively. The blue dotted lines are the correlations from Panessa et al. (2006) converted to the 2–12 keV band (assuming a power-law with $\Gamma = 1.7$ and a Galactic absorption of $N_{\text{H}} = 3 \times 10^{20}$ atoms cm^{-2}).	86
5.19	(a) The velocity dispersion (σ of Gaussian fits to the lines) of Balmer lines are shown against that of forbidden lines, both from the <i>MPA/JHU</i> catalogues. (b) The <i>SDSS</i> spectrum (taken from the <i>SDSS</i> SkyServer Object Explorer) of the outlier 2XMM J095848.6+025243 (SRC: 78830) which is marked as a red diamond in (a).	88
5.20	The 2XMM pn spectrum of 2XMM J095848.6+025243 (SRC: 78830) fitted by a power-law model with $\Gamma = 2.02_{-0.26}^{+0.29}$ (the Galactic absorption was fixed at $N_{\text{H}} = 1.84 \times 10^{20}$ atoms cm^{-2} , Kalberla et al. 2005).	89
5.21	(a) The X-ray hardness ratios (HR2 versus HR3) from the pn camera of the six SF galaxies with $L_{0.2-12\text{keV}} > 10^{42}$ erg s^{-1} . Spectral models defined in § 2.4.4 are overlaid in the plot. (b) The <i>SDSS</i> spectrum (taken from the <i>SDSS</i> SkyServer Object Explorer) of 2XMM J030634.1-001355 (SRCID: 27727).	90
5.22	The X-ray hardness ratio (HR2 versus HR3) density plots for (a) the SF galaxy subsample, (b) SF galaxies with $\log(f_{\text{X}}/f_{\text{O}}) \leq -2$, and (c) SF galaxies with $-2 < \log(f_{\text{X}}/f_{\text{O}}) \leq -1$. Three galaxies were excluded due to undefined pn hardness ratios. Spectral models defined in § 2.4.4 are overlaid in each plot. Contours indicating 68% and 90% levels are also shown.	92

5.23	The X-ray hardness ratio (HR2 versus HR3) density plots for SF galaxies in two X-ray luminosity bins: (a) $L_X \leq 10^{41}$ erg s ⁻¹ and (b) $10^{41} < L_X \leq 10^{42}$ erg s ⁻¹ . SF galaxies with undefined pn hardness ratios were excluded. Spectral models defined in § 2.4.4 are overlaid in each plot. Contours indicating 68% and 90% levels are also shown. . . .	93
5.24	SFRs (as calculated in Brinchmann et al. 2004) are shown against the soft band X-ray (0.5–2 keV) luminosities. The fit to the data is shown as a blue solid line and the correlation from Ranalli et al. (2003) is shown as a green dashed line.	94
5.25	SFRs (as calculated in Brinchmann et al. 2004) are shown against the hard band X-ray (2–12 keV) luminosities. The correlation from Colbert et al. (2004), when no contribution from LMXBs is included, is shown as black solid line. The dashed-dashed line indicates the same correlation but with the LMXBs contribution represented by a stellar mass of $10^9 M_\odot$. The dashed line is also for the same correlation but with the LMXBs contribution calculated from a stellar mass of $10^{11} M_\odot$	95
5.26	The H α line luminosities are plotted against the 2–12 keV luminosities of SF galaxies. The L_X -H α correlation found for the AGN subsample (§ 5.2.3) is marked by the green dashed line. Most of the SF galaxies fall below this correlation.	96
5.27	The smoothed pn hardness ratio (HR2 versus HR3) density plots for (a) composite galaxies, (b) composite galaxies with $\log(f_X/f_O) \leq -2$, and (c) composite galaxies with $-2 < \log(f_X/f_O) \leq -1$. Two galaxies were excluded due to undefined pn hardness ratios. Spectral models defined in § 2.4.4 are overlaid in each plot. Contours indicating 68% and 90% levels are also shown.	97
5.28	The smoothed pn hardness ratio (HR2 versus HR3) density plots for composite galaxies with $L_X \leq 10^{41}$ erg s ⁻¹ (a) and those with $10^{41} < L_X \leq 10^{43}$ erg s ⁻¹ (b). Spectral models defined in § 2.4.4 are overlaid in each plot. Contours at 68% and 90% levels are also shown.	98

5.29	The smoothed pn hardness ratio (HR2 versus HR3) density plots for the unclassified NELGs and its subsets within the two X-ray-to-optical flux ratio bins: (b) $\log(f_X/f_O) \leq -2$ and (c) $-2 < \log(f_X/f_O) \leq -1$. Five galaxies were excluded from the plots due to undefined hardness ratios. Spectral models defined in § 2.4.4 are overlaid in each plot. Contours indicating 68% and 90% levels are also shown.	99
5.30	The smoothed pn hardness ratio (HR2 versus HR3) density plots for the unclassified NELGs in three luminosity bins: (a) $L_X \leq 10^{41} \text{ erg s}^{-1}$, (b) $10^{41} < L_X \leq 10^{42} \text{ erg s}^{-1}$, and (c) $10^{42} < L_X \leq 10^{43} \text{ erg s}^{-1}$. The five galaxies with undefined hardness ratios from the pn camera were excluded. Spectral models defined in § 2.4.4 are overlaid in each plot. Contours at 68% and 90% levels are also shown.	99
5.31	Radio images ($3' \times 3'$) of the five double-lobed radio galaxies from the FIRST Survey. The overlaid regions are centred at the positions of the X-ray sources with radii of the 3σ X-ray positional uncertainties.	101
5.32	Radio image ($3' \times 3'$) of 2XMM J133729.1+481822 (SRCID: 124718) from the FIRST Survey. The overlaid region is centred at the X-ray position with radius of the 3σ X-ray positional uncertainty.	104
5.33	The smoothed X-ray hardness ratio (HR2 versus HR3) density plots for the ALG sub-sample (a) and its subsets in two X-ray-to-optical flux ratio bins: (b) $\log(f_X/f_O) \leq -2$ and (c) $-2 < \log(f_X/f_O) \leq -1$. Spectral models defined in § 2.4.4 are overlaid in each plot. Contours indicating 68% and 90% levels are also shown.	105
5.34	The smoothed X-ray hardness ratio (HR2 versus HR3) density plots for ALGs in two luminosity bins: (a) $L_X \leq 10^{42} \text{ erg s}^{-1}$ and (b) $10^{42} < L_X \leq 10^{43} \text{ erg s}^{-1}$. Spectral models defined in § 2.4.4 are overlaid in each plot. Contours at 68% and 90% levels are also shown.	106

- 5.35 The 0.2–12 keV X-ray luminosities are shown against the dust-corrected stellar masses from Kauffmann et al. (2003b, the median of the probability distributions) for 38 ALGs. The contributions from SF activities to the 0.2–12 keV luminosities have been subtracted from the X-ray luminosities using the correlation from Colbert et al. (2004) and the SFRs estimated in Brinchmann et al. (2004). To be consistent with the SFRs used in Colbert et al. (2004), the SFRs used here have been multiplied by 1.5 to account for the IMF difference (Brinchmann et al. 2004) and then multiplied by 1.4 to account for the bolometric correction applied in Colbert et al. (2004). The blue solid line indicates the least square (bisector) fit to the data. The L_X - L_B correlation from O’Sullivan et al. (2001) has been converted to L_X -Mass assuming the stellar mass-to-light ratio $M_*/L = 1$ and 2. The correlation between X-ray luminosities and stellar masses in Colbert et al. (2004) is also shown. 108
- 5.36 The whole *MJ* sample is marked as pink crosses. The optical emission line ratio classified AGN are marked with red dots. The NLS 1 galaxy is marked with green open circle. Five double-lobed radio galaxies found among the unclassified NELGs are marked with red open circles. One double-lobed radio galaxy found among the ALGs is marked with blue open circle. The fraction of AGN, calculated as the number of optical emission line classified AGN divided by the number of galaxies in a given bin (defined by both the X-ray-to-optical flux ratio and the X-ray luminosity) is also given in the plot; the second number or percentage given inside the brackets corresponds to the NLS 1 galaxy or the radio galaxies. 109
- 5.37 The flux limited subsample from *MJ* (*SDSS r* band Petrosian magnitude brighter than 17.77, the flux limit of the Main Galaxy Sample Strauss et al. 2002) is marked with pink crosses. The optical emission line ratio classified AGN are marked using red dots. The NLS 1 galaxy is marked with green open circle. The double-lobed radio galaxy found among unclassified NELGs is marked with red open circle. The fraction of AGN, calculated as the number of optical emission line classified AGN divided by the number of galaxies in a given bin (defined by both X-ray-to-optical flux ratio and X-ray luminosity) is also given in the plot; the second number or percentage given inside the brackets corresponds to the NLS 1 galaxy or the radio galaxy. 111

5.38	The error weighted mean X-ray hardness ratios of the five <i>MJ</i> subsamples (AGN, SF galaxies, composite galaxies, unclassified NELGs, and ALGs) are shown in five bins. Spectral models defined in § 2.4.4 are overlaid in each plot.	113
C.1	The distributions of <i>SDSS</i> <i>r</i> band magnitudes. In all four plots, the <i>MJ</i> sample and its NELG subsample are marked with black solid histograms and pink filled histograms respectively. The classifiable NELGs are marked with black dashed histograms in (a), (b), and (c). AGN, SF galaxies and composite galaxies are marked with red histogram in (a), green histogram in (b) and blue histogram in (c), respectively. The unclassified NELGs are marked with magenta histogram in (d).	136
C.2	The distributions of redshifts from <i>SDSS</i> . In all four plots, the <i>MJ</i> sample and its NELG subsample are marked with black solid histograms and pink filled histograms respectively. The classifiable NELGs are marked with black dashed histograms in (a), (b), and (c). AGN, SF galaxies and composite galaxies are marked with red histogram in (a), green histogram in (b) and blue histogram in (c), respectively. The unclassified NELGs are marked with magenta histogram in (d).	136
C.3	The distributions of the 0.5–2 keV fluxes. In all four plots, the <i>MJ</i> sample and its NELG subsample are marked with black solid histograms and pink filled histograms respectively. The classifiable NELGs are marked with black dashed histograms in (a), (b), and (c). AGN, SF galaxies and composite galaxies are marked with red histogram in (a), green histogram in (b) and blue histogram in (c), respectively. The unclassified NELGs are marked with magenta histogram in (d).	137
C.4	The distributions of the 0.5–2 keV luminosities. In all four plots, the <i>MJ</i> sample and its NELG subsample are marked with black solid histograms and pink filled histograms respectively. The classifiable NELGs are marked with black dashed histograms in (a), (b), and (c). AGN, SF galaxies and composite galaxies are marked with red histogram in (a), green histogram in (b) and blue histogram in (c), respectively. The unclassified NELGs are marked with magenta histogram in (d).	137

C.5	The distributions of the 2–12 keV fluxes. In all four plots, the <i>MJ</i> sample and its NELG subsample are marked with black solid histograms and pink filled histograms respectively. The classifiable NELGs are marked with black dashed histograms in (a), (b), and (c). AGN, SF galaxies and composite galaxies are marked with red histogram in (a), green histogram in (b) and blue histogram in (c), respectively. The unclassified NELGs are marked with magenta histogram in (d).	138
C.6	The distributions of the 2–12 keV luminosities. In all four plots, the <i>MJ</i> sample and its NELG subsample are marked with black solid histograms and pink filled histograms respectively. The classifiable NELGs are marked with black dashed histograms in (a), (b), and (c). AGN, SF galaxies and composite galaxies are marked with red histogram in (a), green histogram in (b) and blue histogram in (c), respectively. The unclassified NELGs are marked with magenta histogram in (d).	138
C.7	The distributions of the 0.2–12 keV fluxes. In all four plots, the <i>MJ</i> sample and its NELG subsample are marked with black solid histograms and pink filled histograms respectively. The classifiable NELGs are marked with black dashed histograms in (a), (b), and (c). AGN, SF galaxies and composite galaxies are marked with red histogram in (a), green histogram in (b) and blue histogram in (c), respectively. The unclassified NELGs are marked with magenta histogram in (d).	139
C.8	The distributions of the 0.2–12 keV luminosities. In all four plots, the <i>MJ</i> sample and its NELG subsample are marked with black solid histograms and pink filled histograms respectively. The classifiable NELGs are marked with black dashed histograms in (a), (b), and (c). AGN, SF galaxies and composite galaxies are marked with red histogram in (a), green histogram in (b) and blue histogram in (c), respectively. The unclassified NELGs are marked with magenta histogram in (d).	139

LIST OF TABLES

2.1	Data taken from the <i>XMM-Newton</i> Users Handbook (Issue 2.6), Table 26. A_e is the mirror effective area at 1 keV.	29
3.1	(1): Sample size. (2)–(4): Fractions that a subsample possesses in its parent sample(s). (5): Unweighted mean redshifts z . (6): Unweighted mean R band magnitudes. (7): Unweighted mean X-ray-to-optical flux ratios. (8)–(10): Unweighted mean X-ray fluxes in units of 10^{-15} erg s $^{-1}$ cm $^{-2}$. (11)–(13): Unweighted mean X-ray luminosities in units of 10^{41} erg s $^{-1}$	42
3.2	The best-fit models for objects 861 and 2683 were APEC. The best-fit model for object 2677 was a combination of an APEC model and an absorbed power-law model (<code>zpowerlw</code>). The best-fit model for object 2730 was a single power-law model (<code>zpowerlw</code>). (1): XWAS QID. (2): visual classification based on $2dF$ spectrum. (3): redshift from XWAS. (4): plasma temperature from the APEC model (\dagger no errors calculated as $\chi^2_\nu > 2$). (5): 0.2–12 keV luminosity derived from the APEC model (corrected for the Galactic absorption). (6): intrinsic absorption applied only to the power-law component (\dagger no errors calculated as $\chi^2_\nu > 2$). (7): Γ of the power-law model (\dagger no errors calculated as $\chi^2_\nu > 2$). (8): 0.2–12 keV luminosity derived from the power-law model (corrected for the Galactic absorption; * also corrected for intrinsic absorption). (9): χ^2 /degree-of-freedom of the fitting (bold values indicating the best-fit models).	44

- 5.1 (1): Sample size. (2)–(4): Fractions that a subsample possesses in its parent sample(s). (5): Unweighted mean redshifts z . (6): Unweighted mean r band magnitudes. (7): Unweighted mean Galactic extinction corrected $u - r$ colours. Galaxies with magnitudes fainter than the magnitude limits are excluded (six ALGs, one AGN and five unclassified NELGs). (8): Unweighted mean concentration indexes defined as the ratios of Petrosian radii containing 90% and 50% light of the galaxy. (9): Unweighted mean X-ray-to-optical flux ratios. (10) and (11): Numbers of sources satisfying the conditions specified in the brackets. (12)–(14): Unweighted mean X-ray fluxes in units of 10^{-15} erg s^{-1} cm^{-2} . (15)–(17): Unweighted mean X-ray luminosities in units of 10^{41} erg s^{-1} . (18)–(20): Numbers of sources satisfying the conditions specified in the brackets (L_X in the 0.2–12 keV band). (21) and (22): Unweighted mean hardness ratios. 74
- 5.2 The SF galaxies with $L_X > 10^{42}$ erg s^{-1} . The d_{XO} is the offset between the X-ray position and the optical position normalized by the X-ray positional uncertainty (in σ). Hardness ratios HR2 and HR3 are from the pn camera. 91
- 5.3 Unclassified NELGs detected in the FIRST Survey as double-lobed radio galaxies. (1): The unique source ID in *2XMM*. (2): The IAU name of the *2XMM* source. (3): Redshift from *SDSS*. (4): The r band magnitude from *SDSS*. (5): The X-ray-to-optical flux ratio. (6): The soft band (0.5–2 keV) flux in the unit of 10^{-15} erg s^{-1} cm^{-2} . (7): The hard band (2–12 keV) flux in the unit of 10^{-15} erg s^{-1} cm^{-2} . (8): The 0.2–12 keV luminosity in the unit of 10^{41} erg s^{-1} . (9): The integrated 1.4 GHz flux density (mJy) from the FIRST Survey (Becker et al. 2003). (10): The radio loudness defined as the ratio of the flux density in 1.4 GHz (integrated) to that in the r band (Ivezić et al. 2002). 102

5.4	The fractions that each type of galaxies possess in different <i>MJ</i> subsets defined by different X-ray-to-optical flux ratio cut-off and X-ray luminosity cut-off. “SF” denote SF galaxies. “COM” denote composite galaxies. “UNC” denote unclassified NELGs. The 1σ uncertainties are calculated assuming AGN follow Poisson distribution in each subset. * The +5% in brackets includes four double-lobed radio galaxies among unclassified NELGs (the -4% in the bracket) and one among ALGs (the -1% in the bracket); increasing the luminosity from $L_X \leq 10^{42} \text{ erg s}^{-1}$ to $L_X \leq 10^{43} \text{ erg s}^{-1}$ does not include any additional galaxies with $\log(f_X/f_O) \leq -2$ and therefore the values before and after including another bin are identical. † The +3% in the brackets for AGN includes the NLS 1 galaxy identified among SF galaxies (the -0.4% in brackets) and the five double-lobed radio galaxies (the -2% and -0.4% in the brackets following unclassified NELGs and ALGs respectively). ‡ The +2% in the brackets for AGN is calculated from the NLS 1 galaxy (the -0.4% in the brackets following SF galaxies) and six double-lobed radio galaxies (the -2% and -0.4% in the brackets following unclassified NELGs and ALGs).	110
5.5	The fraction of AGN in the flux limited subsample of <i>MJ</i> . The 1σ uncertainties are calculated assuming AGN follow Poisson distribution in each subset. * The +8% in brackets includes one two-lobed radio galaxy among unclassified NELGs; increasing the luminosity from $L_X \leq 10^{42} \text{ erg s}^{-1}$ to $L_X \leq 10^{43} \text{ erg s}^{-1}$ does not include any additional galaxies with $\log(f_X/f_O) \leq -2$ and therefore the values before and after including another bin are identical. † The +5% in brackets includes the five double-lobed radio galaxies and the NLS 1 galaxy identified among SF galaxies. ‡ The +4% in brackets includes six double-lobed radio galaxies and the NLS 1 galaxy.	112
A.1	(1) QID from XWAS. (2) Right ascension in hh:mm:ss.ss for the X-ray source. (3) Declination in dd:mm:ss.ss for the X-ray source. (4) Redshift from XWAS. (5) <i>R</i> band magnitude from SSS or USNO-B 1.0 (marked by *). (6) Logarithm of $f_{0.2-12\text{keV}}$ from XWAS. (7) $\log(f_X/f_O)$ defined as $\log f_{0.2-12\text{keV}} + R/2.5 + 5.5$. (8) Logarithm of $L_{0.2-12\text{keV}}$. (9) Classification from this work. “SF” denote SF galaxies. “COM” denote composite galaxies. “UNC” denote unclassified NELGs.	124

B.1 (1) IAU name of the *2XMM* source. (2) Positional offset between the X-ray position and the optical position (in arcsec). (3) *SDSS* *r* band Petrosian magnitude. (4) Redshift from *SDSS*. (5) Logarithm of $f_{0.2-12\text{keV}}$ from *2XMM*. (6) $\log(f_X/f_O)$ defined as $\log f_{0.2-12\text{keV}} + r/2.5 + 5.5$. (7) Logarithm of $L_{0.2-12\text{keV}}$. (8) Classification from this work. “AGN(L)” denote LINER 2s. “AGN(S)” denote Seyfert 2 galaxies. “SF” denote SF galaxies. “COM” denote composite galaxies. “UNC” denote unclassified NELGs. . 127

Chapter

1

Introduction

1.1 Brief History of X-ray Astronomy

Studying astronomical objects in the X-ray band is a relatively young science that only became possible when humans were able to send detectors above the atmosphere, which absorbs most cosmic X-rays. From the early stage of X-ray astronomy, when X-ray detectors were placed on board sounding rockets and high altitude balloons, to nowadays when X-ray observatories are launched into space, our understanding of cosmic X-ray-emitting objects has significantly advanced in the last 60 years. Various types of astronomical objects are now known to be X-ray emitters (*e.g.*, stars, neutron stars, supernova remnants [SNRs], hot gas in galaxies and clusters, and active galactic nuclei [AGN]).

The discovery of the first extra-solar X-ray source (Sco X-1) in 1962 came as a surprise because the rocket experiment was originally designed to detect X-ray emission from the Moon (Giacconi et al. 1962). This discovery was seen to mark the real beginning of X-ray astronomy. The cosmic X-ray background - X-ray radiation with almost uniform intensity across the whole sky - was also detected for the first time in this rocket flight (Giacconi et al. 1962). Following rocket flights in the 1960s, the first orbiting X-ray observatory, *UHURU* (USA), was launched in 1970. *UHURU* carried out the first all-sky survey in X-rays (2–20 keV; Giacconi et al. 1971) and increased the number of known X-ray sources to 339 (Forman et al. 1978). *UHURU* also discovered diffuse X-ray emission from clusters of galaxies (*e.g.*, Kellogg et al. 1971; Gursky et al. 1971; Forman et al. 1972). A succession of other X-ray missions

were launched in the 1970s, including *Ariel 5* (UK/USA), *SAS-3* (USA), *OSO-8* (USA), *HEAO-1* (USA) and *Einstein* (USA). *HEAO-1*, the first of the NASA High Energy Astrophysical Observatories series, was launched in 1977 and provided the first measurement of the cosmic X-ray background spectrum (Marshall et al. 1980). The second of the series, *HEAO-2*, later renamed as the *Einstein* observatory, was launched in 1978 and carried the first fully imaging X-ray telescope into space (Giacconi et al. 1979). With improved angular resolution (a few arcsec) and sensitivity (a few hundred times greater than previous missions), *Einstein* was able to detect hundreds of normal galaxies whose X-ray emission was not dominated by luminous AGN, resolve numerous individual X-ray sources in nearby galaxies, and also discovered hot interstellar medium (ISM) in elliptical galaxies (Fabbiano 1989 and references therein).

The *Roentgen Satellite (ROSAT)*, a collaboration between Germany, the United States and the United Kingdom, was launched in 1990. The angular resolution of *ROSAT* was comparable to *Einstein* but had lower background and extended to lower X-ray energy (down to ~ 0.1 keV), which made it more suitable for studying the gas component within galaxies. The *ROSAT* All Sky Survey (RASS) was conducted in the 0.1–2.4 keV band and yielded catalogues with more than 100,000 sources (Voges et al. 1999, 2000). In addition, the *ROSAT* Deep Survey resolved ~ 70 – 80% of the 0.5–2 keV cosmic X-ray background (at a limit of $\sim 10^{-15}$ erg s $^{-1}$ cm $^{-2}$) into discrete sources (Hasinger et al. 1998).

After the successes of three modest scale missions in the late 1970s and 1980s, *Hakucho (CORSA-B)*, *Tenma (Astro-B)* and *Ginga (Astro-C)*, in 1993 Japan launched its fourth X-ray observatory, *ASCA* (Advanced Satellite for Cosmology and Astrophysics; Tanaka et al. 1994), for which the United States also provided part of the scientific payload. Charge Coupled Device (CCD) detectors were introduced into X-ray astronomy through this satellite. The good spectral resolution provided by these CCD detectors allowed detailed studies of X-ray sources in ~ 0.5 – 10 keV range and detected for the first time broad Fe line(s) in AGN (Tanaka et al. 1995), an indicator of a strong gravitational field around a black hole.

The year 1999 saw the launches of the most powerful X-ray observatories to date, *Chandra* (Weisskopf et al. 2000) and the *X-ray Multi-Mirror Mission (XMM-Newton)* (Jansen et al. 2001). The unprecedented angular resolution ($<1''$) of *Chandra* allows unambiguous detection of discrete X-ray sources within galaxies (see Fabbiano 2006 and references therein). *XMM-Newton* has more modest angular resolution but large collecting area and throughput. Further details of *XMM-Newton* will be given in § 2.1 and relevant important results will be discussed later in this thesis.

1.2 Important Processes in X-ray Astronomy

1.2.1 Radiation Mechanisms

Several physical processes are known to be important for the production of X-ray emission from astronomical objects. A brief description of these radiation mechanisms is given below:

1. *Blackbody Radiation*: A blackbody is an idealised concept, a perfect absorber and emitter, which is in thermal equilibrium and absorbs all radiation falling onto it. The spectral distribution of blackbody radiation is the Planck function, which gives the power per unit area, unit solid angle and unit frequency ν as:

$$B_\nu(T) = \frac{2h\nu^3}{c^2(e^{\frac{h\nu}{kT}} - 1)}, \quad (1.1)$$

where h is the Planck constant, k is the Boltzmann constant and c is the speed of light. The total luminosity from a spherical blackbody with radius R is $L = 4\pi R^2 \sigma_{SB} T^4$, where σ_{SB} is the Stephan-Boltzmann constant. The wavelength where the distribution peaks is directly related to the temperature of the source as $\lambda_{max} T = 2.9 \times 10^6 \text{ nm K}$ (Wien Displacement Law). Blackbody radiation from emitters with temperature $\gtrsim 10^6 \text{ K}$ will peak in the X-ray band. In detailed studies of individual black hole binaries, blackbody radiation has been found to give good approximation to the soft component observed in the X-ray spectra and is attributed to the accretion discs around the black holes (*e.g.*, McClintock & Remillard 2006).

2. *Thermal Bremsstrahlung Radiation*: The thermal bremsstrahlung radiation is produced when a charge is accelerated or decelerated in the Coulomb field of another charge. A fast-moving electron accelerates due to the Coulomb force from a positive atomic nucleus and produces radiation; this is called free-free emission as the electron is not bound to the atom before or after the event. In an optically-thin collisional thermal plasma in collisional equilibrium, the speeds of electrons follow a thermal distribution, and the bremsstrahlung process is referred to as thermal bremsstrahlung, which produces a continuum spectrum whose shape is determined by the plasma temperature. In a thermal bremsstrahlung spectrum, the power emitted per unit volume per unit frequency, j , is directly related to the temperature T and density of the plasma, and has the form:

$$j \propto n_e n_i T^{-1/2} e^{-\frac{h\nu}{kT}} G(\nu, T), \quad (1.2)$$

where n_e and n_i are the densities of electrons and ions respectively and $G(\nu, T)$ is the Gaunt factor which takes the approximate form $G(\nu, T) \approx (E/kT)^{-0.4}$ for photon energies $E = h\nu \approx kT$. Thermal bremsstrahlung radiation is observed in a wide range of environments, for instance, hot stellar coronae, shocked gas in SNR, the ISM as well as the intracluster media of clusters of galaxies (*e.g.*, Sarazin 1988; Paerels & Kahn 2003).

3. *Line Emission*: The emission from a plasma will also contain discrete emission lines produced by electrons making transitions from higher energy states to lower energy states (bound-bound). The presence of a particular emission line depends on the excitation mechanism (*i.e.*, collisional or photoionized), the temperature as well as the abundance of the plasma; whilst the actual line strength is determined by the density (in the case of collisional equilibrium) or the column density (in the case of photoionization equilibrium). Common lines visible in the X-ray band include lines from $K\alpha$, $K\beta$ and $L\alpha$ transitions of C, O, N, Si, S, Mg, and Fe. In particular, the most notable feature in the X-ray spectra of X-ray binaries and AGN is the Fe $K\alpha$ line at 6.4 keV which is thought to due to fluorescence from cold material close to the compact object (*e.g.*, Nandra & George 1994; Risaliti & Elvis 2004; Netzer 2006).
4. *Synchrotron Radiation*: Synchrotron radiation is produced by relativistic electrons being accelerated around magnetic field lines. Electrons which follow a power-law energy distribution with electron number index p produce a synchrotron spectrum which is a power-law with the energy index $\alpha = (p - 1)/2$. Since synchrotron radiation requires continuous supply of high-energy electrons and magnetic fields, it is expected to be important in sources such as pulsar wind nebulae and jets from accreting black holes (*e.g.*, Worrall 2009).
5. *Inverse Compton Scattering*: In Compton scattering an energetic photon collides with a free electron and transfers energy to the electron. The case where a low energy photon gains energy from a fast-moving electron in the collision is referred to as Inverse Compton scattering. Inverse Compton scattering from electrons with a power-law distribution characterised by electron number index p will produce a spectrum as another power-law whose energy index α is directly related to p as $\alpha = (p - 1)/2$. The power-law X-ray spectra observed in X-ray binaries and AGN are believed to be produced by Inverse Compton scattering of photons from the accretion discs (*e.g.*, Haardt & Maraschi 1991, 1993). In the 2–10 keV X-ray band, up to a few percent of this primary emission can also be reflected via Compton scattering (without changing the power-law slope) (Ghisellini et al. 1994).

6. *Photoelectric Absorption*: Photoelectric absorption occurs when a photon interacts with an atom and is completely absorbed. The photon energy either ejects one of the orbital electrons surrounding the nucleus or excites a transition to a higher energy level. The effective absorption of X-ray depends on the column density of the absorbing material and of course its composition. The main contributions to the photoelectric absorption opacity in the X-ray band are the elements C, O, Ne, Mg, Al, Si, S, Ca, and Fe. The magnitude of the absorption is normally parameterised by an equivalent hydrogen column density and assuming standard relative abundances of the relevant elements. Photoelectric absorption is strongly energy dependent (because of the strong energy-dependence of the cross sections), producing a large effect on the low energy part of the observed X-ray spectra. Photoelectric absorption for lines of sight within the ISM in the Galaxy has typical column density values of 10^{20} to 10^{22} atoms cm^{-2} . Photoelectric absorption is often also seen from material local to the source and the form of the absorption can be significantly modified if the absorbing material is partially ionized.

1.2.2 Accretion

Accretion is an important mechanism in X-ray Astronomy because it is believed to be one of the main power sources producing high energy radiation in the universe. A massive object gradually gains more mass by gravitationally attracting additional matter by accretion. If the material being attracted towards the massive object possesses angular momentum, it cannot fall into the object until a disc is formed, through which the angular momentum can be transferred outwards by viscosity (*e.g.*, Shakura & Syunyaev 1973). Figure 1.1 gives an illustration of a black hole binary system in which the black hole is accreting from a star via an accretion disc. The gravitational potential energy released by the accretion of a mass m on to a object with mass M and radius R is:

$$\Delta E_{acc} = GMm/R, \quad (1.3)$$

where G is the gravitation constant. The accretion luminosity is defined as:

$$L_{acc} = GM\dot{m}/R, \quad (1.4)$$

where \dot{m} is the accretion rate. Accretion on to a neutron star with solar mass and $R \sim 10$ km can release ~ 17 times more energy than that obtained by a nuclear fusion reaction (converting hydrogen to helium) for the same mass (Frank et al. 2002). Thus accretion is a very efficient energy release mechanism.

The Eddington luminosity (or Eddington limit) is the limit of luminosity that an accretion system can achieve via a steady and spherically symmetric accretion flow. Assuming the in-falling material to be fully ionized hydrogen and the radiation pressure mainly due to Thomson scattering, the limit is given when the outwards radial force, $\sigma_T L_{acc}/(4\pi r^2 c)$, equals to the inwards gravitational force, $GM(m_p + m_e)/r^2$ ($\cong GMm_p/r^2$):

$$\frac{\sigma_T L_{acc}}{4\pi r^2 c} = \frac{GMm_p}{r^2}, \quad (1.5)$$

$$\Rightarrow L_{Edd} = 4\pi GMm_p c / \sigma_T \cong 1.3 \times 10^{38} (M/M_\odot) \text{erg s}^{-1}, \quad (1.6)$$

where σ_T is the Thomson cross-section and r is the radial distance from the centre of the accreting object.

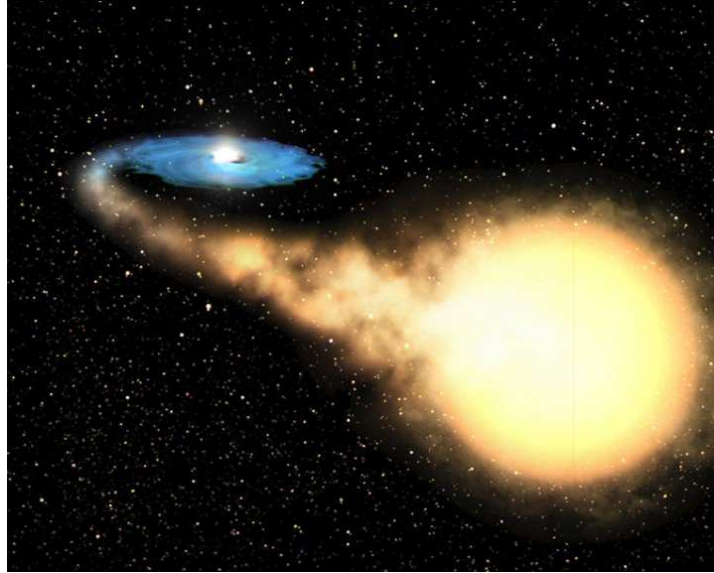


Figure 1.1: An illustration of a black hole accreting from a star via an accretion disc in an X-ray binary system (credit: ESA, NASA, and Felix Mirabel; taken from http://chandra.harvard.edu/press/07_releases/press_010307.html).

1.3 X-ray Components in Galaxies

In this section a brief description is provided for a variety of significant astronomical X-ray populations, for whose X-ray emission the physical processes described in the previous section are responsible.

1.3.1 X-ray Binaries

X-ray binaries, being the first X-ray sources discovered outside the Solar system (*e.g.*, Giacconi et al. 1962; Bowyer et al. 1965), have been found to be an important component of the X-ray populations in galaxies (*e.g.*, Helfand 1984; Fabbiano 1989; Tauris & van den Heuvel 2006; Fabbiano 2006). Several hundred X-ray binaries have been identified in the Milky Way and collectively these binaries contribute most of the X-ray emission of our Galaxy (Watson 1990). High mass X-ray binaries (HMXBs), consisting of a neutron star or black hole fed typically by stellar wind from a star with mass $\gtrsim 10M_{\odot}$, and low mass X-ray binaries (LMXBs), in which a low mass star ($\lesssim 1M_{\odot}$) loses mass to a neutron star or black hole predominantly via Roche-lobe overflow, constitute more than 90% of the most luminous Galactic X-ray sources (Tauris & van den Heuvel 2006). The relative contributions of different types of binaries largely depends on the type of the galaxy. In the Milky Way, the integrated luminosity of LMXBs is ~ 5 times that of HMXBs (Watson 1990). Figure 1.2 gives an illustration of X-ray binaries in a nearby spiral galaxy.

HMXBs, with the high mass companion stars which will evolve on a short timescale ($\sim 10^5$ – 10^7 yr, Tauris & van den Heuvel 2006) are associated with young stellar populations. Typically the X-ray spectra of this population can be fitted with a power-law with $\Gamma \sim 1$ – 2 (*e.g.*, Grimm et al. 2007). HMXBs can contribute a dominant fraction of the X-ray emission of star-forming (SF) galaxies (Helfand & Moran 2001) and thus can serve as an indicator of the recent star-formation rate (SFR) (*e.g.*, Fabbiano & Trinchieri 1985; Fabbiano et al. 1988; Grimm et al. 2003; Ranalli et al. 2003; Colbert et al. 2004; Gilfanov et al. 2004; Persic et al. 2004). Galactic HMXBs have X-ray luminosities in the range of $\sim 10^{34}$ – 10^{38} erg s $^{-1}$ (*e.g.*, Watson 1990; Grimm et al. 2002).

Although LMXBs had long been suggested to contribute a dominant fraction of the X-ray emission in early-type galaxies (Fabbiano 1989), it was not until the time of *Chandra* when they were resolved individually for the first time in external early-type galaxies (NGC4697 was the first reported early-type galaxy to host such population; Sarazin et al. 2000; see Figure 1.3). Since then there has been a large and growing body of work concerning LMXBs in early-type galaxies. Typically the spectra of LMXBs can be fitted with a power-law with photon index $\Gamma \approx 1.6$ or alternatively with a bremsstrahlung with $kT \approx 7$ keV (Irwin et al. 2003). LMXBs in the Milky Way have X-ray luminosities in the range of $\sim 10^{35}$ – 10^{38} erg s $^{-1}$ (*e.g.*, Watson 1990; Grimm et al. 2002), although in external galaxies sources with $L_X \lesssim 10^{36}$ erg s $^{-1}$ are difficult to detect with current observational sensitivity. The number of

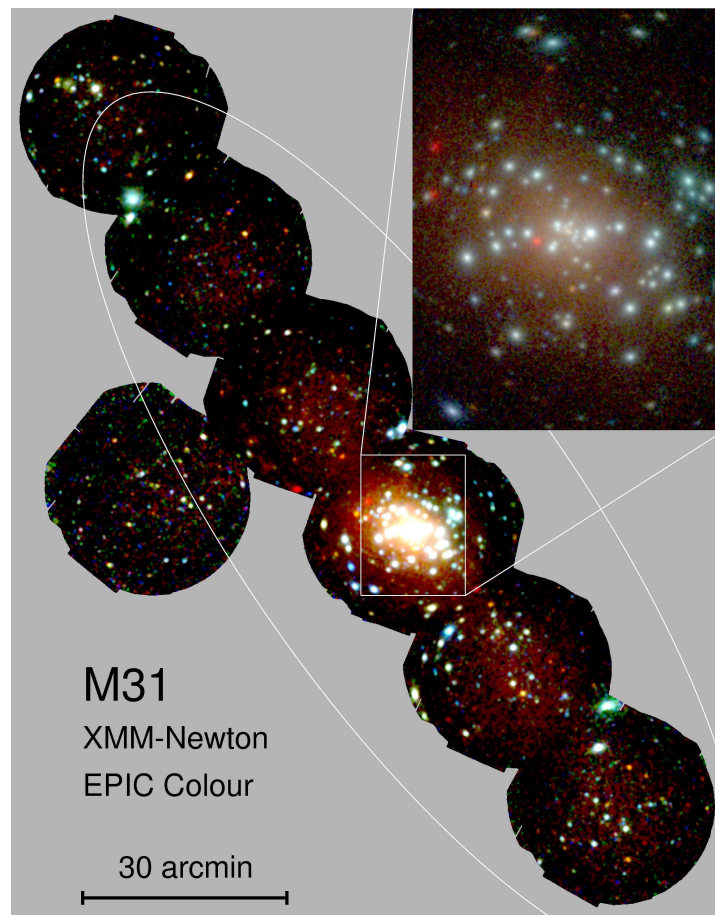


Figure 1.2: A mosaic and a zoom-in image (red: 0.2-1.0 keV; green: 1.0-2.0 keV; blue: 2.0-12.0 keV; white ellipse: the optical extent of the galaxy) from *XMM-Newton* observations covering the Andromeda galaxy (M31), the nearest massive spiral galaxy, in which X-ray binaries (point sources) are clearly seen (image courtesy of W. Pietsch, MPE Garching and *ESA*; taken from http://xmm.esac.esa.int/external/xmm/_science/gallery/images/1990f4.jpg).

detected X-ray sources which are likely to be LMXBs in external galaxies ranges from a few to a few hundred (*e.g.*, Fabbiano & White 2006 and references therein). It has also been found that in early-type galaxies $\sim 10\text{--}70\%$ of the LMXBs appear to be associated with globular clusters of the host galaxy (see review by Fabbiano 2006 and references therein).

1.3.2 Active Galactic Nuclei

Although normal galaxies are believed not to be dominated by active galactic nuclei (AGN), as discussed later in this thesis, the AGN contamination is an important consideration, therefore a brief description of AGN is provided.

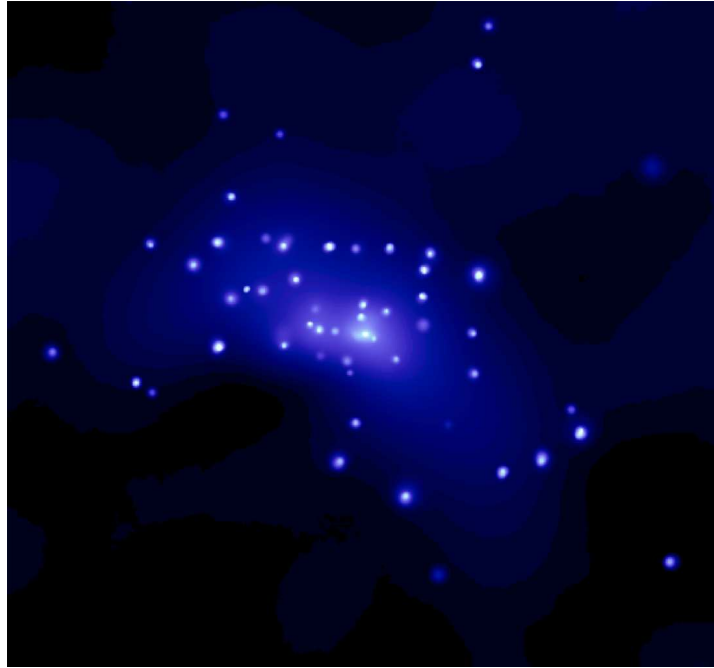


Figure 1.3: *Chandra* image ($4' \times 4'$) of the elliptical galaxy NGC 4697 in which X-ray binaries are clearly seen as point sources along with the diffuse emission (credit: NASA, CXC, UVA and C.Sarazin et al. ; taken from <http://chandra.harvard.edu/photo/2002/1140/>).

AGN were first discovered as extremely bright galactic centres which can outshine the host galaxies. It is widely accepted that the power source of AGN is the accretion of matter onto a super massive black hole ($\sim 10^6$ – $10^{10} M_{\odot}$) in the centre of the host galaxy, since gravitational accretion of matter is the only plausible mechanism to produce the persistent high luminosities observed from AGN (bolometric luminosities $\sim 10^{42}$ – $10^{48} \text{ erg s}^{-1}$). The term ‘quasar’ stands for quasi-stellar radio source and was originally applied to radio-loud objects. Radio-quiet objects were originally referred to as quasi-stellar objects (QSOs). Recently, the term ‘quasar’ has come to be used to refer to any luminous AGN. Seyfert galaxies, originally classified by Seyfert (1943), denote AGN whose host galaxy is clearly seen. Low ionization nuclear emission regions (LINERs), originally defined by Heckman (1980), are often included as a subtype of AGN with luminosities even lower than Seyfert galaxies. In general, the X-ray spectra of AGN in the range of ~ 1 – 10 keV can be well described by a single power-law with slope of ~ 1.8 – 2.0 (Risaliti & Elvis 2004). The most successful model to date to produce such a power-law spectrum is inverse Compton scattering. Soft emission (below 2 keV), the so-called ‘soft excess’, is often observed superimposed on the hard continuum (*e.g.*, Wilkes & Elvis 1987).

AGN are subdivided into two types, broad line AGN (Type 1 AGN) or narrow line AGN (Type 2

AGN), depending on whether broad emission line(s), with full width at half maximum (FWHM) width $\gtrsim 2000 \text{ km s}^{-1}$, are detected or not in the optical/UV spectra. This nomenclature, originally introduced to classify Seyfert galaxies (Seyfert 1 and Seyfert 2 galaxies) and then quasars (Type 1 and Type 2 quasars), has been extended to LINERs (Ho et al. 1997a,b; Ho 2008). It has been found that some Seyfert galaxies have narrow permitted lines which are slightly broader than forbidden lines and strong Fe II lines; these are called narrow line Seyfert 1 (NLS 1) galaxies (*e.g.*, Davidson & Kinman 1978; Osterbrock & Pogge 1985; Goodrich 1989; Grupe 2000; Pogge 2000). Other classification schemes exist for AGN, for instance, one using radio loudness, defined as $R_L = \log(f_{5\text{GHz}}/f_B)$ where $f_{5\text{GHz}}$ is the radio flux at 5 GHz and f_B is the B band flux. Using this classification, objects with $R_L \geq 10$ are referred to as radio-loud objects and the rest are referred to as radio-quiet objects. Instead of using the term ‘Type 1’ or ‘Type 2’, radio-loud AGN are often labelled as broad line radio galaxies (BLRGs) or narrow line radio galaxies (NLRGs). Following Fanaroff & Riley (1974), radio galaxies can be further divided into two subclasses depending on whether the radio morphology is core dominated or lobe dominated: the Fanaroff-Riley 1 (FR 1) radio galaxies and the Fanaroff-Riley 2 (FR 2) radio galaxies.

The detection of a broad emission line in a spectropolarimetric observation of the Seyfert 2 galaxy NGC 1068 (Antonucci & Miller 1985) led to the development of unification models to unify the Type 1 and Type 2 AGN (Antonucci 1993; Urry & Padovani 1995). In the most widely accepted unification model, both Type 1 and Type 2 AGN are powered by accretion onto a black hole, broad lines are from the broad line region (BLR) which is close to the black hole, narrow lines are from the narrow line region (NLR) which is much further away from the black hole. Between the BLR and NLR there is obscuring matter which can block part of the central region. Type 1 AGN are those in which the nuclei region can be seen directly. When the obscuring matter blocks the line of sight, the nuclear region and therefore the BLR can not be seen, the AGN is then spectroscopically classified as Type 2.

In X-rays Type 2 AGN are expected to be more obscured than Type 1 AGN. When the obscuration is less than a few $10^{24} \text{ atoms cm}^{-2}$, the primary power-law component can reveal itself above $\sim 6 \text{ keV}$, in which case its X-ray spectrum observed by *XMM-Newton* can be used to constrain the obscuration. However, when the obscuration is larger than $10^{24} \text{ atoms cm}^{-2}$, X-rays below 10 keV cannot penetrate and therefore X-ray observations above 10 keV are needed to constrain the obscuration. According to unification models, the emission from the NLR is not blocked by the torus and hence can “see” the isotropic emission from the black hole independent of the Type 1/Type 2 classification. Under this assumption, Type 2 AGN are expected to have lower X-ray luminosities than Type 1 AGN at a given

NLR luminosity.

There are also observational results that cannot be explained by unification models, *e.g.*, low luminosity AGN (LLAGN; Ho et al. 1997a) which are often also Type 2 AGN but show little evidence for X-ray absorption (*e.g.*, Panessa & Bassani 2002). For such cases models that require weak or absent BLR have been developed (see Ho 2008, and references therein).

1.3.3 Ultraluminous X-ray Sources

Ultraluminous X-ray sources (ULXs) were first discovered by *Einstein* (*e.g.*, Long & van Speybroeck 1983; Fabbiano & Trinchieri 1987). These sources are defined as extra-nuclear sources with X-ray luminosities greater than 10^{39} erg s⁻¹, the Eddington limit for spherically symmetric accretion onto a $\sim 7M_{\odot}$ compact object. Various models have been developed to explain the high luminosities of ULXs. These models include accretion onto intermediate-mass black holes ($\sim 10^2$ – $10^5 M_{\odot}$; *e.g.*, Colbert & Mushotzky 1999; Makishima et al. 2000; Miller et al. 2003), accretion onto stellar-mass black holes and radiating with anisotropic radiation patterns (*e.g.*, King et al. 2001) or relativistic beaming (*e.g.*, K rding et al. 2002), or accretion onto a stellar-mass black hole via super-Eddington accretion discs (Begelman 2002). Most of the ULXs known have been found in pointed observations of specific galaxies. Serendipitous discoveries of ULXs have also been reported (Watson et al. 2005).

1.3.4 Supernova Remnants

When a star undergoes a supernova explosion, much of its material is ejected into the surrounding ISM at a very high velocity to form a shock wave. The ejected material and the ISM swept up by the expanding shock wave are referred to as a supernova remnant (SNR). The ISM in a SNR can be shock heated to 10^7 – 10^8 K. X-ray emission from synchrotron radiation is also observed in SNR (*e.g.*, Ballet 2006). Individual SNR in the Milky Way and nearby galaxies (*e.g.*, Magellanic Clouds) have $L_X \sim 10^{35}$ – 10^{37} erg s⁻¹ (*e.g.*, Long & Helfand 1979; Watson 1990); the collective contribution of SNRs to these galaxies can be up to 10^{38} erg s⁻¹ (Watson 1990).

1.3.5 Hot ISM in Spiral Galaxies

The diffuse X-ray emission found in spiral galaxies is believed to originate from hot ISM shock heated by stellar winds and/or supernovae (*e.g.*, Cox & Smith 1974; Bregman 1980; Chevalier & Clegg 1985; Heckman et al. 1990; Grimes et al. 2005). The spectrum of this emission is usually characterised by thermal emission from gas with $kT \sim 0.2\text{--}0.8$ keV (*e.g.*, Grimes et al. 2005; Li et al. 2007). Two-temperature fitting ($kT \sim 0.2$ keV and $kT \sim 0.7$ keV) have also been reported for spectra with better signal-to-noise ratios (*e.g.*, Fraternali et al. 2002; Kuntz et al. 2003). This diffuse component has luminosity in the range of $\sim 10^{37}\text{--}10^{41}$ erg s $^{-1}$ in galaxies (*e.g.*, Fabbiano & Trinchieri 1987; Fabbiano 1989; Read et al. 1997; Warwick et al. 2007). In some galaxies this soft diffuse X-ray emission is found to be associated with spiral arms where star formation is maximum (*e.g.*, Tyler et al. 2004; see Figure 1.4).

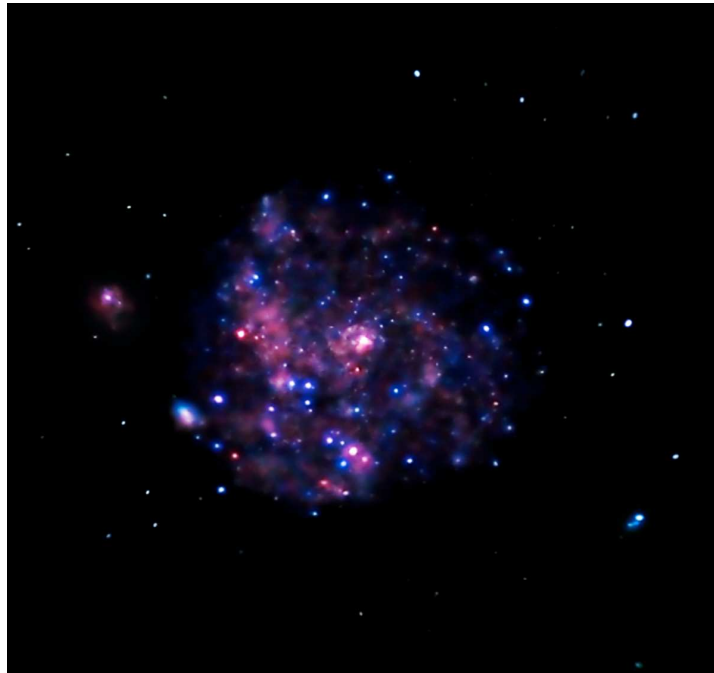


Figure 1.4: *Chandra* image (purple: 0.45–1 keV; blue: 1–2 keV; $16.8' \times 16.8'$) of spiral galaxy M101, in which the X-ray emission loosely shows the spiral structures (taken from <http://chandra.harvard.edu/photo/2008/m101/>; credit: NASA, CXC, JHU and K.Kuntz et al.).

Diffuse X-ray emission is also an important component of starburst galaxies, galaxies characterised by a very high rate of star formation (Weedman et al. 1981). In starburst galaxies the integrated effects of supernovae and strong stellar winds from early-type stars can form a so-called “superwind” which shocks to produce a thermal plasma visible as luminous, large-scale diffuse X-ray emission

(*e.g.*, Chevalier & Clegg 1985). In edge-on starburst galaxies this diffuse X-ray emission is particularly easy to detect (*e.g.*, Watson et al. 1984; Strickland et al. 2000, 2004a,b; a few examples are shown in Figure 1.5).

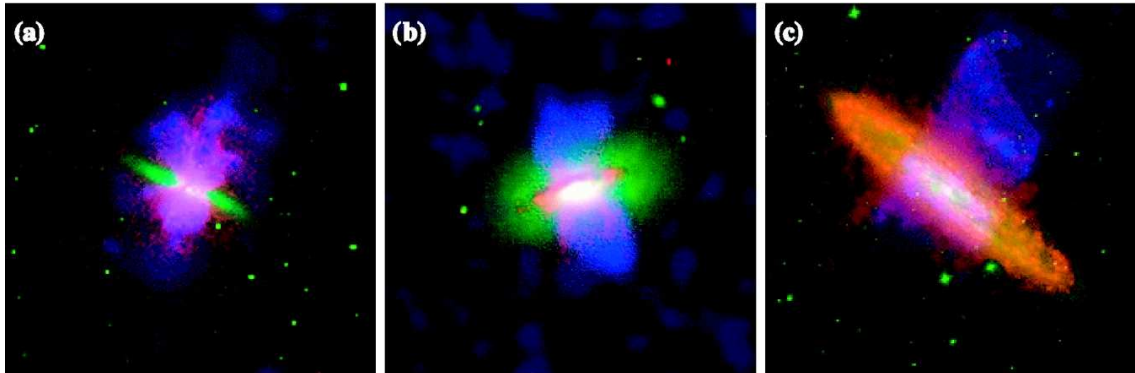


Figure 1.5: Shown here are examples of superwinds from starburst galaxies (a) M82, (b) NGC 1482 and (c) NGC 253 (reproduced by permission of the AAS from Figure 2 (a), (b) and (c) of *A High Spatial Resolution X-Ray and H α Study of Hot Gas in the Halos of Star-forming Disk Galaxies. II. Quantifying Supernova Feedback*, Strickland et al. 2004b, *ApJ*, Volume 606, Issue 2, pp. 836). The 0.3–2 keV X-ray emission is shown in blue, H α emission in red and the optical *R* band emission in green.

1.3.6 Hot ISM in Elliptical Galaxies

The discovery of hot gas within elliptical galaxies dates back to the *Einstein* era (Forman et al. 1979); previously early-type galaxies were believed to be gas-poor systems (see Fabbiano 1989 and references therein). Since then this hot gaseous component has been studied extensively by *ROSAT* and more recently by *XMM-Newton* and *Chandra*. The X-ray spectra from elliptical galaxies show that the temperature of the gas is typically fairly low, ~ 0.3 keV from *Chandra* data (*e.g.*, Sarazin et al. 2001). This component can contribute substantially to the total X-ray emission from early-type galaxies ($\sim 23\%$ – 50% ; *e.g.*, Sarazin et al. 2000; Sivakoff et al. 2003) and can reach a luminosity as high as 10^{43} erg s $^{-1}$ (*e.g.*, O’Sullivan et al. 2001).

1.4 X-ray Studies of Normal Galaxies

Throughout this thesis the term ‘normal galaxy’ is used to refer to a galaxy whose emission is not dominated by an AGN. In the optical band, normal galaxies can be absorption line galaxies (ALGs), whose

spectra are absorption-line-dominated, or narrow emission line galaxies (NELGs), if the narrow emission lines detected in their spectra do not indicate AGN presence (see § 1.4.3). Thus, star-forming galaxies and even starburst galaxies fall into the ‘normal galaxies’ category. In practice, defining whether a galaxy is a normal galaxy or not is sometimes difficult as the relative contribution from a possible AGN can vary significantly from one energy band to the other. Without the effects of AGN activity (§ 1.3.2), X-ray observations of normal galaxies provide information on the X-ray binary population and hot ISM.

Studies of normal galaxies in X-rays date back to the beginning of X-ray astronomy and have provided a growing body of knowledge of our own Galaxy and nearby galaxies. Although individual normal galaxies for which detailed studies are possible with current observational capabilities are still far much nearer than AGN, statistical studies of normal galaxies can be carried out using data from deep or large surveys.

1.4.1 General Results

X-ray studies of normal galaxies before *Einstein* were restricted to only four galaxies: the Milky Way, M31, and the Magellanic Clouds (see Helfand 1984). *Einstein* significantly extended X-ray studies, allowing both detailed investigations of individual galaxies and surveys of a few hundred normal galaxies (see Fabbiano 1989 and references therein; see also Fabbiano et al. 1992). *Einstein* observations of the Milky Way and the Local Group galaxies revealed that individual bright sources (binaries and SNRs) were responsible for the bulk of the X-ray emission with integrated luminosities in the range of $\sim 10^{38} - 10^{41} \text{ erg s}^{-1}$ (e.g., Long & van Speybroeck 1983; Fabbiano et al. 1984; Fabbiano 1986, 1989). *Einstein* detected diffuse X-ray emission from spiral galaxies in the Local Group (M33 – Trinchieri et al. 1988) and more distant galaxies (e.g., NGC 4631 – Fabbiano & Trinchieri 1987) which was consistent with the prediction of thermal emission from the ISM effectively heated to the X-ray range by supernovae (e.g., Cox & Smith 1974; Bregman 1980). ULXs were discovered in a few galaxies (e.g., Fabbiano & Trinchieri 1987). *Einstein* revealed that galaxies with strong starburst activity could have L_X up to $10^{42} \text{ erg s}^{-1}$ and higher X-ray-to-optical flux ratios than normal SF galaxies, although still lower than AGN (e.g., Fabbiano et al. 1982). Extended diffuse emission related to starburst activity was evident in detailed studies of starburst galaxies (e.g., Weedman et al. 1981; Watson et al. 1984; Fabbiano & Trinchieri 1984; Fabbiano 1988), and for the first time, in edge-on starburst galaxies, such as M82,

gaseous outflows from the nuclei region were observed (Watson et al. 1984). These are believed to arise from gas that is shock heated by supernova explosions and stellar winds (Chevalier & Clegg 1985; Suchkov et al. 1994; Grimes et al. 2005).

Einstein detected for the first time hot ISM in elliptical galaxies (Forman et al. 1979), which could be fitted with temperatures $kT \sim 0.5\text{--}2.0$ keV (*e.g.*, Forman et al. 1985; Trinchieri et al. 1986). Such galaxies had X-ray luminosities in the range of $\sim 10^{39}\text{--}10^{42}$ erg s⁻¹ in the *Einstein* band (see Fabbiano 1989 and references therein).

ROSAT and *ASCA* have substantially extended the studies of normal galaxies although did not reveal significantly new findings.

With *Chandra* and *XMM-Newton*, X-ray studies of normal galaxies have advanced significantly. For instance, the sub-arcsec spatial resolution provided by *Chandra* allowed the first direct detections of LMXBs in external early-type galaxies (Sarazin et al. 2000). *XMM-Newton* has provided detailed studies of the X-ray binary populations in many nearby galaxies and spectroscopic measurements of the hot gas components.

In late-type galaxies X-ray emission can serve as a SFR indicator as the dominant X-ray components in these galaxies, both the hot ISM and HMXBs, are directly related to recent star formation. Strong correlations between X-ray emission and conventional SFR indicators (*e.g.*, infrared luminosities [Kennicutt 1998] and radio luminosities [Condon 1992]) have been found in late-type galaxies (Fabbiano et al. 1988; David et al. 1992; Read & Ponman 2001; Fabbiano & Shapley 2002; Ranalli et al. 2003; Lou & Bian 2005).

1.4.2 Normal Galaxies from X-ray Surveys

Normal galaxies have been found in general to have lower X-ray-to-optical flux ratios than AGN in various X-ray surveys¹ (*e.g.*, Medium Sensitivity Survey [MSS] – Stocke et al. 1983; Extended Medium Sensitivity Survey [EMSS] – Gioia et al. 1984; Maccacaro et al. 1988). This is one of the principle

¹The X-ray-to-optical flux ratio has been defined using various bands in the X-ray according the instrument used for the survey, *e.g.*, in MSS and EMSS the 0.3–3.5 keV flux was used (Maccacaro et al. 1982; Stocke et al. 1983; Gioia et al. 1984; Maccacaro et al. 1988).

ways that normal galaxies have been separated from AGN.

Early Einstein and ROSAT Surveys

In the EMSS 835 serendipitous X-ray sources were detected at or above 4σ level from 1435 imaging proportional counter (IPC) fields which covered a total area of 778 deg^2 and reached limiting sensitivities of $\sim 5 \times 10^{-14}$ – $3 \times 10^{-12} \text{ erg s}^{-1} \text{ cm}^{-2}$ (Gioia et al. 1987, 1990). In total 17 were identified as normal galaxies (Maccacaro et al. 1988; Stocke et al. 1991). These normal galaxies were all nearby galaxies ($z < 0.1$) with $\log(f_X/f_O) \lesssim -0.2$ while the AGN identified in EMSS had $\log(f_X/f_O) \gtrsim -1$ (Maccacaro et al. 1988; Gioia et al. 1990; Stocke et al. 1991).

ROSAT data, from both the Position Sensitive Proportional Counters (PSPC) and the High Resolution Imager (HRI), have also been used to search for normal galaxies (Zimmermann et al. 2001; Tajer et al. 2005). By cross-correlating the *ROSAT* All Sky Survey Bright Source Catalogue (RASS-BSC; Voges et al. 1999) with the Catalogue of Principal Galaxies (Paturel et al. 1989) and then excluding those associated with QSO, Seyfert galaxies, LINERs, or Blazars in the literature, Zimmermann et al. (2001) obtained a sample of 198 normal galaxies, which had fluxes of $\sim 10^{-12}$ – $\sim 10^{-10} \text{ erg s}^{-1} \text{ cm}^{-2}$ in 0.1–2.4 keV and $\log(f_X/f_O)$ ranging from ~ -4 to ~ 1 (using *B* band magnitudes). Tajer et al. (2005) carried out a cross-correlation between the *ROSAT* HRI Brera Multi-scale Wavelet (BMW-HRI) catalogue (Panzer et al. 2003) and the Lyon-Meudon Extragalactic Database (LEDA; complete to ~ 15.5 in the *B* band, Paturel et al. 1997) to obtain a sample of 143 normal galaxies from $\sim 314 \text{ deg}^2$. Their sample had 0.1–2 keV fluxes in the range of 10^{-14} – $10^{-11} \text{ erg s}^{-1} \text{ cm}^{-2}$, after rejecting previously reported Seyfert 1 galaxies, QSOs, and BL Lacs. Tajer et al. (2005) retained in their sample Seyfert 2 galaxies that associated with extended X-ray emission, LINERs and any others whose optical emission was not dominated by nuclear sources. Redshifts were available for $\sim 83\%$ (119/143) of these normal galaxies and these ranged from 0 to ~ 0.15 , corresponding to L_X of 10^{38} – $10^{43} \text{ erg s}^{-1}$ (assuming $H_0 = 50 \text{ km s}^{-1} \text{ Mpc}^{-1}$). A flux-limited serendipitous sample of 32 normal galaxies was then selected from these 143 galaxies for a $\log N$ - $\log S$ study. From this study they found that at $\gtrsim 10^{-14} \text{ erg s}^{-1} \text{ cm}^{-2}$ (0.5–2 keV) ~ 1.5 normal galaxies per deg^2 were expected. However, since these authors had to rely on literature to classify the galaxies, these samples in both Zimmermann et al. (2001) and Tajer et al. (2005) might not be unbiased.

XMM-Newton and Chandra Shallow Surveys

More recent work focusing on selecting normal galaxies from X-ray surveys have made extensive use of the X-ray-to-optical flux ratios, especially when complete spectroscopic coverage was not available. In the range $f_X \sim 10^{-15}$ – 10^{-13} erg s⁻¹ cm⁻², *XMM-Newton* data and/or *Chandra* data covering modest sky areas (~ 2 – 11 deg²) have been used to search for normal galaxies.

In a survey using *XMM-Newton* data cross-correlated with the *2dF* Galaxy Redshift Survey (*2dFGRS*; Colless et al. 2001) and reaching a flux limit of $\sim 10^{-14}$ erg s⁻¹ cm⁻² in the 0.5–8 keV range, Georgakakis et al. (2004a) obtained a sample of 26 sources with $\log(f_X/f_O) < -0.9$, amongst which two were classified as normal galaxies and another two were Type 2 LLAGN (all had redshifts < 0.09). This suggests that truly normal galaxies and narrow line LLAGN might have comparable fractions among galaxies with $\log(f_X/f_O) < -0.9$.

In the “Needles in the Haystack Survey” (NHS), Georgakakis et al. (2004b) used *XMM-Newton* archival data to cross-correlate with the *Sloan Digital Sky Survey* (*SDSS*) and found 11 normal galaxies serendipitously detected by *XMM-Newton* within a sky area of 4.5 deg². They required extended morphology in the optical, $\log(f_X/f_O) < -2$ and soft X-ray spectra (a power-law with $\Gamma = 1.9$ and free N_H was used to fit the spectra, so sources with N_H significantly greater than the Galactic value were rejected). Eight out of these 11 galaxies had optical spectra and therefore redshifts, all had $z \leq 0.15$. Six of their galaxies had optical narrow emission lines, amongst which three could be classified using emission line ratios (Ho et al. 1997a) and all were classified as SF galaxies. The authors did not find any Type 2 AGN using the emission line ratios in their sample since the only source classified as a Seyfert 2 galaxy by them was already rejected based on its X-ray spectrum. This implies that if X-ray spectra were not used in the selection function, the AGN contamination in galaxies with $\log(f_X/f_O) < -2$ would be $\sim 8\%$ (1/12), or one third if it was assumed that the three galaxies in their sample without spectra were all AGN. This study suggested ~ 0.2 normal galaxies per deg² could be found at $f_X \sim 6 \times 10^{-14}$ erg s⁻¹ cm⁻². NHS was later extended to cover 11 deg² and the number of normal galaxies increased to 28 (Georgantopoulos et al. 2005). In this extended NHS the soft X-ray spectra requirement was replaced with a hardness ratio ≤ 0 using 0.5–2 keV as the soft band and 2–8 keV as the hard band. This rejected three galaxies with $\log(f_X/f_O) < -2$, although four galaxies did not have enough X-ray photon counts to allow this selection and were therefore still kept in the normal galaxy sample. Twenty-three out of 28 galaxies had optical spectra, amongst which 16 showed narrow emission lines and all were classified as SF galaxies. Hence the suggested AGN contamination in galaxies with $\log(f_X/f_O) < -2$ was $\sim 10\%$ or $\sim 23\%$, assuming the four galaxies in their sample without hardness ratios were

all AGN.

Georgakakis et al. (2006) used the first *XMM-Newton* Serendipitous Source Catalogue (1*XMM*) and the US Naval Observatory A2.0 Catalogue (USNO-A2.0; see Monet et al. 2003) to select 102 X-ray sources with $\log(f_X/f_O) < -2$ (f_X in 0.5–2 keV band) over a sky area $\sim 6 \text{ deg}^2$. Twenty-eight sources were then selected as galaxies based on their optical morphologies and spectroscopy. Five of the 28 galaxies were classified as AGN based on their optical spectra, amongst which two had broad emission lines (spectra with $\sim 10\text{--}18\text{\AA}$ resolution). The normal galaxy number counts from this soft band selected sample was in agreement with the those from NHS, although the latter were derived from full band (0.5–8 keV) selected sample.

Tzanavaris et al. (2006) selected normal galaxies using 1*XMM* and XAssist (Ptak & Griffiths 2003) to cross-correlate with 2*d*FGRS without any flux ratio or luminosity selection in order to evaluate the effect of these two selection criteria. A sample of 18 galaxies was obtained from 1*XMM* and another with 20 galaxies from XAssist, both with similar flux limits ($\sim 10^{-15} \text{ erg s}^{-1} \text{ cm}^{-2}$) and within similar redshift ranges ($\lesssim 0.25$). About $\sim 23\%$ (11/48) of the combined sample were classified as either AGN, tentative AGN or tentative LINERs by these authors. These authors did not find any SF galaxies with $L_X > 10^{42} \text{ erg s}^{-1}$ although no starlight subtraction was carried out for the spectra and a few galaxies with $L_X > 10^{42} \text{ erg s}^{-1}$ remained unclassified. These authors further remarked that $\sim 40\%$ of the normal galaxies had $\log(f_X/f_O) > -2$ and the $\log(f_X/f_O) < -2$ criterion seemed to select against bright elliptical galaxies.

The effectiveness of the X-ray-to-optical flux ratio cut-off was also demonstrated by Georgakakis (2008) in which the prerelease version of the Second *XMM-Newton* Serendipitous Catalogue (2*XMM*p) was used to cross-correlate with *SDSS* and 48 normal galaxies were found (20 ALGs and 28 star-forming galaxies, classifications taken from Brinchmann et al. 2004; Kauffmann et al. 2004). By finding that about half of the ALGs and 30% of the SF galaxies had $\log(f_X/f_O) > -2$, a non-negligible incompleteness caused by the X-ray-to-optical flux ratios cut-off was suggested (Georgakakis 2008).

Using X-ray sources from *Chandra* Multiwavelength Project (ChaMP; Green et al. 2004; Kim et al. 2004a,b; Silverman et al. 2005), Kim et al. (2006) selected 36 normal galaxies by requiring $\log(f_X/f_O) < -2$ (f_X in 0.5–8 keV), amongst which 20 were NELGs. These normal galaxies spanned the redshift range of 0.01–0.3 and had 0.5–8 keV fluxes of $\sim 10^{-15}\text{--}10^{-12} \text{ erg s}^{-1} \text{ cm}^{-2}$.

In a similar redshift and X-ray flux range, Hornschemeier et al. (2005) obtained 42 galaxies by cross-correlating *Chandra* archival data with *SDSS* and found that $\sim 36\%$ had absorption-line dominated spectra and $\sim 17\%$ were SF galaxies (AGN and unclassified NELGs made up the rest).

Deep Chandra Surveys

In a fainter flux regime, $\sim 10^{-16}$ – 10^{-17} erg s $^{-1}$ cm $^{-2}$, *Chandra* deep surveys have been used to provide several samples of normal galaxies.

Hornschemeier et al. (2001) reported the detections of seven optically bright ($R \lesssim 21$), X-ray faint ($f_X \lesssim 3 \times 10^{-16}$ erg s $^{-1}$ cm $^{-2}$) sources in an area of $8.6' \times 8.7'$ in a deep *Chandra* survey of the Hubble Deep Field-North. These authors claimed that these sources might be the analogies of nearby normal galaxies at redshifts ~ 0.1 – 0.6 based on their X-ray luminosities, hardness ratios, optical luminosities and optical spectra (Hornschemeier et al. 2001).

Using data from the 2 Ms *Chandra* Deep Field North (CDF-N), which reached $\sim 10^{-17}$ erg s $^{-1}$ cm $^{-2}$ in the 0.5–2 keV band (Alexander et al. 2003), Hornschemeier et al. (2003a) selected a sample of 43 optically bright, X-ray faint ($\log(f_X/f_O) < -2.3$) sources and classified 36 of them as galaxies (redshifts ~ 0.06 – 0.845) based on their optical spectra. These authors found that 52% of the sample were normal galaxies, while starburst galaxies and LLAGN together could make up 33% of the sample and predicted ~ 300 normal galaxies per deg 2 could be detected at $\gtrsim 10^{-16}$ erg s $^{-1}$ cm $^{-2}$. Based on this study, Hornschemeier et al. (2003b) further remarked that normal galaxies might outnumber AGN at $f_X \lesssim 7 \times 10^{-18}$ erg s $^{-1}$ cm $^{-2}$ (0.5–2 keV).

A similar prediction was also made by Bauer et al. (2004) (Figure 1.6), in which data from the 1 Ms and 2 Ms CDF-N and the 1 Ms *Chandra* Deep Field South surveys (CDF-S; Rosati et al. 2002; Giacconi et al. 2002) were combined. This study allowed more than 100 galaxies to be classified as normal/SF galaxies based on their X-ray-to-optical flux ratios, X-ray spectra, intrinsic X-ray luminosities and optical spectra. Norman et al. (2004), by applying Bayesian statistical methods (X-ray luminosity, hardness ratio and X-ray-to-optical flux ratio from a well classified sample as priors) to the classification procedure of the X-ray sources from these deep surveys, identified 210 normal/SF galaxies up to redshift of 1.2. The discrepancy between the number of normal galaxies in Bauer et al. (2004) and Norman et al. (2004) might not be unexpected as the Bayesian approach took into account the intrinsic scatter of the input parameters rather than placing hard cut-offs on them.

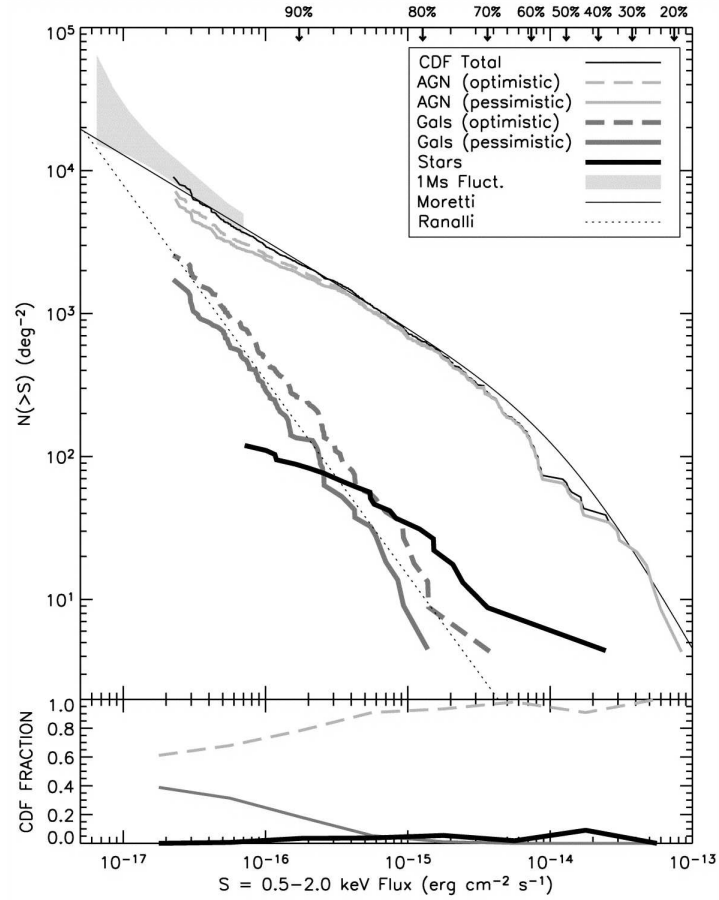


Figure 1.6: Plots of the soft band (0.5–2 keV) number counts for CDFs sources (top panel) and the fractions of these sources that belong to different subsamples (bottom panel) (reproduced by permission of the AAS from Figure 4 of *The Fall of Active Galactic Nuclei and the Rise of Star-forming Galaxies: A Close Look at the Chandra Deep Field X-Ray Number Counts*, Bauer et al. 2004, *AJ*, Volume 128, Issue 5, pp. 2052). The soft band (0.5–2 keV) number counts are shown for all sources in the CDFs (jagged black curves) and three subsamples: shown: AGN (solid and dashed gray curves), galaxies (solid and dashed dark gray curves), and stars (thick solid black curves). The results from the 1Ms CDF-N fluctuation analysis (Miyaji & Griffiths 2002) are marked as gray shaded areas. The thin solid black line marks the fitting from Moretti et al. (2003). The SF galaxy number counts (Ranalli et al. 2003) predicted from radio band (Richards 2000) are marked by the dotted line. At the top of the panels the fractions of the X-ray background resolved into discrete sources at a given flux calculated from the models in (Moretti et al. 2003) are shown. Extrapolations of these number counts suggest that galaxies will likely outnumber AGN at $\lesssim 5 \times 10^{-18} \text{ erg s}^{-1} \text{ cm}^{-2}$.

1.4.3 Diagnostic Methods

In order to select normal galaxies from an X-ray survey, one needs to separate AGN from normal galaxies. It is customary to assume that sources with $L_X \gtrsim 10^{43} \text{ erg s}^{-1}$ are AGN. However, identifying LLAGN and/or absorbed AGN from truly normal galaxies is not trivial.

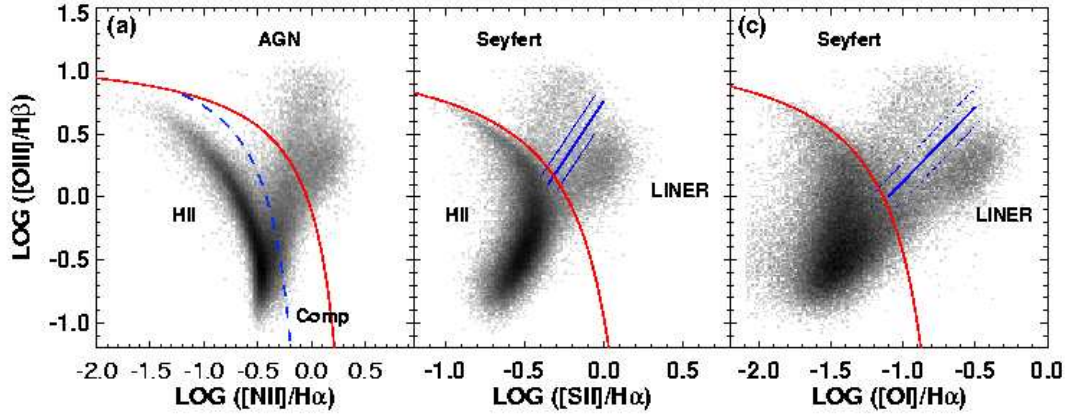


Figure 1.7: The Kewley et al. (2006) classification scheme uses three BPT plots (Figure 4 of *The host galaxies and classification of active galactic nuclei*, Kewley et al. 2006, *MNRAS*, Volume 372, Issue 3, pp. 964) to separate galaxies into SF galaxies (the region marked as ‘HII’ in the plots), AGN (further split into Seyfert 2 galaxies and LINER 2s) and composite galaxies (region marked as ‘Comp’ in [a]).

Baldwin et al. (1981, BPT hereafter) demonstrated that Type 2 AGN and SF galaxies could be empirically separated from each other using plots constructed with each axis presenting the ratio of a pair of strong emission lines. Such plots are commonly referred to as BPT plots. This BPT classification technique was then refined by Veilleux & Osterbrock (1987) and included plots of $[\text{O III}]\lambda 5007/\text{H}\beta$ versus $[\text{N II}]\lambda 6584/\text{H}\alpha$ (BPT [N II] plot), $[\text{O III}]\lambda 5007/\text{H}\beta$ versus $[\text{S II}]\lambda\lambda 6717, 6731/\text{H}\alpha$ (BPT [S II] plot) and $[\text{O III}]\lambda 5007/\text{H}\beta$ versus $[\text{O I}]\lambda 6300/\text{H}\alpha$ (BPT [O I] plot). Throughout this thesis the classification scheme from Kewley et al. (2006) is adopted. The Kewley et al. (2006) scheme is based on the three BPT plots and includes the ‘maximum starburst lines’ from Kewley et al. (2001), the pure SF line from Kauffmann et al. (2003b) and two newly introduced Seyfert/LINER dividing lines (Figure 1.7). This scheme classifies galaxies into SF galaxies, Seyfert 2 galaxies, LINER 2s and composite galaxies, the latter hosts a combination of SF galaxies and either a Seyfert 2 nucleus or a LINER 2. The Kewley et al. (2006) scheme is outlined below for clarity:

1. In the BPT [N II] plot (Figure 1.7(a)), galaxies are classified as SF galaxies if they satisfy

$$\log([O_{III}]/H\beta) < 0.61/(\log([N_{II}]/H\alpha) - 0.05) + 1.3, \quad (1.7)$$

or as AGN if they have

$$\log([O_{III}]/H\beta) > 0.61/(\log([N_{II}]/H\alpha) - 0.47) + 1.19, \quad (1.8)$$

or as composite galaxies if they sit between these two lines:

$$\log([O_{III}]/H\beta) < 0.61/(\log([N_{II}]/H\alpha) - 0.47) + 1.19, \quad (1.9)$$

$$\log([O_{III}]/H\beta) > 0.61/(\log([N_{II}]/H\alpha) - 0.05) + 1.3. \quad (1.10)$$

2. In the BPT [S II] plot (Figure 1.7(b)), SF galaxies are those with

$$\log([O_{III}]/H\beta) < 0.72/(\log([S_{II}]/H\alpha) - 0.32) + 1.30. \quad (1.11)$$

AGN are those with

$$\log([O_{III}]/H\beta) > 0.72/(\log([S_{II}]/H\alpha) - 0.32) + 1.30, \quad (1.12)$$

and are further separated into Seyfert 2 galaxies if they satisfy

$$\log([O_{III}]/H\beta) > 1.89 \log([S_{II}]/H\alpha) + 0.76, \quad (1.13)$$

or LINER 2s if they have

$$\log([O_{III}]/H\beta) < 1.89 \log([S_{II}]/H\alpha) + 0.76. \quad (1.14)$$

3. In the BPT [O I] plot (Figure 1.7(c)), galaxies are classified as SF galaxies if they satisfy

$$\log([O_{III}]/H\beta) < 0.73/(\log([O_I]/H\alpha) + 0.59) + 1.33. \quad (1.15)$$

AGN are those with

$$\log([O_{III}]/H\beta) > 0.73/(\log([O_I]/H\alpha) + 0.59) + 1.33, \quad (1.16)$$

and are further classified as Seyfert 2 galaxies if they have

$$\log([O_{III}]/H\beta) > 1.18 \log([O_I]/H\alpha) + 1.30, \quad (1.17)$$

or LINER 2s if they satisfy

$$\log([O_{III}]/H\beta) < 1.18 \log([S_{II}]/H\alpha) + 1.30. \quad (1.18)$$

Occasionally the three BPT plots may give an inconsistent classification for a given galaxy. Kewley et al. (2006) pointed out that $\sim 8\%$ of the $\sim 85k$ galaxies in their study fell into this category.

1.5 Aims and Outline of This Thesis

The original goal of this study was to search for ULXs in normal galaxies by using X-ray source lists from *XMM-Newton* serendipitous surveys to cross-correlate with large sky area optical surveys, such as *SDSS*, to obtain X-ray sources associated with galaxies, imposing an X-ray-to-optical flux ratio cut-off, an X-ray luminosity cut-off, and optical spectra free from broad lines to select galaxies which were not dominated by luminous AGN, and then looking for ULXs. Although it turned out to be very difficult to pursue this study, due to the problems with deciding whether a X-ray source was off-centre or not, given the angular sizes of most of the matching galaxies, this approach naturally led to the idea of studying X-ray-selected normal galaxy populations.

Unlike studies of optically-selected samples, dominated by well-known nearby objects, normal galaxy samples selected from X-ray serendipitous surveys can provide an unbiased foundation for exploring the following topics:

1. Different methods of selecting normal galaxies can be tested. Without optical classifications imposed as a prior, X-ray-selected normal galaxy samples are expected to contain a variety of types of objects, *e.g.*, Type 2 AGN, SF galaxies and ALGs. By varying the selection criteria, their effectiveness for selecting truly normal galaxies can be investigated and the relative fractions of different types of normal galaxies can be quantified.
2. The X-ray properties of normal galaxies within different optical classes can be examined to constrain the relative proportion of X-ray emission powered by different mechanisms and this can be compared with the optical classifications.
3. In particular, Type 2 AGN will be included in such normal galaxy samples so that the obscuration possibly present in the nuclear region can be investigated. On the other hand, such AGN can also be compared with the nearby detailed-studied LLAGN to gain insights into this population out to a few hundred Mpc.
4. For SF galaxies, the X-ray luminosities might be able to provide a measurement of SFR reasonably free from extinction from which the conventional SFR measurements (*e.g.*, from UV) suffer.

5. For galaxies without even weak AGN and/or SF activities, most of which are early-type galaxies, X-ray emission becomes an important and probably the most reliable way to constrain the amount of hot gas the galaxy possesses.

Chapter 2 presents the instrumentation as well as data reduction and analysis techniques. Chapter 3 covers a pilot study in which a sample of normal galaxy candidates was selected from the *XMM-Newton/2dF* Wide Angle Serendipitous Survey (XWAS) and classified into different types based on their optical spectra from the Anglo-Australian Telescope (AAT) Two Degree Field (*2dF*) multi-fibre spectrograph. However, detailed studies of different types of galaxies in this sample were limited by the quality of the optical spectra, *i.e.*, a large fraction of the sample could not be classified due to the low signal-to-noise ratios of the spectra. In Chapters 4 and 5, a large sample of normal galaxy candidates selected from the Second *XMM-Newton* Serendipitous Catalogue (*2XMM*) cross-correlated with *SDSS* is presented and classified. Thanks to better optical spectra and the availability of several important parameters obtained from the spectra, detailed studies of galaxies with different optical classification, *i.e.*, AGN, SF galaxies and ALGs, could be carried out. The construction and a brief summary of the sample are given in Chapter 4. The optical classification and discussions of different types of galaxies are presented in Chapter 5. A summary of this thesis and a description of future prospects for X-ray studies of normal galaxies are given in Chapter 6.

Throughout this thesis, $H_0 = 70 \text{ km s}^{-1} \text{ Mpc}^{-1}$ is adopted.

Chapter 2

Instrumentation and Data Analysis

2.1 The *XMM-Newton* Observatory

The X-ray data used in this thesis are based on observations taken by the *XMM-Newton* observatory (Jansen et al. 2001). *XMM-Newton* was developed by *ESA* as its second cornerstone mission of the Horizon 2000 science programme. It was launched on 10th December 1999 from Kourou, French Guiana and is still in operation. The satellite is in a 48-hour highly elliptical orbit with the perigee altitude of 7000 km and the apogee altitude of 114000 km, which makes uninterrupted scientific observation up to ~ 40 hours possible (Barré et al. 1999). An artistic view of *XMM-Newton* is shown in Figure 2.1.

XMM-Newton has two types of telescopes: three X-ray telescopes and one optical/UV telescope. The payload of *XMM-Newton* is shown in Figure 2.2. Fifty-eight Wolter-1 type mirror shells were nested in a coaxial and confocal configuration to form the optics of each of the three X-ray telescope (Aschenbach et al. 2000). This design provides each of the X-ray telescopes with a geometric effective area of $\sim 1500 \text{ cm}^2$. The optical/UV telescope (Optical Monitor, or OM; Mason et al. 2001), co-aligned with the X-ray telescopes, can carry out observation of the field of view of the X-ray telescopes in the visible and UV bands (1600–6000Å).

The European Photon Imaging Cameras (EPIC; Turner et al. 2001; Strüder et al. 2001) on the Focal Plane Assembly of *XMM-Newton* provide imaging and spectrometry for the three X-ray telescopes.

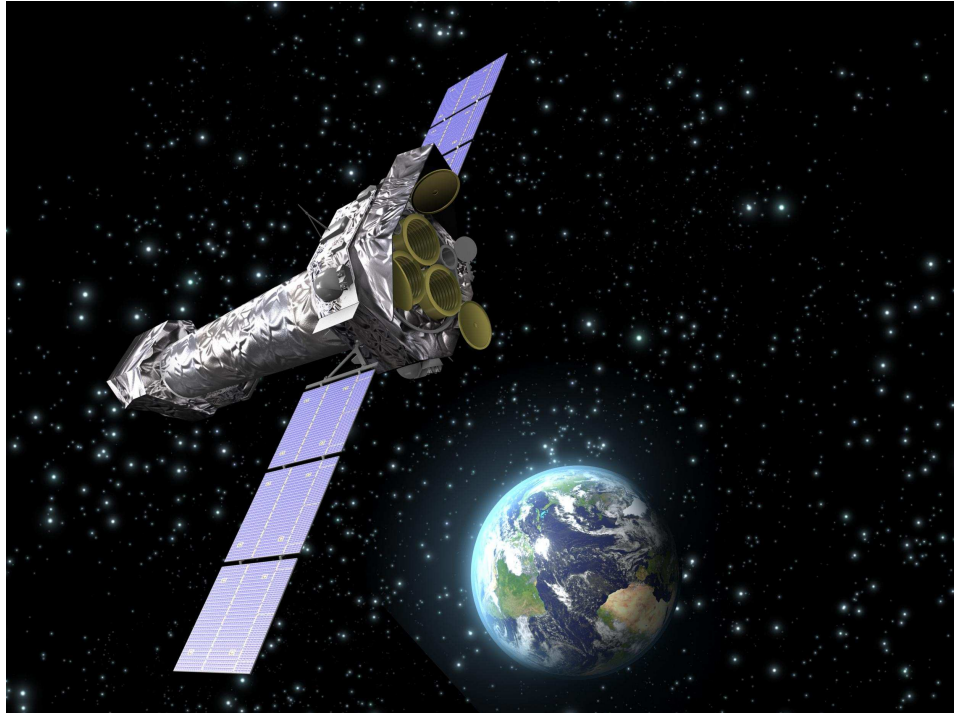


Figure 2.1: The *XMM-Newton* observatory is shown as an artist's impression (image courtesy of C. Carreau and *ESA*; taken from http://xmm.esac.esa.int/external/xmm_science/gallery/images/AI03_02me.jpg).

Two cameras use front illuminated Metal Oxide Semi-conductor (MOS) CCDs and are referred to as the MOS cameras (MOS1 and MOS2 respectively). Each MOS camera consists of seven CCDs with the central one at the focal point of the telescope (Short et al. 1998; Turner et al. 2001). The third camera uses 12 back illuminated pn CCDs integrated on a single silicon wafer and is referred to as the pn camera (Strüder et al. 2001). The imaging area is $\sim 30'$ in diameter in each camera. One pixel covers $1.1'' \times 1.1''$ and $4.1'' \times 4.1''$ of the field-of-view in MOS and pn cameras, respectively.

The telescopes equipped with the MOS cameras are also fitted with the Reflection Grating Assemblies (RGAs) which divert nearly half of the incoming X-ray radiation onto the Reflection Grating Spectrometers (RGS; den Herder et al. 2001) on the Focal Plane Assembly; a small amount of the incident light is also lost due to structural obscuration, therefore only $\sim 44\%$ of the flux reaches the MOS cameras (Turner et al. 2001). The light paths of the X-ray telescopes with and without the RGAs are shown in Figure 2.3.

There are several operating modes to enable variation in the readout time of the CCDs by reducing the area of the CCDs to be read out (Turner et al. 2001; Strüder et al. 2001). Infrared, visible or UV

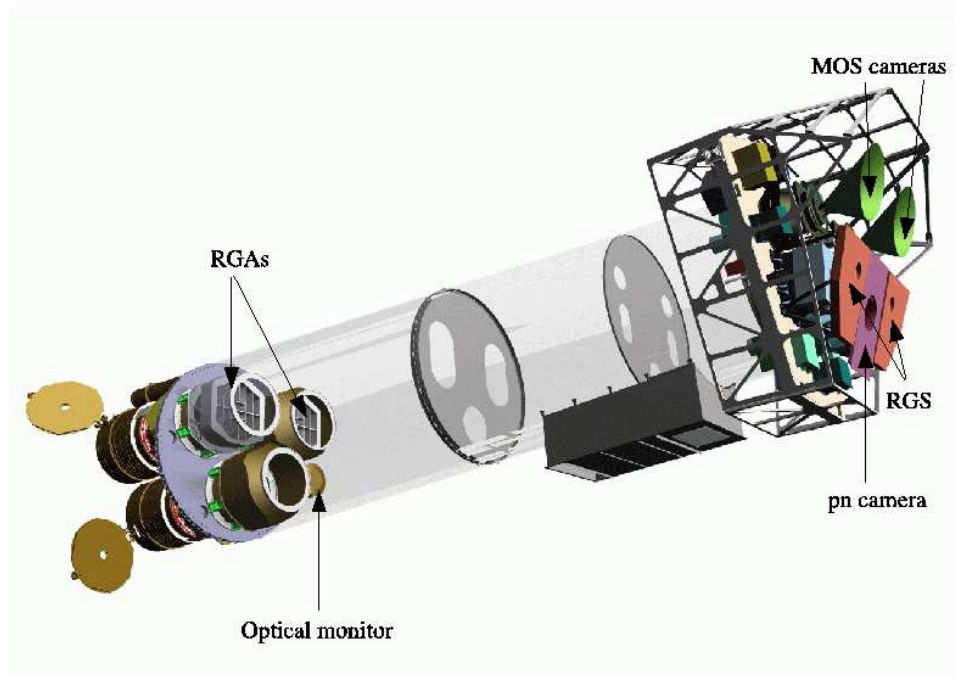
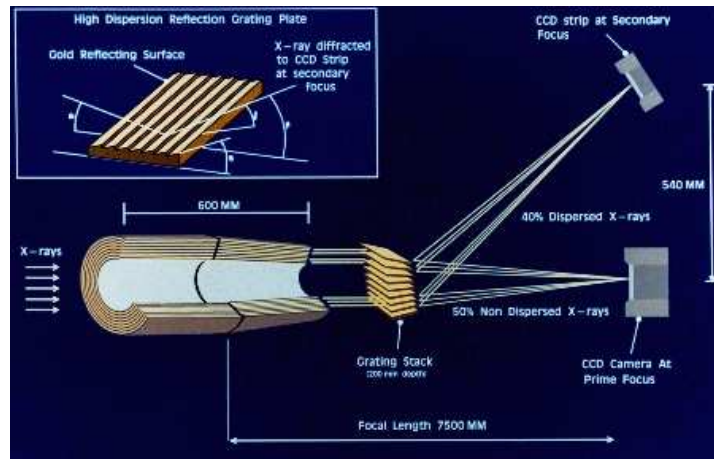


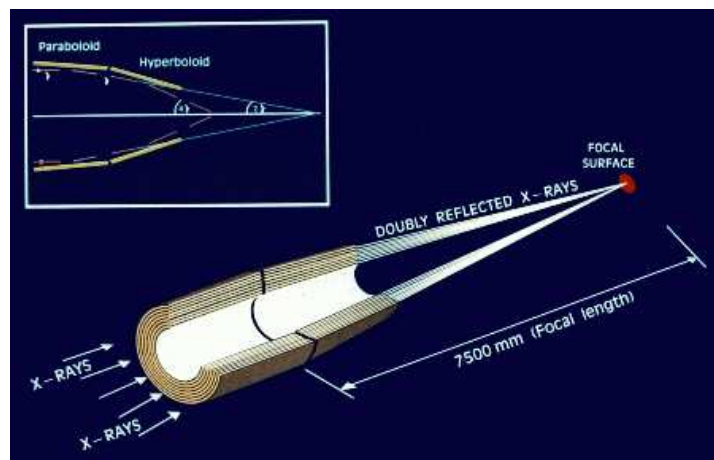
Figure 2.2: The payload of *XMM-Newton*, adapted from http://xmm.esac.esa.int/external/xmm_science/gallery/images/xmm_payl.gif (image courtesy of Dornier Satellitensysteme GmbH and ESA).

light falling onto the EPIC CCDs can affect the accuracy of the measurement of X-rays, therefore, in order to avoid such contamination, each EPIC camera is equipped with four blocking filters of different thickness (two thin filters, one medium and one thick). These four filters occupy four of the six filter positions in the filter wheel. One of the remaining positions, the close position, has a 1.05 mm thick aluminium plate which protects CCDs from soft protons; the other position does not have any filter and is referred to as the open position.

The six scientific instruments on board *XMM-Newton* (*i.e.*, three EPIC, two RGS and the OM) work independently and can also operate simultaneously. This thesis focuses on data from the EPIC instruments. The EPIC camera can perform imaging observations in the 0.2–15 keV band and provides moderate spectral resolution ($E/\Delta E \sim 20\text{--}50$). The angular resolution of EPIC is determined by the point-spread-function (PSF) of each camera. The full-width-at-half-maximum (FWHM) of the on-axis PSF for MOS is $5''$; this PSF for pn is $6''$. Table 2.1 gives a summary of the key characteristics of *XMM-Newton* and a few other important X-ray missions. Compared with other important missions such as *ROSAT*, *ASCA*, and *Chandra*, *XMM-Newton* has the largest effective area.



(a)



(b)

Figure 2.3: The light path in *XMM-Newton* (credit: ESA; taken from the *XMM-Newton* Users Handbook (Issue 2.6), Figure 2 and Figure 3).

2.2 Data Reduction

The work presented in this thesis is based on catalogues, for which the detailed description will be available in Tedds et al. , (in preparation) for the XWAS catalogue and is already available in Watson et al. (2009) for the 2*XMM* catalogue. Therefore this section will only briefly describe the data reduction and source detection and parameterisation that have been used for the two catalogues.

For each *XMM-Newton* observation, the uncalibrated data from the EPIC, RGS and OM instruments, along with their housekeeping and auxiliary files, are processed into the observation data files (ODF) by the Science Operation Centre (SOC: Madrid, Spain). The Survey Science Centre (SSC: Leicester,

Mission	Energy range keV	Mirror PSF FWHM/HEW''	A_e cm ²
<i>XMM-Newton</i>	0.15–15	6/15	4650
<i>Chandra</i>	0.1–10	0.2/0.5	555
<i>ASCA</i>	0.5–10	73/174	350
<i>ROSAT</i>	0.1–2.4	3.5/7	400

Table 2.1: Data taken from the *XMM-Newton* Users Handbook (Issue 2.6), Table 26. A_e is the mirror effective area at 1 keV.

UK) then processes the ODF using the reduction pipeline (or Processing Pipeline Subsystem, PPS) to produce the standard PPS products. The PPS products include the calibrated and cleaned event lists and secondary level products such as the multi-band images, source lists, spectra and light curves for bright sources. Both the ODF and PPS products are available from the *XMM-Newton* Science Archive (XSA). The reduction pipeline is a collection of tasks from the Science Analysis Software (SAS; Gabriel et al. 2004), which has been developed by the SOC and the SSC specifically for the reduction and analysis of *XMM-Newton* data.

Both the *XWAS* and *2XMM* catalogues are based on the EPIC imaging data (event files) from the PPS products. The event files generated for EPIC cameras operating in imaging mode are organized as tables of one registered photon per row with information for the photon such as arrival time, position¹, energy, event pattern (column PATTERN), and quality flag (column FLAG). An event with PATTERN=0 is a single event, in which case the charge produced by the photon is released in one pixel only. PATTERN values of 1 to 4 correspond to double events (two contiguous pixels are involved), 5 to 8 and 9 to 12 correspond to triple and quadruple events respectively. Events with the best quality are marked by FLAG=0. Events detected at the CCD edge or near a bad pixel might have charge loss; these events are assigned FLAG > 0.

In order to reject possible spurious events, an event-by-event filtering should be carried out before further analysis is conducted. The filtering is applied using user-specified selection criteria. The PATTERN selections used in the work presented in this thesis were ‘PATTERN ≤ 4’ for pn data and ‘PATTERN ≤ 12’ for MOS data. Events with FLAG > 0 were also excluded.

Soft protons up to a few hundred eV are believed to cause the high particle background, the ‘flares’, seen in a fraction of *XMM-Newton* observations. Although the events registered during the time intervals

¹Position in raw CCD pixel coordinates (RAWX and RAWY), in detector focal plane coordinates (DETX and DETY), and in the tangential plane in the sky (X and Y).

affected by such flares are not flagged in the pipeline processing, these time intervals can be identified by high and variable background count rate. The good time interval (GTI) files, which defined the time interval with constant low count rates ($2 \text{ counts ks}^{-1} \text{ arcmin}^{-2}$ for MOS data above 14 keV and $10 \text{ counts ks}^{-1} \text{ arcmin}^{-2}$ for pn data between 7 and 15 keV; Watson et al. 2009) were used to exclude the time intervals affected by flares.

2.3 Source Detection Algorithm

The source detection procedure was performed simultaneously in energy bands 1–5 (band 1: 0.2–0.5 keV; band 2: 0.5–1.0 keV; band 3: 1.0–2.0 keV; band 4: 2.0–4.5 keV; band 5: 4.5–12.0 keV) on the imaging data from the three EPIC cameras. A brief description of the basic steps of the source detection routine is give below:

1. Creation of multi-band images: For each of the five energy bands, an image was created with the SAS task `evselect` from the filtered event file. The size of the image is 648×648 pixels (pixel size as $4'' \times 4''$).
2. Creation of multi-band exposure maps: Exposure maps are images with each pixel representing the effective exposure time for that detector point corrected for bad pixel/column and CCD gaps. They were created using the SAS task `eexppmap` for each of the five energy bands as some of the effects taken into account (*e.g.*, mirror vignetting²) are energy dependent.
3. Creation of detection masks: Detection masks were created for individual cameras using the SAS task `emask` and defined the area of the detectors which was suitable for source detection. The areas used for source detection were those with the unvignetted exposure values at least 50% of the maximum exposure value.
4. Source detection using sliding box (local mode): The SAS task `eboxdetect` was run in the local mode to search for sources by sliding a box ($20'' \times 20''$) across the detector areas defined by the detection masks. A $8''$ wide frame around the search box was used as the local background. Detection likelihoods were calculated for each detection in each camera and in each energy band

²The decrease of the effective area as a function of the energy and the off-axis angle of the incident photon.

and then converted into an equivalent total band (0.2–12 keV) EPIC detection likelihood. The output source list included all detections with a total-band EPIC detection likelihood above 5.

5. Source detection using sliding box (map mode): The SAS task `esplinemap` was used to create a background map for each camera and each energy band. For an image from a single camera and energy band, the areas where sources were detected in the last step were removed. A spline fit was then carried out on the source-free image to create a background map for the entire image. The task `eboxdetect` was run again but in map mode, using the background map in the source search. All sources with a total band EPIC detection likelihood above 5 were included in the map-mode source list. This was the final stage of source detection.
6. Source parameter estimation using maximum likelihood fitting: The SAS task `emldetect` was then used to calculate parameters for the sources detected by `eboxdetect` in map mode. For a given source passed on to `emldetect`, the instrumental PSF was fitted to the distribution of counts of the source simultaneously in all five energy bands and for each of the three cameras using a maximum likelihood fitting procedure. The fitting procedure treated the source count rates in different energy bands and different cameras as independent free parameters, while it constrained the source position as well as the source extent to be the same over all energy bands and cameras. Detection likelihoods were calculated based on the best-fit parameters. Source with detection likelihood above 6 were included in the final output source list. The X-ray hardness ratios (HR1–HR4), or X-ray colours, were calculated as $HR_n = (\text{RATE}_{n+1} - \text{RATE}_n) / (\text{RATE}_{n+1} + \text{RATE}_n)$, where RATE_n and RATE_{n+1} were the corrected count rates in energy bands n and $n + 1$. Source fluxes were derived from the count rates assuming a power-law model with a photon index $\Gamma = 1.7$ and absorption of $N_H = 3 \times 10^{20}$ atoms cm^{-2} .

Warning flags for each source in the final source list were set automatically by the SAS task `dpssflag` or manually in the screening process. Based on the information in the `emldetect` source list, `dpssflag` wrote back to the source list the flags 1–9 (changing a flag from default F to T). Sources were flagged if they had low coverage on the detector ($< 50\%$), were near a bright source, were within an extended source, or were in/near problematic areas in the detectors (*e.g.*, the bright corner in MOS1 or bright low gain column in pn). Flags 11 and 12 were set manually. Sources within areas in the images where spurious detections were suspected had flag 11 set. Sources with flag 11 set would also have flag 12 set if they were the sources which caused the spurious detections.

`Emldetect` source lists for bands 1–5 were then merged into a single list by the SAS task `srcmatch`. `Srcmatch` also calculated the combined EPIC fluxes in the five bands, combined EPIC hardness ratios, and their respective errors. In the case that a unique celestial source was detected in several observations, an effort was made to identify such unique sources and to combined parameters from different detections. Detections were regarded to be associated with the same celestial source if their separation was below the matching threshold, three times of the sum of their respective positional uncertainties. Key parameters (*e.g.*, position, EPIC flux, hardness ratios, *etc.*) were then averaged in a error-weighted manner from all detections found to be from the same celestial source.

2.4 Data Analysis

2.4.1 X-ray Spectral Product Extraction

X-ray spectra were extracted from the filtered EPIC event lists using the SAS task `evselect`. Circular apertures centred on the detected source positions were used for the extraction of spectra. Annular regions, which were also centred on the sources wherever possible, were used to extract background spectra. The source spectra linked to the *2XMM* catalogue were extracted from regions with radius $r = 28''$; annuli with $60'' \leq r \leq 180''$ were used for the background spectra (Watson et al. 2009).

The response files required for spectral fitting, the redistribution matrix file (RMF) and auxiliary response file (ARF), were also created for each source spectrum. The RMF provides the mapping from energy space to detector pulse height space and is dependent on the instrument, the observing mode, the pattern selection and the location of the source in the detector. The SAS task `rmfgen` was used to create the RMFs. Alternatively, the pre-computed (or ‘canned’) RMFs publicly available from the *XMM-Newton* website³ can be used. The ARF provides an effective area as a function of energy and was generated using the SAS tasks `arfgen`.

³http://xmm2.esac.esa.int/external/xmm_sw_cal/calib/epic_files.shtml

2.4.2 X-ray Spectral Models

Throughout this thesis, XSPEC v11.3.2 (Arnaud 1996) has been used to carry out the X-ray spectral analysis. A brief description of models which have been used for the spectral analysis is given below⁴.

The ISM absorption model used was the Tuebingen-Boulder ISM (`tbabs`) model. In this model, the contribution to the absorption cross section from the gas-phase ISM, the grain-phase ISM, and molecules (hydrogen only) in the ISM has been taken into account. The equivalent hydrogen column, in units of 10^{22} atoms cm^{-2} , is the free parameter. When modelling the intrinsic absorption of an X-ray source, model `ztbabs`, which allows the user to set a fixed redshift z , was used.

The typical model used to fit the broad band continuum component was a simple power-law model (`zpowerlw` in XSPEC), which has three free parameters: the photon index (or spectral slope) Γ , redshift z and the normalization. The XSPEC model `APEC` was used to model spectra from collisionally-ionized diffuse gas. This model has four free parameters: the plasma temperature kT (in keV), metal abundances, redshift z and the normalization.

2.4.3 X-ray Spectral Analysis

For a source with spectrum $f(E)$, the flux distribution as a function of energy E , the observed spectrum obtained by a spectrometer is photon counts $C(I)$ detected in specific channels I of the instrument:

$$C(I) = \int_0^{\infty} f(E)R(I, E)dE, \quad (2.1)$$

where $R(I, E)$ is the instrumental response defined by RMF and ARF. In the actual fitting, XSPEC compares $C_p(I)$, the predicted count spectrum calculated from a trial model $f(E)$ defined by a few parameters, to the observed $C(I)$ and yields a fit statistic. The ‘best-fit’ model is obtained when the optimum fit statistic is achieved by varying the model parameters. The fit statistic used in XSPEC for the work presented in this thesis was χ^2 , defined as:

$$\chi^2 = \sum ((C(I) - C_p(I))^2 / (\sigma(I))^2), \quad (2.2)$$

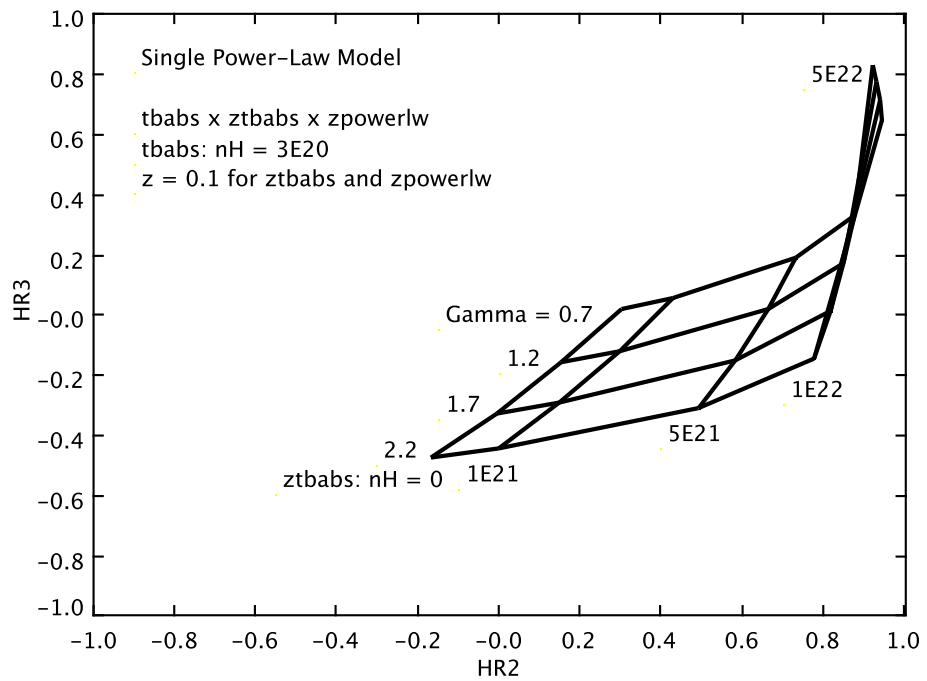
⁴Full details of the spectral models and fitting algorithms can be found online at <http://heasarc.gsfc.nasa.gov/docs/xanadu/xspec/xspec11/index.html>.

where $\sigma(I)$ is the error in the number of counts detected in channel I (usually estimated by $\sigma = \sqrt{C(I)}$). Normally a ‘reduced χ^2 ’ (also χ^2/ν or χ^2_ν , ν being the number of degrees of freedom of the fit) to be approximately equal to one is considered to be a good fit. The confidence interval for a given parameter can be obtained by varying the value of this parameter until the χ^2 increases by $\Delta\chi^2$, the critical value of the required confidence level (a 90% confidence level is used for all the fittings in this thesis). In order to use χ^2 , the FTOOLS task `grppha` was used to bin the X-ray spectra such that each data point contains enough counts to ensure Gaussian statistics were valid.

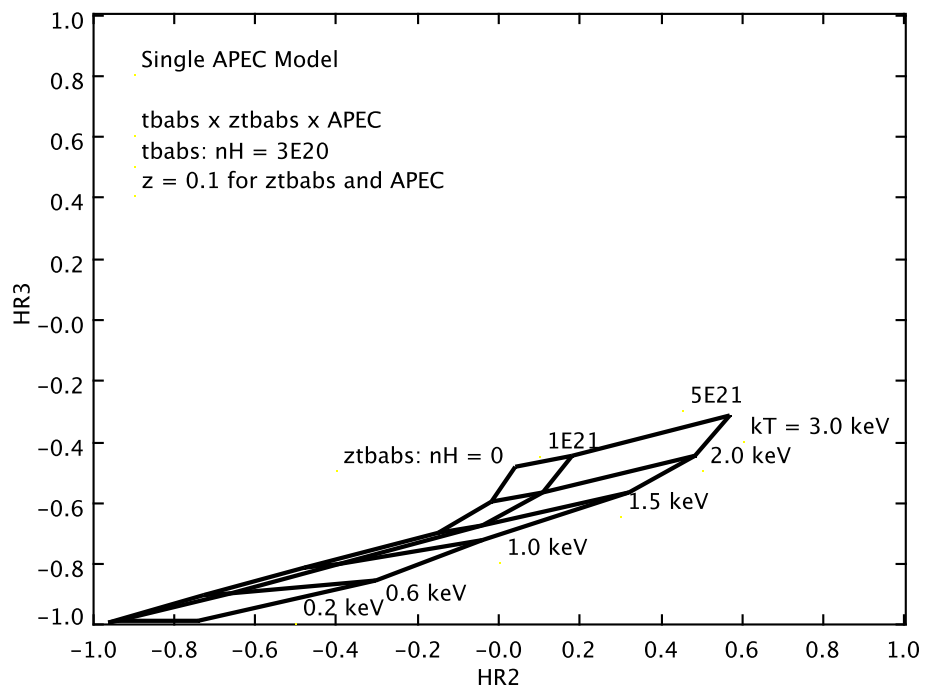
2.4.4 X-ray Hardness Ratios

The X-ray hardness ratios, or colours, calculated in the way described in §2.3 can be used to provide constraints on the broad band spectral shape of the underlying spectral model and are therefore very useful when the X-ray spectrum has low statistics. In this case, the X-ray hardness ratios predicted from spectral models are needed.

The XSPEC v11.3.2 was used to simulate spectra based on various models. The canned RMF for a pn on-axis point source was used; the ARF was created for the pn camera operating with thin optical filter (§ 2.4.1). A redshift of 0.1 and a Galactic absorption of 3×10^{20} atoms cm^{-2} were used for all models. The grid of values shown in Figure 2.4(a) was derived from single power-law models (`zpowerlw` in XSPEC) with $\Gamma = 0.7, 1.2, 1.7,$ and 2.2 from top to bottom, modified by intrinsic absorptions (`ztbabs` in XSPEC; redshifted to $z = 0.1$) of $N_{\text{H}} = 0, 1 \times 10^{21}, 5 \times 10^{21}, 1 \times 10^{22}$ and 5×10^{22} atoms cm^{-2} , from left to right. In Figure 2.4(b), the values were derived from single APEC models with solar abundance and $kT = 0.2, 0.6, 1.0, 1.5, 2.0$ and 3.0 keV, from bottom to top, modified by intrinsic absorptions of $N_{\text{H}} = 0, 1 \times 10^{21}, 5 \times 10^{21}$ atoms cm^{-2} , from left to right. Values in Figure 2.5 were calculated from two-component models: a hard component modelled by `zpowerlw` plus a soft component modelled by APEC. Along each line, values indicate the normalization ratios between the `zpowerlw` and APEC of 10:1, 1:1 and 1:10, from top right to bottom left. $\Gamma = 1.7$ was used in `zpowerlw`. Solar abundance was used in APEC. Open triangles mark values when $kT = 0.6$ keV was assumed for the APEC model. Open circles mark values when $kT = 1.0$ keV was used. In these two cases, the intrinsic absorption (`ztbabs`) was set to 0. The other two lines (marked with open squares and diamonds respectively), from right to the left, indicate the hardness ratios when intrinsic absorption (`ztbabs`) of 1×10^{22} atoms cm^{-2} and 1×10^{23} atoms cm^{-2} were used to modify the `zpowerlw` component.



(a)



(b)

Figure 2.4: X-ray hardness ratio grids from single component models.

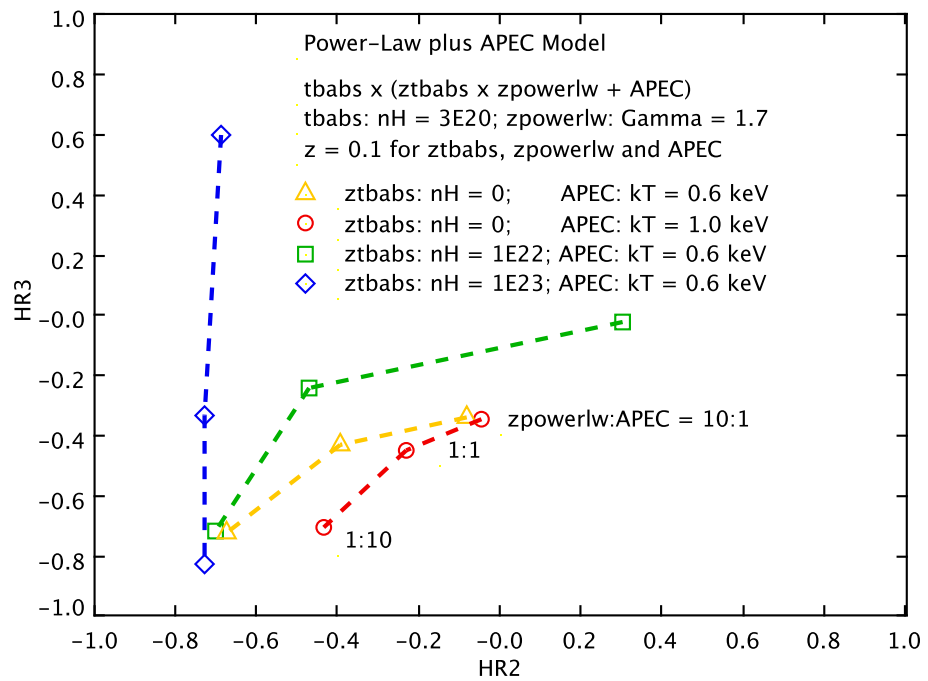


Figure 2.5: X-ray hardness ratio grids from two-component models.

Chapter 3

Normal Galaxies in The *XMM-Newton/2dF* Wide Angle Serendipitous Survey

An X-ray selected sample with significant size requires large sky coverage. Also, information from other energy bands, optical being the most readily available in many cases, is essential for separating AGN from the truly normal galaxies. In this chapter, a galaxy sample selected from the *XMM-Newton/2dF* Wide Angle Serendipitous Survey (XWAS) is presented. Being a pilot project, this study served to develop the approach that was then applied to the much larger project, which will be presented in Chapter 4 and 5. Due to the small sample size and a number of issues of the optical data, only a simple investigation of the nature of this galaxy sample is offered here.

3.1 The *XMM-Newton/2dF* Wide Angle Serendipitous Survey

XWAS is part of the XID programme (Watson et al. 2001) conducted by *XMM-Newton* SSC which aims at providing identifications of serendipitous sources discovered by *XMM-Newton*. This survey was based on sources drawn from 68 pointings made by *XMM-Newton* between June 2000 and May 2003. The survey covers $\sim 11.5 \text{ deg}^2$ net area in the sky. The full description of this survey will be presented in Tedds et al. (in preparation) and is only described briefly here. Optical imaging data from

the *SuperCOSMOS* Sky Survey (SSS¹; Hambly et al. 2001) and the *Isaac Newton Telescope Wide Field Camera (INT WFC)* were used to select potential optical counterparts for the X-ray sources detected in the 68 fields. Optical counterparts ($R \lesssim 21$) were selected for ~ 3000 X-ray sources. Optical spectroscopic follow-up observations were then carried out using the Anglo-Australian Telescope (AAT) Two Degree Field (*2dF*) multi-fibre spectroscope (Lewis et al. 2002). The fibres, which have the entry size of $\sim 2.1''$ in diameter, were placed at the positions of the optical counterparts. The effective resolution $\lambda/\Delta\lambda$ was ~ 600 over the wavelength of $\sim 3850\text{--}8250\text{\AA}$. The typical exposure time was one hour, reaching a signal-to-noise ratio of ~ 5 at 5500\AA for $V = 21$ mag. Some of the *2dF* observations were affected by a fault of the atmospheric dispersion corrector (ADC; Lewis et al. 2002). The ADC, which is intended to remove the effects of atmospheric dispersion, was stuck in a fixed position and caused strongly wavelength-dependent fibre losses. This effect produced a spurious wavelength-dependant ‘tilt’ in the spectra which was difficult to correct. For $\sim 41\%$ of the total ~ 3000 observed sources, the spectra were judged to be of sufficient quality (*i.e.*, classifiable) and were visually classified into ALGs, NELGs, broad line AGN and stars. Most of these classified spectra also yielded reliable redshift measurements. By the time the acquisition of the *2dF* spectra finished, the XWAS fields had been observed by *XMM-Newton* in a total of 119 pointings, including repeat observations at particular pointings. All these 119 observations were then reprocessed with the up-to-date calibration using the pipeline developed for *2XMM* (§ 2.2 and § 2.3) and yielded a source list of ~ 7000 X-ray sources with the 0.2–12 keV detection likelihoods $ML > 6$ and fluxes down to $5 \times 10^{-15} \text{ erg s}^{-1} \text{ cm}^{-2}$. This source list then provided the basic parameters used for each X-ray source in this work.

3.2 Sample Selection

The normal galaxy candidates were selected as those satisfying all the following criteria:

1. The X-ray-to-optical flux ratio $\log(f_X/f_O) < -1$. The $\log(f_X/f_O)$ is defined as:

$$\log \frac{f_X}{f_O} = \log f_X + 5.5 + \frac{R}{2.5}, \quad (3.1)$$

¹<http://www-wfau.roe.ac.uk/sss/>; the SSS catalogue is also available in *SuperCOSMOS* Science Archive (<http://surveys.roe.ac.uk/ssa/index.html>), prepared and hosted by the Wide Field Astronomy Unit, Institute for Astronomy, University of Edinburgh, which is funded by the UK Science and Technology Facilities Council.

where f_X is the full band (0.2–12 keV) flux. The R magnitude was adopted from SSS when available; USNO-B 1.0 (Monet et al. 2003) was used to provide the R magnitude for the rest.

2. The source was classified as an ALG or a NELG based on its $2dF$ spectra.
3. The full band X-ray luminosity $L_X < 10^{43}$ erg s $^{-1}$, using redshifts measured from the $2dF$ spectra.

In total 72 normal galaxies were selected (Figure 3.1) and these are referred to as the $2dF$ sample² hereafter. Thirty-nine of the $2dF$ galaxies were classified as NELGs, the rest (33) as ALGs. Ten sources were detected as extended sources in the *XMM-Newton* data with the source radii in the range of ~ 7 – $24''$ and all of them were ALGs. Examples of the SSS images and $2dF$ spectra of the $2dF$ sample are shown in Figure 3.2.

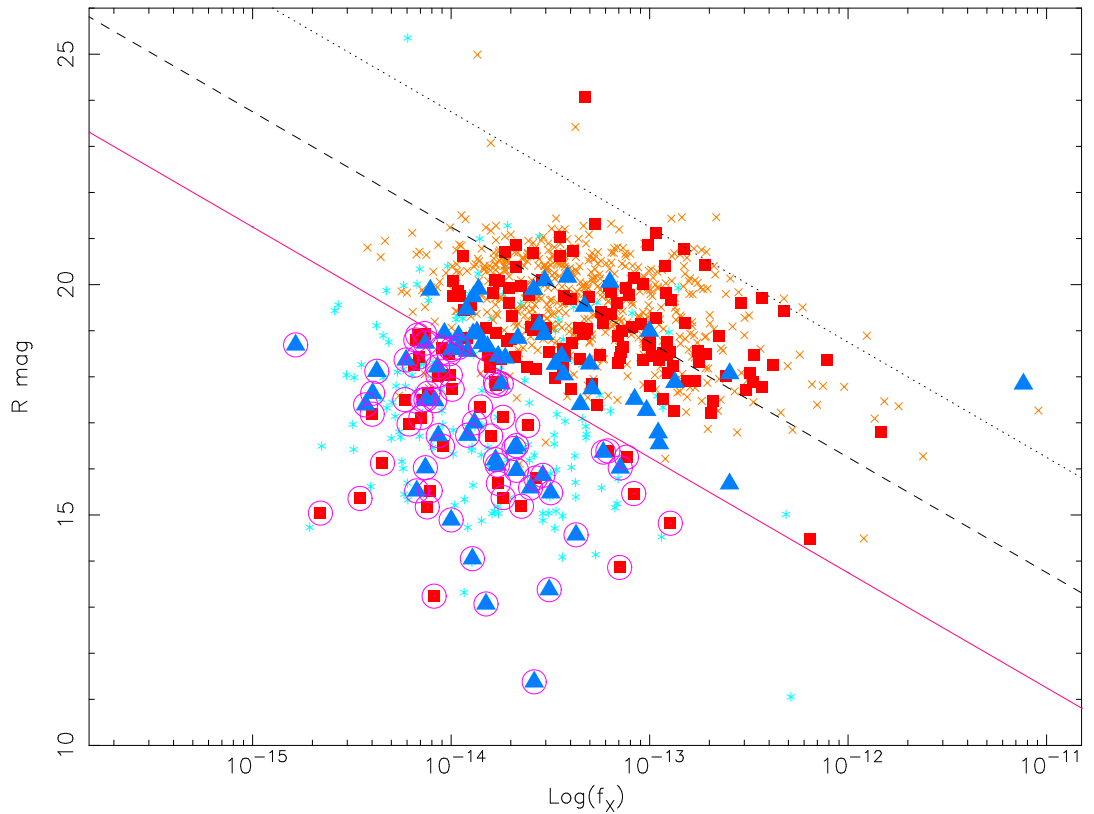


Figure 3.1: The SSS R band magnitudes are shown against 0.2–12 keV fluxes of XWAS sources with both X-ray flux measurements and optical magnitudes, including NELGs (squares), ALGs (triangles), broad line AGN (crosses), and stars (asterisks). The circles mark the sources in the $2dF$ sample. The slanted lines indicate constant X-ray to optical flux ratios of $\log(f_X/f_O) = -1, 0, 1$, marked by solid, dashed and dotted lines, respectively, from bottom to top.

²The whole sample is listed in Table A.1.

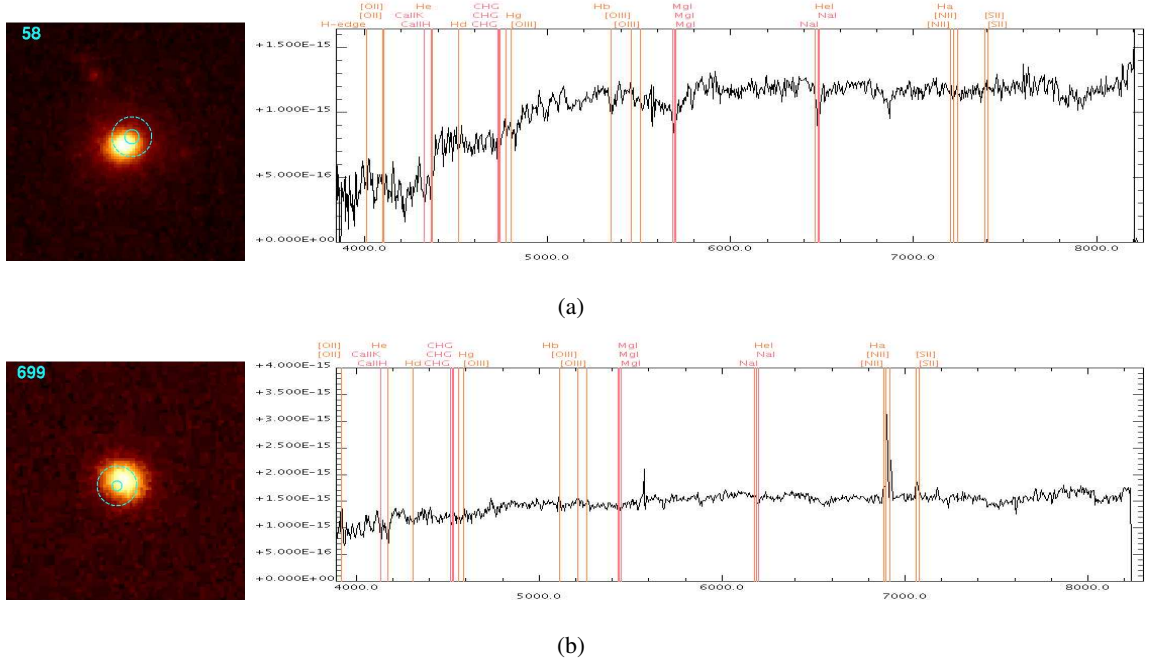


Figure 3.2: Shown here are two examples from the $2dF$ sample, one being an ALG (a) and the other being a NELG (b). The SSS R band image (taken by the UK Schmidt Telescope) is shown on the left with the $2dF$ spectrum on the right. The solid regions are centred at the positions of the X-ray sources and have radii of 1σ X-ray positional uncertainties. The dashed regions have $5''$ radii.

3.3 Classification Based on Narrow Emission Line Ratios

The $2dF$ sample includes 33 ALGs and 39 NELGs. The average properties of the $2dF$ sample, the ALG subsample and the NELG subsample are summarized in Table 3.1. The mean redshifts for the ALGs and the NELGs are 0.145 and 0.119. Although ALGs have a slightly larger mean redshift than the NELGs, the overlap in the redshift distributions of these two subsamples is large as the standard deviations are 0.080 for the ALGs and 0.084 for the NELGs. Although they have larger mean soft band (0.5–2 keV) flux, the ALGs are fainter than the NELGs in the hard band (2–12 keV). The differences in these two bands between the ALGs and the NELGs suggest different X-ray spectra of these two types of galaxies. The ALGs have lower mean X-ray-to-optical flux ratio than the NELGs. However, the differences in these parameters (*i.e.*, the soft band flux, the hard band flux and the X-ray-to-optical flux ratio) between the ALGs and the NELGs are not statistically significant as the null hypothesis that the ALGs and NELGs have the same distributions for each of these parameters cannot be rejected by Kolmogorov-Smirnov (K-S) test at a significance level of 1%.

In order to separate Type 2 AGN from the rest of the NELGs, the emission line fluxes were measured from the $2dF$ spectra. Due to the weakness of the [S II] $\lambda\lambda$ 6717, 6731 and [O I] λ 6300 lines in most of the $2dF$ spectra of these NELGs, only the BPT [N II] plot (Figure 1.7 in § 1.4.3) based on H β , [O III] λ 5007, H α and [N II] λ 6584 was considered here. The parameters of the H β , [O III], H α and [N II] lines were measured using a simple procedure which: (1) estimated the continuum in the vicinity of the lines using a linear fit to adjacent line-free regions of the spectrum; (2) performed a Gaussian fit to each line with initial centroid set by the average redshift for each galaxy. Line fluxes and errors were computed from the Gaussian fits with continuum subtracted. Fits with significant shifts from the expected centroids were rejected. Although the issues in the spectra mean that absolute line fluxes are not reliable (§ 3.1), this has minimal effect on the line *ratios* as the lines used are very close together in the spectra. Among the 39 NELGs, 24 had all four lines measured (weak lines which did not yield meaningful fits were not measured); the remaining 15 galaxies are then referred to as unclassified NELGs hereafter. The classification scheme from Kewley et al. (2006), based on the BPT [N II] plot (Equation 1.7–1.10), was used and classified eight narrow line AGN, seven SF galaxies and nine composite galaxies (Figure 3.3). The average properties of these AGN, SF galaxies, composite galaxies and also the unclassified NELGs are summarized in Table 3.1. Among all the NELGs, AGN tend to be fainter in the R band and brighter in the X-ray (both the soft and the hard bands), hence have the highest mean X-ray-to-optical flux ratio. The unclassified NELGs occupy the highest X-ray luminosity end (the mean $L_{0.2-12\text{keV}} \approx 1.3 \times 10^{42}$ erg s $^{-1}$) of the $2dF$ sample, suggesting that these galaxies might host AGN.

3.4 X-ray Spectral Properties

3.4.1 X-ray Spectra

For sources with sufficient X-ray photon counts, X-ray spectral analysis can be carried out to provide an insight to the nature of the X-ray sources. There were four galaxies (QID: 861, 2677, 2683 and 2730) with more than 300 counts from the pn camera (the deepest observation was considered if more than one were included in XWAS). The spectra of these four galaxies are presented in Figure 3.5 and the fits are summarized in Table 3.2.

The optical counterpart of object 861 (Figure 3.4(a)) is an ALG and is possibly associated with a group

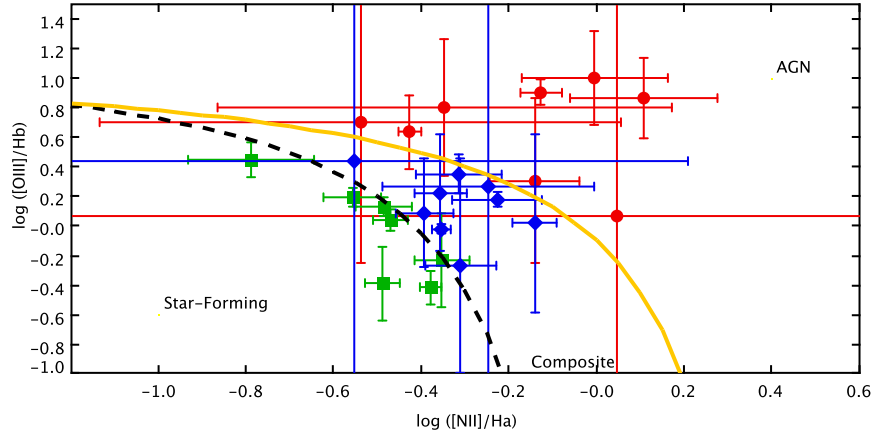


Figure 3.3: Shown here is the BPT [N II] plot used to classified NELGs in the *2dF* sample. Galaxies lying above the ‘maximum starburst line’ (yellow solid line; Equation 1.8) are classified as AGN (red dots). SF galaxies (green squares) are those lying below the pure SF line (black dashed line; Equation 1.7). Galaxies lying between these two lines (Equation 1.9 and 1.10) are composite galaxies (blue diamonds).

No.	Property	<i>2dF</i>	ALG	NELG	Classified	AGN	SF	Composite	Unclassified
(1)	Number	72	33	39	24	8	7	9	15
(2)	% of <i>2dF</i>	100	45.8	54.2	33.3	11.1	9.7	12.5	20.8
(3)	% of NELG	-	-	100	61.5	20.5	17.9	23.1	38.5
(4)	% of Classified NELG	-	-	-	100	33.3	29.2	37.5	-
(5)	z	0.131	0.145	0.119	0.103	0.132	0.089	0.088	0.145
(6)	R	16.63	16.40	16.82	16.84	17.05	16.82	16.67	16.78
(7)	$\log(\frac{f_X}{f_O})$	-1.75	-1.83	-1.68	-1.71	-1.47	-1.88	-1.78	-1.65
(8)	$f_{0.5-2\text{keV}}$	5.91	8.40	3.79	3.94	5.19	3.11	3.48	3.56
(9)	$f_{2-12\text{keV}}$	10.97	6.70	14.58	13.02	25.62	4.47	8.46	17.08
(10)	$f_{0.2-12\text{keV}}$	19.12	17.84	20.20	18.87	33.84	8.53	13.61	22.34
(11)	$L_{0.5-2\text{keV}}$	3.28	4.49	2.26	0.85	1.43	0.46	0.65	4.52
(12)	$L_{2-12\text{keV}}$	3.59	3.02	4.08	3.02	5.24	1.48	2.24	5.76
(13)	$L_{0.2-12\text{keV}}$	8.23	9.12	7.47	4.23	7.12	2.19	3.23	12.67

Table 3.1: (1): Sample size. (2)–(4): Fractions that a subsample possesses in its parent sample(s). (5): Unweighted mean redshifts z . (6): Unweighted mean R band magnitudes. (7): Unweighted mean X-ray-to-optical flux ratios. (8)–(10): Unweighted mean X-ray fluxes in units of 10^{-15} erg s $^{-1}$ cm $^{-2}$. (11)–(13): Unweighted mean X-ray luminosities in units of 10^{41} erg s $^{-1}$.

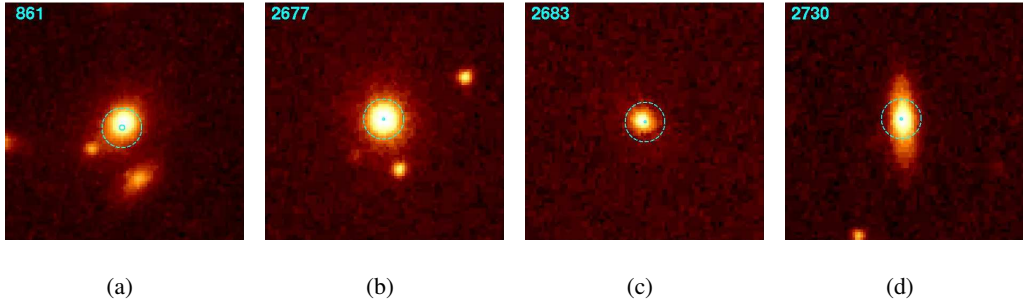


Figure 3.4: The SSS R band images from the UK Schmidt Telescope of the four sources whose X-ray spectra are presented here. The solid regions are centred at the positions of the X-ray sources and have radii of 1σ X-ray positional uncertainties. The dashed regions have $5''$ radii.

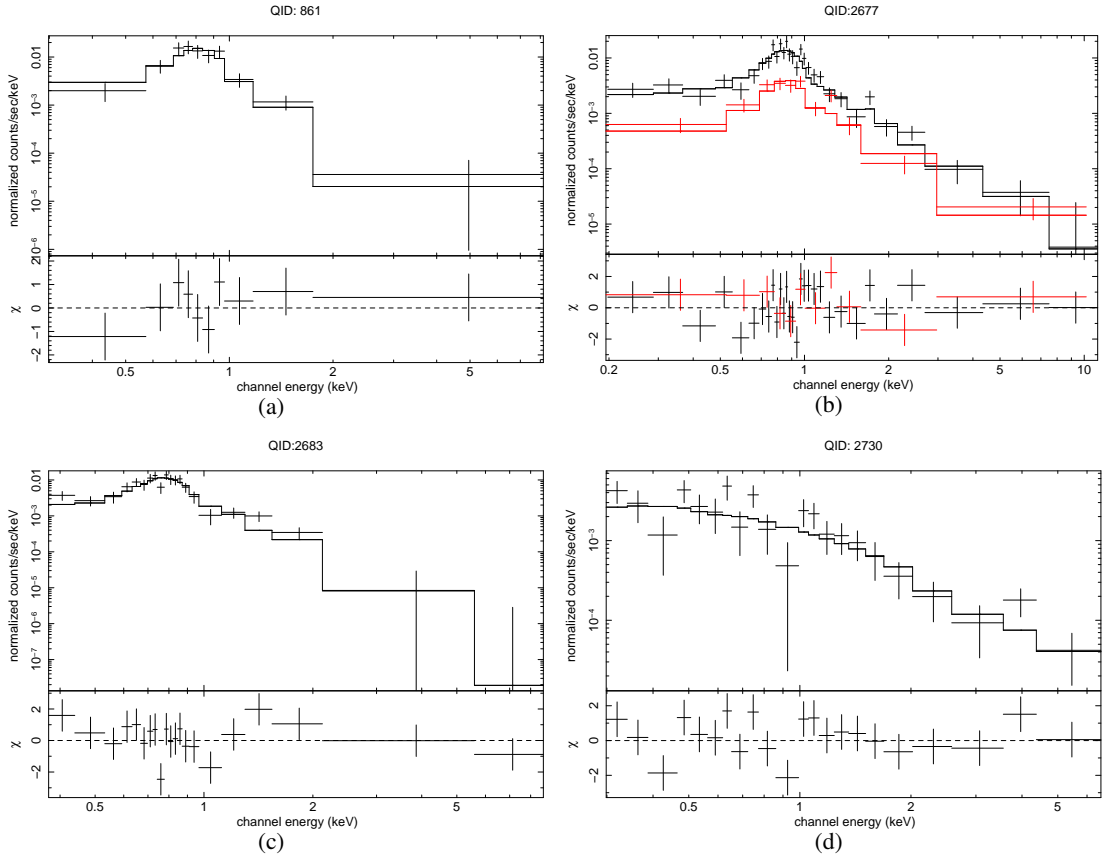


Figure 3.5: *XMM-Newton* spectra of sources with sufficient counts for spectral analysis. The spectra from the pn camera for objects 861 (a) and 2683 (c) were fitted with single *APEC* models. For object 2677 (b) spectra from both pn (black) and MOS2 (red) cameras were fitted and the best-fit model was a two-component model (*APEC* plus *zpower1w*). The pn spectrum of object 2730 (d) was fitted with a single power-law model.

QID	SpecID	z	kT (keV)	$\log L_X$ (erg s $^{-1}$)	N_H (10^{21} atoms cm $^{-2}$)	Γ	$\log L_X$ (erg s $^{-1}$)	χ^2/dof
(1)	(2)	(3)	(4)	(5)	(6)	(7)	(8)	(9)
861	ALG	0.084	$0.75^{+0.09}_{-0.11}$	41.38				6.0/8
						2.07 \dagger	41.41	55.2/8
2677	ALG	0.056	$0.77^{+0.05}_{-0.05}$	41.25	$2.88^{+7.08}_{-2.43}$	$2.16^{+0.38}_{-0.73}$	41.11 (41.39*)	49.2/36
			0.80 \dagger	41.32		9.5 \dagger	41.27 (47.13*)	21.0/7
						1.84 \dagger	41.53	224.3/39
2683	ALG	0.131	$0.73^{+0.06}_{-0.08}$	41.78				21.8/19
						2.57 \dagger	41.96	88.2/19
2730	NELG	0.068						24.4/20
			$3.43^{+1.99}_{-0.93}$	41.22		7.55 \dagger	41.68 (45.39*)	56.0/18
						$1.90^{+0.28}_{-0.26}$	41.30	27.1/20

Table 3.2: The best-fit models for objects 861 and 2683 were APEC. The best-fit model for object 2677 was a combination of an APEC model and an absorbed power-law model (`zpowerlw`). The best-fit model for object 2730 was a single power-law model (`zpowerlw`). (1): XWAS QID. (2): visual classification based on $2dF$ spectrum. (3): redshift from XWAS. (4): plasma temperature from the APEC model (\dagger no errors calculated as $\chi^2_\nu > 2$). (5): 0.2–12 keV luminosity derived from the APEC model (corrected for the Galactic absorption). (6): intrinsic absorption applied only to the power-law component (\dagger no errors calculated as $\chi^2_\nu > 2$). (7): Γ of the power-law model (\dagger no errors calculated as $\chi^2_\nu > 2$). (8): 0.2–12 keV luminosity derived from the power-law model (corrected for the Galactic absorption; * also corrected for intrinsic absorption). (9): $\chi^2/\text{degree-of-freedom}$ of the fitting (bold values indicating the best-fit models).

of galaxies. This source was detected as an extended source in X-rays. The best-fit model of its *XMM-Newton* pn spectrum was an APEC model with $kT = 0.75^{+0.09}_{-0.11}$ keV (Figure 3.5(a)), consistent with X-ray emission from hot ISM of galaxies.

The optical counterpart for object 2677 (Figure 3.4(b)) is classified as an ALG and appeared to be an elliptical galaxy in the SSS image. The best-fit model of its pn and MOS 2 spectra was a two-component model consisting of an APEC model plus an absorbed power-law model (Figure 3.5(b)). The temperature of the APEC component was $kT = 0.77^{+0.05}_{-0.05}$ keV, consistent with hot ISM of the galaxies. The power-law had $\Gamma = 2.16^{+0.38}_{-0.73}$ with absorption of $N_H = 2.88^{+7.08}_{-2.43} \times 10^{21}$ atoms cm $^{-2}$. The 0.2–12 keV luminosity derived from the power-law component was $10^{41.11}$ erg s $^{-1}$ ($10^{41.39}$ erg s $^{-1}$ after corrected for intrinsic absorption), contributing around half of the luminosity of the source. This source was not detected as extended in X-rays. Therefore, the X-ray spectra together with its point-like morphology in the X-ray band suggest AGN presence.

Object 2683 was detected as an extended source X-ray and the host galaxy appeared to be an early-type galaxy in the SSS image (Figure 3.4(c)). The best-fit model of its pn spectrum was an APEC model with $kT = 0.73_{-0.08}^{+0.06}$ keV (Figure 3.5(c)), consistent with hot ISM origin of the X-ray emission.

Object 2730 is an unclassified NELG due to the non-detection of $H\beta$. A power-law model with $\Gamma = 1.90_{-0.26}^{+0.28}$ gave the best-fit of its pn spectrum and yielded the 0.2–12.0 keV luminosity of $L_X = 10^{41.3}$ erg s⁻¹ (corrected for the Galactic absorption). The X-ray spectrum fitting result was consistent with either a collection of X-ray binaries or a LLAGN, the latter being more plausible when taking into account its NELG classification and X-ray luminosity.

3.4.2 X-ray Hardness Ratios

As most of the galaxies in the *2dF* sample did not have sufficient counts to allow detailed spectral analysis, their X-ray hardness ratio were examined to constrain their X-ray spectral properties. Hardness ratios HR2 and HR3 (as defined in § 2.4.4) of all subsamples are shown in Figure 3.6. Due to the small sizes of the *2dF* sample and its subsamples, and the large errors in most of the hardness ratios, only simple interpretation is offered here; more detailed interpretation will be given for the much larger samples presented in Chapter 4 and 5.

As shown in Figure 3.6(a), most of the AGN have hardness ratios consistent with a power-law model, with absorption up to $\sim 10^{22}$ atoms cm⁻². Since, by definition, the AGN included in the *2dF* sample were Type 2 AGN, the absorbed power-law might be expected. An additional soft component is also suggested to contribute significantly for half of these AGN.

The hardness ratios of most of the SF galaxies (Figure 3.6(b)) are consistent with a two-component model, which is dominated by the thermal component, suggesting that the hot ISM in these galaxies contributes significantly to the total X-ray emission.

It seems that most of the composite galaxies have complex spectra consisting of an absorbed power-law component and a non-negligible thermal component. The absorptions suggested by the hardness ratios appear to be higher than those in the AGN subsample.

From the point of view of the optical spectra, in the unclassified NELGs the X-ray emission powered

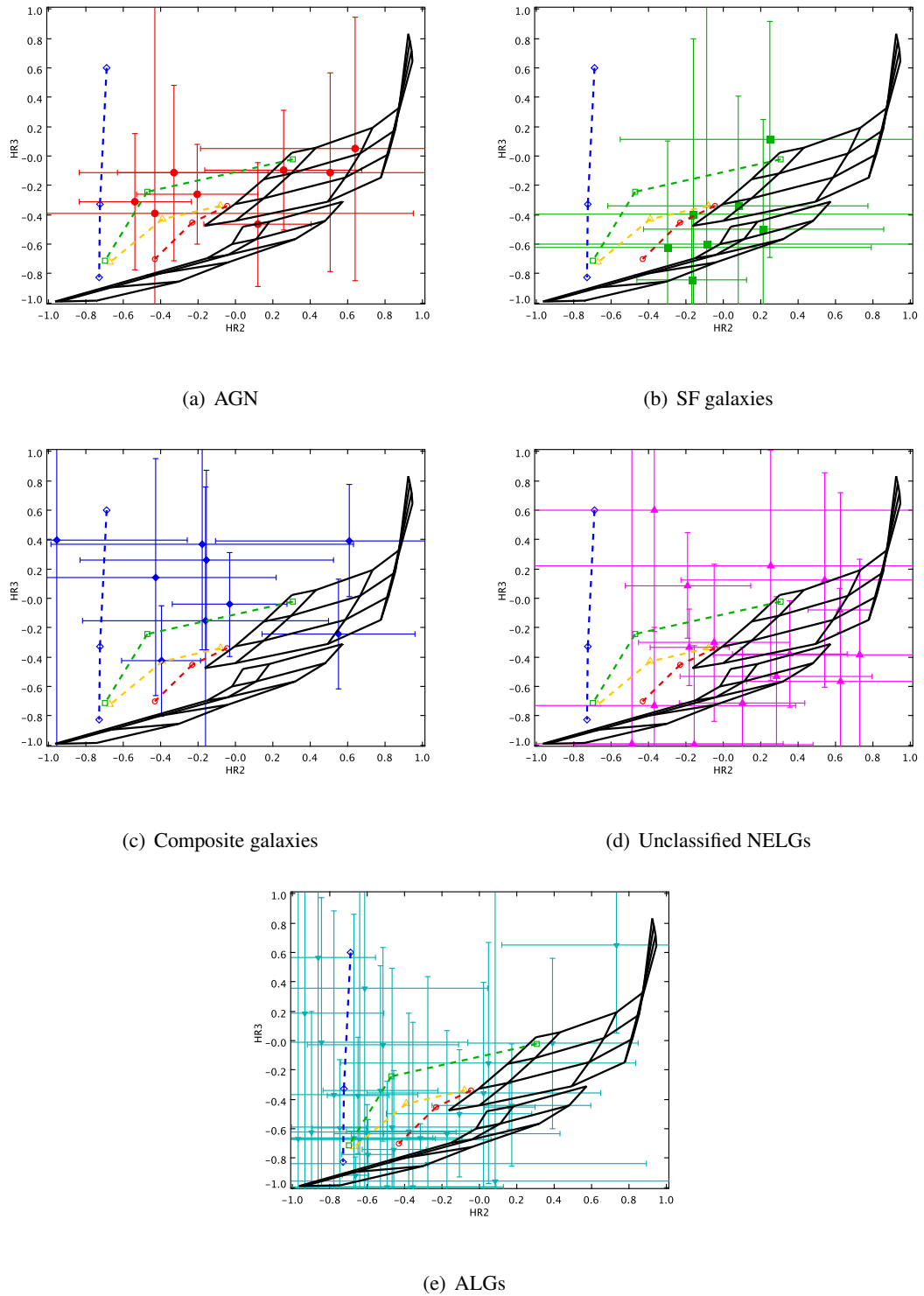


Figure 3.6: Hardness ratios (HR2 versus HR3) for *2dF* subsamples. Counts from all three EPIC cameras were used to calculate the hardness ratios. Values from spectral models described in § 2.4.4 are also shown.

by AGN and/or SF activities appears to be weaker compared with the host galaxy. The X-ray hardness ratios of these galaxies (Figure 3.6(d)) broadly agree with this picture, showing complex components.

A large fraction of the ALGs have hardness ratios that can be reproduced by an APEC model (Figure 3.6(e)), suggesting hot gas as the origin of their X-ray emission. A few sources, which show hardness ratios consistent with a two-component model dominated by an absorbed power-law component ($N_{\text{H}} \sim 10^{22-23}$ atoms cm^{-2}), might host obscured AGN.

Therefore, for the majority of the galaxies in the *2dF* sample, the dominant power sources suggested by the hardness ratios seem to be broadly consistent with the optical classifications.

3.5 Chapter Summary

In this chapter a sample of 72 normal galaxy candidates (the *2dF* sample) was selected using X-ray-to-optical flux ratio, X-ray luminosity and optical spectra. Around 54% (39/72) of the *2dF* sample were NELGs and the rest 46% (33/72) were ALGs. Around 62% (24/39) of the NELGs were classified into eight AGN, seven SF galaxies and nine composite galaxies using the classification scheme from Kewley et al. (2006) based on emission line ratios in the BPT [N II] plot (§ 1.4.3), leaving the remaining 15 NELGs unclassified due to weak emission line(s).

Four galaxies (three ALGs and one NELG) had sufficient X-ray photon counts from *XMM-Newton*, for which the spectral fittings were presented. An APEC model with $kT \sim 0.7-0.8$ keV gave best-fit to two of the three ALGs and contributed half of the 0.2–12 keV emission in the third ALG, suggesting hot gas being the dominant X-ray source in these galaxies. The other half of the X-ray emission from the third ALG was attributed to an absorbed power-law ($N_{\text{H}} = 2.88_{-2.43}^{+7.08} \times 10^{21}$ atoms cm^{-2}), suggesting that the galaxy may host an obscured AGN. The spectrum of the NELG was best-fitted with an unabsorbed power-law which might represent an AGN in this galaxy, although the X-ray binary population might still contribute to part of the X-ray emission of this galaxy.

The X-ray hardness ratios of all the five subsamples, *i.e.*, AGN, SF galaxies, composite galaxies, unclassified NELGs and ALGs, were also examined in order to gain insight of the nature of these X-ray sources when detailed spectral analysis was not allowed for most of them due to small X-ray photon

counts. The hardness ratios suggest a power-law component as the dominant component in most of the AGN, consistent with the optical classification. A thermal component seems to be responsible for a significant fraction of the X-ray emission from SF galaxies. Most of the composite galaxies have hardness ratios consistent with a two-component model consisting of an absorbed power-law and an APEC model. The hardness ratios of the unclassified NELGs suggest complex spectra of these galaxies. The dominant component of ALGs, suggested by their hardness ratios, is a thermal component, which can be interpreted as the hot gas in these systems.

There are a few problems/issues of the $2dF$ spectra that limited the analysis which could be carried out for the $2dF$ sample. Firstly, the $2dF$ spectra were not fully photometrically calibrated, which prevented the extraction of useful information on the emission line luminosities. Another problem was due to the fault of the ADC during some of the $2dF$ observations for XWAS which caused strongly wavelength-dependent fibre losses that are difficult to correct. Compared with $SDSS$, which was used for the studies presented in Chapter 4 and 5, apart from the problems mentioned above, the $2dF$ spectra typically also have lower signal-to-noise ratios, and therefore only simple interpretations are offered for the $2dF$ sample.

Chapter 4

Normal Galaxies in The *XMM-Newton/SDSS* Serendipitous Survey (I): Data and Sample Selection

In this chapter, a large sample of normal-galaxy candidates compiled from the *2XMM* cross-correlated with *SDSS* (the *XMM-Newton/SDSS* Serendipitous Survey, or *XSSS*) is presented. The *2XMM* and *SDSS* catalogues are briefly described in § 4.1 and § 4.2, respectively. Optical counterparts for X-ray sources from *2XMM* are identified in § 4.3.1. The selection functions used to construct the normal galaxy sample for this study are described in § 4.3.2. A summary of this normal galaxy sample is given in § 4.4.

4.1 X-ray Data: *2XMM* Catalogue

The Second *XMM-Newton* Serendipitous Source Catalogue (*2XMM*), constructed by the *XMM-Newton* Survey Science Centre (SSC) on behalf of *ESA*, was released on 22th August 2007. The second largest X-ray source catalogue to date (surpassed by its own incremental release in 2008), *2XMM* contains 246897 X-ray source detections (relating to 191870 unique X-ray sources) drawn from 3491 observations which were published before May 1st 2007. As summarized in Watson et al. (2009), *2XMM*

covers a net area of $\sim 360 \text{ deg}^2$ in the sky and at $\sim 90\%$ of its sky coverage reaches flux limits of $\sim 10^{-14} \text{ erg s}^{-1} \text{ cm}^{-2}$ and $\sim 9 \times 10^{-14} \text{ erg s}^{-1} \text{ cm}^{-2}$ in the soft band (0.5–2 keV) and the hard band (2–12 keV) respectively. The photometric accuracy is $\sim 10\%$ between the three cameras (pn, MOS1, MOS2) and the typical astrometric accuracy is $\sim 1.5''$ (Watson et al. 2009). A detailed description of 2XMM is also available on-line¹.

The data reduction and source detection procedures used for 2XMM have been described in a general way in § 2.3. The 2XMM catalogue includes all detections with a total-band (0.2–12 keV) detection likelihood above 6 ($\sim 3\sigma$). A set of quality flags, which were assigned automatically or manually to detections with potential problems (*e.g.*, objects within extended emission, problematic areas of the CCDs *etc.*), are also provided in the catalogue. Manual flags (flags 11 and 12) were assigned during the visual screening which was focused on masking areas where spurious detections were suspected (problematic areas) and identifying detections within these areas (Watson et al. 2009). In each observation, based on the fraction of problematic areas in the total area observed, an observation classification (column OBS_CLASS in 2XMM) was then assigned. Observations with OBS_CLASS = 5 have the whole field flagged out. Sources included in this study come from observations which satisfy the following criterion:

1. OBS_CLASS < 5 (*i.e.* at least some part of the field is not flagged).
2. Exposure time of the pn camera is longer than 5000 s².
3. The field has been fully covered by SDSS imaging and spectroscopic observations³.

A total of 483 XMM observations satisfy these requirements using the SDSS Sixth Data Release (DR6; Adelman-McCarthy et al. 2008).

After filtering the original XMM-Newton targets from these 483 observations⁴, 36965 sources were re-

¹<http://xmmssc-www.star.le.ac.uk/Catalogue/2XMM/>

²X-ray sources with 0.2–12 keV flux of a typical value, *e.g.*, $10^{-14} \text{ erg s}^{-1} \text{ cm}^{-2}$, would have XMM-Newton pn count rate of $2 \times 10^{-3} \text{ counts s}^{-1}$ predicted by PIMMS v3.9 (Mukai 1993), in which case a exposure time of 5000 s will enable XMM-Newton to collect 10 photons.

³For each XMM-Newton field, the SDSS image with spectroscopic targets overlaid was visually checked to ensure that the whole field was covered by the spectroscopic observations.

⁴Targets are filtered using the target list provided as part of 2XMM in http://xmmssc-www.star.le.ac.uk/Catalogue/2XMM/2xmm_targets.html.

tained as serendipitous sources for the next step. Since a significant fraction of the extended detections in *2XMM* might be uncertain, and even when the detections become more reliable at high detection likelihood they might be dominated by groups and clusters of galaxies (Watson et al. 2009), these detections were excluded from the following study. This should only cause negligible loss of galaxies that appear as real extended sources in *XMM-Newton* because a galaxy with diameter of 10 kpc at redshift of 0.1 (as will be shown later that 0.1 is the average redshift of the galaxies from which the sample will be selected) will have an angular size of $\sim 4''$. As the PSF of *XMM-Newton* is $\sim 6''$, most galaxies in this study will appear as point sources in the *XMM-Newton* images. Hence 35095 point sources were retained for the following step. Although each entry of *2XMM* represents a single detection from an *XMM-Newton* observation, detections related to the same X-ray source were identified during the construction of *2XMM*, therefore one can select unique celestial sources from the catalogue. Source positions, fluxes and hardness ratios (§ 2.3) were calculated as error-weighted mean values from all detections related to a unique source (Watson et al. 2009). Such combined parameters of unique sources were used through this and following chapters unless stated otherwise.

4.2 Optical Data: *Sloan Digital Sky Survey*

The *Sloan Digital Sky Survey*⁵ (*SDSS*; York et al. 2000) is an imaging and spectroscopic survey using a dedicated 2.5 m telescope (Gunn et al. 1998) at Apache Point Observatory (APO), New Mexico. The survey aims to map about one quarter of the whole sky. Standard operations began in April 2000. Imaging and spectroscopic calibrated data and source catalogues are available on-line via the Data

⁵Funding for the *SDSS* and *SDSS-II* has been provided by the Alfred P. Sloan Foundation, the Participating Institutions, the National Science Foundation, the U.S. Department of Energy, the National Aeronautics and Space Administration, the Japanese Monbukagakusho, the Max Planck Society, and the Higher Education Funding Council for England. The *SDSS* Web Site is <http://www.sdss.org/>. The *SDSS* is managed by the Astrophysical Research Consortium for the Participating Institutions. The Participating Institutions are the American Museum of Natural History, Astrophysical Institute Potsdam, University of Basel, University of Cambridge, Case Western Reserve University, University of Chicago, Drexel University, Fermilab, the Institute for Advanced Study, the Japan Participation Group, Johns Hopkins University, the Joint Institute for Nuclear Astrophysics, the Kavli Institute for Particle Astrophysics and Cosmology, the Korean Scientist Group, the Chinese Academy of Sciences (LAMOST), Los Alamos National Laboratory, the Max-Planck-Institute for Astronomy (MPIA), the Max-Planck-Institute for Astrophysics (MPA), New Mexico State University, Ohio State University, University of Pittsburgh, University of Portsmouth, Princeton University, the United States Naval Observatory, and the University of Washington.

Archive Server (DAS)⁶ and Catalogue Archive Server (CAS)⁷; along with detailed documents which give a comprehensive description of the data acquisition, processing and source catalogue construction. The *SDSS* source catalogues were used extensively in the work presented in this chapter. A technical summary is given by York et al. (2000). Description of the official data releases can be found in a series of publications, *e.g.*, Stoughton et al. (2002); Abazajian et al. (2004); Adelman-McCarthy et al. (2006, 2007, 2008). A brief description of the data is given below for clarity.

The imaging data is collected by a 120 megapixel (pixel size $24 \mu\text{m}$, $0.396''$ on the sky) camera which maps the sky in five filters, *ugriz*, covering the range from 3000 to 10000 Å (Fukugita et al. 1996; Stoughton et al. 2002). The *SDSS* imaging data processing pipelines perform the astrometric calibration, detect and deblend objects, measure the properties of these objects, and apply the photometric calibration to these objects. The astrometric calibration making use of the astrometric CCD array in the camera is better than $0.1''$ root mean square per coordinate (Pier et al. 2003). The median PSF width is $1.4''$ in the *r* band. The photometric calibration using a 0.5 m photometric telescope (PT) at the site reaches the accuracy of around 2% root mean square in the *g*, *r*, *i* bands and 3% in the *u* and *z* bands (Ivezić et al. 2004). The 95% completeness limit for point source detection in the *r* band is 22.2 magnitude (Stoughton et al. 2002).

Objects for spectroscopic observations are selected by the *target selection pipeline*. Galaxies (Strauss et al. 2002; Eisenstein et al. 2001) and quasars (Richards et al. 2002) are the main astronomical objects to be observed. Galaxies are separated from stars based on the difference between their PSF and model magnitude in the *r* band (Stoughton et al. 2002). A galaxy target is defined as an object with this difference greater than 0.3 magnitude (star-galaxy separation). Less than 0.5% of true galaxies are rejected and less than 2% of such galaxy targets turn out to be stars (Strauss et al. 2002). Galaxies, satisfying this star-galaxy separation, are included in the Main Galaxy Sample (Strauss et al. 2002) if they have *r* band Petrosian magnitudes (Petrosian 1976) between 15.0 and 17.77. The Main Galaxy Sample has ~ 90 galaxy targets per square degree with a median redshift of 0.104 (Strauss et al. 2002). Strauss et al. (2002) also shows that the completeness of this sample exceeds 99%. Galaxies which are fainter than 17.77 in the *r* band might still be targeted if they belong to either the Luminous Red Galaxy (LRG) Sample (down to 19.5 mag; Eisenstein et al. 2001), *u* band selected galaxies (down to ~ 20.5 mag; Baldry et al. 2005; Adelman-McCarthy et al. 2006), or low-redshift galaxies (down to ~ 19.5

⁶<http://das.sdss.org/>

⁷<http://cas.sdss.org/astro/en/>

mag; Adelman-McCarthy et al. 2006). However, the completeness of these extra galaxy samples are less well defined. All magnitudes used in the selection criteria have been corrected for the Galactic extinction.

The spectroscopy is then carried out by a pair of double fibre-fed spectrographs which use fibre optics (about $3''$ in the focal plane) to simultaneously take spectra of 640 objects. The wavelength from 3800 to 9200 Å is covered with the $\lambda/\Delta\lambda$ varying from 1850 to 2200. Because fibres cannot be placed closer than $55''$ (York et al. 2000), in regions covered by a single plate, sources with a smaller separation than this compete with each other to be targeted. About 10% of selected galaxies in the Main Galaxy sample do not receive a fiber for this reason in the first pass. In the plate overlap area, about 30% of the observed sky, the sources with the second highest priority within $55''$ can also be targeted. This brings the fraction of galaxies that are missed down to about 6% (Strauss et al. 2002).

The published spectra are wavelength- and flux-calibrated. The wavelength calibration uncertainty is $\sim 0.05\text{Å}$ and the flux calibration has an uncertainty of $\sim 5\%$ (Abazajian et al. 2004). The *SDSS* pipelines also carry out redshift determination, spectral classification and line measurements in each spectrum (Stoughton et al. 2002). For clarity a brief summary of the relevant procedures and outputs of these pipelines is given here. Nearly all the targeted galaxies (99.9%) yield reliable redshift measurements with an accuracy of ~ 0.0001 ($\approx 30 \text{ km s}^{-1}$; Stoughton et al. 2002). Objects with $cz < 450 \text{ km s}^{-1}$ are classified as stars. If the redshift is obtained from one of the late-type stellar cross-correlation templates, the object is classified as a late-type star. Quasars are those objects which have any of the identified emission lines broader than 500 km s^{-1} and/or whose final redshift is obtained from lines only expected for quasars (*e.g.*, $\text{Ly}\alpha$, C IV, C III). Object with final redshift larger than 2.3 (so that $\text{Ly}\alpha$ is or should present in the spectrum) is classified as a high- z quasar. Objects with a cross-correlation redshift confidence level below 0.25 are classified as unknown. Objects which do not receive any of the above classifications are classified as galaxies. A set of emission lines (see Table 30 in Stoughton et al. 2002) are fitted with Gaussians after a sliding-window fitted continuum has been subtracted from the spectrum (*i.e.*, the continuum is fitted using a straight line within the sliding window [300 pixels for galaxy]). The output includes detection significance, line equivalent width and magnitude with their errors.

By the time the work presented in this chapter started, *SDSS* had released its Sixth Data Release (DR6; Adelman-McCarthy et al. 2008) which provides imaging for 9583 deg^2 area of the sky and spectra for

objects selected in various samples in 7425 deg^2 of the sky.

4.3 Normal Galaxy Sample from *2XMM* Cross-correlated with *SDSS* DR6

4.3.1 Cross-correlation between *2XMM* and *SDSS* DR6

The *2XMM* sources from the selected observations were used to cross-correlate with *SDSS* DR6. The X-ray positions from the *2XMM* catalogue (SC_RA and SC_DEC) were uploaded to *SDSS* CasJob and then the tool *Neighbour* was run to search within $20''$ for all archived imaging objects in DR6. Potential matches were found for 33586 sources, $\sim 96\%$ of the uploaded 35095 *2XMM* point sources. The distribution of the X-ray positional uncertainties (column SC_POSEERR in *2XMM*) of these 33586 sources is shown in Figure 4.1(a). On average one X-ray source has ~ 3.5 matches in *SDSS* within $20''$. The distribution of the separations between X-ray and optical positions for all *SDSS* matches is shown in Figure 4.1(b).

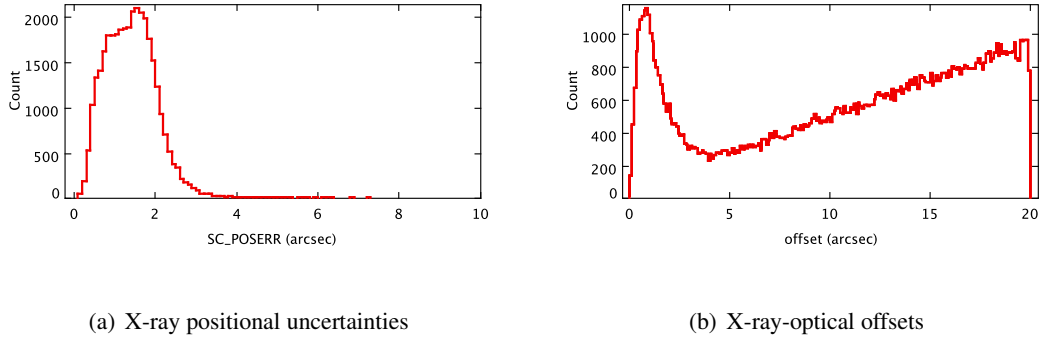


Figure 4.1: (a) The positional uncertainties (column SC_POSEERR in *2XMM*) of all the X-ray sources which have *SDSS* matches (truncated at $10''$). (b) The separations between the X-ray positions and optical positions for all *SDSS* matches.

The positive matching distance was then defined as the minimum between $7''$ and 3.5 times of X-ray positional uncertainty (typical positional error was $1.4''$). In order to estimate the random matching rate, all the uploaded X-ray positions were shifted by $45''$ in four directions and then searched for random matches of these shifted positions. This revealed that at $r \leq 18$ around 1% matches could be random and this random match rate rose to $\sim 8\%$ when going down to $r \sim 21$. As described later, the brightest *SDSS* objects were assigned as the optical counterparts within the positive matching distance and only

objects with *SDSS* spectra and hence generally brighter than 18 magnitude could be selected into the sample studied here, the false matches found by chance should be no more than $\sim 1\%$.

It was found that $\sim 66\%$ (23265/35095) point sources had at least one *SDSS* object within the positive matching distance defined as above. There were 2386 ($\sim 10\%$) point sources which had more than one optical object within the positive matching distance, in which case the brightest one in *SDSS* r band (Petrosian magnitudes were used hereafter) was chosen as the optical counterpart of the given X-ray source. There were 12 cases in which the second brightest objects had *SDSS* spectra and were classified as galaxies by *SDSS* pipeline based on their spectra. A visual check was then carried out for these objects. By checking the *SDSS* imaging of these objects, a few cases were found to be responsible for the situation described above: (1) the *SDSS* pipeline only selected the second brightest object as spectroscopic target because the brightest object failed the target selection criterion; in these cases the brightest and the second brightest sources were normally very close, and sometimes were “children” of a deblended source; or (2) *SDSS* managed to take spectra for both the brightest and the second brightest sources because they happened to be in the plate overlapping area. For the first case, if the second brightest object is nearer to the X-ray position, the second brightest object is assigned as the optical counterpart of the X-ray source. There are six out of 12 such cases. There was no need to manually assign the optical counterpart in the second case. Since these multiple matching cases were rare they would not affect any statistical claim although extra care must be taken for interpretation of individual sources. Therefore the optical counterparts for all of the 23265 X-ray sources were defined.

4.3.2 Sample Selection

The sample was selected in a similar way to that adopted for XWAS in Chapter 3. The steps are described below:

1. The X-ray-to-optical flux ratio cut-off was $\log(f_X/f_O) \leq -1$, where f_X was the full band (0.2–12 keV) X-ray flux from *2XMM* (column `SC_EP_8_FLUX`), and the optical flux f_O was calculated from *SDSS* r band Petrosian magnitude. The $\log(f_X/f_O)$ was defined as below:

$$\log\left(\frac{f_X}{f_O}\right) = \log f_X + 5.5 + \frac{r}{2.5}. \quad (4.1)$$

About 10% (2240/23265) of the X-ray sources passed this filtering (the sources below the $\log(f_X/f_O) = -1$ line in Figure 4.2).

2. Then sources whose *SDSS* counterparts were spectroscopically classified as galaxies (SpecClass = 2 in *SDSS* SpecObj table), 506 in total, were selected (sources marked as green circles and sitting below the $\log(f_X/f_O) = -1$ line in Figure 4.2). Among these 506 galaxies, 21 were originally targeted as QSOs and one as a radio source (Stoughton et al. 2002).
3. Further requirement was on the X-ray luminosity: $L_X \leq 10^{43}$ erg s⁻¹. The luminosity was calculated using the *2XMM* full band flux (column SC_EP_8_FLUX) and *SDSS* redshift. This cut only removed one source, leaving 505 sources.
4. The final step was to exclude source detections within areas where spurious detections were identified unless they were the ‘causing’ sources, which cause those spurious detections (Watson et al. 2009). This was achieved by applying restrictions on the detection flags provided in *2XMM* (see § 4.1). For each source, the flags of the detection from the longest pn exposure (if more than one available) was considered since such detection usually had the highest signal-to-noise ratio among all the detections of a given source. Sources with PN_FLAG 11 set (the source was in a problematic region) but not PN_FLAG 12 (so the source was not the ‘causing’ source) were rejected. This left a sample of 463 sources, referred to as the *XS* sample hereafter (filled green circles in Figure 4.2 and Figure 4.3). The Flowchart in Figure 4.4 provides a simplified view of the selection procedure.

4.4 Sample Summary

4.4.1 Optical Properties

The *SDSS* *r* band Petrosian magnitudes of the *XS* sample objects range from 11.78 to 19.76 and have the mean and median at 16.24 and 16.40. The magnitude distribution is shown in Figure 4.5(a). The *SDSS* redshift measurements of *XS* range from 0.002 to 0.565 with the mean value at ~ 0.11 and median at ~ 0.09 , similar to the mean and median of *SDSS* Main Galaxy sample (Strauss et al. 2002). The redshift distribution of *XS* is shown in Figure 4.5(b).

Due to the way the *XS* sample was selected, galaxies which had *SDSS* spectra showing narrow emission lines were included. Narrow emission line galaxies (NELGs) were defined as those with at least one

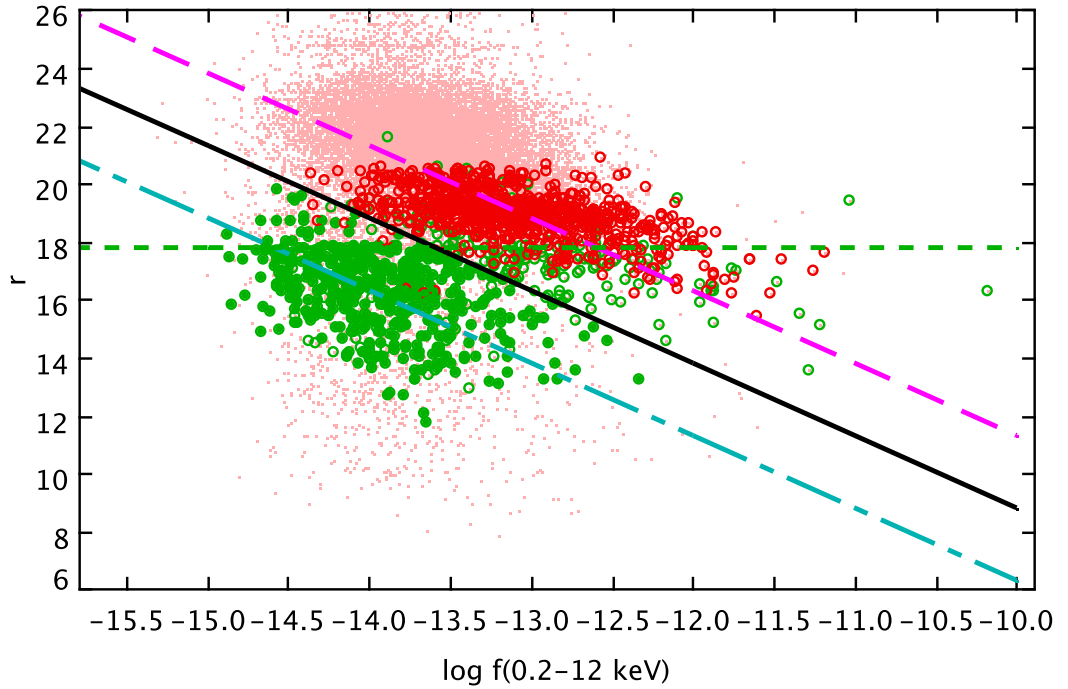


Figure 4.2: All 23265 X-ray sources with *SDSS* matches are shown as pink dots in this *SDSS* *r* band Petrosian magnitude versus 0.2–12 keV X-ray flux plot. Green circles are *SDSS* spectroscopically classified galaxies, with the filled ones representing the *XS* sample. The red circles mark the *SDSS* spectroscopically classified QSOs. The slanted lines indicate constant X-ray-to-optical flux ratios of $\log(f_x/f_o) = 0, -1,$ and -2 , marked by pink dashed line, black solid line and light blue dashed-dotted line, respectively, from top to bottom. The horizontal line indicates the approximate magnitude limit of the *SDSS* Main Galaxy Sample ($r \approx 17.77$; Strauss et al. 2002).

of the following emission lines detected above 3σ significance: $H\beta$, $[O\ III]\lambda 5007$, $H\alpha$, $[N\ II]\lambda 6584$ and $[S\ II]\lambda\lambda 6717, 6731$. These lines have been widely used to separate AGNs from SF galaxies (*e.g.*, Baldwin et al. 1981). There were 376 NELGs, making up $\sim 81\%$ of *XS*. The rest of the sample (87 galaxies) are referred to as Absorption Line Galaxies, or ALGs hereafter. On average NELGs tend to be slightly brighter than ALGs in the *r* band. The mean and median *r* band Petrosian magnitudes of NELGs are 16.08 and 16.27, compared to 16.61 and 16.69 of ALGs. ALGs on average have larger redshifts than NELGs. The mean (median) values of redshift for NELGs and ALGs are 0.09 (0.08) and 0.16 (0.13), respectively. The distributions of *r* band Petrosian magnitudes and redshifts for NELGs and ALGs are also shown in Figure 4.5(a) and 4.5(b).

The concentration index $C_{90/50}$, defined as the ratio of radii containing 90% and 50% of the galaxy

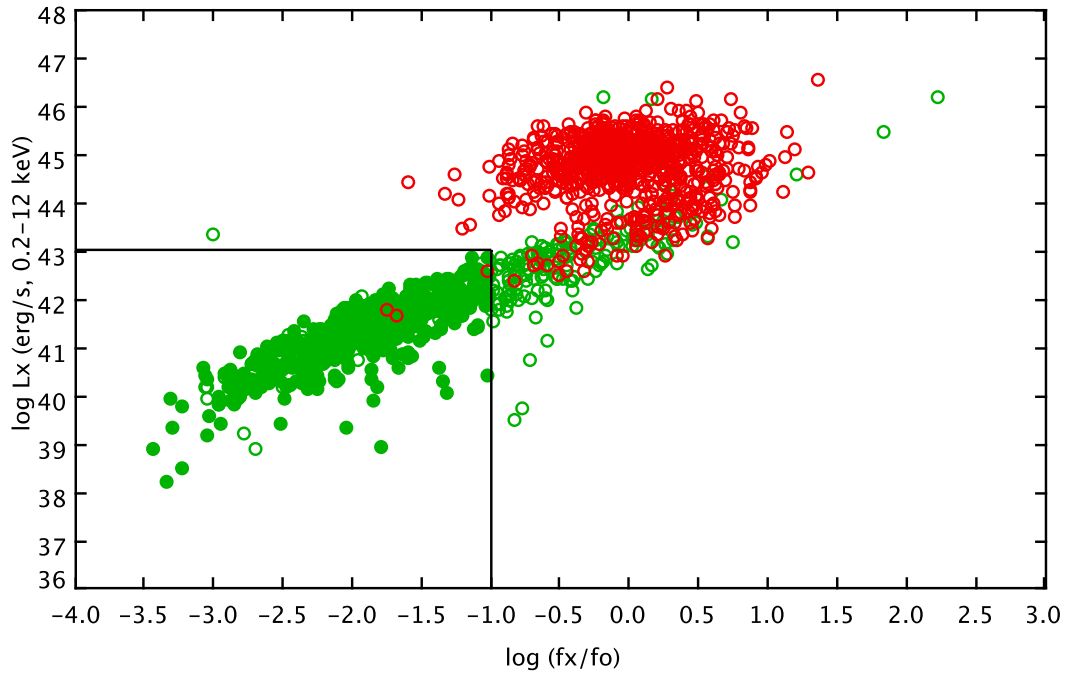
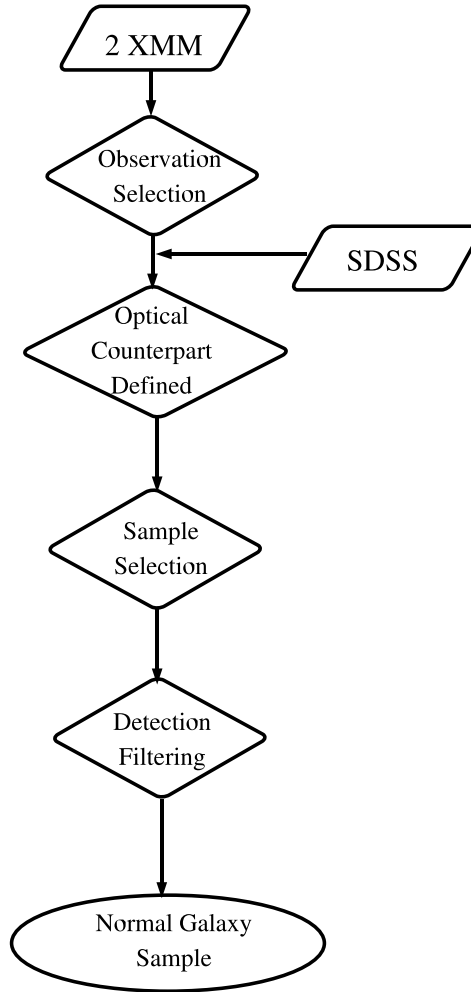


Figure 4.3: All 1556 X-ray sources with *SDSS* spectra are shown here. $\log(f_x/f_o)$ was calculated using Equation 4.1. The 0.2–12 keV luminosity was calculated using the flux from *2XMM* (column *SC_EP_8_FLUX*) and redshift from *SDSS*. Green circles are *SDSS* spectroscopically classified galaxies, with the filled ones denote the *XS* sample. The red circles represent the *SDSS* spectroscopically classified QSOs. The horizontal and vertical lines indicate the values used to selected the *XS* sample.

light, has been found to serve as an indicator of galaxy type. Strateva et al. (2001), using *SDSS* *r* band Petrosian radii, found that $C_{90/50} = 2.6$ can be used as a separator of early-type (E, S0 and Sa) and late-type (Sb, Sc and Irr) galaxies: early-type galaxies tended to have $C_{90/50}$ above 2.6 while late-type galaxies had $C_{90/50}$ below 2.6. These authors also found that early-type galaxies often had $u - r$ above 2.22 while late-type galaxies below this value. Figure 4.6 shows the $u - r$ colour (galactic extinction corrected) against concentration index $C_{90/50}$ for *XS*. Most of the ALGs have $C_{90/50} > 2.6$, which suggests early-type morphologies. The NELGs spread over the whole ranges of $u - r$ and $C_{90/50}$, which suggests that NELGs are mixture of early-type and late-type galaxies.

Figure 4.4: Flow chart to summarize the procedures used to select the *XS* sample.

4.4.2 X-ray Properties

The X-ray sources in the *XS* sample have the mean full band (0.2–12 keV) X-ray flux of $2.07 \times 10^{-14} \text{erg s}^{-1} \text{cm}^{-2}$. The NELGs, which have the mean full band flux of $2.31 \times 10^{-14} \text{erg s}^{-1} \text{cm}^{-2}$, tend to be brighter than the ALGs whose mean full band flux is $1.05 \times 10^{-14} \text{erg s}^{-1} \text{cm}^{-2}$ (Figure 4.7(a)). Using Kolmogorov-Smirnov (K-S) test the null hypothesis that the NELGs and the ALGs have the same underlying distributions of the full band fluxes can be rejected at significance level of 1%. On average the ALGs tend to be more luminous, although not significant, than the NELGs in 0.5–2 keV band. The mean values of $\log(f_X/f_O)$ are -1.92 , -1.91 and -1.98 for all galaxies in *XS*, the NELGs and the ALGs, respectively. Although on average the ALGs have lower X-ray fluxes (Figure 4.7(a)) and also lower $\log(f_X/f_O)$ (Figure 4.7(b)) than the NELGs, the large overlap in the distributions of

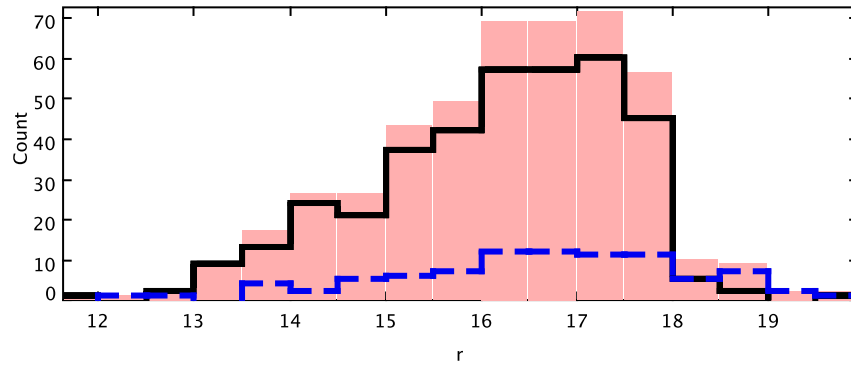
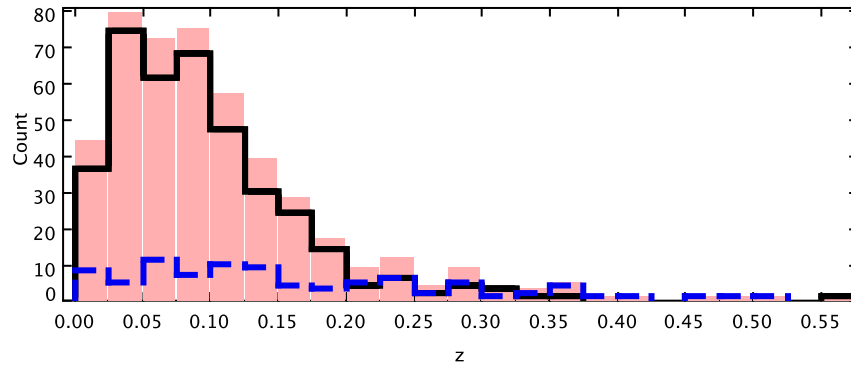
(a) *SDSS* *r* band Petrosian magnitudes(b) *SDSS* redshifts

Figure 4.5: Distributions of *SDSS* *r* band Petrosian magnitudes and redshifts are shown in (a) and (b) respectively. The *XS* sample, its NELG subsample and ALG subsample are marked with filled (pink), solid (black) and dashed (blue) histograms respectively.

these two quantities prevents using them to separate these two galaxy populations. The 0.2–12 keV X-ray luminosities of sources in the *XS* sample range from $\sim 10^{38} \text{erg s}^{-1}$ up to the luminosity cut-off ($10^{43} \text{erg s}^{-1}$), with the mean values as $10^{41.3} \text{erg s}^{-1}$ for the whole sample, $10^{41.2} \text{erg s}^{-1}$ for NELGs and $10^{41.4} \text{erg s}^{-1}$ for ALGs. The distributions of 0.2–12 keV luminosities for the *XS* sample, the NELG and ALG subsamples are shown in Figure 4.7(c). In the observations used for this work, the *XS* X-ray sources have the mean photon counts in the pn camera of 88 (Figure 4.8), making it difficult to carry out spectral fitting for the majority of the sources.

The X-ray hardness ratio (§ 2.4.4), or X-ray colours, can be used to constrain the broad-band X-ray

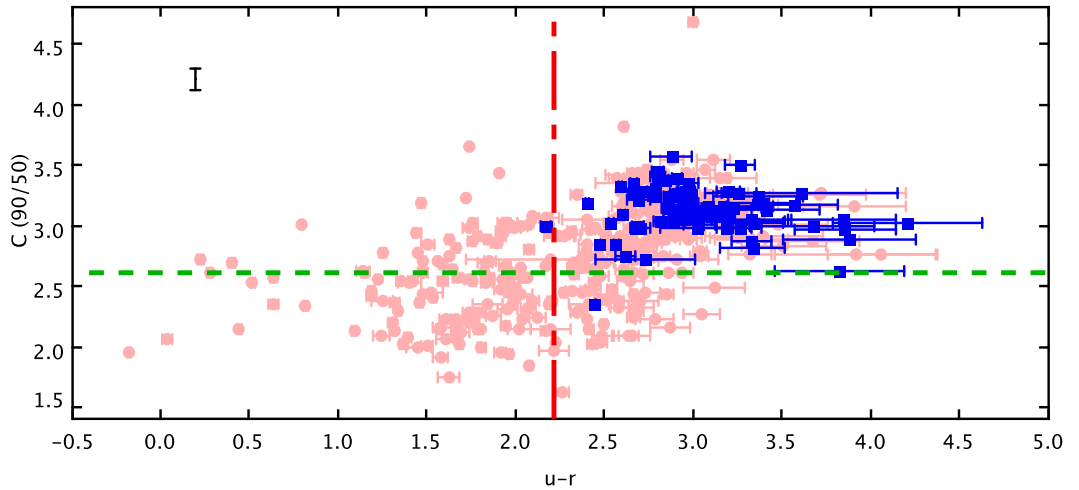
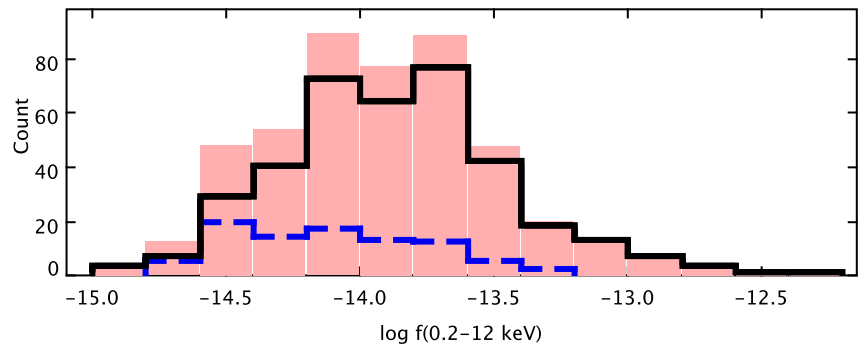
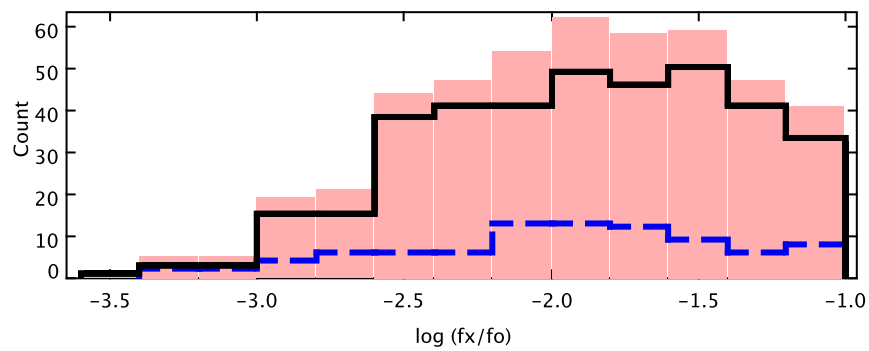


Figure 4.6: The $u - r$ colours are shown against the concentration index $C_{90/50}$ (the ratio of the radii defined as containing 90% and 50% of the galaxy light using a Petrosian profile). Nineteen galaxies which have u band magnitude fainter than the magnitude limit (~ 22 ; Adelman-McCarthy et al. 2008) are excluded. $u - r = 2.22$ is shown as the dashed-dotted vertical line. $C_{90/50} = 2.6$ is indicated by the dotted horizontal line. Strateva et al. (2001) found that early-type (E, S0 and Sa) galaxies tend to have $u - r > 2.22$ and $C_{90/50} > 2.6$ while late-type (Sb, Sc and Irr) galaxies are likely to have $u - r \leq 2.22$ and $C_{90/50} \leq 2.6$. NELGs are shown with pink circles while ALGs are marked with blue squares. The median of the errors of $C_{90/50}$ is 0.09 and is shown as the black bar. For $\sim 2\%$ of the sources the $C_{90/50}$ is not well constrained.

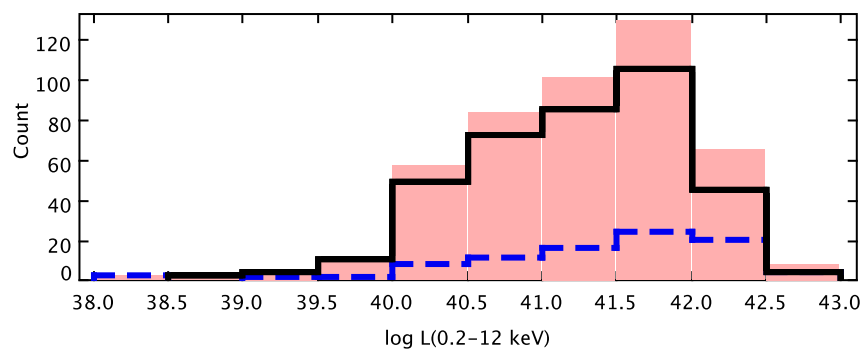
spectral shape. Similar to XWAS, HR2 and HR3 were used here since *XMM-Newton* has good sensitivity over the bandpass covered by HR2 and HR3 (0.5–4.5 keV) and in normal galaxies the X-rays below and above ~ 2 keV may easily be associated with different origins. For the X-ray sources in the *XS* sample, the typical errors on HR2 and HR3 are 0.2 and 0.3, respectively. In order to highlight the average features of the hardness ratios of the sample without ignoring the uncertainties, hardness ratio density plots are used here. To construct a density plot, each data point is weighted based on its own uncertainty. In such weighted density plots, each hardness ratio pair (HR2, HR3) is presented as a two-dimensional Gaussian distribution calculated from two one-dimensional Gaussian distributions, one using the HR2 value and error, the other using the HR3 value and error. Density plots constructed in such a weighted manner are fairly suitable for studying the properties of faint sources whose main features might be difficult to extract from individual detection. Therefore all sources with defined hardness ratios (*i.e.*, not NULL values) were used to produce the hardness ratio density plot, regardless of its detection likelihood in individual bands.



(a)



(b)



(c)

Figure 4.7: Distributions of 0.2–12 keV fluxes, the X-ray-to-optical flux ratios and 0.2–12 keV luminosities are shown in (a), (b) and (c) respectively. The XS sample, its NELG subsample and ALG subsample are marked with filled (pink), solid (black) and dashed (blue) histograms respectively.

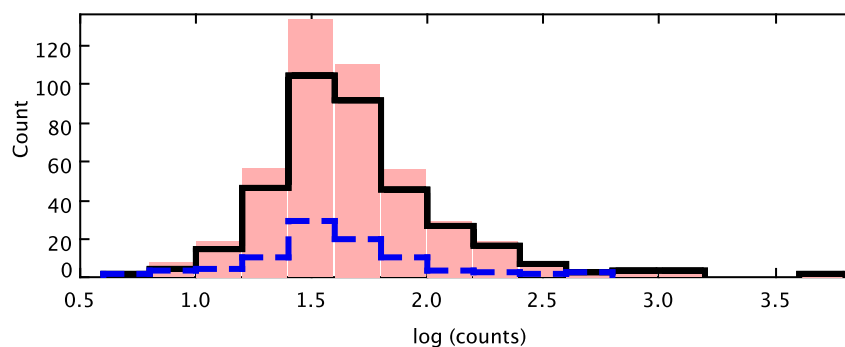


Figure 4.8: Distributions of 0.2–12 keV photon counts from the pn camera. The XS sample, its NELG subsample and ALG subsample are marked with filled (pink), solid (black) and dashed (blue) histograms respectively.

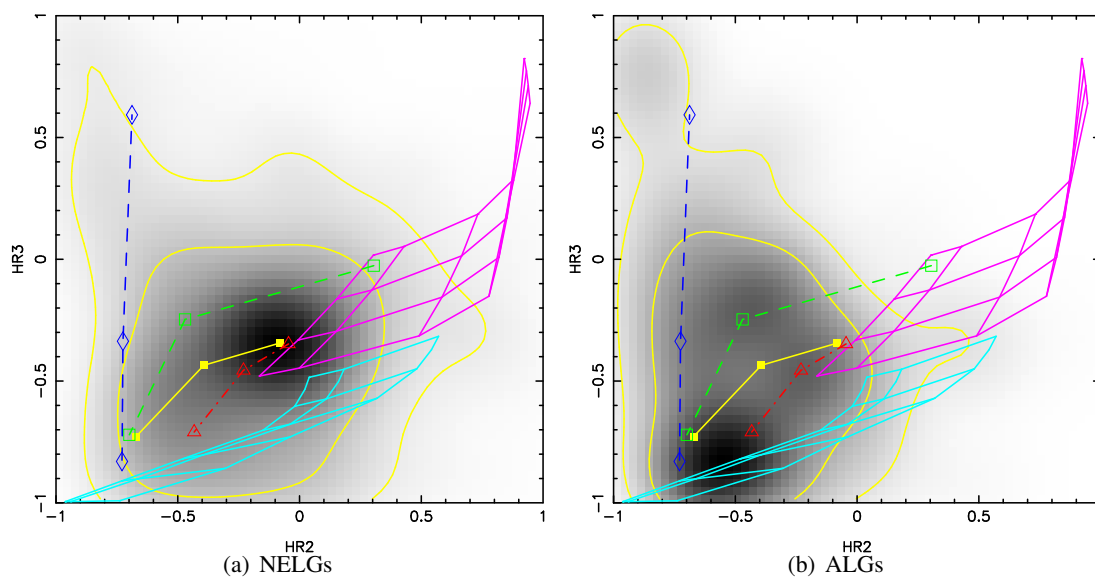


Figure 4.9: The smoothed X-ray hardness ratio (HR2 against HR3) density plots for NELGs and ALGs. Spectral models defined in § 2.4.4 are overlaid in each plot. Contours at 68% and 90% levels are also shown.

The hardness ratios (HR2 versus HR3) from the pn camera for the NELGs and ALGs are shown in Figure 4.9. The density plots are 61 bins across (smoothed using a 4-bin Gaussian box). Comparing the hardness ratios of NELGs with models reveals that while a power-law component appears to be the dominant component, a thermal component is also indicated. On the other hand, ALGs seem to be dominated by a thermal component although some power-law component is also suggested.

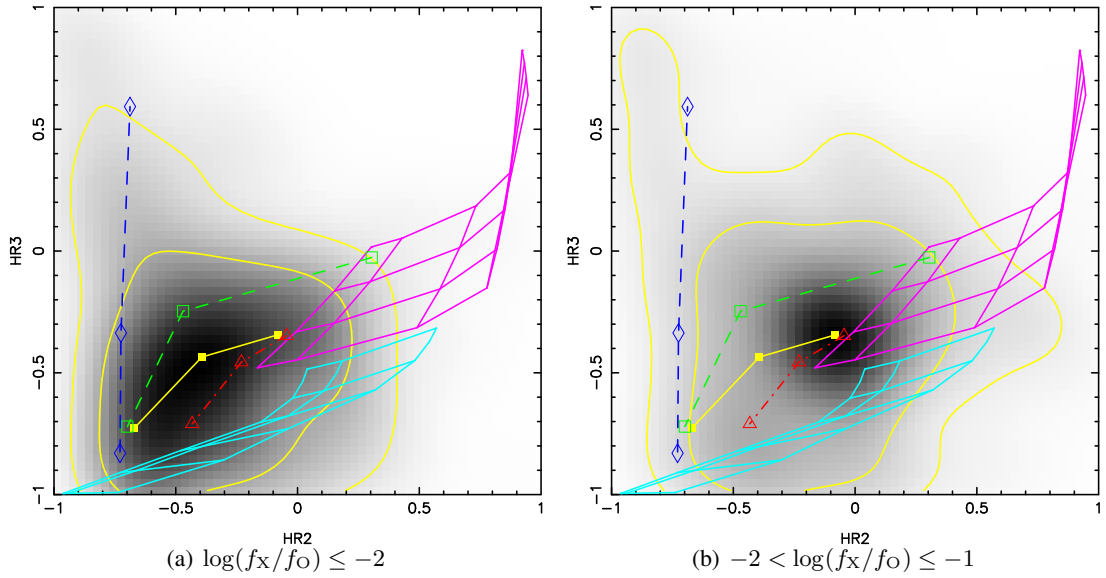


Figure 4.10: The smoothed X-ray hardness ratio (HR2 versus HR3) density plots for XS sources with $\log(f_X/f_O) \leq -2$ and $-2 < \log(f_X/f_O) \leq -1$ respectively. Spectral models defined in § 2.4.4 are overlaid in each plot. Contours at 68% and 90% levels are also shown.

The X-ray-to-optical flux ratio used to select the XS sample is $\log(f_X/f_O) \leq -1$, which allows the study of normal galaxies with $-2 < \log(f_X/f_O) \leq -1$. There are 267 (57.7%) sources in the XS sample with $-2 < \log(f_X/f_O) \leq -1$. The X-ray hardness ratios HR2 versus HR3 for sources with $\log(f_X/f_O)$ below and above -2 are shown in Figure 4.10. The peak in the density plot of sources with $\log(f_X/f_O) \leq -2$ has lower values in both HR2 and HR3, compared with those with $\log(f_X/f_O) > -2$. Comparing these two peaks against the overlaid models reveals that X-ray emission from sources with $\log(f_X/f_O) \leq -2$ has similar contributions from both power-law and thermal components, while sources with $-2 < \log(f_X/f_O) \leq -1$ tend to be dominated by a power-law component.

The XS sample includes galaxies with $L_{0.2-12\text{keV}} > 10^{42}\text{erg s}^{-1}$. Although these galaxies have high X-ray luminosities they do not show optical broad emission line(s) to indicate clear Type 1 AGN activity. There are 160 sources with $L_X \leq 10^{41}\text{erg s}^{-1}$, 230 sources with $10^{41} < L_X \leq 10^{42}\text{erg s}^{-1}$ and 73

sources with $L_X > 10^{42} \text{ erg s}^{-1}$. The X-ray hardness ratios of sources in these three X-ray luminosity bins are shown in Figure 4.11. It is difficult to discern any clear clustering of sources in these three luminosity bins.

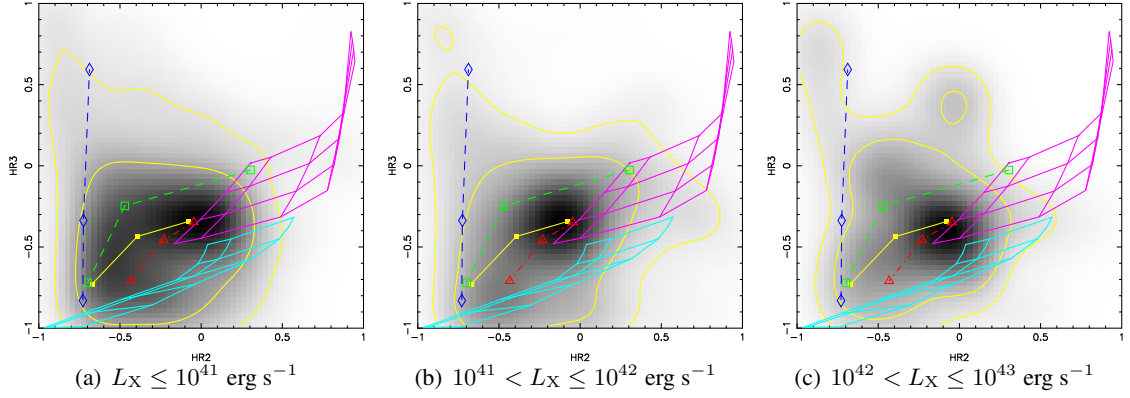


Figure 4.11: The smoothed X-ray hardness ratio (HR2 versus HR3) density plots for XS sources in three X-ray luminosity bins: $L_X \leq 10^{41} \text{ erg s}^{-1}$, $10^{41} < L_X \leq 10^{42} \text{ erg s}^{-1}$, and $10^{42} < L_X \leq 10^{43} \text{ erg s}^{-1}$. Spectral models defined in § 2.4.4 are overlaid in each plot. Contours at 68% and 90% levels are also shown.

To summarize, the XS sample, constructed with completeness and reliability in mind, consists of galaxies from a wide range of optical types and X-ray properties. Based on the SDSS spectra, the XS sample was divided into NELGs and ALGs. On average NELGs have lower redshifts than ALGs. Both late- and early-type galaxies are present in the NELG subsample, while ALGs tend to have early-type morphologies. In the X-ray regime, although they tend to have higher fluxes than ALGs, owing to their lower mean redshifts, NELGs have lower mean luminosity than ALGs. The X-ray hardness ratios from NELGs and ALGs display different patterns in density plots, suggesting different mean spectral shapes for the X-ray emissions. The XS sample was selected to be free from Type 1 AGNs, however Type 2 AGNs are included. Elusive AGNs (*e.g.*, Fiore et al. 2000; Comastri et al. 2002) can also contaminate the ALG subsample. Identifying such AGN contamination in the normal galaxy sample is addressed in the following chapter.

Chapter 5

Normal Galaxies in The *XMM-Newton/SDSS* Serendipitous Survey (II): Subsamples

Emission/absorption line measurements were available for a subset of the *XS* sample, therefore this subset was classified into different types of galaxies using these line measurements (§ 5.1). These classified subsamples are then discussed separately in § 5.2 to § 5.6. Further discussion on the effectiveness of the sample selection criteria is provided in § 5.7. The whole chapter is summarized in § 5.8.

5.1 Optical Classification for NELGs

As described in § 4.4.1, a large fraction ($\sim 81\%$) of the *XS* sample has been classified as NELGs. For these NELGs, the BPT plots (plots of intensity ratios between particular optical emission lines; see § 1.4.3) can be used to separate AGN and SF galaxies.

The *SDSS* official data release includes measurements of emission lines, however, these measurements were previously designed to measure redshifts instead of providing detailed information of lines. Starlight subtraction is not carried out in the *SDSS* official pipeline. Due to the fibre size of *SDSS* ($3''$), a large fraction of a galaxy can be included and the absorption features in the starlight cause a significant effect on the observed intensities of emission lines. Therefore, a series of catalogues published by a group of researchers from the Max-Planck-Institute for Astrophysics or the Johns Hopkins University

(referred to as *MPA/JHU* catalogues¹ hereafter) were used to provide the emission line parameters as these measurements were obtained from starlight-subtracted *SDSS* spectra.

5.1.1 Classification Based on Narrow Emission Line Ratios

Full details of the *MPA/JHU* catalogues are available in Kauffmann et al. (2003b,a), Brinchmann et al. (2004), and Tremonti et al. (2004), but a brief description of these catalogues is given here for clarity. In the construction of the *MPA/JHU* catalogues, the stellar population synthesis code from Bruzual & Charlot (2003) which incorporates an empirical spectral library (Le Borgne et al. 2003) was used to generate single stellar population models. These single stellar population models were then used to construct template spectra of a wide range of age and metallicity. During the fitting of a given *SDSS* spectrum, the template spectra were transformed to the redshift and stellar velocity dispersion (measured by the Princeton/MIT reduction²) and then re-sampled in the form of a non-negative linear combination to give the best-fit model to the line-free continuum regions of the spectrum. The emission lines were fitted with Gaussians after subtracting the best-fit continuum from the observed spectrum. During the line fitting, all Balmer lines ($H\delta$, $H\gamma$, $H\beta$, and $H\alpha$) were required to have the same line width and velocity offset, and the forbidden lines ($[O\ II]\lambda 3726, 3729$, $[O\ III]\lambda 4959, 5007$, $[N\ II]\lambda 6548, 6584$, and $[S\ II]\lambda\lambda 6717, 6731$) were also required to have the same line width and velocity offset. The output line fluxes were corrected for galactic reddening (O’Donnell 1994). The D4000 break³ and the $H\delta$ absorption index⁴ were used to estimate the z band mass-to-light ratio (M_*/L), which was then scaled by the z band absolute magnitude to obtain the stellar mass (M_*). The SFR was estimated using a Bayesian approach from a grid of 2×10^5 nebular models and was aperture corrected. SFRs from galaxies with $M_* \leq 10^5 M_\odot$ were not reliable (Tremonti et al. 2004). The Kroupa (2001) universal initial mass function (IMF) was used in all related measurements.

At the time the work presented in this thesis was carried out, the available versions of the *MPA/JHU* catalogues were constructed only up to the fourth data release of *SDSS* (DR4; Adelman-McCarthy et al. 2006). By visual examination, 319 out of the 483 *XMM-Newton* observations used to construct the *XS*

¹Available at <http://www.mpa-garching.mpg.de/SDSS/>.

²See <http://spectro.princeton.edu/>.

³The ratio of the average flux density F in 3850–3950Å to that in 4000–4100Å (Balogh et al. 1999).

⁴The ‘equivalent width’ defined using flux from a central bandpass and two pseudo-continuum bandpasses (Worthey & Ottaviani 1997).

sample were fully covered by DR4 spectroscopic footprint. There were 284 *XS* galaxies in these 319 observations. These galaxies will be referred to as the *MJ* sample⁵ hereafter. There are 239 NELGs and 45 ALGs in the *MJ* sample. As the *MJ* sample is a complete subset of the *XS* sample, the average *r* magnitudes, redshifts, X-ray fluxes and luminosities of the *MJ* sample are similar to those drawn from the *XS* sample.

Among the 239 NELGs in the *MJ* sample, 96 had all of the $H\beta$, $[O\ III]\lambda 5007$, $H\alpha$, and $[N\ II]\lambda 6584$ lines detected above 3σ ; 14 had all four lines detected with at least one line below 3σ ; another 60 had three out of the four lines detected and the remaining line ($H\beta$ in most cases) recovered after the stellar continuum was subtracted. Hence, in total 170 NELGs could be classified using the BPT diagrams based on $[O\ III]\lambda 5007/H\beta$ and $[N\ II]\lambda 6584/H\alpha$. This left 69 unclassified NELGs.

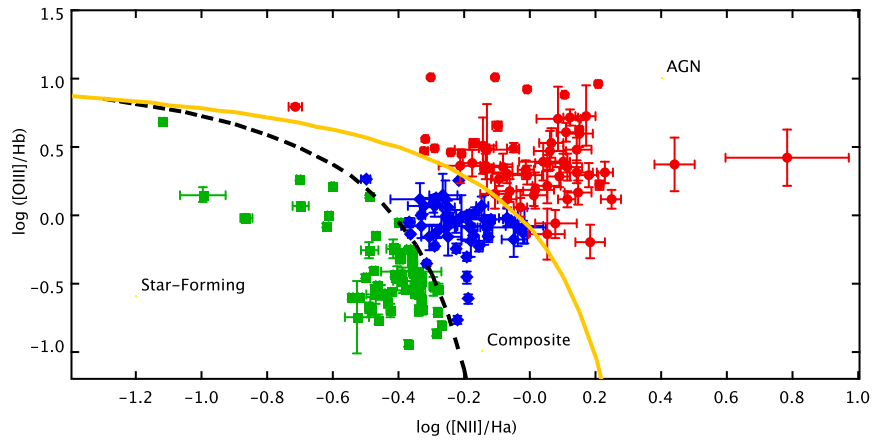
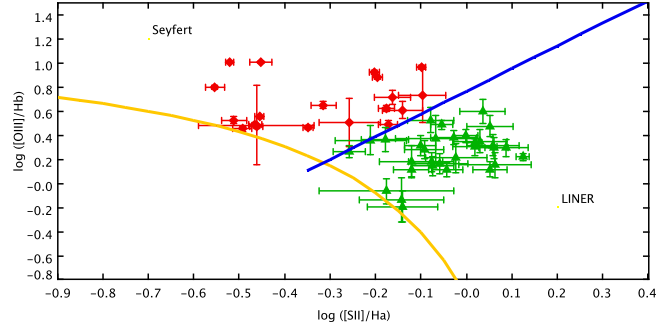


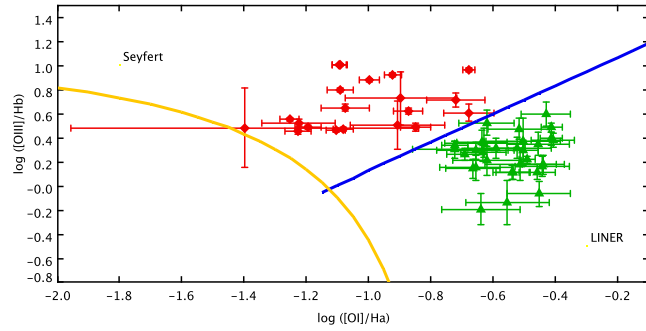
Figure 5.1: The BPT [N II] plot and the classification scheme from Kewley et al. (2006). Galaxies lying above the yellow solid line (Equation 1.8) are classified as AGN and marked with red dots. Galaxies lying below the black dashed line (Equation 1.7) are classified as SF galaxies and marked with green squares. Galaxies lying between these two lines (Equation 1.9 and Equation 1.10) are referred to as composite galaxies and marked with blue diamonds.

Using the BPT [N II] plot and the classification scheme from Kewley et al. (2006) (Figure 5.1; Equation 1.7 – 1.10), the 170 NELGs were classified into 60 AGN, 62 SF galaxies, and 48 composite galaxies. Using the BPT [S II] plot, [O I] plot and the Kewley et al. (2006) classification scheme (Figure 5.2(a) and 5.2(b); Equation 1.11 – 1.18), the 60 AGN were further classified into 20 Seyfert 2 galaxies and 31 LINER 2s, leaving the remaining nine with either undetected [O I] line or inconsistent classifications from the BPT [S II] and [O I] plots.

⁵The whole sample is listed in Table B.1.



(a)



(b)

Figure 5.2: The BPT [S II] plot (a) and the BPT [O I] plot (b) for the AGN classified in Figure 5.1. Also shown is the classification scheme from Kewley et al. (2006). AGN (Equation 1.12 and 1.16) are split into Seyfert 2 galaxies (Equation 1.13 and 1.17; red diamonds) and LINER 2s (Equation 1.14 and 1.18; green triangles).

5.1.2 Summary of The Subsamples

As described in § 5.1.1, there are 239 NELGs and 45 ALGs in the *MJ* sample. The optical emission line measurements from the *MPA/JHU* catalogues enabled 170 NELGs to be classified using the BPT plots. These 170 classifiable NELGs were classified into 60 AGN, 62 SF galaxies and 48 composite galaxies. The remaining 69 NELGs which could not be classified using BPT plots are referred to as ‘unclassified NELGs’ hereafter.

The four NELGs subsamples: AGN, SF galaxies, composite galaxies and unclassified NELGs span similar r band magnitudes⁶. In the $u - r$ colour versus concentration index $C_{90/50}$ plot (Figure 5.3), SF galaxies, composite galaxies, AGN and unclassified NELGs seem to form a continuous sequence from

⁶See Figure C.1 for the r band magnitude distributions.

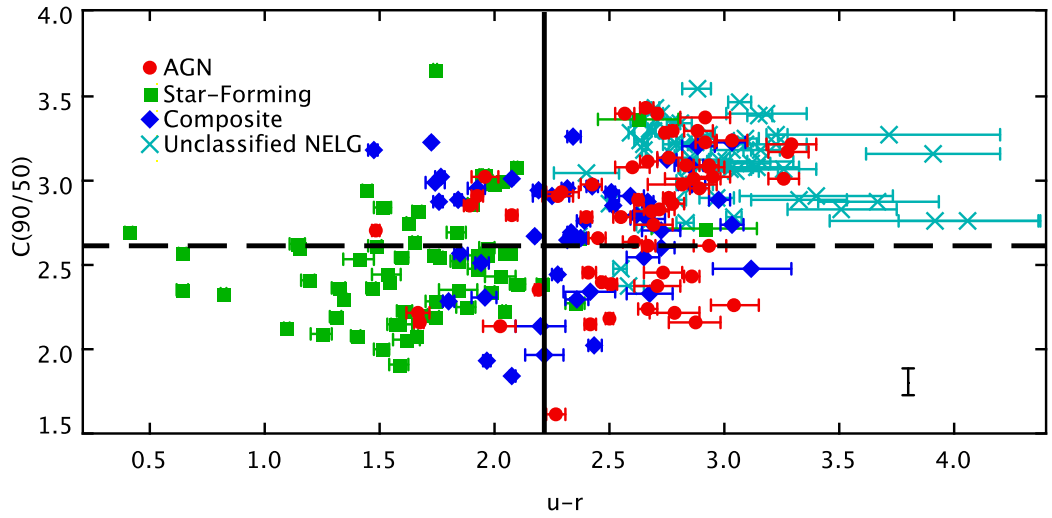


Figure 5.3: The $u - r$ colours are shown against concentration index $C_{90/50}$ (the ratio of the radii defined as containing 90% and 50% of the galaxy light using a Petrosian profile). Six galaxies which have u band magnitude fainter than the magnitude limit (~ 22 ; Adelman-McCarthy et al. 2006) are excluded. $u - r = 2.22$ is shown as the solid vertical line. $C_{90/50} = 2.6$ is indicated by the dashed horizontal line. Strateva et al. (2001) found that early-type (E, S0 and Sa) galaxies tend to have $u - r > 2.22$ and $C_{90/50} > 2.6$ while late-type (Sb, Sc and Irr) galaxies are likely to have $u - r \leq 2.22$ and $C_{90/50} \leq 2.6$. AGN, SF galaxies, composite galaxies and the unclassified NELGs are marked as red dots, green squares, blue diamonds and light blue crosses, respectively. The median of the errors of $C_{90/50}$ is 0.08 and is shown as the black bar. For $\sim 1.7\%$ of the sources the $C_{90/50}$ is not well constrained.

low $u - r$ and low $C_{90/50}$ to high $u - r$ and high $C_{90/50}$. Using the $u - r = 2.22$ and $C_{90/50} = 2.6$ lines as the separators of early-type (E, S0, and Sa) and late-type (Sb, Sc and Irr) galaxy (Strateva et al. 2001), SF galaxies are mainly late-type galaxies; composite galaxies and AGN both are mixtures of late-type and early-type galaxies; unclassified NELGs are dominated by early-type galaxies. The majority of the classified NELGs (AGN, SF galaxies and composite galaxies) have redshifts below ~ 0.18 and have quite similar distributions⁷. NELGs with $z \gtrsim 0.18$ are mainly the members of unclassified subsample (Figure 5.4).

In the soft X-ray band (0.5–2 keV), there is no clear difference in the flux distributions between AGN, SF galaxies, composite galaxies and unclassified NELGs⁸. On average the unclassified NELGs have

⁷See Figure C.2 for the redshift distributions.

⁸See Figure C.3 for the soft band flux distributions.

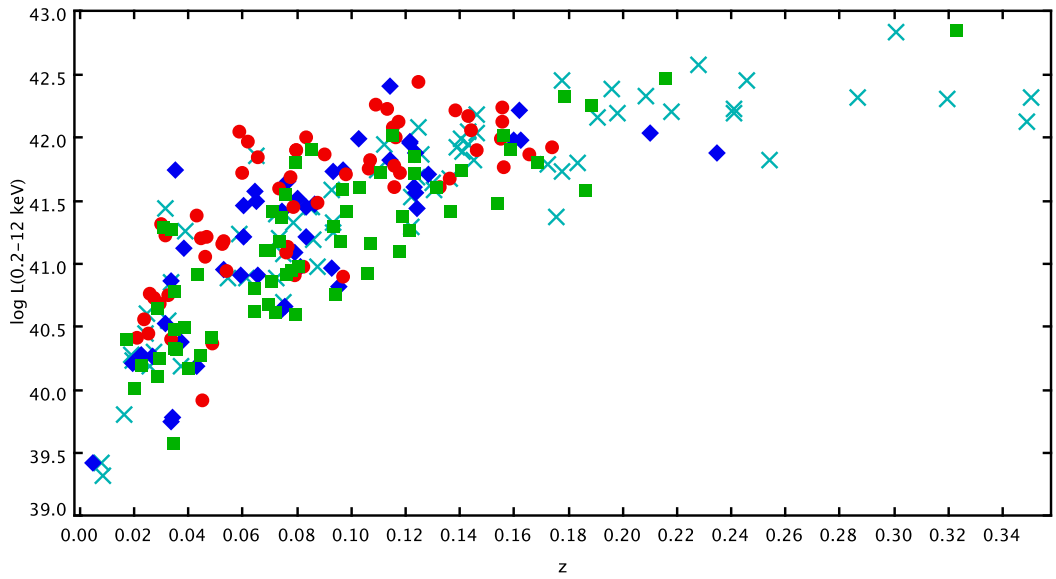


Figure 5.4: Redshifts from *SDSS* are shown against 0.2–12 keV X-ray luminosities. AGN, SF galaxies, composite galaxies and the unclassified NELGs are marked as red dots, green squares, blue diamonds and light blue crosses, respectively.

larger soft band luminosities than the others NELGs⁹; the null hypothesis that the unclassified NELGs have the same soft band luminosity distribution as either AGN, SF galaxies or composite galaxies can be rejected at a significance level of 1% using K-S test. In the hard X-ray band (2–12 keV), there is no clear dividing line in either flux or luminosity which can be used to separate these subsamples although on average AGN are brighter and have higher luminosities than the other NELGs (the null hypothesis that AGN have the same hard band flux distribution as either SF galaxies, composite galaxies or unclassified NELGs can be rejected at a significance level of 1% using K-S test; the null hypothesis that AGN have the same hard band luminosity distribution as SF galaxies can be rejected at the same significance level but not in the case of either composite galaxies or unclassified NELGs)¹⁰.

The full band (0.2–12 keV) X-ray fluxes¹¹ are shown against *SDSS* *r* band magnitudes for all four subsamples in Figure 5.5. The distributions of the X-ray-to-optical flux ratios of these subsamples are shown in Figure 5.6. On average, SF galaxies, composite galaxies and the unclassified NELGs do not differ from each other significantly. The mean $\log(f_X/f_O)$ of these three subsamples are all very

⁹See Figure C.4 for the soft band luminosity distributions.

¹⁰See Figure C.5 for the hard band flux distributions; see also Figure C.6 for the hard band luminosity distributions.

¹¹See Figure C.7 for the full band flux distributions; see also Figure C.8 for the full band luminosity distributions

close to -1.9 (Table 5.1). Although the mean $\log(f_X/f_O)$ for the AGN subsample (-1.7) is slightly higher than these three subsamples and the null hypothesis that AGN have the same distribution as the unclassified NELGs can be rejected at a significance level of 1% using K-S test, it is still difficult to use the X-ray-to-optical flux ratio to separate AGN from the rest of the NELGs due to the large overlap in this quantity between all these subsamples.

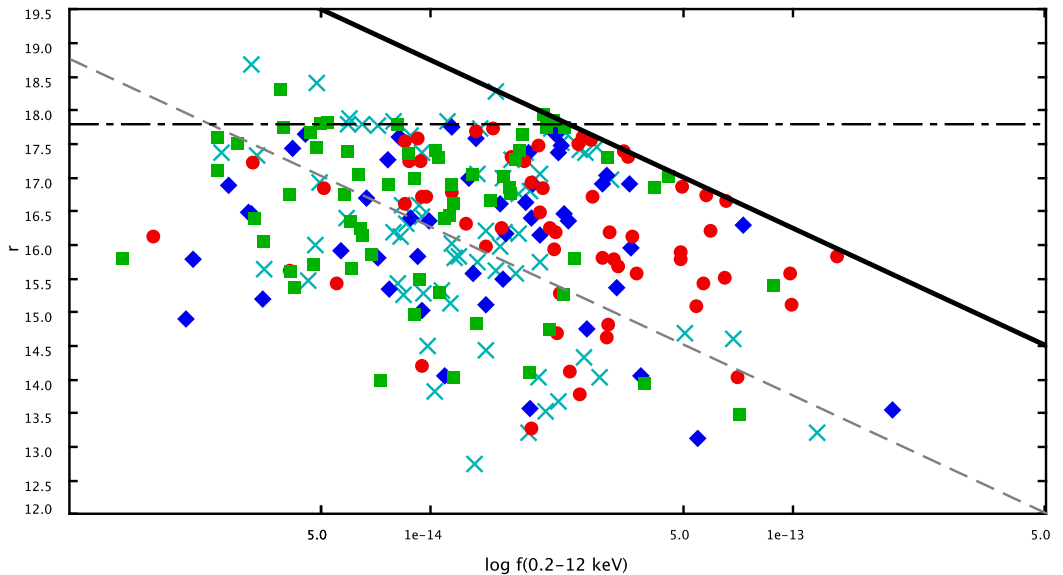


Figure 5.5: The 0.2–12 keV fluxes are shown against the *SDSS* *r* band magnitudes. The solid and dashed lines indicate $\log(f_X/f_O) = -1$ and -2 , respectively. The horizontal dashed-dotted line indicates the approximate magnitude limit of the *SDSS* Main Galaxy Sample ($r \approx 17.77$; Strauss et al. 2002). The *2XMM* catalogue has the flux limits of $\sim 10^{-14}$ $\text{erg s}^{-1} \text{cm}^{-2}$ in the soft band (0.5–2 keV) and $\sim 9 \times 10^{-14}$ $\text{erg s}^{-1} \text{cm}^{-2}$ in the hard band (2–12 keV) at $\sim 90\%$ of its sky coverage (Watson et al. 2009). AGN, SF galaxies, composite galaxies and unclassified NELGs are marked as red dots, green squares, blue diamonds and light blue crosses, respectively.

A brief comparison between NELGs and ALGs has been described in § 4.4 for the *XS* sample. To repeat, ALGs on average are fainter than NELGs in the *r* band and have a higher mean redshift; ALGs are usually early-type galaxies (E, S0 and Sa) galaxies based on their $u - r$ colours and concentration indexes $C_{90/50}$ (using the separators of these two quantities from Strateva et al. 2001); ALGs have a similar mean soft band (0.5–2 keV) flux as NELGs but are fainter in the hard band (2–12 keV); on average ALGs do not have lower luminosities than NELGs regardless of energy band; the mean X-ray-to-optical flux ratio of ALGs is similar to the value for NELGs. All the similarities or differences derived from the *XS* sample still hold for the *MJ* sample as the latter is a complete subset of the former

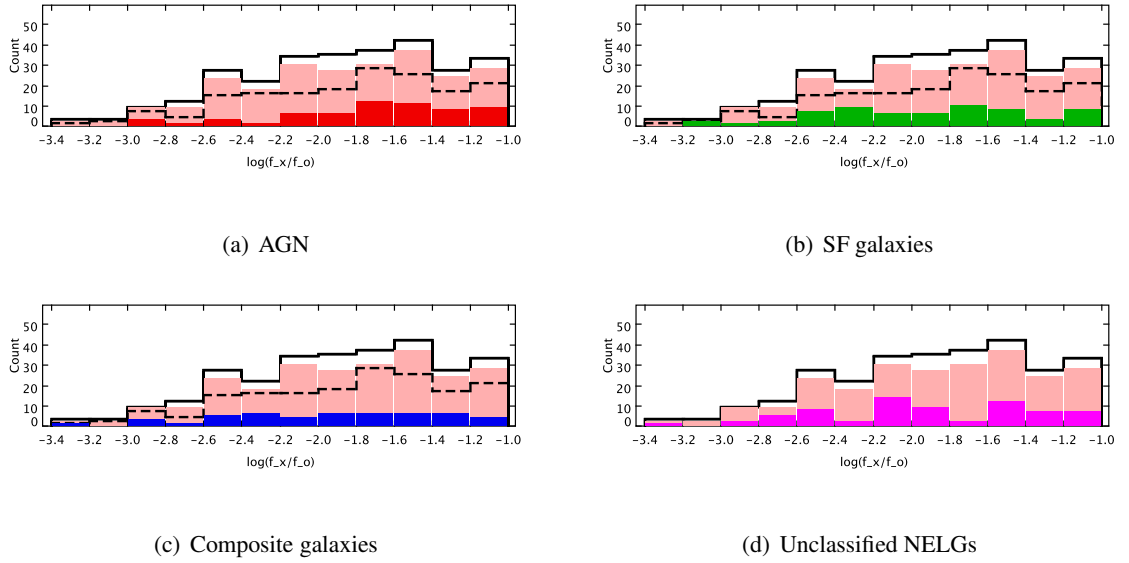


Figure 5.6: The distributions of the X-ray-to-optical flux ratios. In all four plots, the *MJ* sample and its NELG subsample are marked with black solid histograms and pink filled histograms respectively. The classifiable NELGs are marked with black dashed histograms in (a), (b), and (c). AGN, SF galaxies and composite galaxies are marked with red histogram in (a), green histogram in (b) and blue histogram in (c), respectively. The unclassified NELGs are marked with the magenta histogram in (d).

(the only difference between these two samples being the sky area used). In the following sections, individual subsamples from the *MJ* sample are discussed in further detail. The average optical and X-ray properties which have been described above for all *MJ* subsamples (including ALGs) are summarized in Table 5.1.

5.2 Emission Line Ratio Classified AGN

5.2.1 Overall Properties

The AGN subsample contains 60 galaxies, making up $\sim 35\%$ of the classifiable NELGs, $\sim 25\%$ of all NELGs and $\sim 21\%$ of the *MJ* sample. These AGN have the *SDSS* r band magnitudes of 13.25–17.71. As described in § 5.1.2, a large fraction of these AGN have $u - r > 2.22$ and concentration indexes $C_{90/50} > 2.6$, suggesting early-type (E, S0 and Sa) galaxy morphologies (Strateva et al. 2001). Using Figure 5.2(a) and Figure 5.2(b), 20 AGN were further classified as Seyfert 2 galaxies and 31 were classified as LINER 2s. On average the Seyfert 2 galaxies are fainter than the LINER 2s in the r

No.	Property	<i>MJ</i>	ALG	NELG	Classified	AGN	SF	Composite	Unclassified
(1)	Number	284	45	239	170	60	62	48	69
(2)	% of <i>MJ</i>	100	15.8	84.2	59.9	21.1	21.8	16.9	24.3
(3)	% of NELG	-	-	100	71.1	25.1	25.9	20.1	28.9
(4)	% of Classified NELG	-	-	-	100	35.3	36.5	28.2	-
(5)	z	0.110	0.170	0.099	0.087	0.086	0.090	0.085	0.127
(6)	r	16.34	16.77	16.25	16.27	16.17	16.49	16.12	16.20
(7)	$u - r$	2.50	3.07	2.40	2.19	2.60	1.68	2.35	2.97
(8)	$C_{90/50}$	2.83	3.10	2.78	2.65	2.78	2.50	2.70	3.08
(9)	$\log(\frac{f_X}{f_O})$	-1.87	-1.91	-1.86	-1.84	-1.69	-1.91	-1.92	-1.92
(10)	N ($\log(\frac{f_X}{f_O}) \leq -2$)	110	17	93	61	14	27	20	32
(11)	N ($\log(\frac{f_X}{f_O}) > -2$)	174	28	146	109	46	35	28	37
(12)	$f_{0.5-2\text{keV}}$	4.95	3.54	5.21	4.63	5.69	3.73	4.47	6.65
(13)	$f_{2-12\text{keV}}$	10.96	4.41	12.19	14.30	20.54	8.44	14.05	7.01
(14)	$f_{0.2-12\text{keV}}$	18.67	10.17	20.27	21.81	30.25	14.33	20.93	16.46
(15)	$L_{0.5-2\text{keV}}$	1.76	2.84	1.55	0.96	1.15	0.87	0.86	3.00
(16)	$L_{2-12\text{keV}}$	3.29	3.71	3.21	3.01	3.83	2.62	2.48	3.70
(17)	$L_{0.2-12\text{keV}}$	6.18	8.77	5.69	4.74	5.77	4.37	3.93	8.03
(18)	N ($L_X \leq 10^{41}$)	83	7	76	59	14	27	18	17
(19)	N ($L_X \in (10^{41}, 10^{42})$)	150	26	124	91	35	29	27	33
(20)	N ($L_X > 10^{42}$)	51	12	39	20	11	6	3	19
(21)	HR2	-0.31	-0.56	-0.27	-0.23	-0.18	-0.26	-0.24	-0.37
(22)	HR3	-0.30	-0.20	-0.31	-0.28	-0.15	-0.27	-0.46	-0.40

Table 5.1: (1): Sample size. (2)–(4): Fractions that a subsample possesses in its parent sample(s). (5): Unweighted mean redshifts z . (6): Unweighted mean r band magnitudes. (7): Unweighted mean Galactic extinction corrected $u - r$ colours. Galaxies with magnitudes fainter than the magnitude limits are excluded (six ALGs, one AGN and five unclassified NELGs). (8): Unweighted mean concentration indexes defined as the ratios of Petrosian radii containing 90% and 50% light of the galaxy. (9): Unweighted mean X-ray-to-optical flux ratios. (10) and (11): Numbers of sources satisfying the conditions specified in the brackets. (12)–(14): Unweighted mean X-ray fluxes in units of 10^{-15} erg s $^{-1}$ cm $^{-2}$. (15)–(17): Unweighted mean X-ray luminosities in units of 10^{41} erg s $^{-1}$. (18)–(20): Numbers of sources satisfying the conditions specified in the brackets (L_X in the 0.2–12 keV band). (21) and (22): Unweighted mean hardness ratios.

band. Both the mean $u - r$ and $C_{90/50}$ of the Seyfert 2 galaxies are smaller than those of the LINER 2s, suggesting that on average the Seyfert 2 galaxies in the *MJ* sample might have later Hubble types than the LINER 2s. The Seyfert 2 galaxies and the LINER 2s have similar mean redshifts (0.088 and 0.086).

Although Type 1 AGN (*i.e.*, the broad line AGN) have been excluded when selecting the *MJ* sample, NLS 1 galaxies (see § 1.3.2) might still be included. Inspecting the Balmer line widths versus forbidden line widths of the AGN subsample (Figure 5.7) did not indicate any optical object with Balmer line width significantly greater than the forbidden line width. This suggests that this AGN subsample is likely free from NLS 1 galaxies.

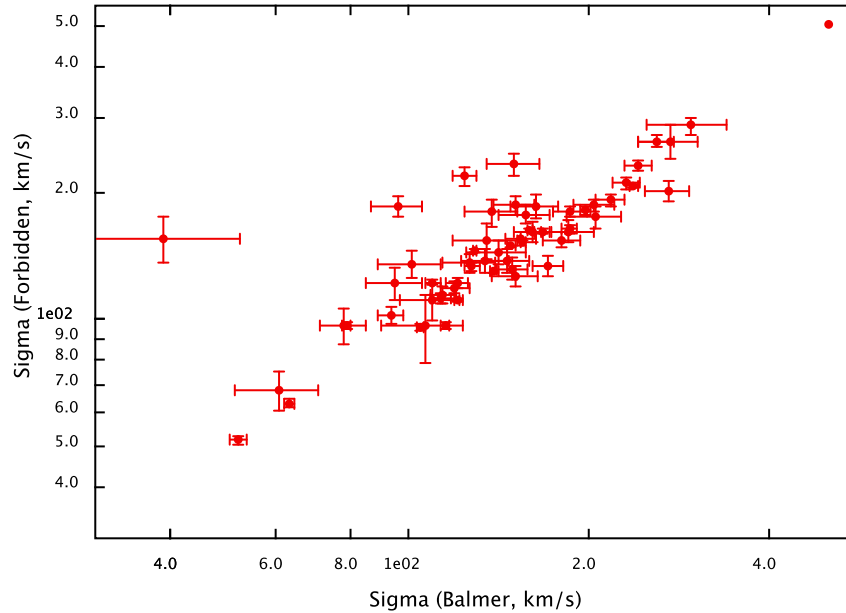


Figure 5.7: Velocity dispersions (σ of the Gaussian fit to the lines) of Balmer lines are shown against those of the forbidden lines, both from the *MPA/JHU* catalogue.

As also described in § 5.1.2, in the soft band (0.5–2 keV), AGN do not differ much from other subsamples although on average they have higher luminosities than SF galaxies and composite galaxies but lower luminosities than the ALGs and the unclassified NELGs. In the hard band (2–12 keV) AGN have the highest mean 2–12 keV flux and luminosity among all subsamples. The mean X-ray-to-optical flux ratio of the AGN is -1.7 , being the highest among all subsamples. Almost a quarter (14/60) of the AGN have $\log(f_X/f_O) \leq -2$, with the lowest one at -2.92 . On average the Seyfert 2 galaxies have

lower mean flux and luminosity than the LINER 2s in the soft band (0.5–2 keV), but higher mean fluxes and luminosities in the hard band (2–12 keV) and total band (0.2–12 keV). The mean $\log(f_X/f_O)$ of the Seyfert 2 galaxies is -1.54 , slightly higher than -1.77 , the mean value of the LINER 2s. Most of the Seyfert 2 galaxies (18 out of 20) have $\log(f_X/f_O) > -2$ while 71% (22 out of 31) of the LINER 2s have such $\log(f_X/f_O)$ values.

5.2.2 X-ray Hardness Ratios and Spectra

The X-ray hardness ratio (HR2 versus HR3) density plot for the AGN subsample is shown in Figure 5.8(a). The hardness ratios used were from the pn camera¹². The peak value of the hardness ratio density is consistent with a power-law model with $\Gamma \sim 1.7\text{--}2.2$. The 68% level contour suggests that for some AGN a thermal component might contribute significantly to the 0.2–4.5 keV emission; it also implies that some AGN might have an obscuration up to 10^{22} atoms cm^{-2} .

X-ray spectrum from a typical Type 1 AGN whose BLR is believed to be seen free from obscuration is continuum dominated and can be well fitted with a power-law model. When the BLR, if is not absent, instead is obscured, in which case the AGN becomes Type 2, an absorbed power-law is expected. Often in such cases the AGN might not be bright enough to outshine the host galaxy, therefore X-ray emission from the host galaxy, *e.g.*, thermal emission from hot gas, can be seen. The hardness ratios of the AGN subsample in *MJ* are consistent with this scenario by showing a clear non-thermal component subjected to absorption up to 10^{22} atoms cm^{-2} and a relatively weak thermal component.

Normal galaxies are usually selected to have the X-ray-to-optical flux ratios below -2 to avoid AGN contamination as luminous AGN have these ratios above -1 (see § 1.4.2). About 23% (14 out of 60) of the AGN subsample have $\log(f_X/f_O) \leq -2$, which provides an opportunity to investigate AGN that would be classified as normal galaxies if only the X-ray-to-optical flux ratio cut-off is used as selection function. The hardness ratios density plot for the 14 AGN with $\log(f_X/f_O) \leq -2$ is shown in Figure 5.8(b). The rest of the AGN subsample, which have $-2 < \log(f_X/f_O) \leq -1$, are shown in Figure 5.8(c). In both plots, a power-law component is clearly suggested by the peaks of the hardness ratio densities, consistent with the AGN classification from the optical spectra. A major

¹²The potential biases could be caused by sources with single band detection likelihood below the threshold but it has been noticed that removing such sources would not change the overall pattern since the density plot was constructed in a way to guarantee that bright sources (hence with high detection thresholds) would have greater weights than the faint ones.

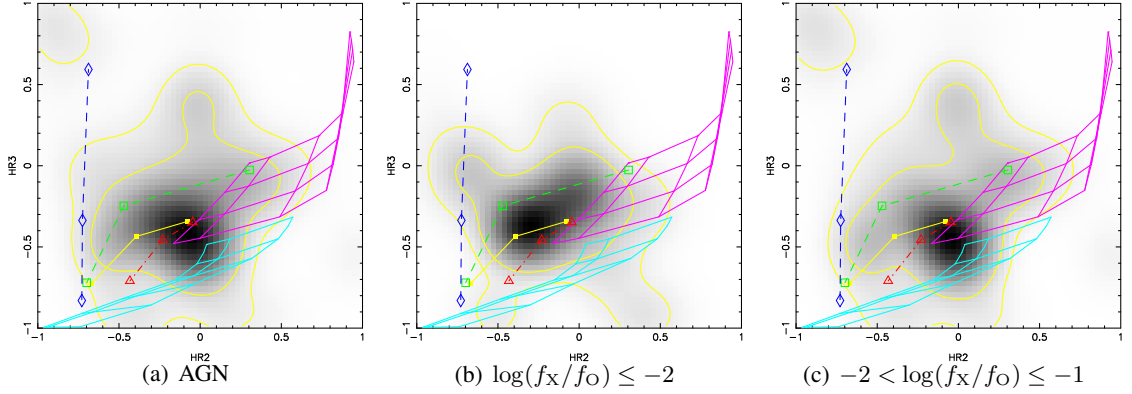


Figure 5.8: The smoothed pn hardness ratio density plots (HR2 versus HR3) for (a) the AGN subsample, (b) AGN with $\log(f_X/f_O) \leq -2$, and (c) AGN with $-2 < \log(f_X/f_O) \leq -1$. Two sources were excluded due to undefined pn hardness ratios. Spectral models defined in § 2.4.4 are overlaid in each plot. Contours at 68% and 90% levels are also shown.

difference between AGN with $\log(f_X/f_O) \leq -2$ and those with $-2 < \log(f_X/f_O) \leq -1$ shown in these two plots is that on average the former tend to have softer spectra than the latter, suggesting that the contribution to the total observed X-ray emission from the host galaxies is higher in the former than in the latter. Intrinsic obscuration up to $\sim 10^{22}$ – 10^{23} atoms cm^{-2} is indicated by the contours on both plots. Assuming the Galactic value for N_H/A_V (1.8×10^{21} ; Predehl & Schmitt 1995) and $A_r/A_V \approx 0.8$ (Gordon et al. 2003), such obscuration translates to ~ 4 – 44 mag in the r band, which means that the intrinsic optical light might have been depressed by a factor of at least 60, consistent with the non-detection of broad $H\alpha$ line in these AGN.

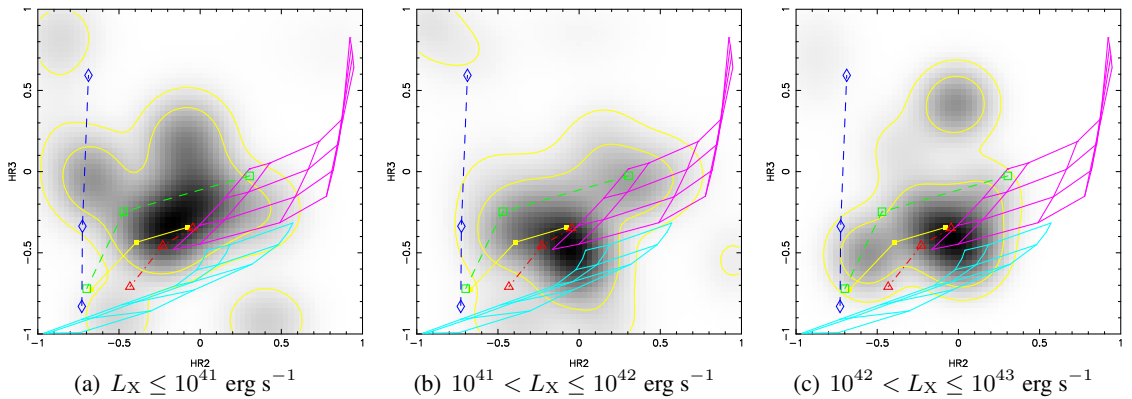


Figure 5.9: The smoothed pn hardness ratio (HR2 versus HR3) density plots for (a) AGN with $L_X \leq 10^{41} \text{ erg s}^{-1}$, (b) AGN with $10^{41} < L_X \leq 10^{42} \text{ erg s}^{-1}$, and (c) AGN with $10^{42} < L_X \leq 10^{43} \text{ erg s}^{-1}$. Two sources were excluded due to undefined pn hardness ratios. Spectral models defined in § 2.4.4 are overlaid in each plot. Contours at 68% and 90% levels are also shown.

X-ray luminosity is often used to separate AGN from truly normal galaxies because X-ray luminosi-

ties above 10^{42} erg s^{-1} are difficult, although possible, to be explained by stellar origins. However, LLAGN can have X-ray luminosities as low as those from normal galaxies. In order to investigate the average spectral properties of the AGN population with low X-ray luminosities, the AGN subsample was divided into three bins, 14 with $L_X \leq 10^{41}$ erg s^{-1} , 35 with $10^{41} < L_X \leq 10^{42}$ erg s^{-1} , and 11 have $L_X > 10^{42}$ erg s^{-1} . The hardness ratio density plots for AGN within these three bins are shown in Figure 5.9. A power-law component is suggested by the peaks in the density plots of AGN within all these three luminosity bins. For AGN with $L_X \leq 10^{41}$ erg s^{-1} , intrinsic obscuration up to $\sim 10^{22}$ atoms cm^{-2} and a non-negligible thermal component are also suggested by the 68% level contours. AGN with $10^{41} < L_X \leq 10^{42}$ erg s^{-1} and those with $L_X > 10^{42}$ erg s^{-1} show similar peaks values in the density plots, which can be reproduced by a power-law model with $\Gamma \sim 1.7-2.2$.

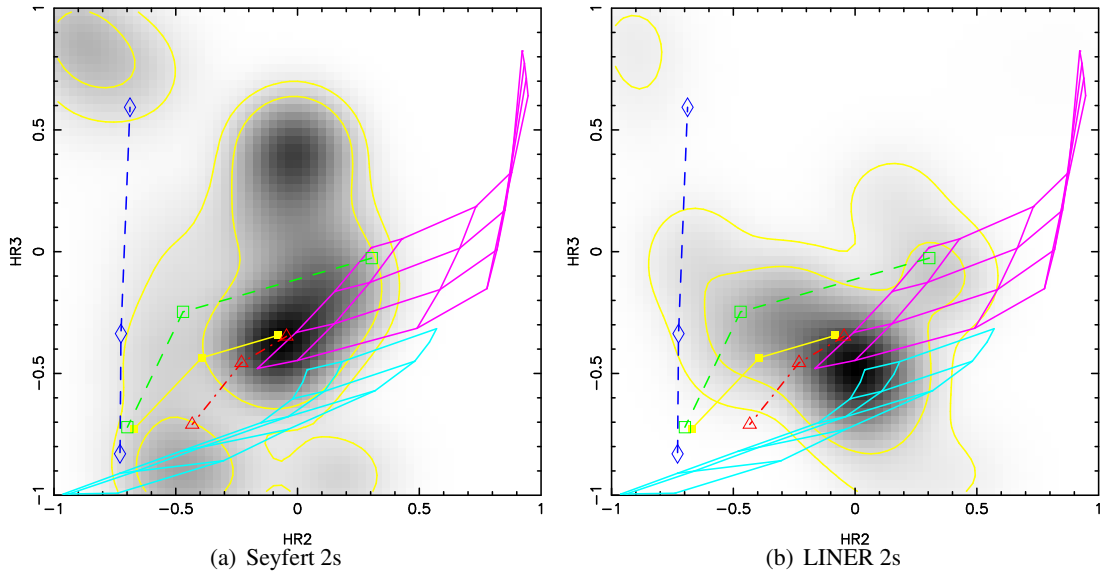


Figure 5.10: The smoothed pn hardness ratio (HR2 versus HR3) density plots for Seyfert 2 galaxies and LINER 2s. Two sources were excluded due to undefined pn hardness ratios. Spectral models defined in § 2.4.4 are overlaid in each plot. Contours at 68% and 90% levels are also shown.

In order to investigate the average X-ray spectral properties of the Seyfert 2 galaxies and the LINER 2s, the X-ray hardness ratio density plots for these two AGN subsets are shown in Figure 5.10(a) and Figure 5.10(b), respectively. The peak of the hardness ratio density of the Seyfert 2 galaxies is consistent with an unabsorbed power-law. The hardness ratios of the LINER 2s are slightly softer than those of the Seyfert 2 galaxies. The 68% level contours suggest that the Seyfert 2 galaxies might have higher obscuration than the LINER 2s.

AGN with $HR3 > 0$ are seen in all bins and a few of them are bright enough to be included inside the

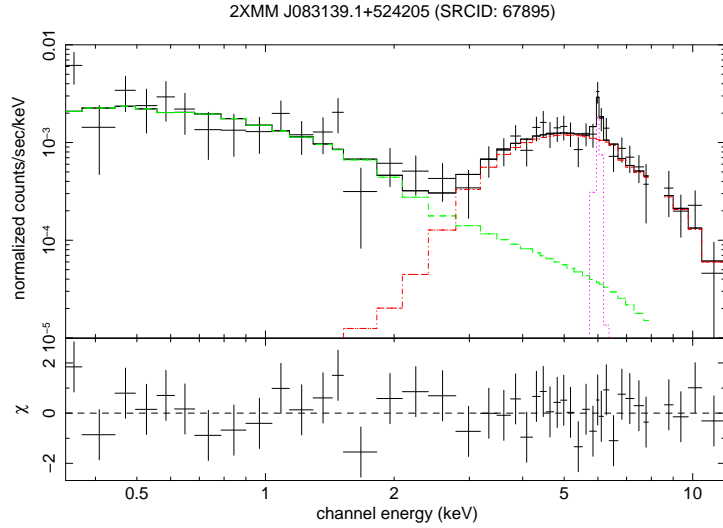


Figure 5.11: The *2XMM* automatically extracted spectrum from the pn camera for 2XMM J083139.1+524205 (SRCID: 67895) fitted with a two-power-law model: an unabsorbed power-law model (green) with $\Gamma = 1.91^{+0.47}_{-0.46}$ and an absorbed power-law model (red) with $\Gamma = 1.80^{+0.70}_{-0.88}$ associated with an absorption of $2.18^{+0.49}_{-0.64} \times 10^{23}$ atoms cm^{-2} . The pink dotted line shows the Gaussian fit to the emission line at ~ 6.4 keV.

68% level contours, for instance, 2XMM J083139.1+524205 (SRCID: 67895) which has HR2 = -0.03 and HR3 = 0.41 (Figure 5.9(c)). This source is one of the four X-ray sources in the AGN subsample that have automatically extracted X-ray spectra and light curves available in *2XMM*. Spectral fitting was then carried out to gain insight into its X-ray power source. An Fe emission line at 6–7 keV is clearly visible in the pn spectrum of this source. This source was reported as to have an intrinsic absorption of $\sim 1.5\text{--}2.4 \times 10^{23}$ atoms cm^{-2} based on spectral fits presented by Georgakakis et al. (2004b), Akylas et al. (2006), and Page et al. (2007). Fitting the *2XMM* automatically extracted pn spectrum using a combination of an APEC model, accounting for the soft component, and an absorbed power-law, representing the hard component (a Gaussian also added to fit the emission line), yielded an accepted fit ($\chi^2 = 26$ for 35 degrees of freedom) with an absorption ($1.99^{+0.99}_{-0.45} \times 10^{23}$ atoms cm^{-2}) similar to that reported in the literature but a higher temperature ($kT = 3.44^{+5.57}_{-1.21}$ keV) than in Page et al. (2007). However, the hot ISM in galaxies rarely has such a high temperature. The soft component was also modelled by an unabsorbed power-law in Page et al. (2007) after an ionized medium failed to give an acceptable fit. Fitting using such a two-power-law combination was then carried out (a Gaussian was also added). The fit was acceptable ($\chi^2 = 25$ for 35 degrees of freedom; Figure 5.11), giving an absorbed power-law with $\Gamma = 1.80^{+0.70}_{-0.88}$ with an associated absorption of $2.18^{+0.49}_{-0.64} \times 10^{23}$ atoms cm^{-2} and an unabsorbed power-law with $\Gamma = 1.91^{+0.47}_{-0.46}$. The centre of the emission line was found at $6.37^{+0.10}_{-0.05}$ keV, consistent with the Fe $K\alpha$ line from neutral material. The Galactic absorption

was fixed at 4.11×10^{20} atoms cm^{-2} (Kalberla et al. 2005). The Galactic absorption corrected 0.2–12 keV luminosities derived from this fit were 9.52×10^{41} erg s^{-1} and 3.76×10^{42} erg s^{-1} , before and after correcting for the intrinsic absorption, respectively. The unabsorbed component plus the emission line contributed 9.54×10^{40} erg s^{-1} . Although the origin of the soft emission is still not clear, the absorbed power-law component together with the emission line at ~ 6.4 keV is evidence of a Type 2 AGN, consistent with the Seyfert 2 galaxy classification from both the BPT [S II] plot (Figure 5.2(a)) and the BPT [O I] plot (Figure 5.2(b)). This source was not classified as a variable source by the *2XMM* catalogue¹³.

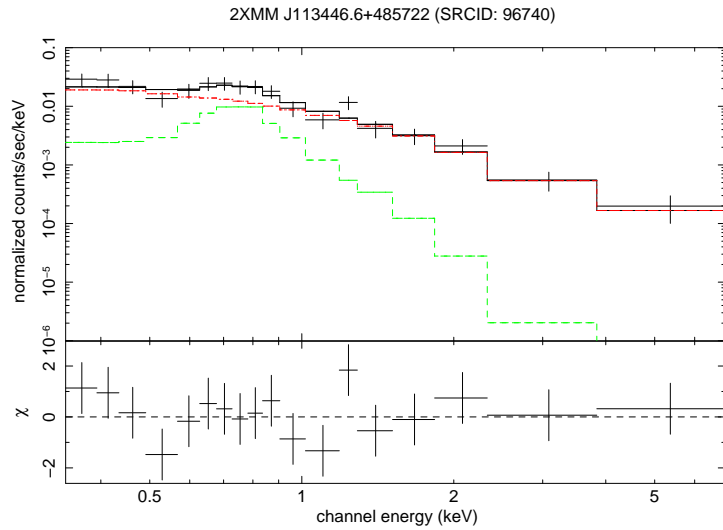


Figure 5.12: The *2XMM* automatically extracted pn spectrum for 2XMM J113446.6+485722 (SRCID: 96740) fitted by a two-component model: a power-law model with $\Gamma = 2.19^{+0.30}_{-0.34}$ (red) and an APEC model with $kT = 0.42^{+0.21}_{-0.12}$ keV (green).

The optical counterpart of 2XMM J113446.6+485722 (SRCID: 96740) is an elliptical galaxy at $z = 0.316$ in the field of Abell 1314. The X-ray hardness ratios from pn are $\text{HR2} = -0.37$ and $\text{HR3} = -0.41$, which can be reproduced by a combination of an unabsorbed power-law and an APEC model. Fitting the *2XMM* automatically extracted pn spectrum yielded $\Gamma = 2.19^{+0.30}_{-0.34}$ for the power-law component and $kT = 0.42^{+0.21}_{-0.12}$ keV for the APEC component ($\chi^2 = 12$ for 14 degrees of freedom; the Galactic absorption fixed to 1.79×10^{20} atoms cm^{-2} [Kalberla et al. 2005]; Figure 5.12). The derived 0.2–12 keV luminosity (corrected for the Galactic extinction) was 2.11×10^{41} erg s^{-1} , with 1.86×10^{41} erg s^{-1} from the power-law component and 2.46×10^{40} erg s^{-1} from the APEC component. It should be noted that the diffuse emission from the target, Abell 1314, extends nearly the whole field-of-view

¹³*2XMM* catalogue classified sources which had at least one of the automatically extracted time-series with a χ^2 probability less than 10^{-5} of being constant as variable sources (Watson et al. 2009).

in the *XMM* observation and therefore both the hardness ratios and automatically extracted spectra might be contaminated by this diffuse emission. This source has not been reported to show variability in its *2XMM* automatically extracted light curves. The *SDSS* counterpart of this source was classified as a Seyfert 2 galaxy on the BPT [S II] plot (Figure 5.2(a)) but a LINER 2 in the BPT [O I] plot (Figure 5.2(b)).

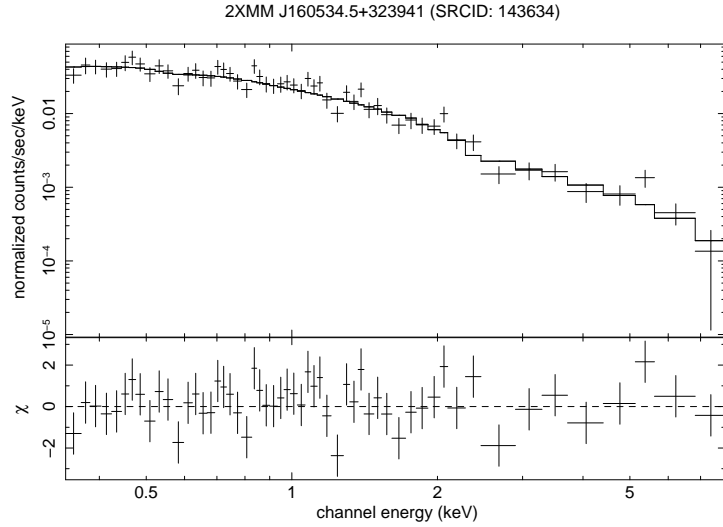


Figure 5.13: The *2XMM* automatically extracted pn spectrum for 2XMM J160534.5+323941 (SRCID: 143634) fitted by a power-law model with $\Gamma = 1.95^{+0.09}_{-0.08}$.

The *SDSS* counterpart of 2XMM J160534.5+323941 (SRCID: 143634) is a spiral galaxy at $z = 0.0297$. This source is a variable source in *2XMM*, and the only variable source in the *MJ* sample. The X-ray hardness ratios from pn are $\text{HR2} = -0.10$ and $\text{HR3} = -0.42$, which can be reproduced by a single power-law with $\Gamma \sim 1.7\text{--}2.2$ modified by a low absorption ($\lesssim 10^{21}$ atoms cm^{-2}). Fitting its *2XMM* pn spectrum using a power-law yielded $\Gamma = 1.95^{+0.09}_{-0.08}$ ($\chi^2 = 54$ for 53 degrees of freedom; the Galactic absorption fixed to 2.39×10^{20} atoms cm^{-2} [Kalberla et al. 2005]; Figure 5.13). Adding absorption did not improve the fit significantly, suggesting that the non-detection of broad emission line(s) in the optical spectra might be due to intrinsic weakness of the BLR rather than obscuration. The Galactic extinction corrected 0.2–12 keV luminosity derived from the best-fit model was 5.53×10^{41} erg s^{-1} . This galaxy was classified as a Seyfert 2 galaxy on both the BPT [S II] plot (Figure 5.2(a)) and the BPT [O I] plot (Figure 5.2(b)).

2XMM J212926.2+000524 (SRCID: 178535) has $\text{HR2} = -0.58$ and $\text{HR3} = -0.53$, consistent with a spectrum dominated by a soft component. Since this source sits close to a CCD gap in pn, spectra from all three EPIC camera were used in the fitting. A single *APEC* model with $kT = 0.65^{+0.08}_{-0.06}$ keV

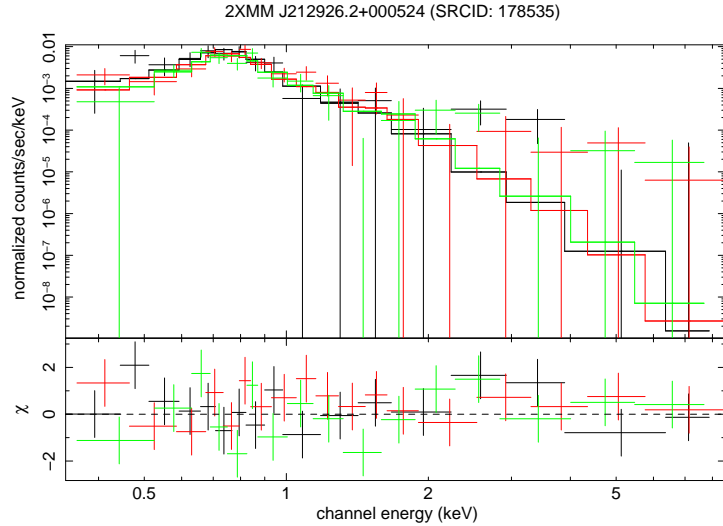


Figure 5.14: The *2XMM* automatically extracted spectrum from EPIC for 2XMM J212926.2+000524 (SRCID: 178535) fitted by an *APEC* model with $kT = 0.65^{+0.08}_{-0.06}$ keV.

gave an acceptable fit ($\chi^2 = 41$ for 49 degrees of freedom; the Galactic extinction fixed to 3.65×10^{20} atoms cm^{-2} [Kalberla et al. 2005]; Figure 5.14). The derived 0.2–12 keV luminosity was 1.15×10^{42} erg s^{-1} , which can be attributed to the hot gas of the host galaxy. Adding an extra power-law component did not improve the fit significantly due to the large uncertainties above 2 keV although it could not be ruled out. Given that this source sits only $\sim 4'$ away from the targeted cluster RX J2129.6+0005 (Böhringer et al. 2000), which has diffuse emission extending to a few arcmins, both the hardness ratios and automatically extracted spectra might be contaminated by the diffuse emission from this cluster. This source was not classified as variable source in *2XMM*. The *SDSS* counterpart of this X-ray source was classified as a LINER 2 on both the BPT [S II] plot (Figure 5.2(a)) and the BPT [O I] plots (Figure 5.2(b)).

5.2.3 X-ray and Optical Emission Line Luminosities

The X-ray and optical emission line luminosities are expected to be closely related to each other in an AGN if the emission lines are directly related to the ionizing continuum of the accreting black hole. A positive correlation between $H\alpha$, [O III] $\lambda 5007$ luminosities and X-ray luminosities have been found in luminous AGN (*e.g.*, Elvis et al. 1984; Mulchaey et al. 1994) as well as in less luminous Seyfert galaxies and LINERs (*e.g.*, Terashima et al. 2000a; Ho et al. 2001). The $H\alpha$ and [O III] fluxes used here were corrected for dust extinction caused by the host galaxy using the Balmer decrement from $H\alpha/H\beta$.

A theoretical value of 3.1 (case B recombination) of $H\alpha/H\beta$ and $\tau_\lambda \propto \lambda^{-0.7}$ (Charlot & Fall 2000) were assumed. In total there are 46 AGN which have $H\alpha/H\beta$ greater than 3.1 and therefore were corrected for the dust extinction. These 46 AGN were used in following investigation. The mean $L_{2-12\text{keV}}$ of these 46 AGN is 4.13×10^{41} erg s $^{-1}$. The histograms of $\log(f_{2-12\text{keV}}/f_{H\alpha})$ and $\log(f_{2-12\text{keV}}/f_{[\text{OIII}]})$ are shown in Figure 5.15(a) and 5.15(b) respectively. No correction was made for the X-ray fluxes to account for any intrinsic absorption.

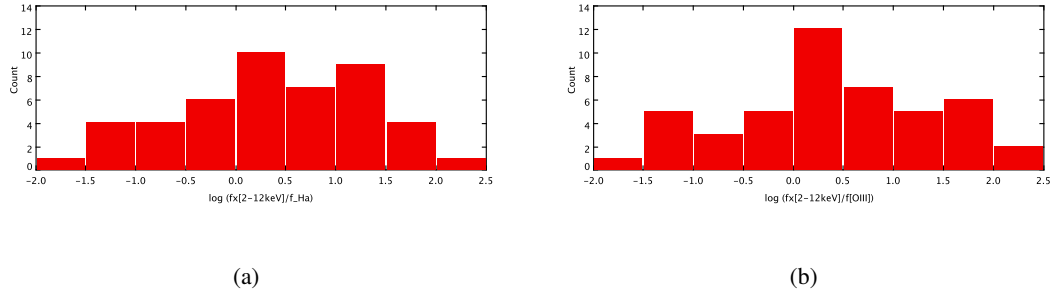
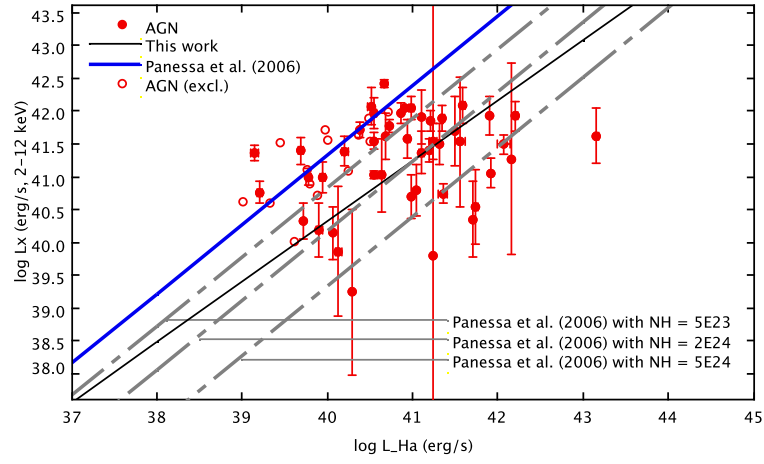


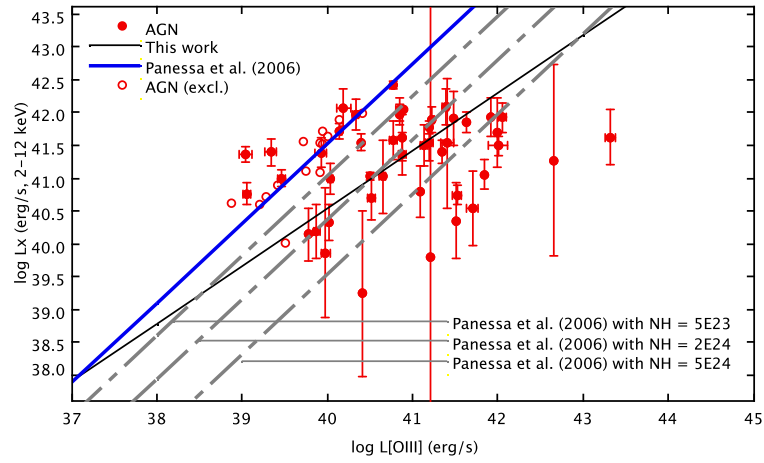
Figure 5.15: Distributions of $\log(f_{2-12\text{keV}}/f_{H\alpha})$ and $\log(f_{2-12\text{keV}}/f_{[\text{OIII}]})$ for the 46 AGN with $H\alpha/H\beta > 3.1$.

Typical $L_X/L_{H\alpha}$ values have been found to range from a few to a few tens (*e.g.*, Elvis et al. 1984; Terashima et al. 2000a; Terashima & Wilson 2003; Flohic et al. 2006; Ho 2008). Different types of LLAGN (*i.e.*, Type 1 and Type 2 Seyfert galaxies and LINERs) in the local universe (< 100 Mpc) have been sampled by a number of groups using the Palomar spectroscopic survey of nearby galaxies (Ho et al. 1997a). It has also been found that Type 2 AGN generally have lower $L_X/L_{H\alpha}$ than Type 1 AGN (*e.g.*, Terashima et al. 2000b,a; Panessa et al. 2006). Panessa et al. (2006) found that after correcting for intrinsic absorption, Type 2 sources could have similar $L_X-L_{H\alpha}$ relation as Type 1 sources, lending support to the unified model (Antonucci & Miller 1985). By combining Type 1 sources (a sample of Seyfert 1 galaxies and a QSO sample from Ward et al. 1988) and absorption-corrected Type 2 sources, Panessa et al. (2006) found a correlation of $\log L_X = (1.06 \pm 0.04) \times \log L_{H\alpha} + (-1.14 \pm 1.78)$.

The 2–12 keV luminosities of the 46 AGN are plotted against $H\alpha$ luminosities in Figure 5.16(a). No correction for intrinsic absorption was made to the X-ray fluxes. Also plotted on that figure is the correlation found in Panessa et al. (2006). A large fraction of the AGN subsample fall below this correlation, indicating that these AGN might be obscured. Comparing the AGN subsample with the Panessa et al. (2006) correlation modified by various absorbing columns reveals that obscuration up to a few 10^{24} atoms cm $^{-2}$ might be present in some of these AGN. An observed 2–12 keV X-ray luminosity of $\sim 4 \times 10^{41}$ erg s $^{-1}$, the mean $L_{2-12\text{keV}}$ of the 46 AGN, will translate to $\sim 4 \times 10^{43}$ erg s $^{-1}$ when



(a)



(b)

Figure 5.16: The extinction corrected $L_{H\alpha}$ and $L_{[OIII]}$ are shown against the observed $L_{2-12\text{keV}}$ for the AGN subsample. The black solid lines are the results of least-square (bisector) fits of the AGN with $H\alpha/H\beta > 3.1$ (filled circles). AGN with $H\alpha/H\beta < 3.1$ are marked by open circles; they were not included in the fit. The blue solid lines are the correlations from Panessa et al. (2006) converted to the 2–12 keV band (assuming a power-law with $\Gamma = 1.7$ and a Galactic absorption of $N_H = 3 \times 10^{20}$ atoms cm^{-2}). The same correlations are also shown with factors of 0.32, 0.07 and 0.01 applied to the $L_{2-12\text{keV}}$ values to represent the effects of intrinsic absorption of 5×10^{23} atoms cm^{-2} , 2×10^{24} atoms cm^{-2} and 5×10^{24} atoms cm^{-2} respectively (shown as grey dashed-dashed lines).

corrected for an intrinsic absorption of 5×10^{24} atoms cm^{-2} . Least-square (bisector) fit to the AGN subsample yielded $\log L_{2-12\text{keV}} = (0.92 \pm 0.08) \times \log L_{\text{H}\alpha} + (3.5 \pm 3.35)$.

The $[\text{O III}]\lambda 5007$ line is believed to come from the NLR and is ionised by UV emission from the central engine of the AGN and hence its luminosity is expected to scale with the AGN power (*e.g.*, Mulchaey et al. 1994; Cappi et al. 2006). Meanwhile, X-rays are a direct probe of the AGN and are also expected to scale with the AGN power when little or no obscuration is present. In Figure 5.16(b) the $[\text{O III}]\lambda 5007$ luminosities are plotted against the 2–12 keV luminosities for the AGN subsample. Also plotted on that figure is the correlation found in Panessa et al. (2006): $\log L_{\text{X}} = (1.22 \pm 0.06) \times \log L_{[\text{OIII}]} + (-7.34 \pm 2.53)$. A large fraction of the AGN subsample sit below the Panessa et al. (2006) correlation, suggesting obscuration affecting the X-ray emission. Least-square (bisector) fit yielded $\log L_{2-12\text{keV}} = (0.88 \pm 0.08) \times \log L_{[\text{OIII}]} + (5.32 \pm 3.38)$.

The X-ray obscuration in Compton thick AGN is greater than 10^{24} atoms cm^{-2} . Panessa & Bassani (2002) found that Compton thick sources tend to have $f_{2-10\text{keV}}/f_{[\text{OIII}]} < 1$. There are 15 AGN with $f_{2-10\text{keV}}/f_{[\text{OIII}]} < 1$ (the X-ray fluxes have been scaled to 2–10 keV from 2–12 keV assuming a power-law with $\Gamma = 1.7$ and a Galactic absorption of 3×10^{20} atoms cm^{-2}). These AGN are referred to as Compton thick candidates and the rest of the AGN subsample are referred to as Compton thin candidates hereafter. No significant differences were found in the r band magnitudes, $u - r$ colours, concentration index $C_{90/50}$ or redshifts between the Compton thin and the Compton thick candidates. The mean $\log(f_{\text{X}}/f_{\text{O}})$ for Compton thin and Compton thick candidates are -1.57 and -1.80 , respectively. Compton thin candidates have higher mean fluxes and luminosities in both the soft band (0.5–2 keV) and the hard band (2–12 keV) compared to the Compton thick candidates.

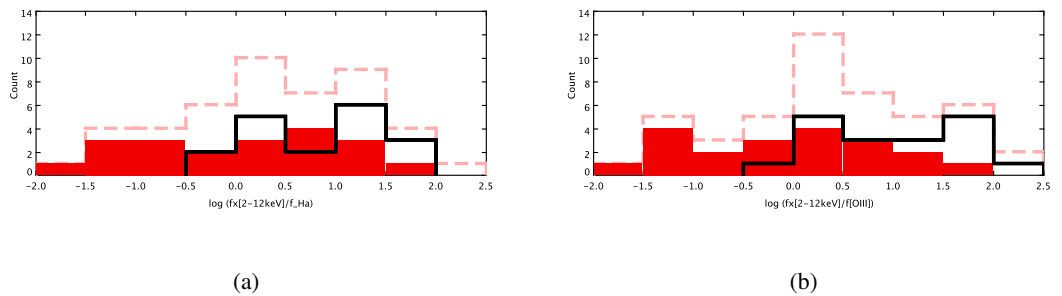
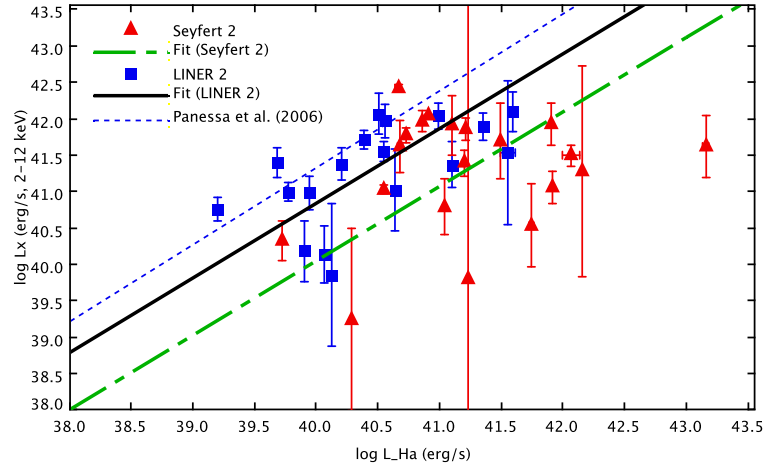
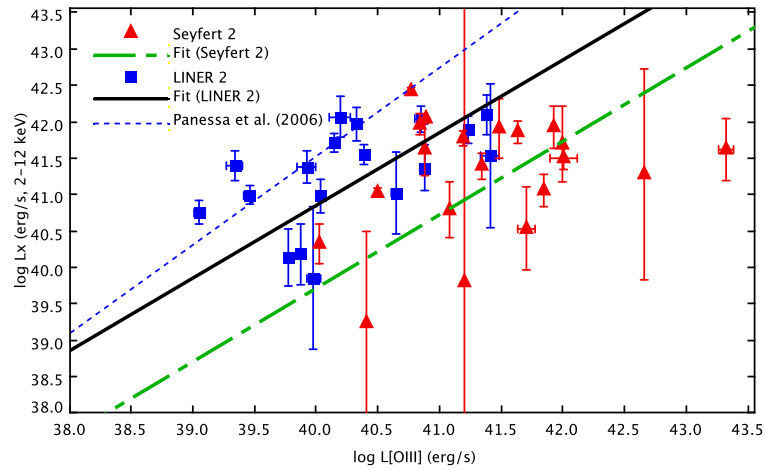


Figure 5.17: Histograms of $\log(f_{2-12\text{keV}}/f_{\text{H}\alpha})$ and $\log(f_{2-12\text{keV}}/f_{[\text{OIII}]})$ are shown for the 46 AGN with $\text{H}\alpha/\text{H}\beta > 3.1$ (pink dashed histograms). On average Seyfert 2 galaxies (red filled histograms) have lower $f_{2-12\text{keV}}/f_{\text{H}\alpha}$ and $f_{2-12\text{keV}}/f_{[\text{OIII}]}$ than LINER 2s (black histograms).



(a)



(b)

Figure 5.18: The extinction corrected $L_{H\alpha}$ and $L_{[OIII]}$ are shown against the observed $L_{2-12\text{keV}}$ for the 46 AGN with $H\alpha/H\beta > 3.1$. The Seyfert 2 galaxies are marked with red triangles. The LINER 2s are marked with blue squares. The least-square (bisector) fits to the Seyfert 2 galaxies and the LINER 2s are shown as the green dashed-dashed lines and the black solid lines, respectively. The blue dotted lines are the correlations from Panessa et al. (2006) converted to the 2–12 keV band (assuming a power-law with $\Gamma = 1.7$ and a Galactic absorption of $N_H = 3 \times 10^{20}$ atoms cm^{-2}).

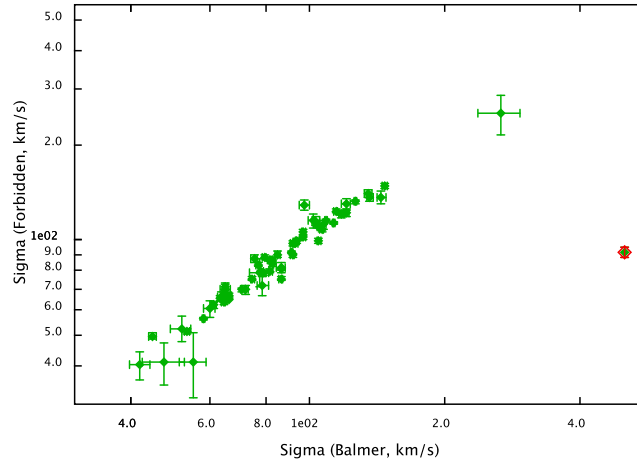
The Seyfert 2 galaxies have a mean $f_{2-10\text{keV}}/f_{\text{H}\alpha} \approx 5$ and a mean $f_{2-10\text{keV}}/f_{[\text{O III}]}$ ≈ 4 . The LINER 2s have a mean $f_{2-10\text{keV}}/f_{\text{H}\alpha} \approx 12$ and a mean $f_{2-10\text{keV}}/f_{[\text{O III}]}$ ≈ 21 (Figure 5.17), both higher than those of the Seyfert 2 galaxies, in contrast to what Terashima et al. (2000a) found using *ASCA* data. More than half (11 out of 20) of the Seyfert 2 galaxies are Compton thick candidates based on the $f_{2-10\text{keV}}/f_{[\text{O III}]}$ ratio, making up to $\sim 73\%$ of the overall Compton thick candidates. Only one LINER is a Compton thick candidate. The $\text{H}\alpha$ and $[\text{O III}]\lambda 5007$ luminosities are plotted against the 2–12 keV luminosities for Seyfert 2 galaxies and LINER 2s in Figure 5.18(a) and 5.18(b), respectively. On average the LINER 2s appear to lie closer to the X-ray- $\text{H}\alpha$ and the X-ray- $[\text{O III}]$ correlations found in Panessa et al. (2006) than the Seyfert 2 galaxies, suggesting that LINER 2s might have lower X-ray obscuration than Seyfert 2 galaxies. Least-square (bisector) fits yielded $\log L_{2-12\text{keV}} = (1.03 \pm 0.19) \times \log L_{\text{H}\alpha} + (-0.37 \pm 7.66)$ and $\log L_{2-12\text{keV}} = (1.00 \pm 0.18) \times \log L_{[\text{O III}]} + (0.84 \pm 7.11)$ for the 18 LINER 2s (13 were excluded from the fitting due their Balmer decrement $\text{H}\alpha/\text{H}\beta < 3.1$ in which case the extinction correction could not be carried out for the emission lines). Most of the Seyfert 2 galaxies fall below the correlations from Panessa et al. (2006). Least-square (bisector) fits yielded $\log L_{2-12\text{keV}} = (1.02 \pm 0.11) \times \log L_{\text{H}\alpha} + (-0.76 \pm 4.63)$ and $\log L_{2-12\text{keV}} = (1.01 \pm 0.13) \times \log L_{[\text{O III}]} + (-0.70 \pm 5.42)$ for the 20 Seyfert 2 galaxies. If the optical emission lines in LINER 2s are not underestimated or intrinsically faint, low intrinsic X-ray obscuration is suggested for these galaxies. The differences in the X-ray- $\text{H}\alpha$ and X-ray- $[\text{O III}]$ correlations between the Seyfert 2 galaxies and the LINER 2s also suggest that the BLRs in LINER 2s might be intrinsically weaker than those of Seyfert 2 galaxies.

5.3 Emission Line Ratio Classified SF Galaxies

5.3.1 Overall Properties

The SF galaxy subsample includes 62 galaxies. As previously described in § 5.1.2, these galaxies are relatively bluer (in $u - r$) galaxies with younger stellar populations compared to the rest of the NELGs in the *MJ* sample. These galaxies have lower X-ray-to-optical flux ratios than the AGN and are fainter in both soft and hard bands.

One SF galaxy shows a larger velocity dispersion for its Balmer lines than for its forbidden lines (Figure 5.19(a)). The outlier, namely 2XMM J095848.6+025243 (SRCID: 78830), is probably a NLS

(a) σ_{Balmer} VS. $\sigma_{\text{Forbidden}}$

RA=149.70278, DEC= 2.87868, MJD=51994, Plate= 500, Fiber=536

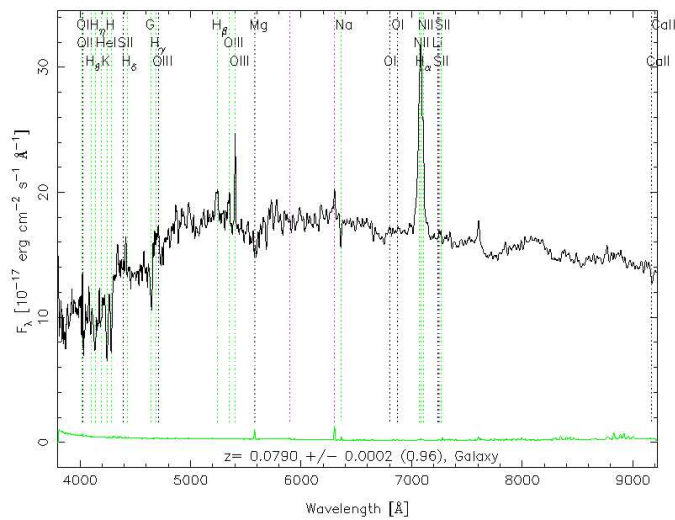
(b) *SDSS* spectrum for 2XMM J095848.6+025243 (SRC: 78830)

Figure 5.19: (a) The velocity dispersion (σ of Gaussian fits to the lines) of Balmer lines are shown against that of forbidden lines, both from the *MPA/JHU* catalogues. (b) The *SDSS* spectrum (taken from the *SDSS* SkyServer Object Explorer) of the outlier 2XMM J095848.6+025243 (SRC: 78830) which is marked as a red diamond in (a).

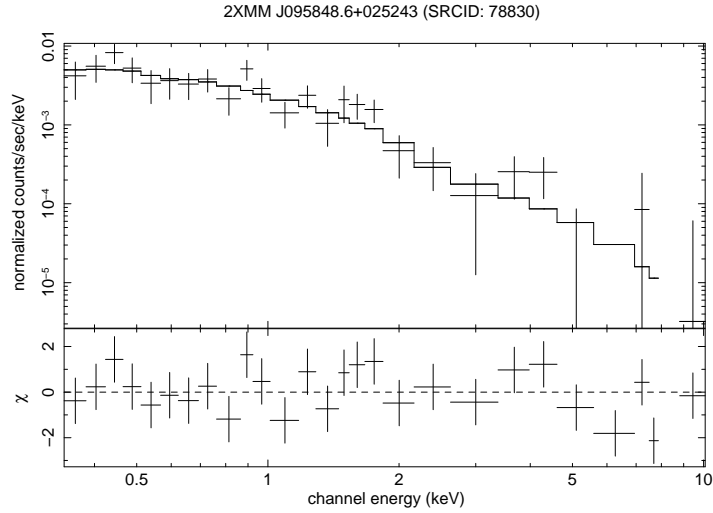


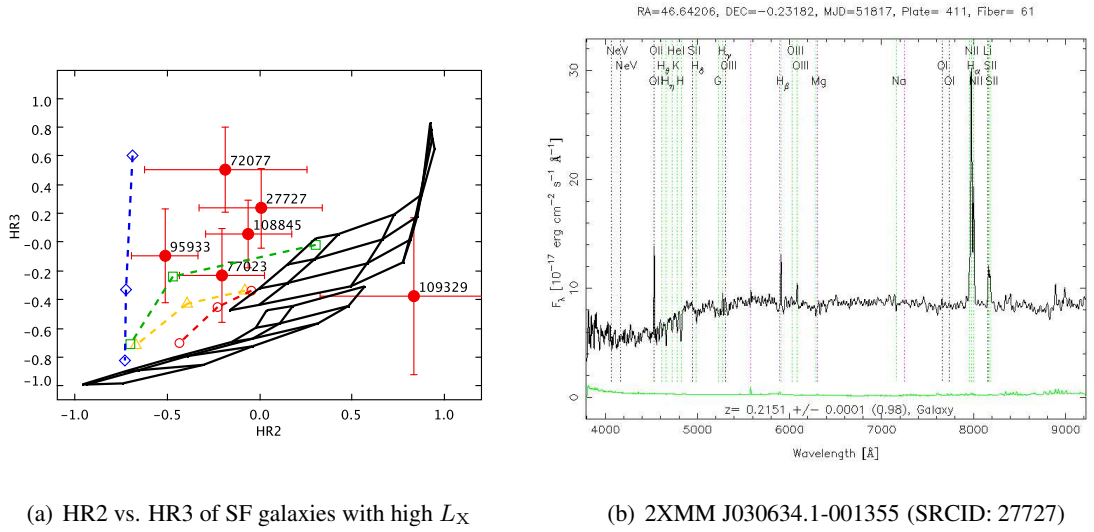
Figure 5.20: The *2XMM* pn spectrum of 2XMM J095848.6+025243 (SRC: 78830) fitted by a power-law model with $\Gamma = 2.02^{+0.29}_{-0.26}$ (the Galactic absorption was fixed at $N_{\text{H}} = 1.84 \times 10^{20}$ atoms cm^{-2} , Kalberla et al. 2005).

1 galaxy as its *SDSS* spectrum shows a possible broad $\text{H}\alpha$ line (Figure 5.19(b)). This source was also detected by *ROSAT* and was classified as a Seyfert 1 galaxy (Brinkmann et al. 1999). The automatically extracted *2XMM* spectrum of this source (Figure 5.20) can be fitted by a power-law model with $\Gamma = 2.02^{+0.29}_{-0.26}$ ($\chi^2 = 25$ for 25 degrees of freedom; the Galactic absorption was fixed at $N_{\text{H}} = 1.84 \times 10^{20}$ atoms cm^{-2} , Kalberla et al. 2005). The 0.2–12 keV luminosity derived from this model is 4.98×10^{41} erg s^{-1} . This source is not reported as a variable source in *2XMM*. Visual checking for the *SDSS* spectra of the other SF galaxies did not find any high ionization emission lines which were not considered in the classification schema but can indicate AGN activity.

5.3.2 SF Galaxies with $L_{\text{X}} > 10^{42}$ erg s^{-1}

To date no nearby SF galaxy has been found to have $L_{\text{X}} > 10^{42}$ erg s^{-1} . Hence SF galaxies with such high L_{X} might have additional power sources contributing to the X-ray emission. Six of the SF galaxies have $L_{0.2-12\text{keV}} > 10^{42}$ erg s^{-1} and are listed in Table 5.2. The redshifts of these galaxies range from 0.115 to 0.323; all are above the average value of the SF subsample (0.09). The galactic extinction-corrected *SDSS* r band Petrosian magnitudes of these galaxies range from 16.95 to 17.82. Four galaxies have $C_{90/50}$ around the early-type and late-type galaxy dividing line of 2.6 (Strateva et al. 2001). All six galaxies have $\log(f_{\text{X}}/f_{\text{O}}) > -2$, ranging from -1.49 to -1.02 . The average full band photon counts from the pn camera are ~ 56 , making detailed X-ray spectral analysis on individual

galaxies difficult. The X-ray hardness ratios HR2 and HR3 (with 1σ uncertainties) of these galaxies are plotted in Figure 5.21(a).

(a) HR2 vs. HR3 of SF galaxies with high L_X

(b) 2XMM J030634.1-001355 (SRCID: 27727)

Figure 5.21: (a) The X-ray hardness ratios (HR2 versus HR3) from the pn camera of the six SF galaxies with $L_{0.2-12\text{keV}} > 10^{42} \text{ erg s}^{-1}$. Spectral models defined in § 2.4.4 are overlaid in the plot. (b) The *SDSS* spectrum (taken from the *SDSS* SkyServer Object Explorer) of 2XMM J030634.1-001355 (SRCID: 27727).

The *SDSS* counterpart of 2XMM J030634.1-001355 (SRCID: 27727), was classified as a Seyfert 1 galaxy by Véron-Cetty & Véron (2003). However, inspection of the *SDSS* spectrum did not reveal significantly broadened Balmer line(s) (Figure 5.21(b)). The X-ray hardness ratios of this source can be reproduced by a power-law model modified by an absorption up to $10^{22} \text{ atoms cm}^{-2}$. Although the X-ray hardness ratios of 2XMM J085931.2+390753 (SRCID: 72077) cannot be reproduced by any model overlaid in the plot, the relatively high HR3 (0.45 ± 0.26) suggests an obscured power-law component. 2XMM J094639.0+095847 (SRCID: 77023) has X-ray hardness ratios well represented by a two-component model with the power-law component contributing the majority of its X-ray emission. The *SDSS* counterpart of 2XMM J112758.1+583557 (SRCID: 95933) was classified as a possible dwarf galaxy candidate around NGC 3690 (Deeg et al. 1998). However, the redshift of this galaxy measured by *SDSS* (0.178; Abazajian et al. 2004) rules out association with NGC 3690 ($z \approx 0.01$ from Nordgren et al. 1997). The stellar mass of this galaxy estimated by Kauffmann et al. (2003b) is $10^{10.88} M_{\odot}$. The X-ray hardness ratios of this source suggests a non-negligible thermal component in the X-ray emission. The optical counterpart of 2XMM J123608.7+131340 (SRCID: 108845) was not selected as a spectral target in the *SDSS* Main Galaxy Sample, instead it was selected as a luminous red galaxy (LRG; Strauss et al. 2002). This galaxy has $u - r = 2.62$ and $C_{90/50} = 3.35$, suggesting a early-type morphology

SRCID	IAUNAME	z	r (mag)	$u - r$ (mag)	$C_{\frac{90}{50}}$	d_{XO} (σ_X)	$\log(\frac{f_X}{f_O})$	$\log L_{2-12\text{keV}}$ (erg s^{-1})	HR2	HR3
27727	2XMM J030634.1-001355	0.215	17.65	1.44	2.44	0.97	-1.03	42.25	0.01 ± 0.33	0.23 ± 0.27
72077	2XMM J085931.2+390753	0.155	16.95	1.88	2.59	0.66	-1.49	41.45	-0.18 ± 0.44	0.50 ± 0.29
77023	2XMM J094639.0+095847	0.115	17.22	1.74	2.54	1.07	-1.10	41.94	-0.21 ± 0.23	-0.24 ± 0.33
95933	2XMM J112758.1+583557	0.178	17.68	2.31	2.42	0.97	-1.04	42.20	-0.51 ± 0.18	-0.10 ± 0.33
108845	2XMM J123608.7+131340	0.323	17.82	2.62	3.35	0.58	-1.02	42.60	-0.06 ± 0.24	0.05 ± 0.24
109329	2XMM J123735.4+622600	0.188	17.36	1.49	1.90	1.38	-1.29	42.20	0.84 ± 0.51	-0.39 ± 0.55

Table 5.2: The SF galaxies with $L_X > 10^{42}$ erg s^{-1} . The d_{XO} is the offset between the X-ray position and the optical position normalized by the X-ray positional uncertainty (in σ). Hardness ratios HR2 and HR3 are from the pn camera.

(Strateva et al. 2001). There is no reliable SFR estimated in Brinchmann et al. (2004) for this galaxy. The X-ray hardness ratios of this source can be reproduced by a power-law with $\Gamma \sim 1.7$ modified by an absorption of a few 10^{21} atoms cm^{-2} . The X-ray hardness ratios of 2XMM J123735.4+622600 (SRCID: 109329) cannot be reproduced by any of the models overlaid in Figure 5.21(a) although they are consistent within the uncertainties with either an absorbed power-law model or an APEC model. Therefore, for these six galaxies, the high X-ray luminosities and the X-ray hardness ratios suggest that the X-ray emission of these galaxies might be significantly contaminated by AGN.

5.3.3 X-ray Hardness Ratios

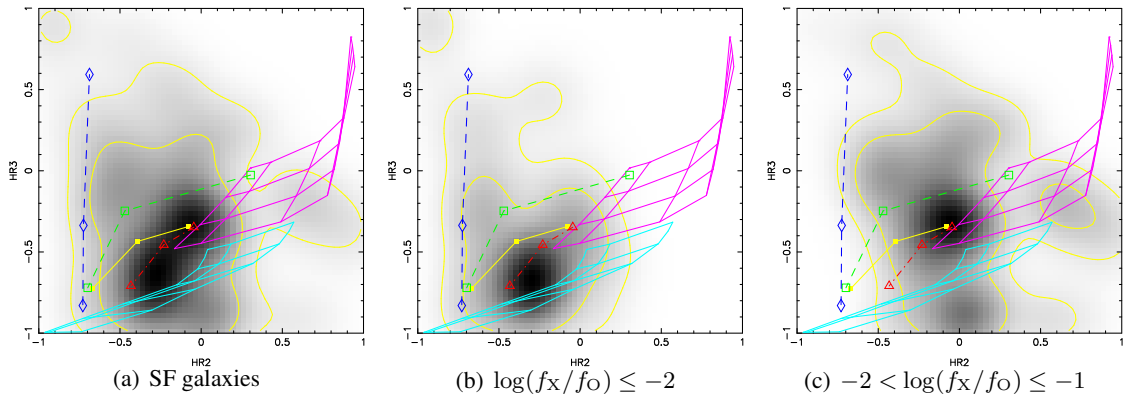


Figure 5.22: The X-ray hardness ratio (HR2 versus HR3) density plots for (a) the SF galaxy subsample, (b) SF galaxies with $\log(f_X/f_O) \leq -2$, and (c) SF galaxies with $-2 < \log(f_X/f_O) \leq -1$. Three galaxies were excluded due to undefined pn hardness ratios. Spectral models defined in § 2.4.4 are overlaid in each plot. Contours indicating 68% and 90% levels are also shown.

The X-ray hardness ratio (HR2 versus HR3) density plot for the SF galaxy subsample is shown in Figure 5.22(a). The pattern in the density plot suggests that a thermal component is contributing a significant fraction of the total X-ray emission of these galaxies. There are 27 SF galaxies with $\log(f_X/f_O) \leq -2$ and 35 SF galaxies with $-2 < \log(f_X/f_O) \leq -1$. The hardness ratios of sources in these two $\log(f_X/f_O)$ bins are also shown in Figure 5.22(b) and 5.22(c). The hardness ratios of most the SF galaxies with $\log(f_X/f_O) \leq -2$ are consistent with soft spectra dominated by an APEC component, which suggests that the X-ray emission of these galaxies are probably dominated by hot ISM. SF galaxies with $-2 < \log(f_X/f_O) \leq -1$ tend to have harder spectra, consistent with a power-law model, indicating contributions from X-ray binaries and/or contamination of AGN. Absorptions up to 10^{22} atoms cm^{-2} are also suggested in a few galaxies by the hardness ratios, in these cases AGN

contamination might be present.

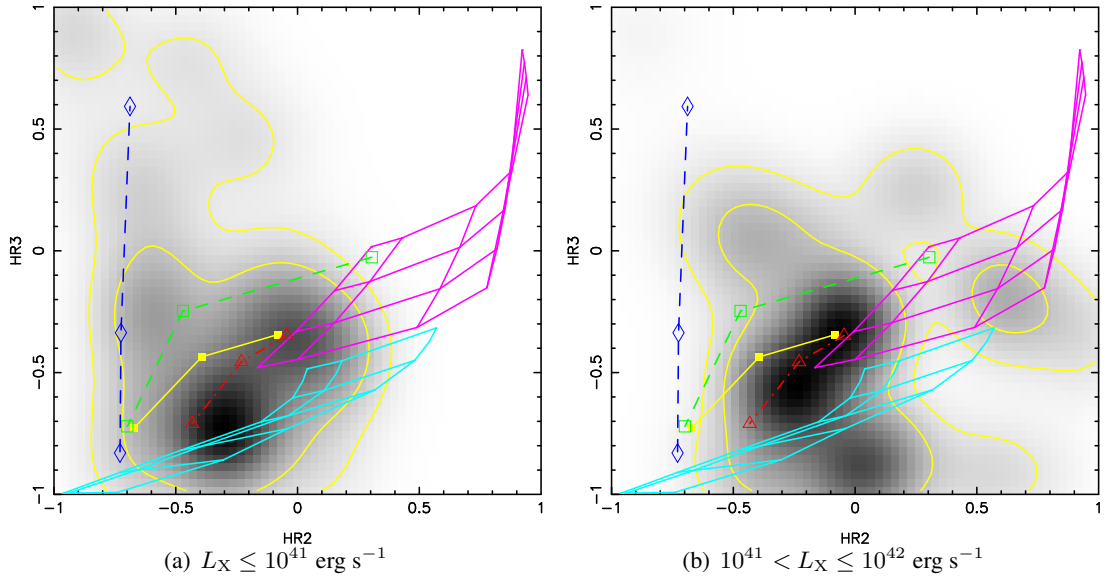


Figure 5.23: The X-ray hardness ratio (HR2 versus HR3) density plots for SF galaxies in two X-ray luminosity bins: (a) $L_X \leq 10^{41} \text{ erg s}^{-1}$ and (b) $10^{41} < L_X \leq 10^{42} \text{ erg s}^{-1}$. SF galaxies with undefined pn hardness ratios were excluded. Spectral models defined in § 2.4.4 are overlaid in each plot. Contours indicating 68% and 90% levels are also shown.

The 56 galaxies which have $L_X \leq 10^{42} \text{ erg s}^{-1}$ were divided into two luminosity bins: 27 with $L_X \leq 10^{41} \text{ erg s}^{-1}$ and 29 with $L_X > 10^{41} \text{ erg s}^{-1}$. The hardness ratio densities of galaxies in these two bins are shown in Figure 5.23(a) and 5.23(b). It appears that on average SF galaxies with $L_X \leq 10^{41} \text{ erg s}^{-1}$ have soft spectra, consistent with hot gas origin. The contribution from the power-law component to the overall X-ray emission in a given galaxy seems to increase with the X-ray luminosity.

5.3.4 X-ray Luminosities and SFRs

The X-ray emission from SF galaxies without significant AGN contribution can be attributed to a combination of an hot ISM, SNR and X-ray binaries (*e.g.*, Fabbiano 1989). The X-ray emission arising from the hot ISM effectively heated by supernovae explosions and/or stellar winds appears to dominate the soft X-ray ($\lesssim 2 \text{ keV}$) emission of SF galaxies (*e.g.*, Grimes et al. 2005). Therefore soft X-ray emission can serve as an indicator of SFR (Ranalli et al. 2003; Persic & Rephaeli 2007). Strong correlations between soft X-ray and SFR proxies such as infrared/radio luminosities have been observed in nearby SF galaxies (*e.g.*, Read & Ponman 2001; Ranalli et al. 2003; Lou & Bian 2005). On the other hand, HMXBs, whose lifetime is dependant on the evolution time scale of the high mass donor ($\sim 10^6$ –

10^7 years), trace the current star formation in galaxies. The X-ray emission from HMXBs can dominate the X-ray emission of starburst galaxies (*e.g.*, Helfand & Moran 2001; Persic et al. 2004). Correlation between hard X-ray ($\gtrsim 2$ keV) emission, which is believed to be dominated by binaries, and SFRs have been seen in nearby SF galaxies (*e.g.*, Ranalli et al. 2003; Grimm et al. 2003; Persic et al. 2004; Persic & Rephaeli 2007) and may hold up to $z \sim 1.5$ (Ranalli et al. 2003; Persic et al. 2004; Persic & Rephaeli 2007; Lehmer et al. 2008). LMXBs instead have much longer lifetime and thus are less relevant to the current SF activity (*e.g.*, Grimm et al. 2003; Colbert et al. 2004; Persic & Rephaeli 2007). In external galaxies LMXBs are very difficult to separate from HMXBs and introduce uncertainties in the measurement of X-ray emission that are used to derive SFRs. Studies which corrected for the possible contamination from LMXBs (*e.g.*, Colbert et al. 2004; Persic & Rephaeli 2007) predicted around one order higher SFRs per X-ray luminosities than those which did not (*e.g.*, Ranalli et al. 2003).

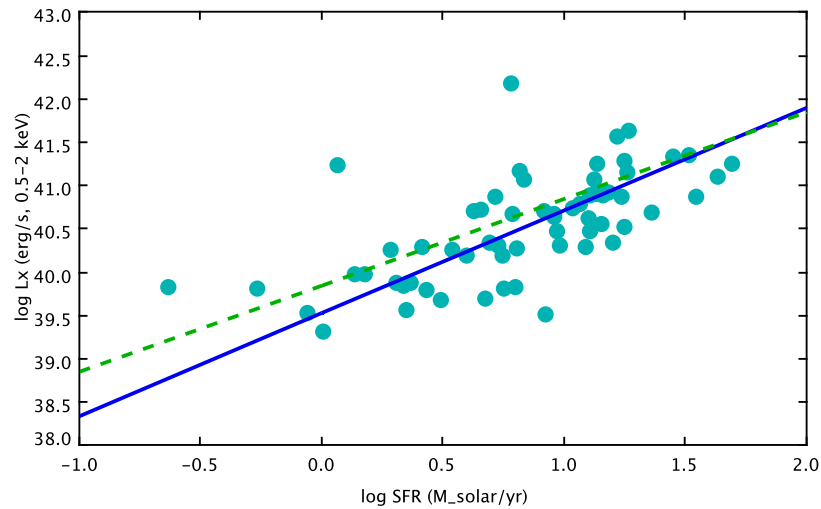


Figure 5.24: SFRs (as calculated in Brinchmann et al. 2004) are shown against the soft band X-ray (0.5–2 keV) luminosities. The fit to the data is shown as a blue solid line and the correlation from Ranalli et al. (2003) is shown as a green dashed line.

SFRs are available in the *MPA/JHU* catalogues (Brinchmann et al. 2004) for all but one SF galaxy (2XMM J12368.7+131340 [SRCID: 108845]). The SFRs are plotted against the 0.5–2 keV luminosities in Figure 5.24. The soft X-ray luminosities of the SF galaxies seem to correlate well with SFRs and are consistent with the calibration found by Ranalli et al. (2003) for nearby (distance $\lesssim 70$ Mpc) SF galaxies whose $L_{0.5-2\text{keV}}$ were in the range of $\sim 10^{38.5}-10^{41.5}$ erg s $^{-1}$. By comparing the Ranalli et al. (2003) calibration with evolutionary population synthesis models Mas-Hesse et al. (2008) concluded that the Ranalli et al. (2003) calibration was consistent with the predictions for relatively

unevolved, continuous star formation over ~ 10 Myr. Least-square (bisector) fit yielded a correlation as: $\log L_{0.5-2\text{keV}} = (39.51 \pm 0.12) + (1.19 \pm 0.11) \times \log \text{SFR}$.

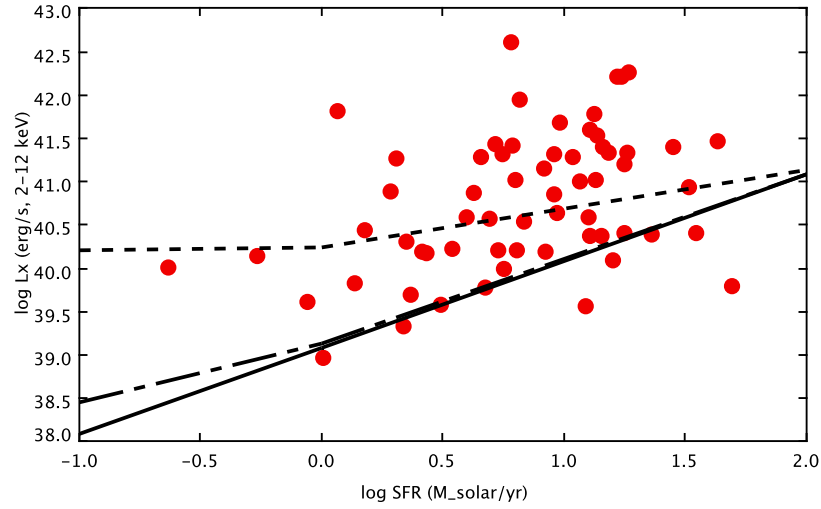


Figure 5.25: SFRs (as calculated in Brinchmann et al. 2004) are shown against the hard band X-ray (2–12 keV) luminosities. The correlation from Colbert et al. (2004), when no contribution from LMXBs is included, is shown as black solid line. The dashed-dashed line indicates the same correlation but with the LMXBs contribution represented by a stellar mass of $10^9 M_{\odot}$. The dashed line is also for the same correlation but with the LMXBs contribution calculated from a stellar mass of $10^{11} M_{\odot}$.

In the hard X-ray band (2–12 keV) the situation is less clear. Firstly, $\sim 15\%$ of the SF galaxies have hard band (2–12 keV) luminosities $> 10^{41.5} \text{ erg s}^{-1}$, which have only been reported for very luminous SF galaxies (*e.g.*, NGC 3256, Lira et al. 2002) and are not very common for ordinary SF galaxies. AGN contamination seems to be a more plausible explanation for such high hard band luminosities. Using 32 nearby (distance < 30 Mpc) galaxies Colbert et al. (2004) found that the X-ray luminosities were linearly correlated with both SFRs and stellar mass, the latter representing the old stellar population (*e.g.*, LMXBs). The SF galaxies with $L_{2-12\text{keV}} \lesssim 41.5 \text{ erg s}^{-1}$ are loosely consistent with the Colbert et al. (2004) correlation, although a large fraction of them sit above the line which presents only the L_X from SFR (Figure 5.25). The simplest explanation of this discrepancy is a hidden AGN contribution. Therefore, it seems that in order to use the hard X-ray luminosity as a SFR proxy for a SF galaxy, one must account for contamination from both LMXBs and hidden AGN in the galaxy; on the other hand, soft X-ray luminosity can serve as a SFR proxy even when the contribution from LMXBs and/or AGN cannot be removed.

5.3.5 X-ray and Optical Emission Line Luminosities

The $H\alpha$ line luminosities of the SF galaxies are plotted against the hard band (2–12 keV) luminosities in Figure 5.26. Most of the SF galaxies fall below the L_X - $L_{H\alpha}$ correlation found in the AGN subsample (green dashed line in Figure 5.26; see also § 5.2.3), indicating that SF galaxies produce more $H\alpha$ emission than AGN of a comparable X-ray luminosity. The ratios between X-ray and $H\alpha$ fluxes range from ~ 0.001 to ~ 4.3 . The mean $f_{2-12\text{keV}}/f_{H\alpha}$ is 0.38, ~ 30 times lower than the value associated with AGN (§ 5.2). Perez-Olea & Colina (1996) found that the $L_X/L_{H\alpha}$ for pure SF galaxies could be two orders lower than those for AGN. Therefore, since SF activity seems to be more efficient in producing $H\alpha$ emission than AGN of a similar L_X , the optical classification only reveals the SF nature of the galaxy even when an AGN maybe present.

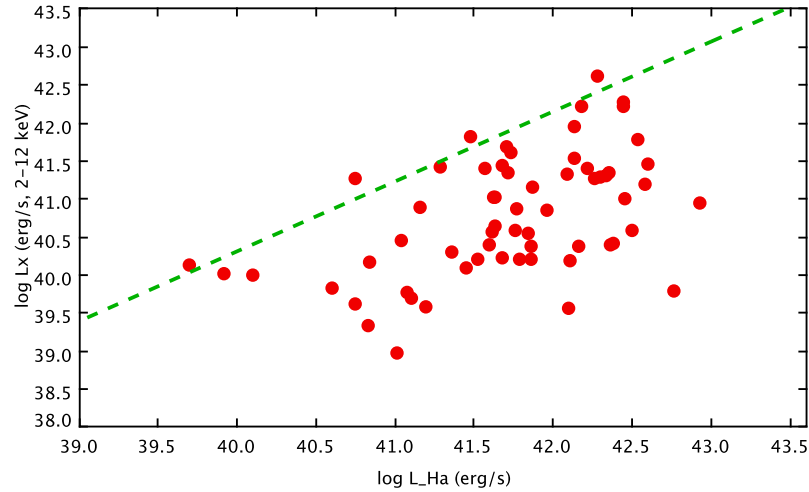


Figure 5.26: The $H\alpha$ line luminosities are plotted against the 2–12 keV luminosities of SF galaxies. The L_X - $H\alpha$ correlation found for the AGN subsample (§ 5.2.3) is marked by the green dashed line. Most of the SF galaxies fall below this correlation.

5.4 Emission Line Ratio Classified Composite Galaxies

Both AGN and SF activity contribute significant fractions of the optical emission lines of composite galaxies (Kewley et al. 2006). There are 48 NELGs in the *MJ* sample that have been classified as composite galaxies. In both the $u - r$ colour and concentration index $C_{90/50}$ these galaxies have mean values between those of AGN and SF galaxies. In the soft (0.5–2 keV) and hard (2–12 keV) bands

these galaxies have mean fluxes between those of AGN and SF galaxies. The mean luminosities in these two bands are similar to those of SF galaxies, however, somewhat lower than AGN. The mean X-ray-to-optical ratio of composite galaxies is similar to the ones of SF galaxies and unclassified NELGs, but lower than AGN.

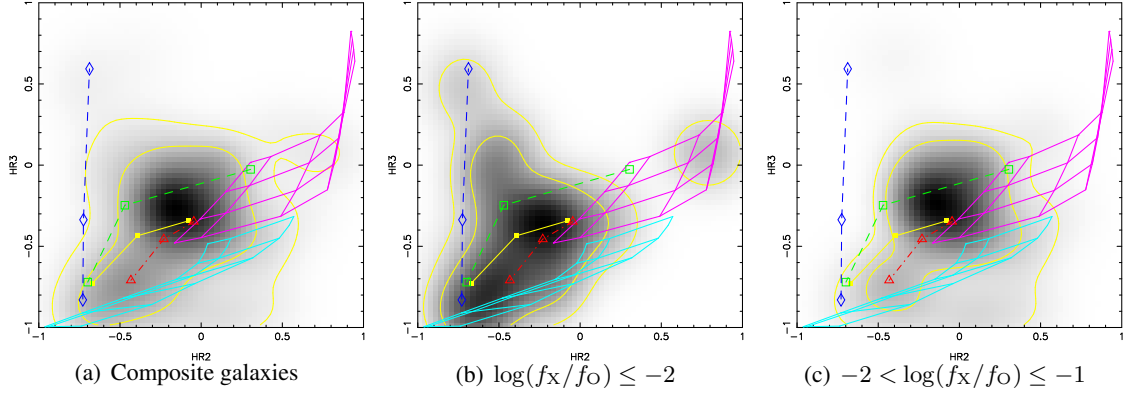


Figure 5.27: The smoothed pn hardness ratio (HR2 versus HR3) density plots for (a) composite galaxies, (b) composite galaxies with $\log(f_X/f_O) \leq -2$, and (c) composite galaxies with $-2 < \log(f_X/f_O) \leq -1$. Two galaxies were excluded due to undefined pn hardness ratios. Spectral models defined in § 2.4.4 are overlaid in each plot. Contours indicating 68% and 90% levels are also shown.

The hardness ratio (HR2 versus HR3) density plot of these composite galaxies (Figure 5.27(a)) indicates a mixed nature. The peak of the hardness ratio density is consistent with a two-component model. Compared with the AGN subsample (§ 5.2.2), the fraction that the power-law component contributes to the overall X-ray emission of the galaxy seems to be lower in the composite galaxies. Dividing the composite galaxies by their X-ray-to-optical ratio gives 20 with $\log(f_X/f_O) \leq -2$ and 28 with $-2 < \log(f_X/f_O) \leq -1$. The hardness ratio density plots of composite galaxies within these two bins (Figure 5.27(b) and 5.27(c)) suggest that galaxies with $\log(f_X/f_O) \leq -2$ appear to have higher fraction of their X-ray emission coming from a thermal component compared with those within the higher $\log(f_X/f_O)$ bin. The hardness ratio densities of composite galaxies with $L_X \leq 10^{41}$ erg s $^{-1}$ and $10^{41} < L_X \leq 10^{43}$ erg s $^{-1}$ are shown in Figure 5.28(a) and 5.28(b), respectively. A significant fraction of the composite galaxies with $L_X \leq 10^{41}$ erg s $^{-1}$ seem to have soft spectra with small contribution from a power-law component, resembling SF galaxies rather than AGN in the same luminosity range. The peak in the density plot of composite galaxies with $10^{41} < L_X \leq 10^{43}$ erg s $^{-1}$ suggests that a power-law component contributes the bulk of the X-ray emission from these galaxies.

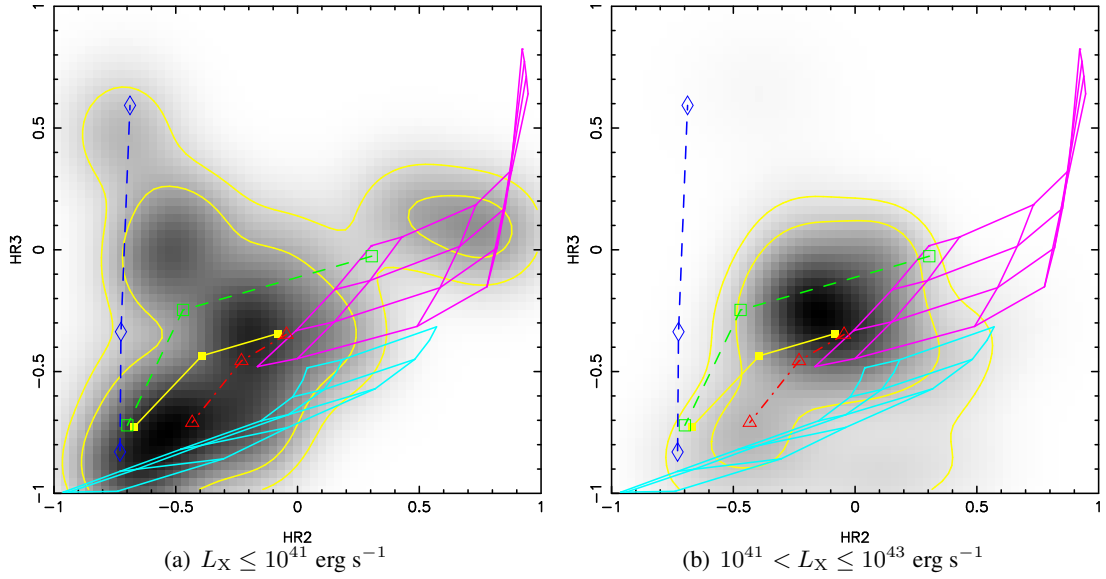


Figure 5.28: The smoothed pn hardness ratio (HR2 versus HR3) density plots for composite galaxies with $L_X \leq 10^{41} \text{ erg s}^{-1}$ (a) and those with $10^{41} < L_X \leq 10^{43} \text{ erg s}^{-1}$ (b). Spectral models defined in § 2.4.4 are overlaid in each plot. Contours at 68% and 90% levels are also shown.

5.5 Unclassified NELGs

5.5.1 Overall Properties and X-ray Hardness Ratios

About 29% (69/239) of the NELGs could not be classified using BPT plots due to weakness ($< 3\sigma$) or absence of one or more lines involved in BPT plots. In terms of $u - r$ colours and concentration index $C_{90/50}$, these galaxies resemble ALGs rather than the other NELGs (§ 5.1.2). The mean redshift of these galaxies is 0.127, higher than the classified NELGs (AGN, SF galaxies, and composite galaxies) but lower than ALGs. The mean X-ray-to-optical ratio is similar to those of SF galaxies, composite galaxies and ALGs, but lower than AGN. The unclassified NELGs have the highest mean X-ray flux and mean luminosity in the soft band (0.5–2 keV) compared with other NELGs and ALGs. In the hard band (2–12 keV), these galaxies have the lowest mean flux among the NELG subsamples although still higher than ALGs. The mean luminosity in the hard band, probably due to the higher L mean redshift, is higher than SF galaxies and composite galaxies, but still lower than AGN and ALGs. In the total band (0.2–12 keV), these galaxies have the second highest mean luminosity, only surpassed by ALGs. As shown in Figure 5.29(a), on average the unclassified NELGs have X-ray hardness ratios consistent with a two-component model with a significant contribution from a thermal component.

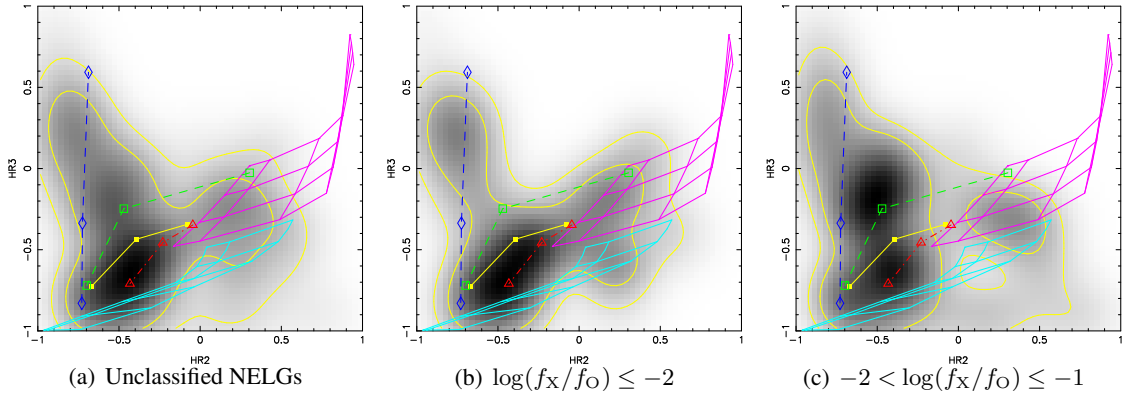


Figure 5.29: The smoothed pn hardness ratio (HR2 versus HR3) density plots for the unclassified NELGs and its subsets within the two X-ray-to-optical flux ratio bins: (b) $\log(f_x/f_o) \leq -2$ and (c) $-2 < \log(f_x/f_o) \leq -1$. Five galaxies were excluded from the plots due to undefined hardness ratios. Spectral models defined in § 2.4.4 are overlaid in each plot. Contours indicating 68% and 90% levels are also shown.

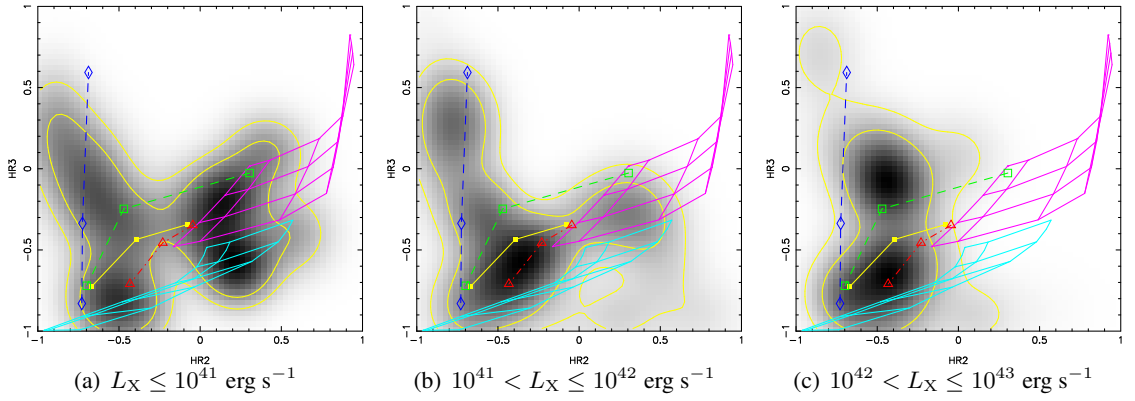


Figure 5.30: The smoothed pn hardness ratio (HR2 versus HR3) density plots for the unclassified NELGs in three luminosity bins: (a) $L_X \leq 10^{41} \text{ erg s}^{-1}$, (b) $10^{41} < L_X \leq 10^{42} \text{ erg s}^{-1}$, and (c) $10^{42} < L_X \leq 10^{43} \text{ erg s}^{-1}$. The five galaxies with undefined hardness ratios from the pn camera were excluded. Spectral models defined in § 2.4.4 are overlaid in each plot. Contours at 68% and 90% levels are also shown.

There are 32 unclassified NELGs with $\log(f_X/f_O) \leq -2$ and 37 with $-2 < \log(f_X/f_O) \leq -1$. The X-ray hardness ratio density plots of galaxies in these two bins are shown in Figure 5.29(b) and 5.29(c) respectively. The peaks of the hardness ratio densities are consistent with two-component models. The soft component seems to be responsible for a large fraction of the X-ray emission of galaxies within both bins, suggesting that hot gas contributes significantly to the X-ray emission from these galaxies. Dividing this subsample by L_X gives 17 galaxies with $L_X \leq 10^{41}$ erg s⁻¹, 33 with $10^{41} < L_X \leq 10^{42}$ erg s⁻¹, and 19 with $L_X > 10^{42}$ erg s⁻¹. In Figure 5.30(a), the pattern in the density plot of galaxies with $L_X < 10^{41}$ erg s⁻¹ is less concentrated with the 68% contour encompassing areas consistent with a single power-law model, a single APEC model and a two-component model. For galaxies with $10^{41} < L_X \leq 10^{42}$ erg s⁻¹, the peak in the density plot is consistent with a two-component model dominated by a thermal component (Figure 5.30(b)), indicating that the X-ray emission from these galaxies is dominated by hot ISM within the galaxies. The hardness ratios of galaxies with $10^{42} < L_X \leq 10^{43}$ erg s⁻¹ also seem to be consistent with a two-component model (Figure 5.30(c)). In some of these galaxies the power-law component might be associated with an absorption up to a few 10^{22} atoms cm⁻², suggesting possible AGN contamination.

5.5.2 Double-Lobed Radio Galaxies

All but two unclassified NELGs sit within the sky area covered by the Faint Images of the Radio Sky at Twenty centimeters (FIRST) Survey¹⁴ (Becker et al. 1995; White et al. 1997; Becker et al. 2003) and $\sim 28\%$ (19/67) have FIRST detections within 7'' from the X-ray positions. For five of the unclassified NELGs, the FIRST counterparts clearly show double-lobed morphologies with bright cores (Figure 5.31), strong indication of AGN presence. These five galaxies are listed in Table 5.3. One of these galaxies, 2XMM 080822.2+390059 (SRCID: 65610), has $\log(f_X/f_O) = -1.08$ and $L_{0.2-12\text{keV}} = 2.37 \times 10^{42}$ erg s⁻¹. Also the X-ray position of this galaxy is consistent with the bright core of the radio galaxy (Figure 5.31(a)). Therefore, for this galaxy, an AGN presence is reinforced by its X-ray properties. All but one (2XMM J132947.7+114232 [SRCID: 122338]) of these five radio galaxies also appear as bent-tail radio galaxies, suggesting that these galaxies are interacting with the intergalactic medium in a group or cluster environment (*e.g.*, Gull & Northover 1973; Begelman et al. 1984).

¹⁴<http://sundog.stsci.edu/index.html>

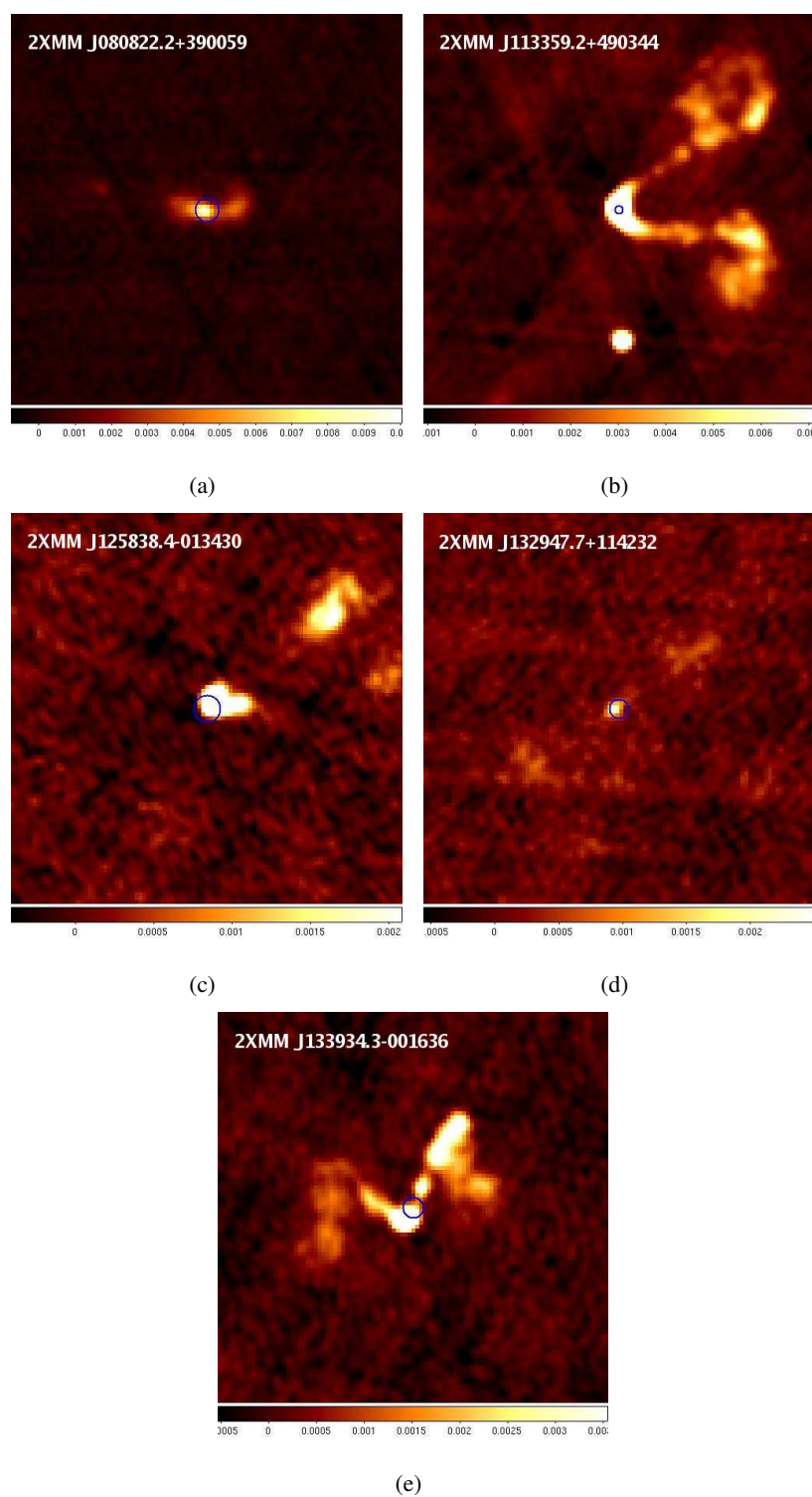


Figure 5.31: Radio images (3' \times 3') of the five double-lobed radio galaxies from the FIRST Survey. The overlaid regions are centred at the positions of the X-ray sources with radii of the 3 σ X-ray positional uncertainties.

SRCID	IAUNAME	z	r	$\log(\frac{f_X}{f_O})$	$f_{0.5-2\text{keV}}$	$f_{2-12\text{keV}}$	$L_{0.2-12\text{keV}}$	$S_{1.4\text{GHz}}$	R_{ro}
(1)	(2)	(3)	(4)	(5)	(6)	(7)	(8)	(9)	(10)
65610	2XMM J080822.2+390059	0.196	17.71	-1.08	7.50	9.94	23.69	39.63	2.12
96686	2XMM J113359.2+490344	0.032	13.19	-2.16	60.38	40.90	2.69	166.97	0.94
114704	2XMM J125838.4-013430	0.086	15.41	-2.43	1.59	1.32	1.50	34.99	1.15
122338	2XMM J132947.7+114232	0.085	15.61	-2.08	3.72	6.48	2.75	3.76	0.26
125285	2XMM J133934.3-001636	0.145	16.00	-2.04	6.47	5.18	6.49	30.44	1.32

Table 5.3: Unclassified NELGs detected in the FIRST Survey as double-lobed radio galaxies. (1): The unique source ID in *2XMM*. (2): The IAU name of the *2XMM* source. (3): Redshift from *SDSS*. (4): The r band magnitude from *SDSS*. (5): The X-ray-to-optical flux ratio. (6): The soft band (0.5–2 keV) flux in the unit of 10^{-15} erg s^{-1} cm^{-2} . (7): The hard band (2–12 keV) flux in the unit of 10^{-15} erg s^{-1} cm^{-2} . (8): The 0.2–12 keV luminosity in the unit of 10^{41} erg s^{-1} . (9): The integrated 1.4 GHz flux density (mJy) from the FIRST Survey (Becker et al. 2003). (10): The radio loudness defined as the ratio of the flux density in 1.4 GHz (integrated) to that in the r band (Ivezić et al. 2002).

5.6 Absorption Line Galaxies

5.6.1 Overall Properties

There are 87 ALGs in the *XS* sample, 45 of which are in the *MJ* sample. The average properties of ALGs in the *XS* sample have been briefly described in § 4.4 and given that the *MJ* sample is a complete subset of the *XS* sample, ALGs in the *MJ* sample are representative of the ALGs in the *XS* sample. In order to compare these galaxies with the optical-emission-line classified NELGs, the following discussion is restricted in the 45 ALGs in the *MJ* sample unless stated otherwise.

ALGs make up 15.8% of the *MJ* sample and have a higher mean redshift (0.17) than NELGs (0.099). Compared with NELGs, ALGs are redder in $u - r$ colour. The mean concentration index $C_{90/50}$ of ALGs is 3.10, indicating their early-type morphologies (Strateva et al. 2001). On average ALGs have similar X-ray-to-optical flux ratios as SF galaxies, composite galaxies and unclassified NELGs, but lower than AGN. In both the soft (0.5–2 keV) and hard band (2–12 keV) band ALGs have the lowest mean fluxes compared with all NELG subsamples (classified or unclassified). Due to their higher, on average, redshifts, ALGs have the second highest mean luminosities in these two bands (surpassed by the unclassified NELGs in the soft band and by AGN in the hard band) and the highest in the total band (0.2–12 keV).

About 27% (12/45) of the ALGs have $L_{0.2-12\text{keV}} > 10^{42} \text{ erg s}^{-1}$, all have $-2 < \log(f_X/f_O) \leq -1$. Such galaxies might be members of X-ray Bright Optically Normal Galaxies (XBONGs; *e.g.*, Fiore et al. 2000; Comastri et al. 2002; Georgantopoulos & Georgakakis 2005; Caccianiga et al. 2007). Most of these sources are faint, with average fluxes of $4.45 \times 10^{-15} \text{ erg s}^{-1} \text{ cm}^{-2}$ in the soft band and $6.61 \times 10^{-15} \text{ erg s}^{-1} \text{ cm}^{-2}$ in the hard band. The highest detection likelihood in 2–4.5 keV band is only 5.8 (detection likelihood 6 corresponds to $\sim 3\sigma$), belonging to source 2XMM J134341.6+554253 (SRCID: 126189). This source has $L_{2-12\text{keV}} = 1.48 \times 10^{42} \text{ erg s}^{-1}$. The hardness ratios of this source are $\text{HR2} = -0.15 \pm 0.16$ and $\text{HR3} = -0.36 \pm 0.53$, which can be reproduced by an unabsorbed power-law model with $\Gamma \sim 1.7-2.2$. Therefore, it seems that an AGN provides the simplest explanation for the high X-ray luminosity and hard X-ray hardness ratios of this source. The reason why there was little AGN indication in the optical spectrum of this source might be that the AGN was outshone by the host galaxy in the optical band. For 2XMM J113317.1+530744 (SRCID: 96655), there are two *SDSS* objects

within $5''$ ($\sim 2\sigma$ of the X-ray positional uncertainty) from the X-ray position. The brighter object with $r = 17.11$ sits $4.3''$ from the X-ray position and was chosen as the optical counterpart. The fainter one with $r = 20.77$ lies slightly closer to the X-ray position ($4.1''$ from the X-ray position), however, no *SDSS* spectrum is available to investigate its nature. Note also that 2XMM J093619.1+612723 (SRCID: 75781) and 2XMM J130251.6+672519 (SRCID: 116139), both with $L_{0.2-12\text{keV}}$ of $< 10^{42}$ erg s^{-1} , were included in a XBONG sample studied by Georgantopoulos & Georgakakis (2005) but no clear AGN evidence was found by these authors.

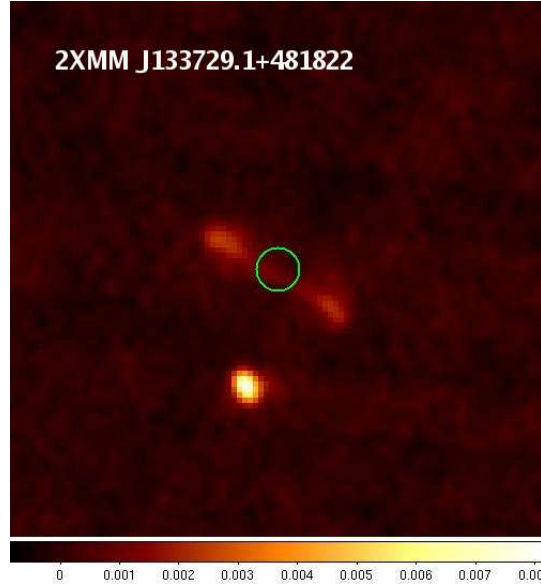


Figure 5.32: Radio image ($3' \times 3'$) of 2XMM J133729.1+481822 (SRCID: 124718) from the FIRST Survey. The overlaid region is centred at the X-ray position with radius of the 3σ X-ray positional uncertainty.

All but three of the 45 ALGs are in the area covered by the FIRST Survey (Becker et al. 2003) and five have matches within $7''$ from the X-ray positions. The FIRST counterpart of 2XMM J133729.1+481822 (SRCID: 124718) is a double-lobed radio galaxy (Figure 5.32), however, no clear bright radio core is detected at the X-ray position, which is also the centre of the radio galaxy. Therefore, the AGN, suggested by the double-lobed morphology, might be very weak or even quiescent at the time the radio observation was taken. The $f_{0.2-12\text{keV}}$ of the X-ray source is 3.60×10^{-15} $\text{erg s}^{-1} \text{cm}^{-2}$, corresponding to a luminosity of 1.33×10^{41} erg s^{-1} at a redshift of 0.119. The hardness ratios of this source are $\text{HR2} = -0.06 \pm 0.32$ and $\text{HR3} = -0.44 \pm 0.41$, which can be reproduced by an unabsorbed power-law model. Hence, the X-ray luminosity and hardness ratios of this galaxy seem to be consistent with emission from X-ray binaries, although a weak AGN cannot be ruled out.

5.6.2 X-ray Hardness Ratios

Around 16% (7/45) of the ALGs have undefined HR3 from the pn camera (five undetected above 1 keV and two outside the field-of-view of pn), therefore the combined hardness ratios (columns SC_HR2 and SC_HR3 in *2XMM*) were used to construct the hardness ratio density plots for ALGs. For *2XMM* J103401.2+584827 (SRCID: 85148), the HR3 was still undefined as it was not detected above 1 keV in the pn camera and the area in the two MOS cameras where it lies were not read out. This source has $L_{0.2-12\text{keV}} = 4.73 \times 10^{40} \text{ erg s}^{-1}$ and $\log(f_X/f_O) = -2.58$.

The hardness ratio (HR2 versus HR3) density plot of the other 44 ALGs is shown in Figure 5.33(a). The hardness ratios suggest that, for the majority of the ALGs, a thermal component contributes a significant fraction of the total X-ray emission from these galaxies, although the contribution from a power-law component is non-negligible. Divided by $\log(f_X/f_O)$, 16 ALGs have $\log(f_X/f_O) \leq -2$ and 28 have $-2 < \log(f_X/f_O) \leq -1$. The hardness ratio density plots of ALGs within these two bins are shown in Figure 5.33(b) and 5.33(c) respectively. For galaxies with $\log(f_X/f_O) \leq -2$, the peak of the hardness ratio density is consistent with a two-component model dominated by the thermal component. This suggests that the bulk of the X-ray emission of these galaxies come from hot gas. On the other hand, galaxies with $-2 < \log(f_X/f_O) \leq -1$ seem to have higher contributions from the non-thermal component, which might also be associated with absorption up to $\sim 10^{23} \text{ atoms cm}^{-2}$ in some cases. This indicates that at least in some ALGs with $-2 < \log(f_X/f_O) \leq -1$, AGN contamination cannot be ruled out.

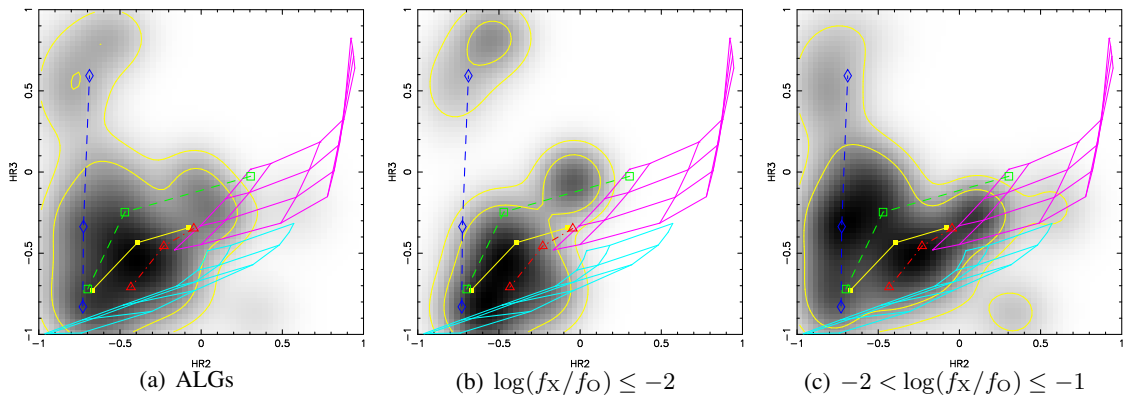


Figure 5.33: The smoothed X-ray hardness ratio (HR2 versus HR3) density plots for the ALG sub-sample (a) and its subsets in two X-ray-to-optical flux ratio bins: (b) $\log(f_X/f_O) \leq -2$ and (c) $-2 < \log(f_X/f_O) \leq -1$. Spectral models defined in § 2.4.4 are overlaid in each plot. Contours indicating 68% and 90% levels are also shown.

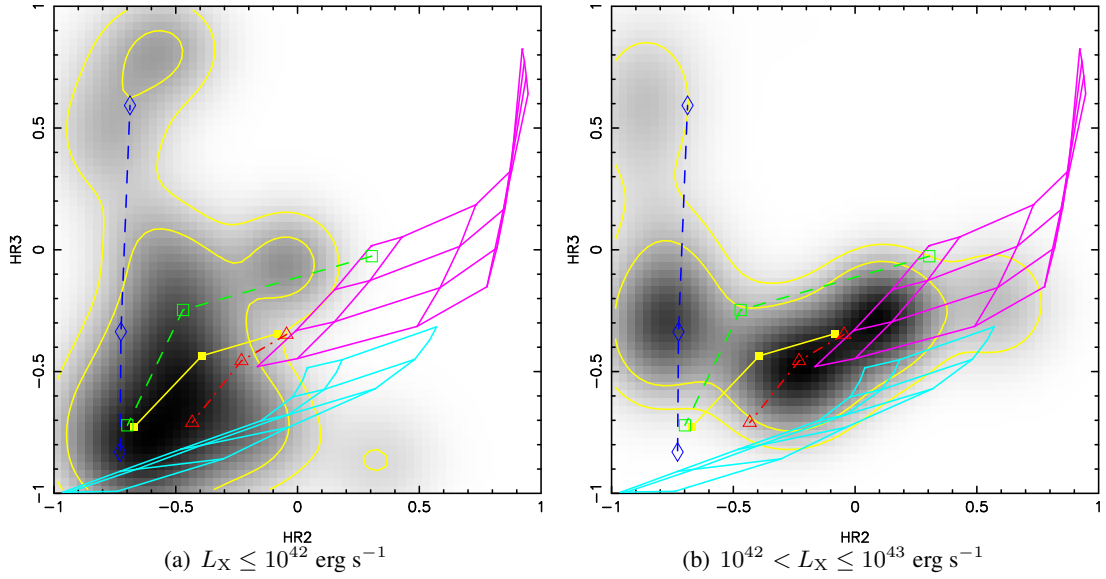


Figure 5.34: The smoothed X-ray hardness ratio (HR2 versus HR3) density plots for ALGs in two luminosity bins: (a) $L_X \leq 10^{42} \text{ erg s}^{-1}$ and (b) $10^{42} < L_X \leq 10^{43} \text{ erg s}^{-1}$. Spectral models defined in § 2.4.4 are overlaid in each plot. Contours at 68% and 90% levels are also shown.

The 44 ALGs were further divided on X-ray luminosities. Since there are only seven galaxies with $L_X < 10^{41} \text{ erg s}^{-1}$, these galaxies were put into the same bin as those with $10^{41} < L_X \leq 10^{42} \text{ erg s}^{-1}$. Therefore, the 44 ALGs were then plotted in two luminosity bins: 32 with $L_X \leq 10^{42} \text{ erg s}^{-1}$ (Figure 5.34(a)) and 12 with $10^{42} < L_X \leq 10^{43} \text{ erg s}^{-1}$ (Figure 5.34(b)). The X-ray emission from ALGs with $L_X \leq 10^{42} \text{ erg s}^{-1}$ seems to be dominated by thermal emission, although for a fraction of galaxies significant contributions are from an absorbed power-law component. On the other hand, ALGs with $10^{42} < L_X \leq 10^{43} \text{ erg s}^{-1}$ seem to have harder spectra than those with lower X-ray luminosities. The peak of the hardness ratio density of these ALGs is consistent with a two-component model dominated by a power-law component. Although typically X-ray binaries have power-law spectra, X-ray luminosities greater than $10^{42} \text{ erg s}^{-1}$ are difficult to explain by an X-ray binary origin. AGN contamination seems to be the simplest explanation. Hence, considering the whole ALG subsample, the X-ray emission has a thermal plus non-thermal origin: ALGs with low X-ray-to-optical ratios and/or low luminosities have higher proportions of their X-ray emission from the thermal component than galaxies with high X-ray-to-optical ratio and/or high luminosities.

5.6.3 X-ray Luminosities and Stellar Masses

Thirty-eight ALGs have stellar masses estimated in Kauffmann et al. (2003b). Their 0.2–12 keV X-ray luminosities are plotted against stellar mass in Figure 5.35. The X-ray luminosities have been corrected for the expected HMXB component (scaling with the SFR) using the L_X -SFR correlation from Colbert et al. (2004), but this component is small, contributing a median value of 2.5% of the total luminosities. For most of the ALGs the X-ray luminosities exceed the values predicted from X-ray binaries (*i.e.*, LMXBs; Colbert et al. 2004) (*i.e.*, assuming this scales with galaxy mass which in turn scales linearly with optical luminosity).

A least-square (bisector) fit to the data shown in Figure 5.35 yielded $\log L_X \text{ (erg s}^{-1}\text{)} = (20.26 \pm 1.78) + (1.89 \pm 0.16) \times \log M \text{ (M}_\odot\text{)}$. This non-linear correlation between X-ray luminosities and stellar masses broadly agrees with the correlations between X-ray luminosities and optical luminosities for early-type galaxies found by other authors: these non-linear correlations have been attributed to hot gas in these galaxies (*e.g.*, Fabbiano et al. 1992). Hornschemeier et al. (2005) found $L_X \propto M^{1.81}$ from 15 galaxies that were detected by *Chandra* and had absorption-line-dominated *SDSS* spectra (*i.e.*, similar spectra as those of the ALGs in this study). Using a large sample (~ 360) of early-type galaxies, O’Sullivan et al. (2001) obtained a correlation between X-ray luminosities and the *B* band luminosities: $L_X \propto L_B^{2.2}$. Assuming stellar mass-to-light ratio $M_*/L = 2$, the X-ray-mass correlation for the ALGs in this study is consistent with the result of O’Sullivan et al. (2001). Therefore, the results for the ALGs in the *MJ* sample are consistent with X-ray emission from these galaxies being dominated by hot gas.

5.7 Discussion

5.7.1 AGN in The *MJ* Sample

Early X-ray studies of normal galaxies based on *Einstein* data showed that galaxies with X-ray-to-optical flux ratios $\log(f_X/f_O) \leq -2$ were mainly normal galaxies while quasars usually had $\log(f_X/f_O) > -1$ (*e.g.*, Maccacaro et al. 1988). However normal galaxies with $\log(f_X/f_O) > -2$ and AGN with $\log(f_X/f_O) \leq -1$ are less well studied. On the other hand, although an X-ray luminosity above 10^{42} erg s⁻¹ has been widely used as an indicator of AGN, LLAGN can have an X-ray luminosity as low as

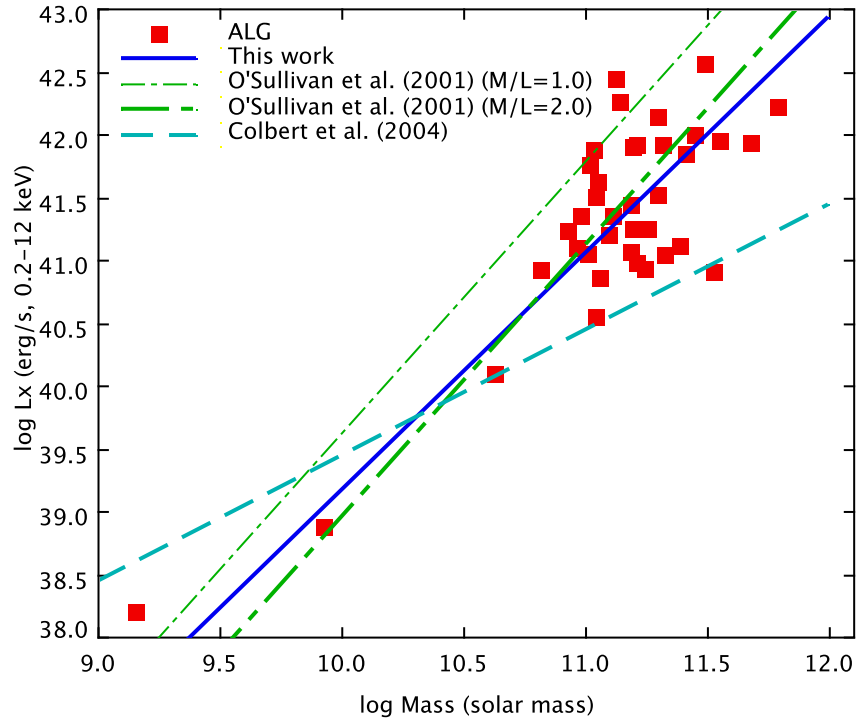


Figure 5.35: The 0.2–12 keV X-ray luminosities are shown against the dust-corrected stellar masses from Kauffmann et al. (2003b, the median of the probability distributions) for 38 ALGs. The contributions from SF activities to the 0.2–12 keV luminosities have been subtracted from the X-ray luminosities using the correlation from Colbert et al. (2004) and the SFRs estimated in Brinchmann et al. (2004). To be consistent with the SFRs used in Colbert et al. (2004), the SFRs used here have been multiplied by 1.5 to account for the IMF difference (Brinchmann et al. 2004) and then multiplied by 1.4 to account for the bolometric correction applied in Colbert et al. (2004). The blue solid line indicates the least square (bisector) fit to the data. The L_X - L_B correlation from O’Sullivan et al. (2001) has been converted to L_X -Mass assuming the stellar mass-to-light ratio $M_*/L = 1$ and 2. The correlation between X-ray luminosities and stellar masses in Colbert et al. (2004) is also shown.

$10^{38} \text{ erg s}^{-1}$ (e.g., Ho 2008). In order to investigate how a ‘normal galaxy sample’ selected using X-ray-to-optical flux ratio and X-ray luminosity is affected by these two parameters, the *MJ* sample was divided into five bins: $-2 < \log(f_X/f_O) \leq -1$ and $10^{42} < L_X \leq 10^{43} \text{ erg s}^{-1}$, $-2 < \log(f_X/f_O) \leq -1$ and $10^{41} < L_X \leq 10^{42} \text{ erg s}^{-1}$, $-2 < \log(f_X/f_O) \leq -1$ and $L_X \leq 10^{41} \text{ erg s}^{-1}$, $\log(f_X/f_O) \leq -2$ and $10^{41} < L_X \leq 10^{42} \text{ erg s}^{-1}$, and $\log(f_X/f_O) \leq -2$ and $L_X \leq 10^{41} \text{ erg s}^{-1}$. There is no galaxy in the whole *MJ* sample with $\log(f_X/f_O) \leq -2$ and $L_X > 10^{42} \text{ erg s}^{-1}$.

In order to investigate the fraction of the AGN population in different X-ray-to-optical flux ratio and X-ray luminosity bins of the *MJ* sample, Figure 5.36 is produced. The AGN fraction increases with X-

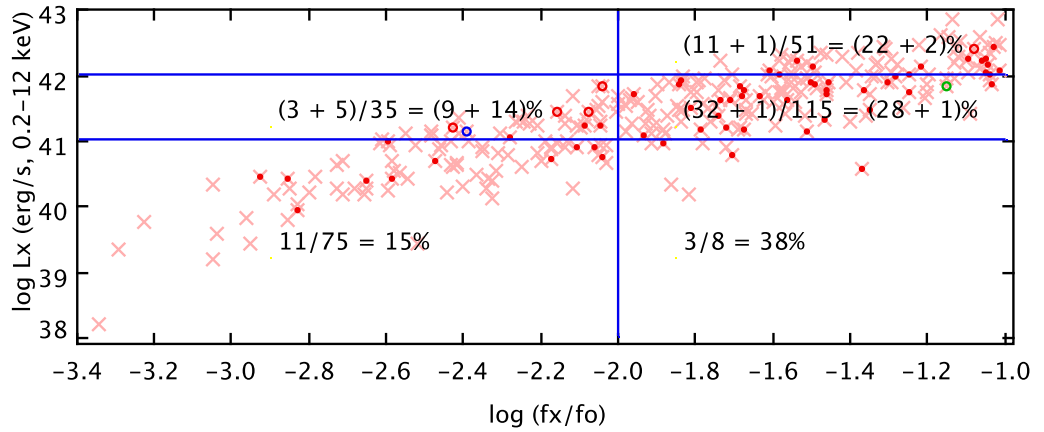


Figure 5.36: The whole *MJ* sample is marked as pink crosses. The optical emission line ratio classified AGN are marked with red dots. The NLS 1 galaxy is marked with green open circle. Five double-lobed radio galaxies found among the unclassified NELGs are marked with red open circles. One double-lobed radio galaxy found among the ALGs is marked with blue open circle. The fraction of AGN, calculated as the number of optical emission line classified AGN divided by the number of galaxies in a given bin (defined by both the X-ray-to-optical flux ratio and the X-ray luminosity) is also given in the plot; the second number or percentage given inside the brackets corresponds to the NLS 1 galaxy or the radio galaxies.

ray-to-optical flux ratio, but seems to be significant in all bins. For galaxies with X-ray-to-optical flux ratios between -2 and -1 the optical emission line classification seems to quite robustly separate AGN from truly normal galaxies. Other methods (*e.g.*, emission line width ratio or radio morphology here) only added two more possible AGN. However, for galaxies with X-ray-to-optical flux ratio below -2 , AGN missed by the optical emission line classification increase. On the other hand, the AGN fraction decreases with X-ray luminosity, suggesting that X-ray luminosity might be a less robust parameter for separating AGN from normal galaxies unless the classification scheme used here missed far more hidden AGN in the high X-ray luminosity bin. This possibility can be seen in galaxies with $\log(f_x/f_o) \leq -2$, among which possible AGN indicated by radio morphologies outnumber those classified by optical emission lines in the higher X-ray luminosity bin, while no such radio galaxy is found in the lower X-ray luminosity bin.

The fractions of the *MJ* sample that belong to different subsamples are presented in a cumulative manner in Table 5.4. Again the AGN fractions increase with X-ray-to-optical flux ratios regardless of the X-ray luminosity cut-off. The AGN fractions are less sensitive to the X-ray luminosity cut-off, *i.e.*, they do not change much as long as the X-ray-to-optical flux ratio cut-off has been imposed.

$f_{\text{subsample}}$	$\log(\frac{f_X}{f_O}) \leq -2$	$\log(\frac{f_X}{f_O}) \leq -1$
$\log L_X \leq 10^{41} \text{ erg s}^{-1}$	AGN (15 ± 4)%	AGN (17 ± 5)%
	SF (32 ± 7)%	SF (33 ± 6)%
	COM (21 ± 5)%	COM (22 ± 5)%
	UNC (23 ± 5)%	UNC (20 ± 5)%
	ALG (9 ± 4)%	ALG (8 ± 3)%
$\log L_X \leq 10^{42} \text{ erg s}^{-1}$	AGN (13 ± 3)% (+5%)*	AGN (21 ± 3)% (+3%) [†]
	SF (25 ± 5)% *	SF (24 ± 3)% (-0.4%) [†]
	COM (18 ± 4)% *	COM (19 ± 3)%
	UNC (29 ± 5)% (-4%)*	UNC (21 ± 3)% (-2%) [†]
	ALG (15 ± 4)% (-1%)*	ALG (14 ± 2)% (-0.4%) [†]
$\log L_X \leq 10^{43} \text{ erg s}^{-1}$	AGN (13 ± 3)% (+5%)*	AGN (21 ± 3)% (+2%) [‡]
	SF (25 ± 5)% *	SF (22 ± 3)% (-0.4%) [‡]
	COM (18 ± 4)% *	COM (17 ± 2)%
	UNC (29 ± 5)% (-4%)*	UNC (24 ± 3)% (-2%) [‡]
	ALG (15 ± 4)% (-1%)*	ALG (16 ± 2)% (-0.4%) [‡]

Table 5.4: The fractions that each type of galaxies possess in different MJ subsets defined by different X-ray-to-optical flux ratio cut-off and X-ray luminosity cut-off. “SF” denote SF galaxies. “COM” denote composite galaxies. “UNC” denote unclassified NELGs. The 1σ uncertainties are calculated assuming AGN follow Poisson distribution in each subset. * The +5% in brackets includes four double-lobed radio galaxies among unclassified NELGs (the -4% in the bracket) and one among ALGs (the -1% in the bracket); increasing the luminosity from $L_X \leq 10^{42} \text{ erg s}^{-1}$ to $L_X \leq 10^{43} \text{ erg s}^{-1}$ does not include any additional galaxies with $\log(f_X/f_O) \leq -2$ and therefore the values before and after including another bin are identical. † The +3% in the brackets for AGN includes the NLS 1 galaxy identified among SF galaxies (the -0.4% in brackets) and the five double-lobed radio galaxies (the -2% and -0.4% in the brackets following unclassified NELGs and ALGs respectively). ‡ The +2% in the brackets for AGN is calculated from the NLS 1 galaxy (the -0.4% in the brackets following SF galaxies) and six double-lobed radio galaxies (the -2% and -0.4% in the brackets following unclassified NELGs and ALGs).

There is a slight drop in the SF galaxy fraction when the X-ray luminosity cut-off increases. The ALG fractions increase with X-ray luminosity, suggesting that X-ray luminosity cut-off selects against luminous ALGs.

In order to estimate the AGN fraction in a flux limited galaxy sample, a subsample was selected from MJ to have *SDSS* r band Petrosian magnitude brighter than 17.77, the flux limit of the Main Galaxy Sample (Strauss et al. 2002). This optical magnitude cut-off translates to $f_{0.2-12\text{keV}} \gtrsim 2.5 \times 10^{-14} \text{ erg s}^{-1} \text{ cm}^{-2}$, which is also approximately the flux limit in *2XMM* at $\sim 90\%$ sky coverage. This flux limited subsample only includes 56 galaxies. It seems that at these fluxes the AGN contamination is significant in the galaxy population with $-2 < \log(f_X/f_O) \leq -1$ as AGN make up $\gtrsim 50\%$ of all three luminosity bins (Figure 5.37). Due to the small numbers of galaxies in all bins, the uncertainties of the

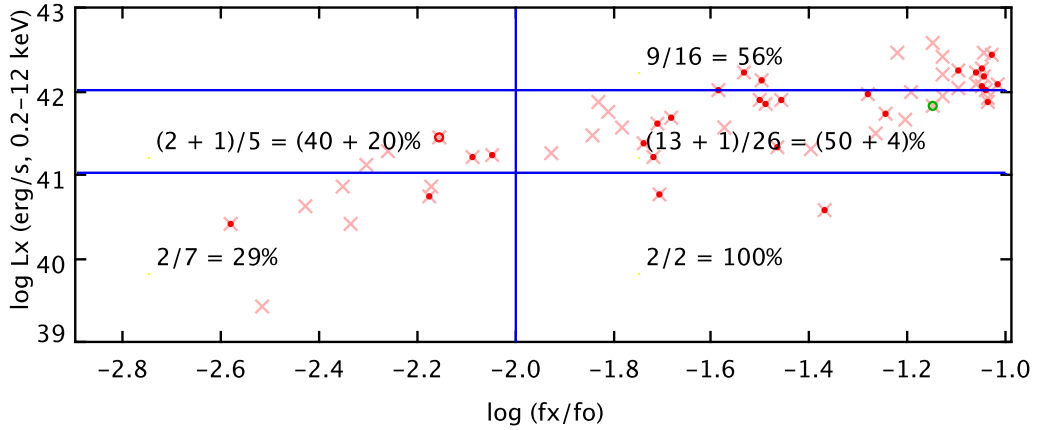


Figure 5.37: The flux limited subsample from *MJ* (*SDSS* *r* band Petrosian magnitude brighter than 17.77, the flux limit of the Main Galaxy Sample Strauss et al. 2002) is marked with pink crosses. The optical emission line ratio classified AGN are marked using red dots. The NLS 1 galaxy is marked with green open circle. The double-lobed radio galaxy found among unclassified NELGs is marked with red open circle. The fraction of AGN, calculated as the number of optical emission line classified AGN divided by the number of galaxies in a given bin (defined by both X-ray-to-optical flux ratio and X-ray luminosity) is also given in the plot; the second number or percentage given inside the brackets corresponds to the NLS 1 galaxy or the radio galaxy.

AGN fraction are so large that the differences between these fractions are not statistically significant (Table 5.5). This suggests that in order to address the galaxy populations with $\log(f_X/f_O) \leq -1$ and $L_X < 10^{43}$ erg s $^{-1}$ more accurately, a flux limited sample with significant number of galaxies is needed.

5.7.2 Mean X-ray Hardness Ratios

The 0.2–10 keV spectra of AGN are generally continuum dominated and can be well described by a power-law with typical photon index ~ 1.8 – 2.0 ; this power law component can be subjected to intrinsic obscuration up to $\sim 10^{24}$ atoms cm $^{-2}$ (see § 1.3.2). The X-ray emission of normal galaxies is believed to be dominated by X-ray binaries and hot ISM. The spectra of X-ray binaries can be described by a power law with photon index $\Gamma \sim 1$ – 2 (e.g., Irwin et al. 2003; Grimm et al. 2007). On the other hand the hot ISM mainly contributes to the soft band and rarely has a temperature above 1 keV (see § 1.3.5 and § 1.3.6). If a galaxy also hosts a LLAGN, then the AGN can contribute substantially

f_{AGN}	$\log(\frac{f_X}{f_O}) \leq -2$	$\log(\frac{f_X}{f_O}) \leq -1$
$\log L_X \leq 10^{41} \text{ erg s}^{-1}$	$(29 \pm 20)\%$	$(44 \pm 22)\%$
$\log L_X \leq 10^{42} \text{ erg s}^{-1}$	$(33 \pm 17)\% (+8\%)*$	$(48 \pm 11)\% (+5\%)\dagger$
$\log L_X \leq 10^{43} \text{ erg s}^{-1}$	$(33 \pm 17)\% (+8\%)*$	$(50 \pm 9)\% (+4\%)\ddagger$

Table 5.5: The fraction of AGN in the flux limited subsample of *MJ*. The 1σ uncertainties are calculated assuming AGN follow Poisson distribution in each subset. * The +8% in brackets includes one two-lobed radio galaxy among unclassified NELGs; increasing the luminosity from $L_X \leq 10^{42} \text{ erg s}^{-1}$ to $L_X \leq 10^{43} \text{ erg s}^{-1}$ does not include any additional galaxies with $\log(f_X/f_O) \leq -2$ and therefore the values before and after including another bin are identical. † The +5% in brackets includes the five double-lobed radio galaxies and the NLS 1 galaxy identified among SF galaxies. ‡ The +4% in brackets includes six double-lobed radio galaxies and the NLS 1 galaxy.

to the hard band ($\gtrsim 2 \text{ keV}$). The X-ray spectra suggested by hardness ratios (HR2 and HR3) of the *MJ* subsamples (AGN, SF galaxies, composite galaxies, the unclassified NELGs, and the ALGs) are generally consistent with the above expectations (see § 5.2.2, § 5.3.3, § 5.4, § 5.5.1, and § 5.6.2). It has also been shown in these sections that the hardness ratios of sources with different X-ray-to-optical flux ratios and/or X-ray luminosities often display different patterns. In order to gain insight of the underlying spectra of sources within different subsamples and with different X-ray-to-optical flux ratios and different X-ray luminosities, the error weighted mean hardness ratios were calculated for the subsamples in five bins: $-2 < \log(f_X/f_O) \leq -1$ and $10^{42} < L_X \leq 10^{43} \text{ erg s}^{-1}$, $-2 < \log(f_X/f_O) \leq -1$ and $10^{41} < L_X \leq 10^{42} \text{ erg s}^{-1}$, $-2 < \log(f_X/f_O) \leq -1$ and $L_X \leq 10^{41} \text{ erg s}^{-1}$, $\log(f_X/f_O) \leq -2$ and $10^{41} < L_X \leq 10^{42} \text{ erg s}^{-1}$, and $\log(f_X/f_O) \leq -2$ and $L_X \leq 10^{41} \text{ erg s}^{-1}$. These mean hardness ratios and their standard deviations are shown in Figure 5.38.

It appears that in most bins the mean hardness ratios of different subsamples are consistent with two-component models, which is expected for normal galaxies. There is no clear cut in the mean hardness ratios between AGN and either SF galaxies or composite galaxies, which means that using hardness ratios to select against AGN might cause a loss of SF galaxies. The unclassified NELGs and the ALGs tend to have softer spectra than AGN, SF galaxies and composite galaxies. In almost all bins the unclassified NELGs and the ALGs have mean HR2 $\lesssim -0.3$, while for AGN, only those with $\log(f_X/f_O) \leq -2$ and $L_X \leq 10^{41} \text{ erg s}^{-1}$ have such a low mean hardness ratio. AGN, SF galaxies and composite galaxies with $-2 < \log(f_X/f_O) \leq -1$ have mean HR2 > -0.1 regardless of the X-ray luminosity range. This implies that the hot ISM contributes significantly to the X-ray emission from the unclassified NELGs and the ALGs although it is still difficult to make a hard division between these galaxies and the classified NELGs (*i.e.*, AGN, SF galaxies or composite galaxies) due to the large scatter (represented as the standard deviations in the plots) using the mean hardness ratios.

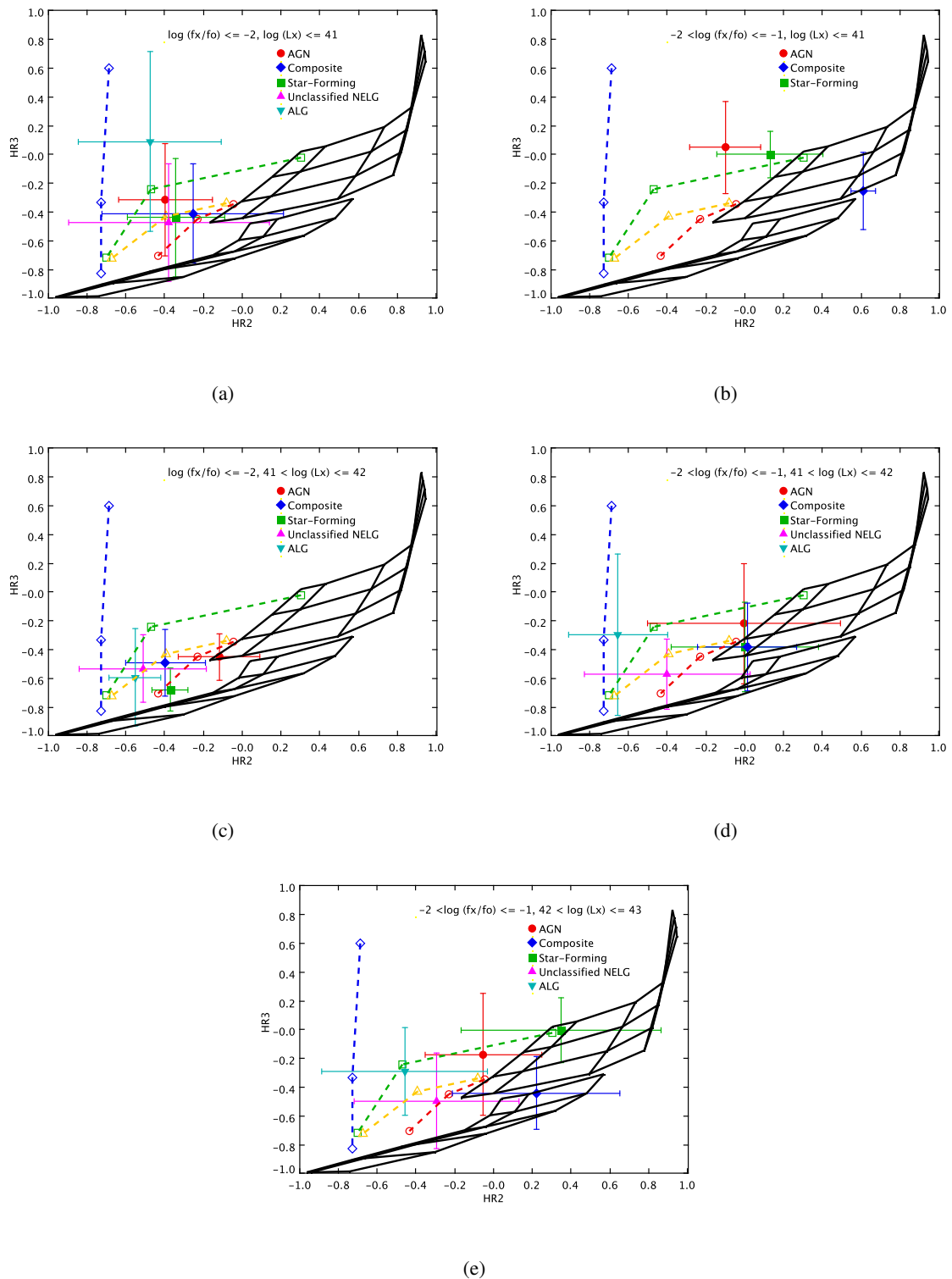


Figure 5.38: The error weighted mean X-ray hardness ratios of the five *MJ* subsamples (AGN, SF galaxies, composite galaxies, unclassified NELGs, and ALGs) are shown in five bins. Spectral models defined in § 2.4.4 are overlaid in each plot.

The X-ray spectra of AGN seem to become harder with the X-ray-to-optical flux ratios, which is consistent with the expectation that galaxies with high X-ray-to-optical flux ratios are likely to host AGN. The trend that spectra become harder with the X-ray-to-optical flux ratios is also seen in SF galaxies and composite galaxies. AGN contamination seems to be the simplest explanation for this trend in these galaxies.

5.7.3 Comparison with Normal Galaxies from XWAS

The *2dF* sample, presented in Chapter 3, can be used directly to compare with the *MJ* sample since these two samples were constructed using almost the same selection criteria. As seen from Table 3.1 and Table 5.1, the NELG fraction in the *2dF* sample ($\sim 54\%$) is lower than the one in the *MJ* sample ($\sim 84\%$). One possible reason of this discrepancy might be due to the fainter spectroscopic limit of the *2dF* spectra ($R \lesssim 21$) compared with the *SDSS* main galaxy sample ($r \lesssim 17.77$; Strauss et al. 2002). Around 28% (20/72) of the *2dF* sample have $R > 17.77$, among which 60% are NELGs, therefore the inclusion of sources fainter in the optical does not seem to be able to explain the lower fraction of NELGs in the *2dF* sample as a whole. Another possible reason for this discrepancy might lie in the quality of the spectra, as weak emission line(s) detected in spectra with high signal-to-noise ratios might not be detected in those with lower signal-to-noise ratio. Among NELGs, the fractions of all the classified subsamples (*i.e.*, AGN, SF galaxies, and composite galaxies) and the unclassified subsample are consistent within uncertainties in the two surveys. The overall lower fractions of these different subsamples in the *2dF* sample compared with the *MJ* sample are mainly due the lower fraction of galaxies for which emission line(s) could be detected.

5.7.4 Comparison with Normal Galaxies from Other Surveys

The X-ray-to-optical flux ratio definitions and cut-offs used in many surveys to select normal galaxies are based on that used for the EMSS (Maccacaro et al. 1988; Gioia et al. 1990; Stocke et al. 1991) which was based on 0.3–3.5 keV fluxes and Johnson *V* band magnitudes. Assuming a power-law with $\Gamma = 1.7$, the Galactic absorption of 3×10^{20} atoms cm^{-2} and $V - r = 0.2$ (Kim et al. 2006), the $\log(f_X/f_O) \leq -2$ cut-off for normal galaxies in the EMSS is equivalent to $\log(f_X/f_O) \leq -1.7$ when 0.2–12 keV flux and *r* magnitude are used (Equation 4.1). Selecting a subsample from the *MJ*

sample with $\log(f_X/f_O) \leq -1.7$ gives 166 galaxies, of which $\sim 81.3\%$ are NELGs ($\sim 15.7\%$ being AGN, $\sim 22.9\%$ being SF galaxies, $\sim 17.5\%$ being composite galaxies, and the rest $\sim 25.3\%$ being unclassified). Conversely, the $\log(f_X/f_O) \leq -1$ cut-off used in this thesis is equivalent to $\log(f_X/f_O) \leq -1.3$ in the EMSS form. In the following comparison whenever the X-ray-to-optical flux ratio is converted from another energy band to 0.2–12 keV, a power-law with $\Gamma = 1.7$ and the Galactic absorption of 3×10^{20} atoms cm^{-2} are assumed. The differences in $\log(f_X/f_O)$ caused by assuming power-laws with $\Gamma = 1.8$ and 2.0 (as used in Georgakakis et al. 2004b; Georgantopoulos et al. 2005; Georgakakis et al. 2006; Tzanavaris et al. 2006 and Hornschemeier et al. 2003a) to convert definitions in the 0.3–3.5 keV band to the 0.2–12 keV band are $\sim 5\%$ and $\sim 13\%$, respectively.

Georgantopoulos et al. (2005) found 28 galaxies using an X-ray-to-optical flux ratio cut-off equivalent to that used in the EMSS and soft X-ray spectra (hardness ratios < 0) in the $\sim 11 \text{ deg}^2$ NHS. Twenty-three out of the 28 galaxies had *SDSS* spectra, 14 of which were NELGs. The fraction of NELGs is consistent with the *MJ* sample within the uncertainties. None of these 14 NELGs turned out to be AGN. The AGN fraction in the *MJ* sample at the equivalent X-ray-to-optical flux ratio cut-off ($\log(f_X/f_O) < -1.7$) is $\sim 16\%$, which translates to $\sim 3\text{--}4$ AGN expected in a sample with size of 23. Note that the selection criteria in NHS included a restriction in hardness ratio which rejected three galaxies. If the NHS sample were selected without the hardness ratio cut-off and if all these three galaxies were AGN, the AGN fraction in NHS and the *MJ* sample are consistent. These authors did not distinguish SF galaxies and composite galaxies, the latter being a mixture of AGN and SF galaxies (Kewley et al. 2006).

A sample of 28 galaxies was selected by Georgakakis et al. (2006), using an X-ray-to-optical flux ratio cut-off equivalent to that used in the EMSS, from the *1XMM* catalogue cross-correlated with USNO-A.0. The breakdown of different types of the 26 galaxies with spectra were: AGN ($\sim 19\%$), SF (and composite) galaxies ($\sim 35\%$) and ALGs ($\sim 46\%$). Assuming in this sample, galaxies with weak lines were grouped into the ALG subsample rather than the unclassified NELGs as in the *MJ* sample, the breakdowns of this sample and the *MJ* sample seem to be consistent.

Kim et al. (2006) selected 36 galaxies from ChaMP as normal galaxies based on X-ray-to-optical cut-off converted from the one used in EMSS, of which $\sim 56\%$ (20/36) were NELGs. This NELG fraction is lower than that calculated from the *MJ* sample ($\sim 81\%$), probably due to the poorer resolution of the optical spectra ($\sim 2.4\text{--}13.5 \text{ \AA}$; Green et al. 2004) compared with those from *SDSS* ($\sim 2\text{--}4 \text{ \AA}$).

Another sample which can be directly compared with the *MJ* sample is that selected by Hornschemeier et al. (2005) using *Chandra* archival data cross-correlated with *SDSS*. Around 36% of the sample were ALGs. This higher ALG fraction compared to that of the *MJ* sample ($\sim 16\%$) might be due to the fact that there was no X-ray-to-optical flux ratio restriction in this sample.

Tzanavaris et al. (2006) compiled a galaxy sample from two X-ray datasets (*1XMM* and *XAssist*) cross-correlated with *2dFGRS*. Neither X-ray-to-optical flux ratio or X-ray luminosity was used as a selection criterion. The breakdown of this 38-galaxy sample was $\sim 29\%$ AGN (including LINERs), $\sim 21\%$ SF galaxies, $\sim 29\%$ ALGs, and the rest $\sim 21\%$ had featureless or unclassifiable *2dF* spectra. Applying the -1.3 equivalent cut-off to the X-ray-to-optical flux ratios provided in Tzanavaris et al. (2006) gave a subsample of 23 galaxies, of which $\sim 17\%$ were AGN, $\sim 30\%$ were SF galaxies, $\sim 43\%$ were ALGs, and the rest had featureless or unclassifiable spectra. These fractions broadly agree with those of the *MJ* sample.

Using the *Chandra* Deep Field North Survey data, which reached $\approx 2.5 \times 10^{-17}$ erg s $^{-1}$ cm $^{-2}$ in the 0.5–2 keV band (Alexander et al. 2003), Hornschemeier et al. (2003a) selected a sample of 43 sources. The X-ray-to-optical flux ratio cut-off -2.3 using the 0.5–2 keV band is equivalent to -1.7 in the 0.2–12 keV band. X-ray hardness ratios were used to exclude sources with hard spectra. Thirty-six out of the 43 sources turned out to be galaxies based on their optical spectra, of which 75% (27/36) showed emission line(s). This fraction is lower but consistent, within uncertainty, with the NELG fraction in the *MJ* subsample with equivalent $\log(f_X/f_O)$ cut-off. Based on X-ray luminosities these authors argued that about one third of their galaxy sample might host LLAGN and/or starburst. Considering the fractions of AGN, composite galaxies and SF galaxies together, the AGN/starburst fraction in this sample is lower than that of the *MJ* sample, which might be an effect of the hardness ratio cut-off which was used in their sample to minimise AGN contamination.

5.8 Chapter Summary

In this chapter detailed studies of the *MJ* sample, which contains 284 X-ray normal galaxies candidates, was presented along with a comparison with the pilot study of the *2dF* sample in Chapter 3 and normal galaxy samples in the literature. The main findings are:

1. Based on *SDSS* spectra and BPT plots, 21% of the *MJ* sample are AGN, 22% are SF galaxies, 17% are composite galaxies, 24% are unclassified NELGs and the remaining 16% are ALGs. The X-ray properties of these different subsamples are broadly consistent with their optical classifications.
2. For the AGN, on the basis of their X-ray spectra and hardness ratios, a power-law component appears to dominate the X-ray emission, although a non-negligible thermal component is also suggested. Loose correlations between hard X-ray luminosities and $H\alpha$ and [O III] line luminosities have been found in the AGN subsample. For some cases, these correlations are consistent with only modest absorption, which suggest that the non-detection of broad line(s) in these AGN might be due to intrinsic weakness of the BLR rather than high obscuration; for the rest of the subsample intrinsic absorption up to a few 10^{24} atoms cm^{-2} is suggested. The AGN subsample was further classified into Seyfert 2 galaxies and LINER 2s. The X-ray properties for the Seyfert 2 galaxies are consistent with typical Type 2 AGN. However the X-ray hardness ratios, $L_X-L_{H\alpha}$ and $L_X-L_{[\text{OIII}]}$ of LINER 2s suggest low absorption in these objects, reinforcing the possibility of intrinsically weak broad lines in these systems.
3. A tight correlation between soft X-ray luminosity and SFR has been found in the SF subsample. Such a correlation can provide an independent estimate of SFR which is supplemental to the conventional estimates from the radio and/or infrared bands. Compared with the $L_{0.5-2\text{keV}}$ -SFR, the $L_{2-12\text{keV}}$ -SFR is less well constrained and suggests that the hard X-ray emission might be contaminated by a weak AGN whose emission lines in the optical bands have been masked by the SF activity. The possibility of AGN contamination is reinforced by the fact that 10% of this subsample have L_X above 10^{42} erg s^{-1} , which is difficult to explain by stellar processes.
4. Composite galaxies, as the class name implies, are believed to have both AGN and SF activities. The optical morphologies and X-ray properties are consistent with their optical classifications.
5. For the unclassified NELGs, the optical morphologies indicate that they are early-type galaxies. The X-ray hardness ratios suggest that a thermal component, representing the hot ISM, tends to dominate the X-ray emission from these galaxies, although five of them are found to be double-lobed radio galaxies with bright cores indicating AGN presence.
6. ALGs in the *MJ* sample are predominately early-type galaxies and have X-ray hardness ratios consistent with a thermal model, which suggests a gas origin for their X-ray emission. This is

reinforced by the fact that the X-ray luminosities of these galaxies are generally greater than the prediction from stellar mass. This X-ray excess can be attributed to hot gas in these galaxies, as suggested in the earlier studies. One of the ALGs is found to be a double-lobed radio galaxy with faint core in FIRST, suggesting that an AGN was present in this galaxy but might be much weaker or even turned off at the time the radio observation was taken.

7. Compared with the *2dF* sample, the better quality optical spectra and more sophisticated emission line measurements available for *MJ* leads to higher percentage of NELGs and classified NELGs.
8. Investigation of how the parameters used as selection function, the X-ray-to-optical flux ratio and X-ray luminosity affect the sample content and comparison between *MJ* and normal galaxy samples in the literatures suggest that the X-ray-to-optical flux ratio is very efficient in selecting against AGN in that changing $\log(f_X/f_O)$ from -1 to -2 can reduce the AGN proportion from $\sim 21\%$ to $\sim 13\%$ although at the cost of losing truly normal galaxies which are relatively bright in the X-ray compared with optical waveband. On the other hand, the X-ray luminosity cut-off seems to select against luminous ALGs: the ALG fraction falls from $\sim 16\%$ to $\sim 8\%$ when the X-ray luminosity cut-off reduces from 10^{43} erg s $^{-1}$ to 10^{41} erg s $^{-1}$. The comparison also suggests that in order to separate AGN from truly normal galaxies, good quality optical spectra and robust star light subtraction are crucial, particularly due to the similarity in X-ray hardness ratios between SF galaxies and galaxies with weak AGN.

There are a few limitations in this study of the *MJ* sample. The non-uniform flux limits of the X-ray pointings, which are unavoidable in serendipitous surveys, cause unknown incompleteness to the sample. Around 43% (123/284) of the sample have detection likelihood below 15 (equivalent to $\sim 5\sigma$ significance); the inclusion of sources with low detection significance introduces significant uncertainties in the average properties of the sample. Due to the modest angular resolution of *XMM-Newton*, it is difficult to distinguish extended X-ray emission from single galaxies and that associated with clusters of galaxies. Therefore, the rejection of extended X-ray sources from the sample, although minimizing the potential contamination from clusters, caused a loss of truly normal galaxies with extended X-ray morphologies. A small fraction of the galaxies that satisfied the target selection for *SDSS* spectroscopic observations were not observed because fibres could not be placed closer than $55''$ (see § 4.2). Nearby normal galaxies were also effectively missed in the sample as they were resolved by *SDSS* and would

not appear as single objects in the *SDSS* images.

Chapter 6

Summary and Future Directions

In this thesis two samples of normal galaxies selected from *XMM-Newton* serendipitous surveys have been presented and discussed. This chapter provides a brief summary of the results from these two studies. Future work that can be performed to improve the current studies of normal galaxies are also described.

6.1 Summary

Chapter 3 presented a sample of 72 normal galaxy candidates, the *2dF* sample, which was selected from XWAS based on X-ray-to-optical flux ratios, X-ray luminosities and optical spectra. The *2dF* sample contained ALGs (45.8%) and NELGs (54.2%). Using the optical emission line ratios the NELGs were classified into four subsamples: AGN (11.1%), SF galaxies (9.7%), composite galaxies (12.5%), and unclassified NELGs (20.8%). For each of these NELG and ALG subsamples, the average X-ray properties were discussed based on their X-ray spectra and hardness ratios.

In Chapter 4, the *2XMM* catalogue was used to cross-correlate with *SDSS*, yielding a sample of 463 normal galaxy candidates, the *XS* sample. A 284-galaxy subset, the *MJ* sample, was presented in Chapter 5. NELGs made up 84.2% of the *MJ* sample, leaving the remaining 15.8% as ALGs. The NELGs were also classified into four subsamples based on their optical emission lines: AGN (21.1%), SF galaxies (21.8%), composite galaxies (16.9%), and unclassified NELGs (24.3%). Detailed discussions

of the average X-ray properties of the ALG subsample as well as all the NELG subsamples were also offered in Chapter 5. The aims listed in § 1.5 that have been addressed throughout these chapters are:

- The *MJ* sample contains a sufficient number of normal galaxy candidates to allow subsets with different X-ray-to-optical flux ratios and/or X-ray luminosities to be selected in order to test the effectiveness of these two parameters in selecting truly normal galaxies. The X-ray-to-optical flux ratio was found to be an efficient discriminator to identify AGN: changing $\log(f_X/f_O)$ from -1 to -2 reduced the AGN fraction from $\sim 21\%$ to $\sim 13\%$ although unrecognised AGN might still be present amongst the other NELGs. On the other hand, selecting galaxies with low X-ray luminosity was found to select against luminous ALGs: changing the X-ray luminosity cut-off from 10^{43} erg s $^{-1}$ to 10^{41} erg s $^{-1}$ reduced the ALG fraction from $\sim 16\%$ to $\sim 8\%$. From the point of view of X-ray hardness ratios, the large scatter in each subsample and the large overlaps between these subsamples suggested that using hardness ratios to select against AGN would also cause a loss of truly normal galaxies. Comparison between the *MJ* sample and the *2dF* sample, as well as previous studies, also demonstrated that optical spectra played a crucial role in separating AGN from truly normal galaxies: weak AGN might only reveal themselves in optical spectra with sufficient signal-to-noise ratios.
- In both the *2dF* sample and the *MJ* sample, spectral analysis of bright sources together with X-ray-hardness-ratio analysis suggested that the origin of the X-ray emission from different types of galaxies was broadly consistent with their optical classifications: a power-law component dominates the X-ray emission of AGN; hot ISM, related to the SF activity, contributes a large fraction of the X-ray emission from SF galaxies; the X-ray emission from composite galaxies has significant contributions from both thermal and non-thermal components; the unclassified NELGs have complex underlying X-ray spectra in which a thermal component, representing the hot gas in galaxies, tends to dominate, although a non-thermal component, probably related to hidden AGN, is non-negligible; the X-ray emission from ALGs predominantly has gas origin.
- The AGN in the *MJ* sample were found typically to have only modest obscuration, which suggested that the non-detection of broad emission line(s) in their optical spectra might be due to an intrinsically weak BLR. Particularly, among these AGN, LINER 2s tended to have lower X-ray obscuration than Seyfert 2 galaxies.
- For SF galaxies in the *MJ* sample, a tight correlation between soft X-ray (0.5–2 keV) luminosities

and SFRs was found which suggested that soft X-ray luminosities could be used as a SFR proxy to provide a SFR estimate supplemental to conventional estimates from the radio and/or infrared bands. However, hard X-ray (2–12 keV) luminosities of SF galaxies did not correlate well with SFRs; this was attributed to AGN contamination in the hard band.

- For ALGs in both the *2dF* sample and the *MJ* sample, thermal emission was suggested as the dominant component of their X-ray emission based on the X-ray spectra and hardness ratios. For ALGs in *MJ*, the X-ray luminosities were found to exceed the predictions from LMXB alone. The non-linear correlation found ($L_X \propto M_*^{1.89 \pm 0.16}$) was consistent with the hypothesis that hot gas dominated the X-ray emission of these galaxies.

6.2 Future Prospects

Although the work presented in this thesis has benefited from the rich data from large *XMM-Newton* serendipitous surveys and optical surveys, there are still a few aspects that could be improved with existing instrumentation and with future missions:

- A comparison of the *MJ* sample and the *2dF* sample, as well as earlier work which also used optical spectra to separate AGN and truly normal galaxies emphasizes the need for spectra with high signal-to-noise ratios and good resolution, and the ability to isolate the spectra of the nucleus from the stellar continuum of the host galaxy. Spectra with better quality than those used in this thesis (*i.e.*, from *2dF* and *SDSS*) can be obtained with the current instruments on large telescopes (although hundred of hours would be needed for a sample the size of *MJ*!).

Since the fibre sizes in *2dF* and *SDSS* are $\sim 2''$ and $\sim 3''$ respectively, a large fraction of the host galaxy is sampled along with the nuclear region. Spectra taken from fibres or slits with smaller effective angular sizes would be invaluable in revealing hidden AGN whose spectra might be masked by the host galaxies otherwise. Integral field spectroscopy also holds great promise as a sampling size of $0.2''$ can be achieved (*e.g.*, in the Gemini Multi-Object Spectrographs) whilst also providing simultaneous spatially-resolved spectroscopy.

- The incremental version of *2XMM*, the *2XMMi*, which contains 17% more detections than *2XMM*, together with the latest *SDSS* data release, the seventh data release (DR7; Abazajian & Sloan

Digital Sky Survey 2008), will allow a larger sample of normal galaxies to be identified for better statistical studies of this population although such sample still will have the incompleteness problems due to flux thresholds.

- Although, compared with previous studies, the normal galaxy samples presented in this thesis have reached significant sizes which allow much tighter constraints of their average properties to be made, for a large fraction of these galaxies, the investigation of the X-ray spectral properties were limited by their faintness in X-rays, which limits the X-ray spectral characterisation. Deeper surveys ($\gtrsim 100$ ks) will allow *XMM-Newton* pn camera to collect ~ 200 photons from a galaxy with flux of $\sim 10^{-14}$ erg s $^{-1}$ cm $^{-2}$ (assuming a power-law with $\Gamma = 1.7$, $N_{\text{H}} = 3 \times 10^{20}$ atoms cm $^{-2}$), in which case detailed spectral analysis can be performed to gain insight on the origin of the X-ray emission. Future missions, such as the *International X-ray Observatory (IXO)*, which will have ~ 10 – 100 times better sensitivity than *XMM-Newton*, will be able to provide data with sufficient signal-to-noise ratios for spectral analysis for a much large number of normal galaxies and to a much fainter flux limit.
- Although galaxies with substantial SF activity have been classified using the optical emission line ratios, possible AGN contamination has not been identified unambiguously. Such AGN might reveal themselves in X-ray images with sub-arcsec resolution. Although such resolution has been achieved by *Chandra*, the smaller field of view of *Chandra* compared with *XMM-Newton* means far more pointings are needed to collect a normal galaxy sample with significant size. Future missions with sub-arcsec resolution and large collecting area will allow spatial isolation of AGN from the host galaxies.
- A fraction of Type 2 AGN in the *MJ* sample appear to have only modest obscuration up to ~ 12 keV. However, the current data do not allow clear discrimination between underestimated obscuration due to contribution from other component(s) in the galaxy and intrinsically low obscuration. X-ray observations up to a few tens of keV are needed to distinguish heavily obscured AGNs from truly normal galaxies. However, most of the galaxies in *2dF* and *MJ* are too faint for current instruments with higher energy coverage (*e.g.*, *Suzaku*). *IXO*, which will have higher sensitivity over current missions and provide coverage up to ~ 40 keV, will play a crucial role in the studies of the obscuration present in AGN.

Appendix A

The $2dF$ Sample

Table A.1: (1) QID from XWAS. (2) Right ascension in hh:mm:ss.ss for the X-ray source. (3) Declination in dd:mm:ss.ss for the X-ray source. (4) Redshift from XWAS. (5) R band magnitude from SSS or USNO-B 1.0 (marked by *). (6) Logarithm of $f_{0.2-12\text{keV}}$ from XWAS. (7) $\log(f_X/f_O)$ defined as $\log f_{0.2-12\text{keV}} + R/2.5 + 5.5$. (8) Logarithm of $L_{0.2-12\text{keV}}$. (9) Classification from this work. “SF” denote SF galaxies. “COM” denote composite galaxies. “UNC” denote unclassified NELGs.

QID	RA (J2000)	Dec (J2000)	z	R	$\log f_X$ ($\text{erg s}^{-1} \text{cm}^{-2}$)	$\log(f_X/f_O)$	$\log L_X$ (erg s^{-1})	Class
(1)	(2)	(3)	(4)	(5)	(6)	(7)	(8)	(9)
15	00:03:15.19	-26:09:28.8	0.280	18.64	-13.96	-1.01	42.43	ALG
36	00:03:46.25	-26:00:42.1	0.075	18.43	-14.16	-1.29	40.98	UNC
58	00:02:42.02	-25:54:12.3	0.100	15.59	-13.60	-1.86	41.80	ALG
82	00:00:25.32	-25:11:40.5	0.090	16.20	-13.78	-1.80	41.53	ALG
173	20:42:13.88	-32:36:06.4	0.124	16.94*	-13.61	-1.34	41.99	AGN
183	20:41:18.77	-32:27:12.1	0.135	17.12*	-13.74	-1.39	41.95	COM
218	01:41:04.01	-68:01:08.4	0.224	17.50	-14.23	-1.73	41.94	SF
252	01:39:52.32	-67:44:37.8	0.164	18.22	-14.07	-1.28	41.80	ALG
285	00:50:41.74	-52:13:11.8	0.027	13.38	-13.51	-2.65	40.72	ALG
305	00:50:07.06	-52:07:28.9	0.027	14.05	-13.89	-2.77	40.33	ALG
586	22:51:49.36	-17:52:24.1	0.077	15.69	-13.76	-1.99	41.40	COM
601	22:51:42.57	-17:47:36.7	0.301	18.12	-14.37	-1.63	42.09	ALG
699	22:16:05.00	-17:48:07.2	0.051	15.36	-14.46	-2.81	40.33	COM
731	22:15:21.31	-17:40:57.6	0.231	18.90	-14.17	-1.11	42.03	AGN
803	02:24:02.76	-04:41:37.1	0.043	13.86	-13.15	-2.11	41.49	UNC

Continued on next page

Table A.1 – continued from previous page

QID	RA	Dec	z	R	$\log f_X$	$\log(\frac{f_X}{f_O})$	$\log L_X$	Class
(1)	(J2000) (2)	(J2000) (3)	(4)	(5)	($\text{erg s}^{-1} \text{cm}^{-2}$) (6)	(7)	(erg s^{-1}) (8)	(9)
823	02:24:16.68	-05:03:27.6	0.143	16.72	-14.06	-1.88	41.67	ALG
827	02:24:18.88	-05:00:42.8	0.040	16.12	-14.35	-2.40	40.23	SF
839	02:25:52.98	-05:15:36.0	0.296	17.81	-13.77	-1.15	42.67	UNC
859	02:25:38.31	-05:08:08.3	0.061	17.11	-14.15	-1.81	40.80	SF
861	02:24:56.17	-05:08:00.8	0.084	15.48	-13.50	-1.81	41.74	ALG
872	02:25:37.82	-05:02:23.1	0.053	16.08	-13.77	-1.83	41.06	ALG
883	02:26:17.49	-05:04:43.9	0.054	14.82	-12.90	-1.47	41.95	AGN
908	02:27:36.73	-05:08:20.1	0.077	18.63	-14.05	-1.10	41.12	SF
956	02:23:13.29	-04:31:01.0	0.017	15.80	-13.57	-1.75	40.24	COM
970	02:26:04.45	-04:59:34.2	0.054	15.47	-13.08	-1.39	41.76	AGN
985	02:26:17.16	-04:47:24.7	0.140	17.88	-13.78	-1.12	41.94	COM
1010	02:27:03.75	-04:34:09.6	0.068	15.52	-14.17	-2.46	40.88	ALG
1029	02:26:51.71	-04:21:17.9	0.312	18.94	-14.13	-1.06	42.37	UNC
1127	02:22:49.66	-04:04:42.5	0.289	18.21	-13.81	-1.02	42.62	UNC
1353	02:24:54.56	-03:28:37.4	0.174	16.51	-13.67	-1.57	42.26	ALG
1410	05:08:27.92	-37:39:25.1	0.052	15.38	-13.74	-2.09	41.07	SF
1416	05:08:10.78	-37:37:44.4	0.051	15.04	-14.66	-3.14	40.13	UNC
1420	05:08:30.21	-37:36:37.9	0.053	14.89	-14.00	-2.54	40.82	ALG
1435	05:07:23.64	-37:33:21.2	0.093	16.98	-14.21	-1.92	41.12	COM
1557	00:15:30.02	-39:26:37.1	0.103	15.86*	-13.54	-1.69	41.89	ALG
1563	00:16:08.95	-39:25:04.6	0.041	15.53	-14.11	-2.39	40.49	SF
1569	00:15:39.69	-39:22:25.9	0.057	17.64	-14.12	-1.56	40.77	UNC
1605	00:15:37.02	-39:09:47.8	0.063	13.24*	-14.09	-3.29	40.89	UNC
1619	00:15:01.80	-39:05:36.0	0.055	16.49*	-14.04	-1.95	40.81	UNC
1770	23:03:36.62	+08:58:28.3	0.232	17.73*	-13.99	-1.40	42.21	UNC
1815	23:02:46.79	+08:48:18.8	0.041	13.07*	-13.82	-3.10	40.77	ALG
1841	05:22:21.25	-36:29:51.5	0.057	15.18	-14.12	-2.55	40.77	AGN
1842	05:22:38.20	-36:29:24.2	0.066	16.25	-13.12	-1.11	41.91	UNC
1932	21:51:23.66	-30:24:35.6	0.239	17.85	-13.75	-1.11	42.49	ALG
2144	00:43:07.95	-20:31:49.1	0.272	18.36	-14.23	-1.38	42.14	ALG
2264	03:35:38.99	-25:39:39.7	0.133	18.25	-14.18	-1.38	41.49	AGN
2325	03:38:16.37	-25:14:52.8	0.285	18.03	-14.00	-1.29	42.40	UNC
2349	01:53:21.98	-13:47:32.5	0.221	18.50*	-14.01	-1.11	42.15	UNC
2381	01:52:53.17	-13:34:41.8	0.175	18.73	-14.13	-1.14	41.80	ALG
2495	02:36:23.73	-52:30:36.9	0.118	17.19	-14.40	-2.02	41.16	COM
2496	02:36:13.43	-52:30:35.4	0.113	16.71	-13.80	-1.61	41.72	COM
2538	02:36:56.87	-52:18:01.3	0.195	18.80	-14.18	-1.16	41.86	AGN
2590	02:38:25.34	-52:14:29.0	0.189	18.69	-14.78	-1.81	41.22	ALG
2593	02:38:50.62	-52:13:00.6	0.044	17.35	-13.85	-1.41	40.80	COM
2636	23:18:51.75	-42:31:17.4	0.115	16.02	-13.15	-1.24	42.39	ALG
2666	23:18:14.39	-42:18:26.4	0.210	18.03	-14.07	-1.36	42.04	AGN

Continued on next page

Table A.1 – continued from previous page

QID	RA (J2000)	Dec (J2000)	z	R	$\log f_X$ ($\text{erg s}^{-1} \text{cm}^{-2}$)	$\log(\frac{f_X}{f_O})$	$\log L_X$ (erg s^{-1})	Class
(1)	(2)	(3)	(4)	(5)	(6)	(7)	(8)	(9)
2677	23:17:56.38	-42:13:33.2	0.056	14.57	-13.37	-2.04	41.50	ALG
2683	23:18:13.08	-42:11:34.6	0.131	16.36	-13.23	-1.19	42.42	ALG
2720	23:13:50.27	-42:49:58.8	0.154	17.51	-14.13	-1.62	41.68	ALG
2727	23:14:32.94	-42:47:25.6	0.206	18.59	-14.00	-1.06	42.09	ALG
2730	23:14:21.71	-42:45:59.3	0.068	15.19	-13.65	-2.07	41.40	UNC
2742	23:14:56.18	-42:41:00.3	0.253	17.64	-14.40	-1.84	41.90	ALG
2770	23:13:57.61	-42:31:45.8	0.099	16.03	-14.13	-2.22	41.27	ALG
2786	03:38:10.04	+00:16:10.0	0.198	17.00	-13.88	-1.58	42.17	ALG
2885	03:36:26.27	+00:35:08.6	0.128	17.50	-14.14	-1.65	41.49	SF
2934	04:10:02.21	-71:18:11.0	0.070	11.38*	-13.58	-3.53	41.49	ALG
2962	04:11:04.16	-71:11:18.9	0.126	15.97	-13.67	-1.78	41.95	ALG
3030	03:39:07.34	-35:25:17.7	0.245	17.39	-14.43	-1.97	41.83	ALG
3071	03:39:14.80	-35:15:49.0	0.062	16.39	-13.21	-1.15	41.76	UNC
3109	05:05:17.04	-28:50:24.1	0.130	16.44	-13.68	-1.60	41.97	ALG
3111	05:05:22.16	-28:50:02.7	0.300	17.48	-14.08	-1.59	42.38	ALG
3145	05:06:07.63	-28:42:44.0	0.135	16.73	-13.92	-1.72	41.77	ALG

Appendix B

The *MJ* Sample

Table B.1: (1) IAU name of the *2XMM* source. (2) Positional offset between the X-ray position and the optical position (in arcsec). (3) *SDSS* *r* band Petrosian magnitude. (4) Redshift from *SDSS*. (5) Logarithm of $f_{0.2-12\text{keV}}$ from *2XMM*. (6) $\log(f_X/f_O)$ defined as $\log f_{0.2-12\text{keV}} + r/2.5 + 5.5$. (7) Logarithm of $L_{0.2-12\text{keV}}$. (8) Classification from this work. “AGN(L)” denote LINER 2s. “AGN(S)” denote Seyfert 2 galaxies. “SF” denote SF galaxies. “COM” denote composite galaxies. “UNC” denote unclassified NELGs.

IAUNAME	δ_{XO} (")	<i>r</i>	<i>z</i>	$\log f_X$ ($\text{erg s}^{-1} \text{cm}^{-2}$)	$\log(\frac{f_X}{f_O})$	$\log L_X$ (erg s^{-1})	Class
(1)	(2)	(3)	(4)	(5)	(6)	(7)	(8)
2XMM J004244.6-093316	0.8	15.30	0.0544	-13.97	-2.35	40.88	UNC
2XMM J004301.6-094723	1.7	16.40	0.1299	-14.02	-1.96	41.63	UNC
2XMM J005611.3+004052	3.6	15.08	0.0674	-13.77	-2.24	41.27	ALG
2XMM J010631.4+141146	4.1	18.26	0.2459	-13.82	-1.01	42.44	UNC
2XMM J010714.0+135723	5.7	14.04	0.0381	-13.42	-2.30	41.11	COM
2XMM J010730.3+141759	2.1	16.40	0.0757	-14.04	-1.98	41.11	ALG
2XMM J010730.4+141222	0.3	15.78	0.0775	-13.49	-1.68	41.68	AGN(L)
2XMM J011832.2-011150	0.7	14.81	0.0468	-13.51	-2.09	41.20	AGN(L)
2XMM J011854.8-010551	5.7	16.44	0.1216	-13.63	-1.55	41.96	COM
2XMM J011923.5-011009	2.3	17.72	0.1844	-13.71	-1.12	42.28	ALG
2XMM J023117.6-073456	0.5	17.74	0.1285	-13.94	-1.35	41.70	COM
2XMM J024024.2-082559	4.2	13.11	0.0046	-13.26	-2.52	39.41	COM
2XMM J030222.1-000532	6.0	17.02	0.0847	-13.35	-1.04	41.91	SF
2XMM J030548.1-001034	2.0	14.03	0.0198	-13.94	-2.83	40.01	SF
2XMM J030559.3-001003	3.7	16.18	0.1071	-13.65	-1.68	41.81	AGN(S)

Continued on next page

Table B.1 – continued from previous page

IAUNAME	δ_{XO} (")	r	z	$\log f_X$ ($\text{erg s}^{-1} \text{cm}^{-2}$)	$\log(\frac{f_X}{f_O})$	$\log L_X$ (erg s^{-1})	Class
(1)	(2)	(3)	(4)	(5)	(6)	(7)	(8)
2XMM J030611.3-000821	2.5	16.65	0.1080	-14.27	-2.11	41.21	ALG
2XMM J030614.4-002039	1.4	15.27	0.0285	-13.64	-2.03	40.63	SF
2XMM J030617.3-000824	0.2	16.15	0.1096	-13.76	-1.79	41.73	UNC
2XMM J030621.5-000810	3.7	16.87	0.1082	-14.12	-1.87	41.36	ALG
2XMM J030625.0+001309	2.9	17.47	0.1554	-13.70	-1.22	42.12	AGN(L)
2XMM J030634.1-001355	1.0	17.85	0.2151	-13.66	-1.03	42.47	SF
2XMM J030650.3-002105	1.5	17.54	0.1164	-13.56	-1.04	41.99	AGN
2XMM J030658.7+000832	1.1	15.62	0.0751	-14.46	-2.71	40.68	UNC
2XMM J032511.5-061051	0.4	13.47	0.0338	-13.15	-2.26	41.27	SF
2XMM J032523.4-060048	0.9	16.89	0.1028	-13.45	-1.19	41.98	COM
2XMM J032531.0-060741	5.9	14.73	0.0348	-13.68	-2.28	40.77	SF
2XMM J033810.0+001609	1.0	17.03	0.1981	-13.87	-1.56	42.18	UNC
2XMM J080820.3+390123	1.7	14.83	0.0225	-13.87	-2.44	40.18	SF
2XMM J080822.2+390059	0.8	17.71	0.1957	-13.66	-1.08	42.37	UNC
2XMM J083059.2+523746	1.3	17.82	0.1363	-14.29	-1.66	41.41	SF
2XMM J083114.6+524224	0.7	15.38	0.0640	-14.38	-2.73	40.62	SF
2XMM J083139.1+524205	0.6	15.82	0.0585	-12.88	-1.05	42.04	AGN(S)
2XMM J083153.7+523242	5.6	17.41	0.1407	-13.99	-1.53	41.74	SF
2XMM J083228.0+523623	1.0	13.94	0.0169	-13.41	-2.34	40.40	SF
2XMM J083816.2+384018	1.1	16.20	0.0600	-13.23	-1.24	41.71	AGN
2XMM J085630.0+380450	6.0	17.73	0.0400	-14.41	-1.82	40.16	SF
2XMM J085931.2+390753	1.7	17.02	0.1554	-13.80	-1.49	42.02	SF
2XMM J090031.0+391449	0.9	17.36	0.0971	-13.65	-1.20	41.73	COM
2XMM J090036.0+391648	2.2	17.05	0.0961	-14.20	-1.88	41.17	SF
2XMM J090920.3+542538	1.6	16.38	0.0718	-14.49	-2.43	40.61	SF
2XMM J091247.1+525727	3.8	18.00	0.2856	-14.48	-1.77	41.93	ALG
2XMM J091324.2+525356	1.3	15.36	0.0601	-13.48	-1.84	41.45	COM
2XMM J091325.9+525852	0.3	13.25	0.0253	-13.72	-2.92	40.44	AGN(L)
2XMM J091404.9+405250	2.5	17.39	0.1464	-13.59	-1.13	42.17	UNC
2XMM J092039.8+370616	4.5	17.62	0.2347	-14.34	-1.80	41.87	COM
2XMM J092131.2+371115	2.3	17.82	0.2866	-14.10	-1.48	42.31	UNC
2XMM J092327.0+512058	0.7	15.50	0.0657	-13.19	-1.49	41.83	AGN(S)
2XMM J093414.4+611734	3.1	17.24	0.2083	-13.78	-1.38	42.32	UNC
2XMM J093434.5+550620	3.8	17.28	0.0739	-13.77	-1.36	41.36	SF
2XMM J093518.5+612831	0.9	16.68	0.1241	-14.18	-2.00	41.43	COM
2XMM J093619.1+612723	2.1	16.63	0.1310	-14.13	-1.98	41.52	ALG
2XMM J094046.2+033929	0.7	16.23	0.0873	-13.80	-1.81	41.48	AGN(S)
2XMM J094046.2+032446	1.7	15.79	0.0732	-13.53	-1.71	41.59	AGN(L)
2XMM J094132.4+390023	0.6	17.78	0.1677	-14.53	-1.92	41.36	ALG
2XMM J094506.4+035552	1.8	17.22	0.1559	-14.06	-1.67	41.76	AGN(S)
2XMM J094524.9+095535	2.7	16.86	0.0965	-13.79	-1.54	41.58	SF

Continued on next page

Table B.1 – continued from previous page

IAUNAME	δ_{XO} (")	r	z	$\log f_X$ ($\text{erg s}^{-1} \text{cm}^{-2}$)	$\log(\frac{f_X}{f_O})$	$\log L_X$ (erg s^{-1})	Class
(1)	(2)	(3)	(4)	(5)	(6)	(7)	(8)
2XMM J094639.0+095847	1.4	17.29	0.1147	-13.51	-1.10	42.02	SF
2XMM J095847.6+024532	1.6	17.10	0.0792	-14.59	-2.25	40.60	SF
2XMM J095848.6+025243	0.6	16.84	0.0790	-13.38	-1.15	41.80	SF
2XMM J095852.2+025122	2.3	16.39	0.0723	-14.23	-2.17	40.87	UNC
2XMM J095905.5+023811	1.8	15.33	0.0792	-14.11	-2.48	41.08	COM
2XMM J095907.5+024215	3.9	16.83	0.0792	-14.30	-2.06	40.89	AGN(S)
2XMM J095925.5+051143	2.0	16.98	0.1622	-13.89	-1.60	41.96	COM
2XMM J095929.0+051322	0.5	16.29	0.1218	-14.07	-2.05	41.52	UNC
2XMM J095943.1+023528	5.8	17.22	0.0787	-13.74	-1.35	41.44	AGN(L)
2XMM J095945.3+023441	3.2	17.35	0.1237	-13.73	-1.29	41.87	COM
2XMM J095946.9+025525	0.9	17.44	0.1247	-13.54	-1.06	42.07	UNC
2XMM J095959.7+024608	1.5	16.70	0.1656	-14.02	-1.84	41.86	AGN
2XMM J100007.1+051802	2.0	16.91	0.1220	-14.31	-2.04	41.28	UNC
2XMM J100008.1+024555	1.0	15.47	0.0289	-14.03	-2.34	40.25	SF
2XMM J100022.8+021312	0.9	18.30	0.1860	-14.42	-1.60	41.57	SF
2XMM J100046.6+023303	2.8	17.80	0.1069	-14.31	-1.69	41.16	SF
2XMM J100055.1+022344	0.9	15.66	0.0446	-13.48	-1.72	41.19	AGN(L)
2XMM J100120.5+021817	0.2	17.03	0.1229	-13.89	-1.58	41.71	SF
2XMM J100122.6+021700	2.2	18.72	0.3735	-14.30	-1.31	42.38	ALG
2XMM J100130.6+022442	2.1	18.67	0.3488	-14.49	-1.53	42.12	UNC
2XMM J100136.3+022643	2.7	16.78	0.1234	-14.67	-2.46	40.93	ALG
2XMM J100136.8+023032	1.2	16.39	0.1236	-14.06	-2.00	41.55	COM
2XMM J100139.8+022548	0.7	15.79	0.1241	-13.93	-2.11	41.67	UNC
2XMM J100141.9+020357	0.4	16.63	0.1248	-13.18	-1.03	42.43	AGN(S)
2XMM J100142.5+014058	3.1	17.81	0.2178	-13.95	-1.33	42.19	UNC
2XMM J100200.3+025139	5.4	16.67	0.1029	-13.83	-1.67	41.60	SF
2XMM J100225.8+024026	2.6	17.60	0.0940	-14.59	-2.05	40.76	SF
2XMM J100327.8+554155	1.9	17.67	0.1460	-13.87	-1.30	41.88	AGN(S)
2XMM J100505.7+410538	0.8	15.56	0.0925	-13.76	-2.04	41.57	UNC
2XMM J100816.0+534213	2.1	16.74	0.0691	-14.39	-2.20	40.67	SF
2XMM J101117.6+553813	1.0	16.04	0.1173	-14.46	-2.55	41.09	SF
2XMM J101756.8+390526	1.5	16.30	0.0539	-13.90	-1.88	40.94	AGN(S)
2XMM J101821.2+411913	2.6	17.68	0.1534	-14.33	-1.76	41.47	SF
2XMM J102138.8+131845	0.4	14.68	0.0461	-13.65	-2.28	41.05	AGN(L)
2XMM J102141.7+130551	1.9	17.56	0.0765	-14.03	-1.51	41.12	AGN(S)
2XMM J102142.6+130654	2.4	17.02	0.0763	-13.51	-1.21	41.64	COM
2XMM J102306.3+040805	1.8	15.70	0.0485	-14.33	-2.54	40.42	SF
2XMM J102355.1+040137	0.3	15.93	0.0646	-13.44	-1.57	41.56	COM
2XMM J102406.7+041632	1.4	17.47	0.1218	-13.64	-1.15	41.95	COM
2XMM J102408.4+040035	1.9	16.23	0.0641	-14.20	-2.21	40.80	SF
2XMM J102446.2+465921	3.8	15.18	0.0430	-14.46	-2.89	40.17	COM

Continued on next page

Table B.1 – continued from previous page

IAUNAME	δ_{XO} (")	r	z	$\log f_X$ ($\text{erg s}^{-1} \text{cm}^{-2}$)	$\log(\frac{f_X}{f_O})$	$\log L_X$ (erg s^{-1})	Class
(1)	(2)	(3)	(4)	(5)	(6)	(7)	(8)
2XMM J102451.2+470739	0.8	17.59	0.1430	-13.58	-1.04	42.16	AGN(L)
2XMM J102513.5+470656	1.7	16.62	0.0605	-13.74	-1.59	41.20	COM
2XMM J102557.3+385217	0.5	17.38	0.1151	-13.47	-1.01	42.07	AGN(S)
2XMM J102625.2+384447	0.1	16.11	0.0612	-14.08	-2.14	40.87	UNC
2XMM J102644.8+384235	4.8	17.42	0.0928	-14.38	-1.91	40.95	COM
2XMM J103043.0+052319	0.4	17.35	0.1757	-14.58	-2.14	41.36	UNC
2XMM J103240.3+584601	1.6	16.04	0.0736	-13.88	-1.97	41.24	ALG
2XMM J103259.6+575320	1.3	16.33	0.1232	-14.00	-1.97	41.6	COM
2XMM J103346.3+600126	1.4	17.69	0.2287	-14.19	-1.61	42.0	ALG
2XMM J103401.2+584827	2.1	15.92	0.0739	-14.45	-2.58	40.67	ALG
2XMM J103409.5+595544	3.0	17.32	0.2542	-14.48	-2.05	41.82	UNC
2XMM J103729.6+415226	5.4	16.75	0.1257	-13.76	-1.55	41.86	UNC
2XMM J104043.6+394746	0.9	15.07	0.0429	-13.27	-1.74	41.37	AGN
2XMM J104045.6+092210	2.7	17.59	0.2100	-14.09	-1.55	42.02	COM
2XMM J104109.9+061724	1.7	14.88	0.0336	-14.67	-3.22	39.74	COM
2XMM J104112.7+060739	3.2	15.77	0.0343	-14.66	-2.85	39.78	COM
2XMM J104113.0+062212	1.9	14.02	0.0193	-13.70	-2.59	40.22	UNC
2XMM J104120.9+061644	3.2	15.80	0.0339	-14.85	-3.03	39.57	SF
2XMM J104133.7+061528	0.8	14.31	0.0335	-13.57	-2.35	40.84	UNC
2XMM J104144.3+400227	1.5	14.10	0.0429	-13.73	-2.59	40.91	SF
2XMM J104218.2+060848	2.6	16.60	0.0761	-14.07	-1.93	41.08	AGN(S)
2XMM J105126.7+574236	2.5	14.99	0.0729	-14.11	-2.61	41.01	ALG
2XMM J105128.0+573502	0.6	16.90	0.0731	-13.94	-1.69	41.17	SF
2XMM J105554.5+572634	1.1	16.24	0.0729	-14.13	-2.13	40.99	ALG
2XMM J110052.0+110050	5.6	14.60	0.0273	-13.51	-2.17	40.72	AGN(L)
2XMM J110426.2+405026	5.8	14.42	0.0323	-13.85	-2.58	40.53	UNC
2XMM J111024.7+434942	1.3	15.24	0.0752	-14.08	-2.48	41.07	UNC
2XMM J111703.3+411216	4.8	15.80	0.0754	-13.60	-1.78	41.54	SF
2XMM J111912.1+431253	0.9	17.29	0.0980	-13.98	-1.57	41.40	SF
2XMM J112310.6+053338	1.6	15.45	0.0373	-14.34	-2.66	40.17	UNC
2XMM J112758.1+583557	1.0	17.73	0.1779	-13.63	-1.04	42.32	SF
2XMM J112845.5+583539	3.6	15.00	0.0595	-14.03	-2.52	40.90	COM
2XMM J112856.3+582919	2.6	16.97	0.0931	-14.05	-1.76	41.29	SF
2XMM J113246.6+525622	5.2	15.11	0.0273	-13.94	-2.40	40.29	UNC
2XMM J113317.1+530744	4.3	17.11	0.2542	-14.08	-1.74	42.21	ALG
2XMM J113359.2+490344	0.9	13.19	0.0317	-12.93	-2.16	41.43	UNC
2XMM J113428.8+485706	4.0	15.85	0.0282	-14.16	-2.32	40.09	SF
2XMM J113446.6+485722	0.8	14.02	0.0316	-13.15	-2.05	41.21	AGN
2XMM J114019.4+030004	2.0	14.04	0.0268	-13.96	-2.85	40.25	COM
2XMM J115036.8+013923	1.6	17.57	0.1596	-13.88	-1.35	41.97	COM
2XMM J115042.9+545638	3.2	17.66	0.2281	-13.63	-1.06	42.56	UNC

Continued on next page

Table B.1 – continued from previous page

IAUNAME	δ_{XO} (")	r	z	$\log f_X$ ($\text{erg s}^{-1} \text{cm}^{-2}$)	$\log(\frac{f_X}{f_O})$	$\log L_X$ (erg s^{-1})	Class
(1)	(2)	(3)	(4)	(5)	(6)	(7)	(8)
2XMM J115050.9+550836	1.4	13.56	0.0193	-13.72	-2.80	40.20	COM
2XMM J115157.6+550808	0.7	15.77	0.0797	-13.31	-1.50	41.89	AGN(L)
2XMM J115205.0+545955	2.2	15.72	0.0589	-13.70	-1.91	41.22	UNC
2XMM J115657.8+550820	0.9	15.89	0.0798	-13.31	-1.46	41.89	AGN(S)
2XMM J115732.1+435716	0.6	16.39	0.0697	-13.97	-1.91	41.11	SF
2XMM J115822.4+434854	0.7	15.64	0.0700	-14.22	-2.46	40.86	SF
2XMM J115849.8+435140	4.5	17.36	0.2411	-14.02	-1.58	42.22	UNC
2XMM J120047.2-033647	0.7	17.51	0.3009	-13.64	-1.13	42.82	UNC
2XMM J120333.6+020111	5.6	15.41	0.0833	-13.25	-1.58	41.99	AGN(S)
2XMM J120337.4+020243	6.2	13.66	0.0189	-13.64	-2.68	40.26	UNC
2XMM J120405.9+015048	1.3	13.82	0.0164	-13.99	-2.96	39.79	UNC
2XMM J120406.9+014644	1.2	17.61	0.2409	-14.06	-1.51	42.19	UNC
2XMM J120708.2+645816	3.7	16.31	0.1139	-13.76	-1.74	41.76	ALG
2XMM J120841.7+435330	2.5	16.90	0.0652	-13.52	-1.26	41.49	COM
2XMM J120900.7+422829	1.6	16.70	0.0236	-13.55	-1.37	40.55	AGN(S)
2XMM J120937.0+421907	4.9	15.47	0.0226	-13.80	-2.11	40.26	COM
2XMM J120947.3+423844	4.6	17.78	0.1684	-14.10	-1.49	41.80	SF
2XMM J121052.8+503815	3.5	17.87	0.3196	-14.22	-1.58	42.30	UNC
2XMM J121101.1+503431	0.9	17.33	0.1701	-14.66	-2.23	41.24	ALG
2XMM J121205.5+131220	0.7	14.58	0.0649	-13.16	-1.83	41.84	UNC
2XMM J121335.7+024836	1.2	17.52	0.1326	-14.07	-1.56	41.60	AGN(L)
2XMM J121353.1+024145	1.0	16.47	0.0746	-14.50	-2.42	40.63	COM
2XMM J121354.8+024754	1.2	16.38	0.0743	-13.72	-1.67	41.41	COM
2XMM J121838.9+054857	2.5	17.63	0.1233	-13.75	-1.20	41.85	SF
2XMM J121935.7+055049	1.1	12.72	0.0084	-13.88	-3.29	39.31	UNC
2XMM J121955.6+055336	3.0	17.75	0.1725	-14.14	-1.54	41.77	UNC
2XMM J122011.6+054802	0.3	16.89	0.1143	-13.72	-1.46	41.81	COM
2XMM J122257.7+103255	1.7	14.49	0.0259	-14.01	-2.71	40.18	UNC
2XMM J122400.9+104035	3.4	16.58	0.1305	-14.08	-1.95	41.58	UNC
2XMM J122541.8+124837	2.2	12.07	0.0018	-13.67	-3.34	38.20	ALG
2XMM J122702.1+125205	3.1	16.67	0.1320	-14.22	-2.06	41.44	ALG
2XMM J122755.5+012315	0.8	15.72	0.0788	-13.87	-2.08	41.31	UNC
2XMM J122807.6+020251	0.7	17.30	0.0903	-13.46	-1.03	41.85	AGN(S)
2XMM J122820.4+020915	2.8	16.62	0.1581	-13.94	-1.79	41.90	SF
2XMM J122957.3+105453	1.8	15.56	0.0258	-13.43	-1.71	40.75	AGN(L)
2XMM J123023.7+110051	1.6	16.43	0.0679	-13.95	-1.88	41.10	SF
2XMM J123055.7+414704	3.2	16.69	0.1741	-14.01	-1.84	41.91	AGN(L)
2XMM J123057.7+104811	1.3	15.60	0.0489	-14.39	-2.65	40.36	AGN(L)
2XMM J123218.6+641500	2.6	15.91	0.0811	-14.25	-2.38	40.96	COM
2XMM J123222.3+000039	2.9	15.60	0.0442	-14.39	-2.65	40.27	SF
2XMM J123310.9+000454	0.9	16.45	0.0753	-14.50	-2.42	40.65	COM

Continued on next page

Table B.1 – continued from previous page

IAUNAME	δ_{XO} (")	r	z	$\log f_X$ ($\text{erg s}^{-1} \text{cm}^{-2}$)	$\log(\frac{f_X}{f_O})$	$\log L_X$ (erg s^{-1})	Class
(1)	(2)	(3)	(4)	(5)	(6)	(7)	(8)
2XMM J123321.1+000656	2.1	17.77	0.2033	-13.94	-1.33	42.14	ALG
2XMM J123545.2+131117	4.5	18.30	0.3249	-14.13	-1.31	42.41	ALG
2XMM J123550.6+620722	1.1	19.53	0.4720	-14.43	-1.12	42.49	ALG
2XMM J123608.7+131340	0.8	17.93	0.3225	-13.69	-1.02	42.84	SF
2XMM J123631.4+125943	2.5	16.17	0.0934	-14.10	-2.13	41.24	UNC
2XMM J123646.6+125611	1.8	16.35	0.0935	-13.62	-1.58	41.72	COM
2XMM J123735.4+622600	2.7	17.40	0.1882	-13.75	-1.29	42.25	SF
2XMM J123747.6+120047	4.2	16.13	0.0804	-13.70	-1.74	41.51	COM
2XMM J123755.5+113849	2.5	16.73	0.0759	-14.24	-2.05	40.91	SF
2XMM J124001.3+474705	3.4	14.67	0.0390	-13.30	-1.93	41.25	UNC
2XMM J124114.7-015558	6.3	17.21	0.1564	-13.91	-1.53	41.91	ALG
2XMM J124114.9-015715	1.4	17.25	0.0654	-14.12	-1.72	40.90	COM
2XMM J124214.3+023301	1.7	16.19	0.1203	-14.46	-2.48	41.12	ALG
2XMM J124301.9+025414	1.1	17.49	0.1555	-13.59	-1.10	42.23	AGN(L)
2XMM J124452.2-002550	0.8	15.41	0.0822	-14.26	-2.60	40.96	AGN
2XMM J125611.9+565703	6.3	17.38	0.0777	-14.23	-1.78	40.94	SF
2XMM J125838.4-013430	2.6	15.41	0.0862	-14.09	-2.43	41.18	UNC
2XMM J130221.7-023005	4.1	15.52	0.0798	-14.12	-2.41	41.08	ALG
2XMM J130251.6+672519	1.9	16.63	0.1094	-13.86	-1.71	41.62	ALG
2XMM J130307.4-022154	0.3	16.60	0.0866	-13.81	-1.67	41.46	COM
2XMM J130721.9+533517	4.5	14.11	0.0292	-13.61	-2.47	40.68	AGN(L)
2XMM J130805.9+533556	1.1	17.45	0.1211	-14.32	-1.84	41.26	SF
2XMM J130827.4+533303	0.3	17.77	0.1775	-14.23	-1.62	41.72	UNC
2XMM J130922.5-014258	1.4	17.04	0.1430	-13.70	-1.38	42.04	UNC
2XMM J131113.5-013222	1.7	16.86	0.1130	-13.30	-1.06	42.21	AGN(L)
2XMM J131204.3-012452	1.7	16.77	0.1107	-13.78	-1.57	41.72	SF
2XMM J131848.3-005138	1.5	17.78	0.1833	-14.19	-1.58	41.79	UNC
2XMM J131904.6-005329	1.9	15.47	0.0849	-14.30	-2.62	40.95	ALG
2XMM J131929.9-010841	2.7	16.17	0.1391	-13.80	-1.83	41.91	UNC
2XMM J131951.8-004354	2.8	17.36	0.1119	-13.57	-1.13	41.94	UNC
2XMM J132402.1+031501	2.8	18.39	0.3505	-14.32	-1.46	42.30	UNC
2XMM J132643.4+010817	1.5	15.82	0.0834	-14.03	-2.21	41.20	COM
2XMM J132650.1+012121	1.5	16.33	0.0801	-14.22	-2.19	40.98	SF
2XMM J132657.0+011154	1.6	16.15	0.0831	-13.79	-1.83	41.44	COM
2XMM J132841.5+113631	2.1	14.01	0.0244	-13.53	-2.43	40.60	UNC
2XMM J132929.2+113730	1.3	13.76	0.0208	-13.59	-2.58	40.41	AGN(L)
2XMM J132930.9+114446	1.9	13.50	0.0241	-13.68	-2.78	40.44	UNC
2XMM J132947.7+114232	2.2	15.61	0.0854	-13.82	-2.08	41.44	UNC
2XMM J132951.4+115731	5.1	17.17	0.2029	-13.52	-1.15	42.56	ALG
2XMM J133032.3-014736	0.9	15.97	0.0877	-14.32	-2.43	40.96	UNC
2XMM J133042.2+582755	1.9	15.97	0.1177	-13.85	-1.96	41.71	AGN

Continued on next page

Table B.1 – continued from previous page

IAUNAME	δ_{XO} (")	r	z	$\log f_X$ ($\text{erg s}^{-1} \text{cm}^{-2}$)	$\log(\frac{f_X}{f_O})$	$\log L_X$ (erg s^{-1})	Class
(1)	(2)	(3)	(4)	(5)	(6)	(7)	(8)
2XMM J133729.1+481822	2.1	16.38	0.1192	-14.44	-2.39	41.12	ALG
2XMM J133753.1+481356	6.0	17.15	0.1883	-14.09	-1.72	41.92	ALG
2XMM J133933.3-002222	3.0	16.20	0.1411	-13.85	-1.87	41.88	UNC
2XMM J133934.3-001636	2.5	16.00	0.1451	-13.94	-2.04	41.81	UNC
2XMM J134045.2-002753	3.0	16.97	0.1432	-13.80	-1.51	41.94	UNC
2XMM J134222.3+402201	1.6	17.35	0.1311	-14.06	-1.62	41.60	SF
2XMM J134341.6+554253	2.6	16.75	0.1355	-13.24	-1.04	42.44	ALG
2XMM J134427.6+560130	2.3	17.74	0.0706	-13.68	-1.09	41.40	SF
2XMM J134450.7+554305	0.5	16.13	0.1186	-14.19	-2.24	41.37	SF
2XMM J134510.1+560146	1.2	16.48	0.1439	-13.70	-1.61	42.05	AGN(L)
2XMM J134719.1+581437	0.8	16.89	0.0347	-14.12	-1.86	40.33	SF
2XMM J135141.7+634450	1.9	17.51	0.1060	-14.53	-2.03	40.92	SF
2XMM J135345.5+402022	3.3	13.20	0.0079	-13.73	-2.95	39.41	UNC
2XMM J135400.4+401640	2.2	13.62	0.0081	-13.99	-3.05	39.16	ALG
2XMM J135828.5+651550	4.8	15.26	0.0326	-13.64	-2.04	40.75	AGN
2XMM J135830.4+652629	3.7	16.90	0.1066	-13.72	-1.46	41.74	AGN(L)
2XMM J140046.5+024743	0.6	17.24	0.1360	-14.03	-1.63	41.66	AGN(L)
2XMM J140118.3+025950	1.8	15.28	0.0346	-13.98	-2.37	40.47	SF
2XMM J140305.2+541452	4.9	17.70	0.1905	-13.86	-1.28	42.15	UNC
2XMM J141340.0+435159	0.7	13.98	0.0351	-14.14	-3.05	40.31	SF
2XMM J141429.0-002231	3.0	16.57	0.1361	-14.03	-1.90	41.66	UNC
2XMM J141443.7-001651	6.2	14.97	0.0385	-14.05	-2.56	40.49	SF
2XMM J141618.3+522943	0.2	18.34	0.3564	-14.39	-1.55	42.25	ALG
2XMM J141701.6+450533	2.1	16.27	0.1142	-13.13	-1.13	42.39	COM
2XMM J141742.9+522019	4.1	17.21	0.0969	-14.49	-2.11	40.88	AGN(L)
2XMM J141822.6+522708	2.1	17.76	0.2809	-14.44	-1.83	41.96	ALG
2XMM J142407.1+421408	3.6	16.78	0.0722	-13.72	-1.51	41.38	UNC
2XMM J142930.6+425148	1.4	17.71	0.1549	-13.83	-1.24	41.99	AGN(S)
2XMM J143050.8+420028	1.1	17.27	0.1403	-13.74	-1.33	41.98	UNC
2XMM J143418.7+033955	4.8	14.18	0.0336	-14.02	-2.85	40.39	AGN(L)
2XMM J143439.9+033820	0.7	17.36	0.1460	-13.74	-1.29	42.02	UNC
2XMM J143459.3+033627	1.8	17.25	0.1460	-14.25	-1.85	41.51	ALG
2XMM J150121.1+013813	0.0	13.54	0.0351	-12.73	-1.81	41.73	COM
2XMM J150422.1+474112	0.9	15.27	0.0934	-14.02	-2.41	41.32	UNC
2XMM J151427.1+365452	3.1	17.31	0.2063	-14.42	-2.00	41.67	ALG
2XMM J151614.6-004910	0.8	16.11	0.1175	-13.44	-1.50	42.11	AGN(L)
2XMM J151626.9+002302	1.3	15.92	0.0529	-13.66	-1.79	41.17	AGN(L)
2XMM J151638.8-000227	2.2	15.80	0.0374	-14.15	-2.33	40.36	COM
2XMM J151652.1-005409	1.0	16.76	0.1156	-13.94	-1.74	41.60	AGN(L)
2XMM J152550.8+513013	3.3	18.69	0.3689	-14.68	-1.71	41.99	ALG
2XMM J153510.4+543552	5.1	15.62	0.1099	-13.64	-1.90	41.85	ALG

Continued on next page

Table B.1 – continued from previous page

IAUNAME	δ_{XO} (")	r	z	$\log f_X$ ($\text{erg s}^{-1} \text{cm}^{-2}$)	$\log(\frac{f_X}{f_O})$	$\log L_X$ (erg s^{-1})	Class
(1)	(2)	(3)	(4)	(5)	(6)	(7)	(8)
2XMM J153627.2+542628	2.8	18.71	0.3723	-14.40	-1.42	42.27	ALG
2XMM J154406.5+535700	3.4	18.63	0.3883	-14.12	-1.16	42.61	ALG
2XMM J154407.2+534600	1.0	16.72	0.1091	-13.24	-1.05	42.25	AGN(L)
2XMM J155719.4+271632	2.4	16.82	0.0981	-13.69	-1.46	41.70	AGN
2XMM J155743.3+272752	1.9	15.09	0.0315	-13.85	-2.31	40.51	COM
2XMM J155832.0+272822	1.5	15.39	0.0306	-13.05	-1.40	41.28	SF
2XMM J160534.5+323941	1.0	15.09	0.0297	-13.00	-1.47	41.30	AGN(S)
2XMM J160537.9+325611	0.7	15.57	0.0531	-13.88	-2.16	40.94	COM
2XMM J160545.0+325219	0.4	17.29	0.1157	-13.78	-1.36	41.76	AGN(S)
2XMM J162857.9+391905	3.3	14.74	0.0337	-13.57	-2.17	40.85	COM
2XMM J162916.3+392404	2.2	14.43	0.0281	-14.00	-2.73	40.26	ALG
2XMM J164110.2+384955	0.2	15.56	0.0617	-13.01	-1.28	41.96	AGN(L)
2XMM J164225.2+385226	2.4	17.64	0.1622	-13.66	-1.10	42.20	COM
2XMM J171342.7+640454	1.3	15.96	0.0846	-13.81	-1.92	41.44	UNC
2XMM J171422.0+624740	4.4	16.96	0.1776	-13.50	-1.22	42.44	UNC
2XMM J212850.0+000509	3.0	16.96	0.1403	-13.79	-1.51	41.93	ALG
2XMM J212900.6+001058	2.3	17.21	0.1335	-13.79	-1.41	41.88	ALG
2XMM J212926.2+000524	1.3	16.18	0.1384	-13.51	-1.54	42.20	AGN(L)
2XMM J212933.9+000135	0.8	16.23	0.0523	-13.67	-1.68	41.14	AGN(L)
2XMM J221722.6+002107	1.9	16.87	0.0954	-14.56	-2.31	40.80	COM
2XMM J221741.7+000906	1.4	16.10	0.0451	-14.77	-2.83	39.91	AGN(S)
2XMM J235340.5-102419	0.8	15.20	0.0740	-13.83	-2.26	41.29	ALG
2XMM J235405.7-101831	1.0	15.82	0.0733	-13.92	-2.09	41.20	UNC

Appendix C

Additional Figures

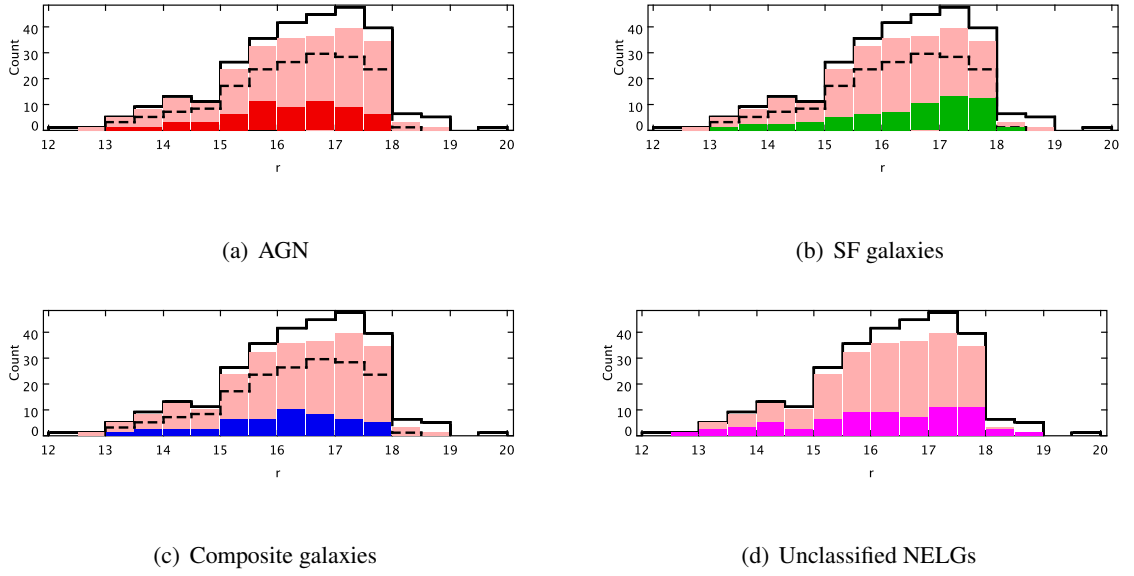


Figure C.1: The distributions of *SDSS* *r* band magnitudes. In all four plots, the *MJ* sample and its NELG subsample are marked with black solid histograms and pink filled histograms respectively. The classifiable NELGs are marked with black dashed histograms in (a), (b), and (c). AGN, SF galaxies and composite galaxies are marked with red histogram in (a), green histogram in (b) and blue histogram in (c), respectively. The unclassified NELGs are marked with magenta histogram in (d).

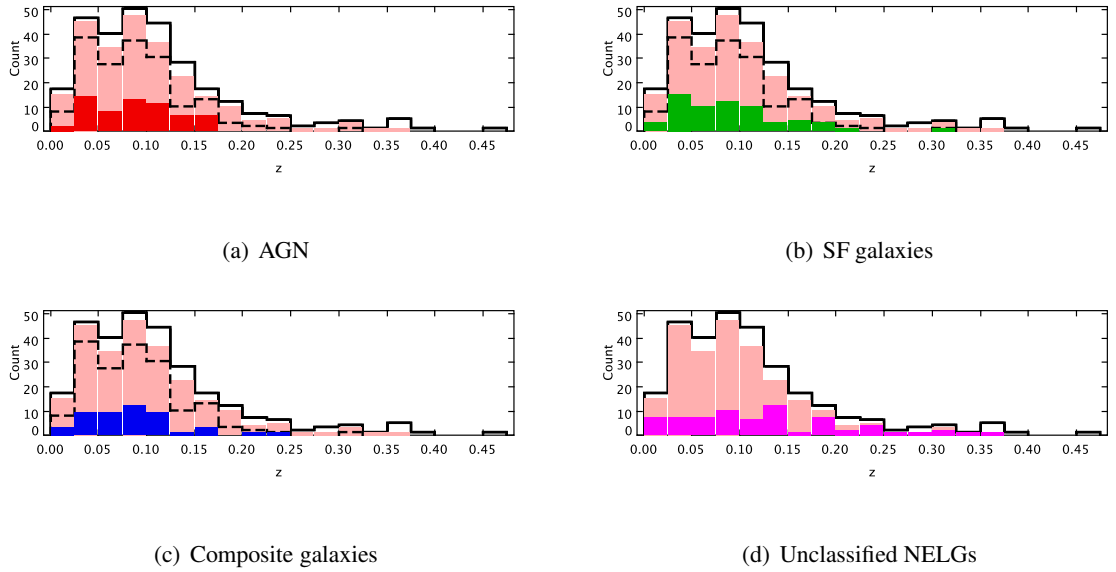


Figure C.2: The distributions of redshifts from *SDSS*. In all four plots, the *MJ* sample and its NELG subsample are marked with black solid histograms and pink filled histograms respectively. The classifiable NELGs are marked with black dashed histograms in (a), (b), and (c). AGN, SF galaxies and composite galaxies are marked with red histogram in (a), green histogram in (b) and blue histogram in (c), respectively. The unclassified NELGs are marked with magenta histogram in (d).

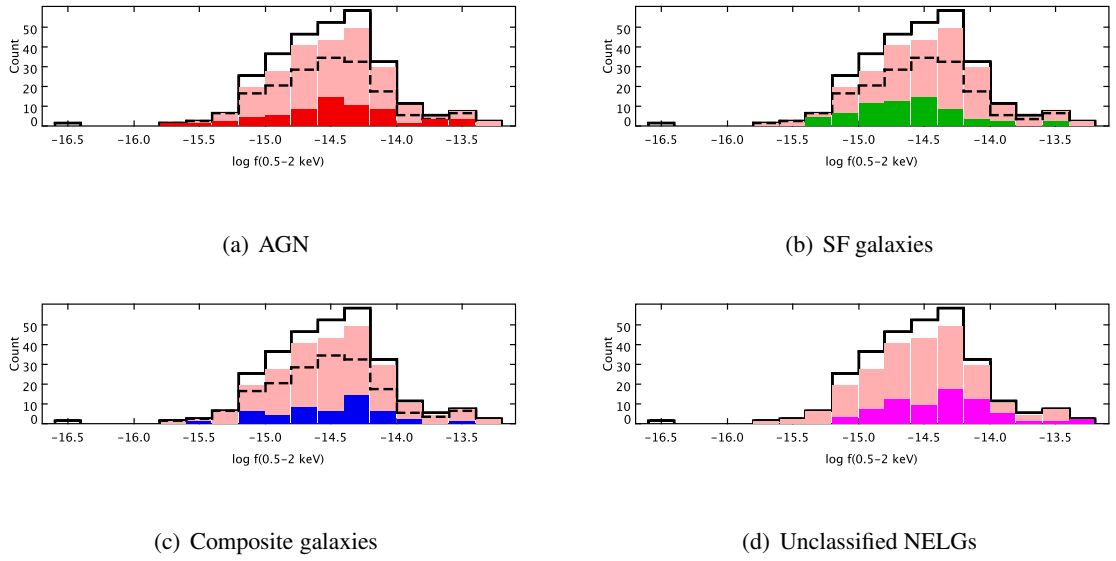


Figure C.3: The distributions of the 0.5–2 keV fluxes. In all four plots, the *MJ* sample and its NELG subsample are marked with black solid histograms and pink filled histograms respectively. The classifiable NELGs are marked with black dashed histograms in (a), (b), and (c). AGN, SF galaxies and composite galaxies are marked with red histogram in (a), green histogram in (b) and blue histogram in (c), respectively. The unclassified NELGs are marked with magenta histogram in (d).

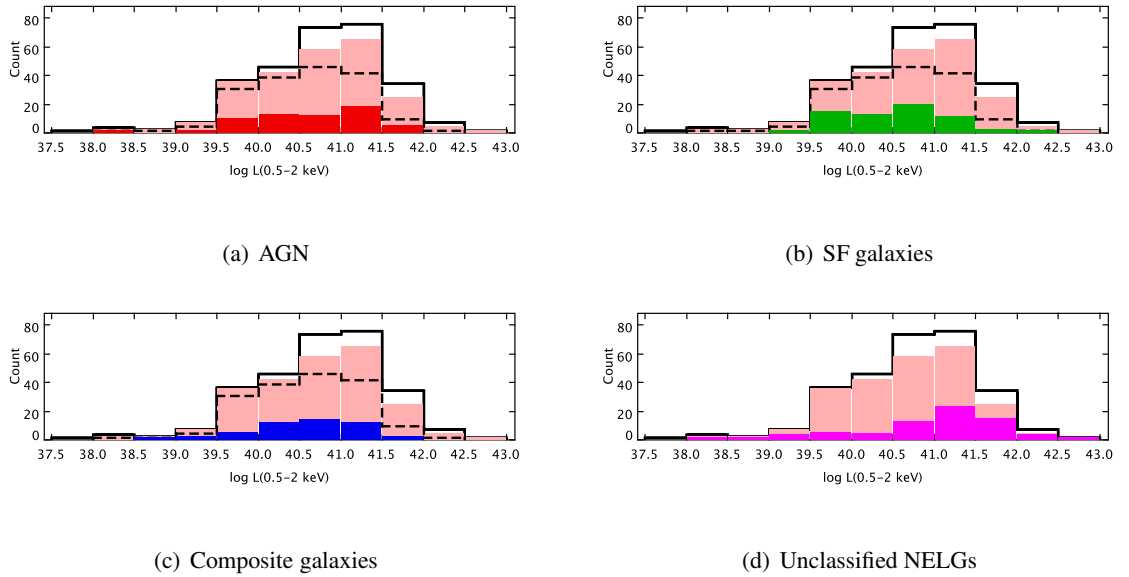


Figure C.4: The distributions of the 0.5–2 keV luminosities. In all four plots, the *MJ* sample and its NELG subsample are marked with black solid histograms and pink filled histograms respectively. The classifiable NELGs are marked with black dashed histograms in (a), (b), and (c). AGN, SF galaxies and composite galaxies are marked with red histogram in (a), green histogram in (b) and blue histogram in (c), respectively. The unclassified NELGs are marked with magenta histogram in (d).

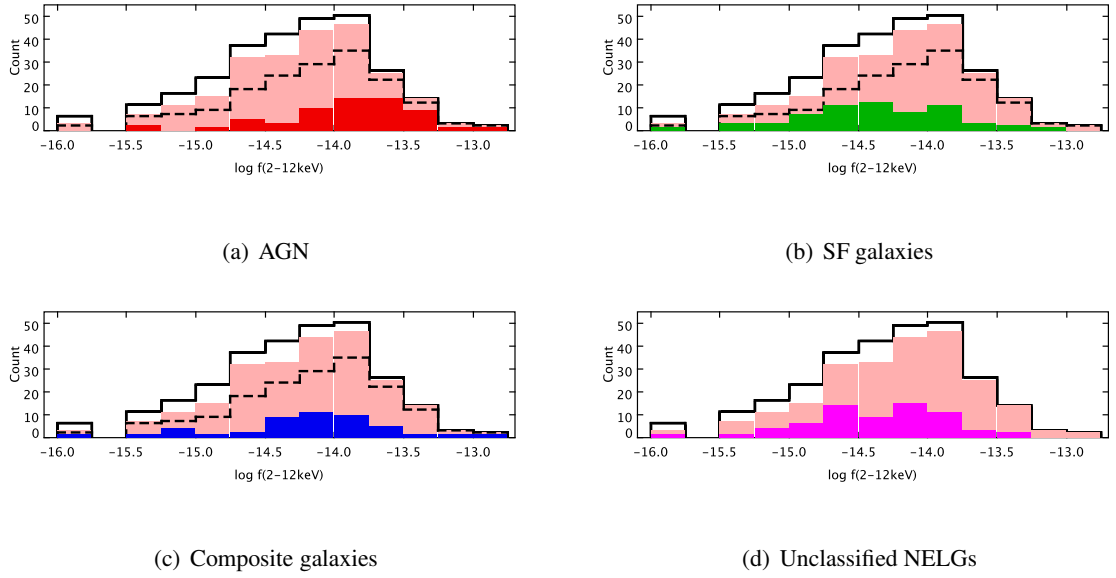


Figure C.5: The distributions of the 2–12 keV fluxes. In all four plots, the *MJ* sample and its NELG subsample are marked with black solid histograms and pink filled histograms respectively. The classifiable NELGs are marked with black dashed histograms in (a), (b), and (c). AGN, SF galaxies and composite galaxies are marked with red histogram in (a), green histogram in (b) and blue histogram in (c), respectively. The unclassified NELGs are marked with magenta histogram in (d).

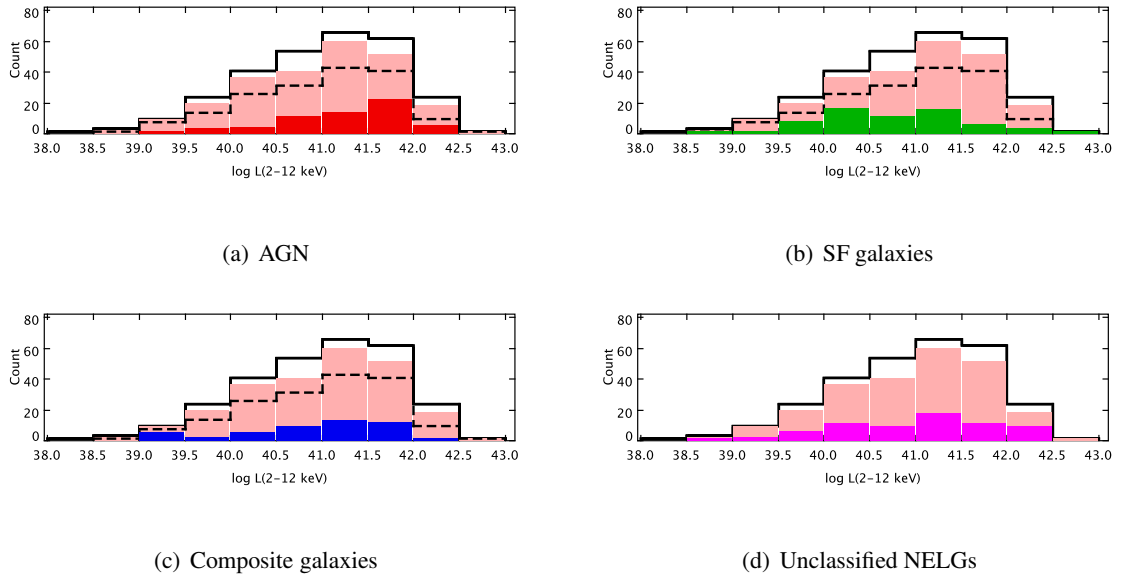


Figure C.6: The distributions of the 2–12 keV luminosities. In all four plots, the *MJ* sample and its NELG subsample are marked with black solid histograms and pink filled histograms respectively. The classifiable NELGs are marked with black dashed histograms in (a), (b), and (c). AGN, SF galaxies and composite galaxies are marked with red histogram in (a), green histogram in (b) and blue histogram in (c), respectively. The unclassified NELGs are marked with magenta histogram in (d).

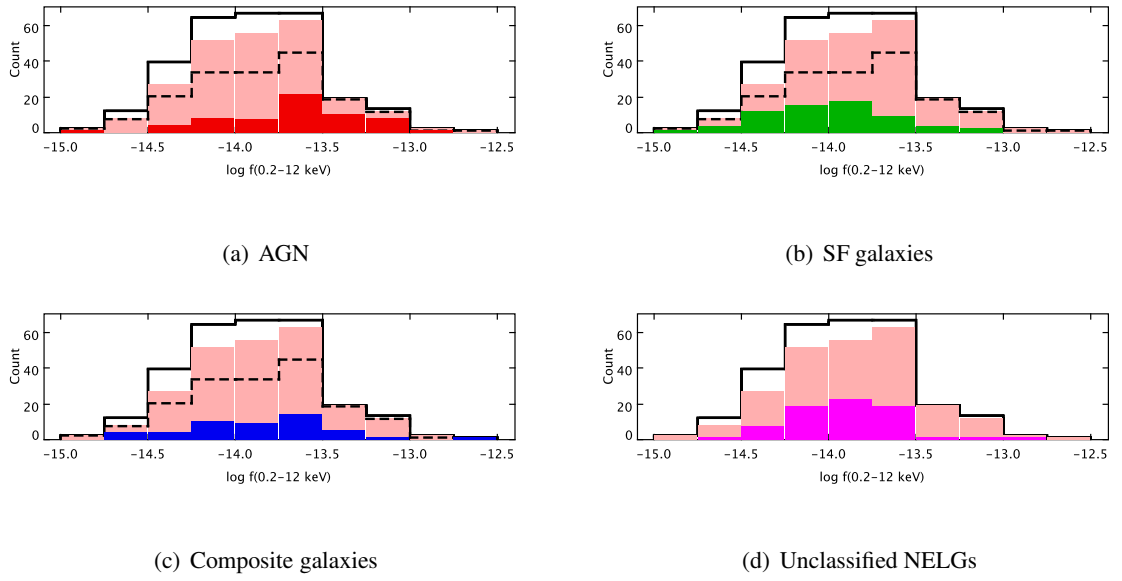


Figure C.7: The distributions of the 0.2–12 keV fluxes. In all four plots, the *MJ* sample and its NELG subsample are marked with black solid histograms and pink filled histograms respectively. The classifiable NELGs are marked with black dashed histograms in (a), (b), and (c). AGN, SF galaxies and composite galaxies are marked with red histogram in (a), green histogram in (b) and blue histogram in (c), respectively. The unclassified NELGs are marked with magenta histogram in (d).

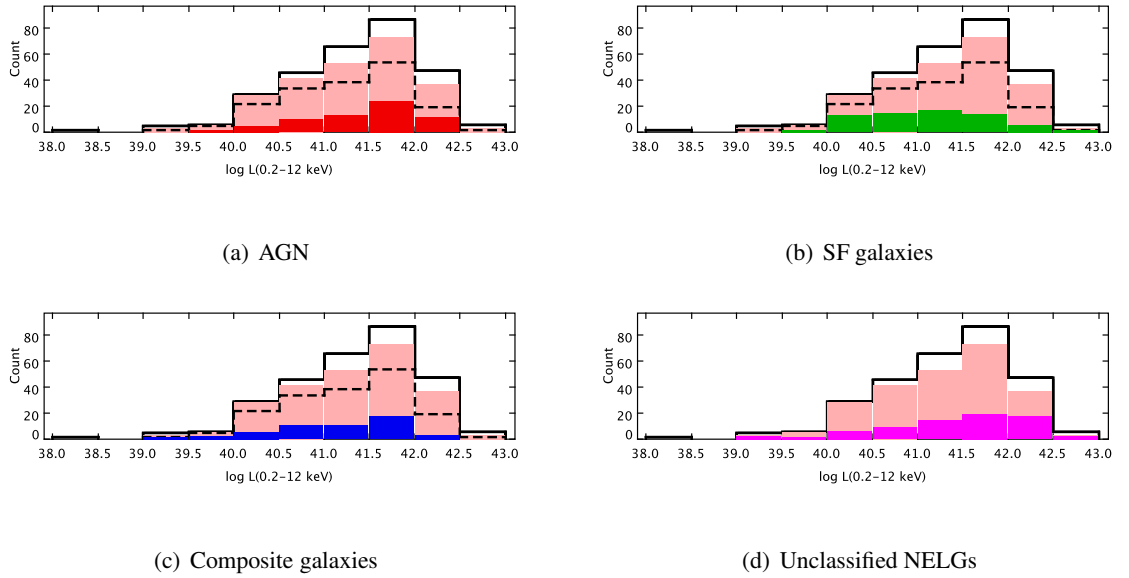


Figure C.8: The distributions of the 0.2–12 keV luminosities. In all four plots, the *MJ* sample and its NELG subsample are marked with black solid histograms and pink filled histograms respectively. The classifiable NELGs are marked with black dashed histograms in (a), (b), and (c). AGN, SF galaxies and composite galaxies are marked with red histogram in (a), green histogram in (b) and blue histogram in (c), respectively. The unclassified NELGs are marked with magenta histogram in (d).

BIBLIOGRAPHY

- Abazajian, K., Adelman-McCarthy, J. K., Agüeros, M. A., et al. 2004, *AJ*, 128, 502
- Abazajian, K. & Sloan Digital Sky Survey, f. t. 2008, ArXiv e-prints
- Adelman-McCarthy, J. K., Agüeros, M. A., Allam, S. S., et al. 2008, *ApJS*, 175, 297
- Adelman-McCarthy, J. K., Agüeros, M. A., Allam, S. S., et al. 2007, *ApJS*, 172, 634
- Adelman-McCarthy, J. K., Agüeros, M. A., Allam, S. S., et al. 2006, *ApJS*, 162, 38
- Akylas, A., Georgantopoulos, I., Georgakakis, A., Kitsionas, S., & Hatziminaoglou, E. 2006, *A&A*, 459, 693
- Alexander, D. M., Bauer, F. E., Brandt, W. N., et al. 2003, *AJ*, 126, 539
- Antonucci, R. 1993, *ARA&A*, 31, 473
- Antonucci, R. R. J. & Miller, J. S. 1985, *ApJ*, 297, 621
- Arnaud, K. A. 1996, in *Astronomical Society of the Pacific Conference Series*, Vol. 101, *Astronomical Data Analysis Software and Systems V*, ed. G. H. Jacoby & J. Barnes, 17–+
- Aschenbach, B., Briel, U. G., Haberl, F., et al. 2000, in *Society of Photo-Optical Instrumentation Engineers (SPIE) Conference Series*, Vol. 4012, *Society of Photo-Optical Instrumentation Engineers (SPIE) Conference Series*, ed. J. E. Truemper & B. Aschenbach, 731–739
- Baldry, I. K., Glazebrook, K., Budavári, T., et al. 2005, *MNRAS*, 358, 441
- Baldwin, J. A., Phillips, M. M., & Terlevich, R. 1981, *PASP*, 93, 5

- Ballet, J. 2006, *Advances in Space Research*, 37, 1902
- Balogh, M. L., Morris, S. L., Yee, H. K. C., Carlberg, R. G., & Ellingson, E. 1999, *ApJ*, 527, 54
- Barré, H., Nye, H., & Janin, G. 1999, *ESA Bulletin*, 100, 15
- Bauer, F. E., Alexander, D. M., Brandt, W. N., et al. 2004, *AJ*, 128, 2048
- Becker, R. H., Helfand, D. J., White, R. L., Gregg, M. D., & Laurent-Muehleisen, S. A. 2003, *VizieR Online Data Catalog*, 8071, 0
- Becker, R. H., White, R. L., & Helfand, D. J. 1995, *ApJ*, 450, 559
- Begelman, M. C. 2002, *ApJL*, 568, L97
- Begelman, M. C., Blandford, R. D., & Rees, M. J. 1984, *Reviews of Modern Physics*, 56, 255
- Böhringer, H., Voges, W., Huchra, J. P., et al. 2000, *ApJS*, 129, 435
- Bowyer, S., Byram, E. T., Chubb, T. A., & Friedman, H. 1965, in *IAU Symposium, Vol. 23, Astronomical Observations from Space Vehicles*, ed. J.-L. Steinberg, 227–+
- Bregman, J. N. 1980, *ApJ*, 237, 681
- Brinchmann, J., Charlot, S., White, S. D. M., et al. 2004, *MNRAS*, 351, 1151
- Brinkmann, W., Chester, M., Kollgaard, R., et al. 1999, *A&AS*, 134, 221
- Bruzual, G. & Charlot, S. 2003, *MNRAS*, 344, 1000
- Caccianiga, A., Severgnini, P., Della Ceca, R., et al. 2007, *A&A*, 470, 557
- Cappi, M., Panessa, F., Bassani, L., et al. 2006, *A&A*, 446, 459
- Charlot, S. & Fall, S. M. 2000, *ApJ*, 539, 718
- Chevalier, R. A. & Clegg, A. W. 1985, *Nature*, 317, 44
- Colbert, E. J. M., Heckman, T. M., Ptak, A. F., Strickland, D. K., & Weaver, K. A. 2004, *ApJ*, 602, 231
- Colbert, E. J. M. & Mushotzky, R. F. 1999, *ApJ*, 519, 89
- Colless, M., Dalton, G., Maddox, S., et al. 2001, *MNRAS*, 328, 1039

- Comastri, A., Mignoli, M., Ciliegi, P., et al. 2002, *ApJ*, 571, 771
- Condon, J. J. 1992, *ARA&A*, 30, 575
- Cox, D. P. & Smith, B. W. 1974, *ApJL*, 189, L105+
- David, L. P., Jones, C., & Forman, W. 1992, *ApJ*, 388, 82
- Davidson, K. & Kinman, T. D. 1978, *ApJ*, 225, 776
- Deeg, H. J., Munoz-Tunon, C., Tenorio-Tagle, G., et al. 1998, *A&AS*, 129, 455
- den Herder, J. W., Brinkman, A. C., Kahn, S. M., et al. 2001, *A&A*, 365, L7
- Eisenstein, D. J., Annis, J., Gunn, J. E., et al. 2001, *AJ*, 122, 2267
- Elvis, M., Soltan, A., & Keel, W. C. 1984, *ApJ*, 283, 479
- Fabbiano, G. 1986, *PASP*, 98, 525
- Fabbiano, G. 1988, *ApJ*, 330, 672
- Fabbiano, G. 1989, *ARA&A*, 27, 87
- Fabbiano, G. 2006, *ARA&A*, 44, 323
- Fabbiano, G., Feigelson, E., & Zamorani, G. 1982, *ApJ*, 256, 397
- Fabbiano, G., Gioia, I. M., & Trinchieri, G. 1988, *ApJ*, 324, 749
- Fabbiano, G., Kim, D.-W., & Trinchieri, G. 1992, *ApJS*, 80, 531
- Fabbiano, G. & Shapley, A. 2002, *ApJ*, 565, 908
- Fabbiano, G. & Trinchieri, G. 1984, *ApJ*, 286, 491
- Fabbiano, G. & Trinchieri, G. 1985, *ApJ*, 296, 430
- Fabbiano, G. & Trinchieri, G. 1987, *ApJ*, 315, 46
- Fabbiano, G., Trinchieri, G., & MacDonald, A. 1984, *ApJ*, 284, 65
- Fabbiano, G. & White, N. E. 2006, Compact stellar X-ray sources in normal galaxies (Compact stellar X-ray sources), 475–506

- Fanaroff, B. L. & Riley, J. M. 1974, *MNRAS*, 167, 31P
- Fiore, F., La Franca, F., Vignali, C., et al. 2000, *New Astronomy*, 5, 143
- Flohic, H. M. L. G., Eracleous, M., Chartas, G., Shields, J. C., & Moran, E. C. 2006, *ApJ*, 647, 140
- Forman, W., Jones, C., Cominsky, L., et al. 1978, *ApJS*, 38, 357
- Forman, W., Jones, C., & Tucker, W. 1985, *ApJ*, 293, 102
- Forman, W., Kellogg, E., Gursky, H., Tananbaum, H., & Giacconi, R. 1972, *ApJ*, 178, 309
- Forman, W., Schwarz, J., Jones, C., Liller, W., & Fabian, A. C. 1979, *ApJL*, 234, L27
- Frank, J., King, A., & Raine, D. J. 2002, *Accretion Power in Astrophysics: Third Edition* (*Accretion Power in Astrophysics*, by Juhan Frank and Andrew King and Derek Raine, pp. 398. ISBN 0521620538. Cambridge, UK: Cambridge University Press, February 2002.)
- Fraternali, F., Cappi, M., Sancisi, R., & Oosterloo, T. 2002, *ApJ*, 578, 109
- Fukugita, M., Ichikawa, T., Gunn, J. E., et al. 1996, *AJ*, 111, 1748
- Gabriel, C., Denby, M., Fyfe, D. J., et al. 2004, in *Astronomical Society of the Pacific Conference Series*, Vol. 314, *Astronomical Data Analysis Software and Systems (ADASS) XIII*, ed. F. Ochsenbein, M. G. Allen, & D. Egret, 759–+
- Georgakakis, A. 2008, *Astronomische Nachrichten*, 329, 174
- Georgakakis, A., Georgantopoulos, I., Vallbé, M., et al. 2004a, *MNRAS*, 349, 135
- Georgakakis, A. E., Chavushyan, V., Plionis, M., et al. 2006, *MNRAS*, 367, 1017
- Georgakakis, A. E., Georgantopoulos, I., Basilakos, S., Plionis, M., & Kolokotronis, V. 2004b, *MNRAS*, 354, 123
- Georgantopoulos, I. & Georgakakis, A. 2005, *MNRAS*, 358, 131
- Georgantopoulos, I., Georgakakis, A., & Koulouridis, E. 2005, *MNRAS*, 360, 782
- Ghisellini, G., Haardt, F., & Matt, G. 1994, *MNRAS*, 267, 743
- Giacconi, R., Branduardi, G., Briel, U., et al. 1979, *ApJ*, 230, 540

- Giacconi, R., Gursky, H., Paolini, F. R., & Rossi, B. B. 1962, *Physical Review Letters*, 9, 439
- Giacconi, R., Kellogg, E., Gorenstein, P., Gursky, H., & Tananbaum, H. 1971, *ApJL*, 165, L27+
- Giacconi, R., Zirm, A., Wang, J., et al. 2002, *ApJS*, 139, 369
- Gilfanov, M., Grimm, H.-J., & Sunyaev, R. 2004, *MNRAS*, 347, L57
- Gioia, I. M., Maccacaro, T., Schild, R. E., et al. 1984, *ApJ*, 283, 495
- Gioia, I. M., Maccacaro, T., Schild, R. E., et al. 1990, *ApJS*, 72, 567
- Gioia, I. M., Maccacaro, T., & Wolter, A. 1987, in *IAU Symposium*, Vol. 124, *Observational Cosmology*, ed. A. Hewitt, G. Burbidge, & L. Z. Fang, 593–595
- Goodrich, R. W. 1989, *ApJ*, 342, 224
- Gordon, K. D., Clayton, G. C., Misselt, K. A., Landolt, A. U., & Wolff, M. J. 2003, *ApJ*, 594, 279
- Green, P. J., Silverman, J. D., Cameron, R. A., et al. 2004, *ApJS*, 150, 43
- Grimes, J. P., Heckman, T., Strickland, D., & Ptak, A. 2005, *ApJ*, 628, 187
- Grimm, H.-J., Gilfanov, M., & Sunyaev, R. 2002, *A&A*, 391, 923
- Grimm, H.-J., Gilfanov, M., & Sunyaev, R. 2003, *MNRAS*, 339, 793
- Grimm, H.-J., McDowell, J., Zezas, A., Kim, D.-W., & Fabbiano, G. 2007, *ApJS*, 173, 70
- Grupe, D. 2000, *New Astronomy Review*, 44, 455
- Gull, S. F. & Northover, K. J. E. 1973, *Nature*, 244, 80
- Gunn, J. E., Carr, M., Rockosi, C., et al. 1998, *AJ*, 116, 3040
- Gursky, H., Kellogg, E., Murray, S., et al. 1971, *ApJL*, 167, L81+
- Haardt, F. & Maraschi, L. 1991, *ApJL*, 380, L51
- Haardt, F. & Maraschi, L. 1993, *ApJ*, 413, 507
- Hambly, N. C., MacGillivray, H. T., Read, M. A., et al. 2001, *MNRAS*, 326, 1279
- Hasinger, G., Burg, R., Giacconi, R., et al. 1998, *A&A*, 329, 482

- Heckman, T. M. 1980, *A&A*, 87, 152
- Heckman, T. M., Armus, L., & Miley, G. K. 1990, *ApJS*, 74, 833
- Helfand, D. J. 1984, *PASP*, 96, 913
- Helfand, D. J. & Moran, E. C. 2001, *ApJ*, 554, 27
- Ho, L. C. 2008, *ARA&A*, 46, 475
- Ho, L. C., Feigelson, E. D., Townsley, L. K., et al. 2001, *ApJL*, 549, L51
- Ho, L. C., Filippenko, A. V., & Sargent, W. L. W. 1997a, *ApJS*, 112, 315
- Ho, L. C., Filippenko, A. V., Sargent, W. L. W., & Peng, C. Y. 1997b, *ApJS*, 112, 391
- Hornschemeier, A. E., Bauer, F. E., Alexander, D. M., et al. 2003a, *AJ*, 126, 575
- Hornschemeier, A. E., Bauer, F. E., Alexander, D. M., et al. 2003b, *Astronomische Nachrichten*, 324, 12
- Hornschemeier, A. E., Brandt, W. N., Garmire, G. P., et al. 2001, *ApJ*, 554, 742
- Hornschemeier, A. E., Heckman, T. M., Ptak, A. F., Tremonti, C. A., & Colbert, E. J. M. 2005, *AJ*, 129, 86
- Irwin, J. A., Athey, A. E., & Bregman, J. N. 2003, *ApJ*, 587, 356
- Ivezić, Ž., Lupton, R. H., Schlegel, D., et al. 2004, *Astronomische Nachrichten*, 325, 583
- Ivezić, Ž., Menou, K., Knapp, G. R., et al. 2002, *AJ*, 124, 2364
- Jansen, F., Lumb, D., Altieri, B., et al. 2001, *A&A*, 365, L1
- Kalberla, P. M. W., Burton, W. B., Hartmann, D., et al. 2005, *A&A*, 440, 775
- Kauffmann, G., Heckman, T. M., Tremonti, C., et al. 2003a, *MNRAS*, 346, 1055
- Kauffmann, G., Heckman, T. M., White, S. D. M., et al. 2003b, *MNRAS*, 341, 33
- Kauffmann, G., White, S. D. M., Heckman, T. M., et al. 2004, *MNRAS*, 353, 713
- Kellogg, E., Gursky, H., Leong, C., et al. 1971, *ApJL*, 165, L49+

- Kennicutt, Jr., R. C. 1998, *ApJ*, 498, 541
- Kewley, L. J., Dopita, M. A., Sutherland, R. S., Heisler, C. A., & Trevena, J. 2001, *ApJ*, 556, 121
- Kewley, L. J., Groves, B., Kauffmann, G., & Heckman, T. 2006, *MNRAS*, 372, 961
- Kim, D.-W., Barkhouse, W. A., Romero-Colmenero, E., et al. 2006, *ApJ*, 644, 829
- Kim, D.-W., Cameron, R. A., Drake, J. J., et al. 2004a, *ApJS*, 150, 19
- Kim, D.-W., Wilkes, B. J., Green, P. J., et al. 2004b, *ApJ*, 600, 59
- King, A. R., Davies, M. B., Ward, M. J., Fabbiano, G., & Elvis, M. 2001, *ApJL*, 552, L109
- Körding, E., Falcke, H., & Markoff, S. 2002, *A&A*, 382, L13
- Kroupa, P. 2001, *MNRAS*, 322, 231
- Kuntz, K. D., Snowden, S. L., Pence, W. D., & Mukai, K. 2003, *ApJ*, 588, 264
- Le Borgne, J.-F., Bruzual, G., Pelló, R., et al. 2003, *A&A*, 402, 433
- Lehmer, B. D., Brandt, W. N., Alexander, D. M., et al. 2008, *ApJ*, 681, 1163
- Lewis, I. J., Cannon, R. D., Taylor, K., et al. 2002, *MNRAS*, 333, 279
- Li, Z., Wang, Q. D., & Hameed, S. 2007, *MNRAS*, 376, 960
- Lira, P., Ward, M., Zezas, A., Alonso-Herrero, A., & Ueno, S. 2002, *MNRAS*, 330, 259
- Long, K. S. & Helfand, D. J. 1979, *ApJL*, 234, L77
- Long, K. S. & van Speybroeck, L. P. 1983, in *Accretion-Driven Stellar X-ray Sources*, ed. W. H. G. Lewin & E. P. J. van den Heuvel, 117–146
- Lou, Y.-Q. & Bian, F.-Y. 2005, *MNRAS*, 358, 1231
- Maccacaro, T., Gioia, I. M., Wolter, A., Zamorani, G., & Stocke, J. T. 1988, *ApJ*, 326, 680
- Maccacaro, T., Gioia, I. M., Zamorani, G., et al. 1982, *ApJ*, 253, 504
- Makishima, K., Kubota, A., Mizuno, T., et al. 2000, *ApJ*, 535, 632
- Marshall, F. E., Boldt, E. A., Holt, S. S., et al. 1980, *ApJ*, 235, 4

- Mas-Hesse, J. M., Oti-Floranes, H., & Cerviño, M. 2008, *A&A*, 483, 71
- Mason, K. O., Breeveld, A., Much, R., et al. 2001, *A&A*, 365, L36
- McClintock, J. E. & Remillard, R. A. 2006, Black hole binaries, ed. W. H. G. Lewin & M. van der Klis, 157–213
- Miller, J. M., Fabbiano, G., Miller, M. C., & Fabian, A. C. 2003, *ApJL*, 585, L37
- Miyaji, T. & Griffiths, R. E. 2002, *ApJL*, 564, L5
- Monet, D. G., Levine, S. E., Canzian, B., et al. 2003, *AJ*, 125, 984
- Moretti, A., Campana, S., Lazzati, D., & Tagliaferri, G. 2003, *ApJ*, 588, 696
- Mukai, K. 1993, *Legacy* (HEASARC journal), 3, 21
- Mulchaey, J. S., Koratkar, A., Ward, M. J., et al. 1994, *ApJ*, 436, 586
- Nandra, K. & George, I. M. 1994, *MNRAS*, 267, 974
- Netzer, H. 2006, in *Lecture Notes in Physics*, Berlin Springer Verlag, Vol. 693, *Physics of Active Galactic Nuclei at all Scales*, ed. D. Alloin, 1–+
- Nordgren, T. E., Chengalur, J. N., Salpeter, E. E., & Terzian, Y. 1997, *AJ*, 114, 77
- Norman, C., Ptak, A., Hornschemeier, A., et al. 2004, *ApJ*, 607, 721
- O'Donnell, J. E. 1994, *ApJ*, 422, 158
- Osterbrock, D. E. & Pogge, R. W. 1985, *ApJ*, 297, 166
- O'Sullivan, E., Forbes, D. A., & Ponman, T. J. 2001, *MNRAS*, 328, 461
- Paerels, F. B. S. & Kahn, S. M. 2003, *ARA&A*, 41, 291
- Page, M. J., Lehmann, I., Boller, T., et al. 2007, *MNRAS*, 378, 1335
- Panessa, F. & Bassani, L. 2002, *A&A*, 394, 435
- Panessa, F., Bassani, L., Cappi, M., et al. 2006, *A&A*, 455, 173
- Panzer, M. R., Campana, S., Covino, S., et al. 2003, *A&A*, 399, 351

- Paturel, G., Andernach, H., Bottinelli, L., et al. 1997, *A&AS*, 124, 109
- Paturel, G., Fouque, P., Bottinelli, L., & Gouguenheim, L. 1989, *A&AS*, 80, 299
- Perez-Olea, D. E. & Colina, L. 1996, *ApJ*, 468, 191
- Persic, M. & Rephaeli, Y. 2007, *A&A*, 463, 481
- Persic, M., Rephaeli, Y., Braito, V., et al. 2004, *A&A*, 419, 849
- Petrosian, V. 1976, *ApJL*, 209, L1
- Pier, J. R., Munn, J. A., Hindsley, R. B., et al. 2003, *AJ*, 125, 1559
- Pogge, R. W. 2000, *New Astronomy Review*, 44, 381
- Predehl, P. & Schmitt, J. H. M. M. 1995, *A&A*, 293, 889
- Ptak, A. & Griffiths, R. 2003, in *Astronomical Society of the Pacific Conference Series*, Vol. 295, *Astronomical Data Analysis Software and Systems XII*, ed. H. E. Payne, R. I. Jedrzejewski, & R. N. Hook, 465–+
- Ranalli, P., Comastri, A., & Setti, G. 2003, *A&A*, 399, 39
- Read, A. M. & Ponman, T. J. 2001, *MNRAS*, 328, 127
- Read, A. M., Ponman, T. J., & Strickland, D. K. 1997, *MNRAS*, 286, 626
- Richards, E. A. 2000, *ApJ*, 533, 611
- Richards, G. T., Fan, X., Newberg, H. J., et al. 2002, *AJ*, 123, 2945
- Risaliti, G. & Elvis, M. 2004, in *Astrophysics and Space Science Library*, Vol. 308, *Supermassive Black Holes in the Distant Universe*, ed. A. J. Barger, 187–+
- Rosati, P., Tozzi, P., Giacconi, R., et al. 2002, *ApJ*, 566, 667
- Sarazin, C. L. 1988, *X-ray emission from clusters of galaxies*, ed. C. L. Sarazin
- Sarazin, C. L., Irwin, J. A., & Bregman, J. N. 2000, *ApJL*, 544, L101
- Sarazin, C. L., Irwin, J. A., & Bregman, J. N. 2001, *ApJ*, 556, 533
- Seyfert, C. K. 1943, *ApJ*, 97, 28

- Shakura, N. I. & Syunyaev, R. A. 1973, *A&A*, 24, 337
- Short, A. D., Keay, A., & Turner, M. J. 1998, in Society of Photo-Optical Instrumentation Engineers (SPIE) Conference Series, Vol. 3445, Society of Photo-Optical Instrumentation Engineers (SPIE) Conference Series, ed. O. H. Siegmund & M. A. Gummin, 13–27
- Silverman, J. D., Green, P. J., Barkhouse, W. A., et al. 2005, *ApJ*, 618, 123
- Sivakoff, G. R., Sarazin, C. L., & Irwin, J. A. 2003, *ApJ*, 599, 218
- Stoche, J. T., Liebert, J., Gioia, I. M., et al. 1983, *ApJ*, 273, 458
- Stoche, J. T., Morris, S. L., Gioia, I. M., et al. 1991, *ApJS*, 76, 813
- Stoughton, C., Lupton, R. H., Bernardi, M., et al. 2002, *AJ*, 123, 485
- Strateva, I., Ivezić, Ž., Knapp, G. R., et al. 2001, *AJ*, 122, 1861
- Strauss, M. A., Weinberg, D. H., Lupton, R. H., et al. 2002, *AJ*, 124, 1810
- Strickland, D. K., Heckman, T. M., Colbert, E. J. M., Hoopes, C. G., & Weaver, K. A. 2004a, *ApJS*, 151, 193
- Strickland, D. K., Heckman, T. M., Colbert, E. J. M., Hoopes, C. G., & Weaver, K. A. 2004b, *ApJ*, 606, 829
- Strickland, D. K., Heckman, T. M., Weaver, K. A., & Dahlem, M. 2000, *AJ*, 120, 2965
- Strüder, L., Briel, U., Dennerl, K., et al. 2001, *A&A*, 365, L18
- Suchkov, A. A., Balsara, D. S., Heckman, T. M., & Leitherer, C. 1994, *ApJ*, 430, 511
- Tajer, M., Trinchieri, G., Wolter, A., et al. 2005, *A&A*, 435, 799
- Tanaka, Y., Inoue, H., & Holt, S. S. 1994, *PASJ*, 46, L37
- Tanaka, Y., Nandra, K., Fabian, A. C., et al. 1995, *Nature*, 375, 659
- Tauris, T. M. & van den Heuvel, E. P. J. 2006, Formation and evolution of compact stellar X-ray sources (Compact stellar X-ray sources), 623–665
- Terashima, Y., Ho, L. C., & Ptak, A. F. 2000a, *ApJ*, 539, 161

- Terashima, Y., Ho, L. C., Ptak, A. F., et al. 2000b, *ApJ*, 533, 729
- Terashima, Y. & Wilson, A. S. 2003, *ApJ*, 583, 145
- Tremonti, C. A., Heckman, T. M., Kauffmann, G., et al. 2004, *ApJ*, 613, 898
- Trinchieri, G., Fabbiano, G., & Canizares, C. R. 1986, *ApJ*, 310, 637
- Trinchieri, G., Fabbiano, G., & Peres, G. 1988, *ApJ*, 325, 531
- Turner, M. J. L., Abbey, A., Arnaud, M., et al. 2001, *A&A*, 365, L27
- Tyler, K., Quillen, A. C., LaPage, A., & Rieke, G. H. 2004, *ApJ*, 610, 213
- Tzanavaris, P., Georgantopoulos, I., & Georgakakis, A. 2006, *A&A*, 454, 447
- Urry, C. M. & Padovani, P. 1995, *PASP*, 107, 803
- Veilleux, S. & Osterbrock, D. E. 1987, *ApJS*, 63, 295
- Véron-Cetty, M.-P. & Véron, P. 2003, *A&A*, 412, 399
- Voges, W., Aschenbach, B., Boller, T., et al. 1999, *A&A*, 349, 389
- Voges, W., Aschenbach, B., Boller, T., et al. 2000, *VizieR Online Data Catalog*, 9029, 0
- Ward, M. J., Done, C., Fabian, A. C., Tennant, A. F., & Shafer, R. A. 1988, *ApJ*, 324, 767
- Warwick, R. S., Jenkins, L. P., Read, A. M., Roberts, T. P., & Owen, R. A. 2007, *MNRAS*, 376, 1611
- Watson, M. G. 1990, in *Astrophysics and Space Science Library*, Vol. 160, *Windows on Galaxies*, ed. G. Fabbiano, J. S. Gallagher, & A. Renzini, 177–+
- Watson, M. G., Auguères, J.-L., Ballet, J., et al. 2001, *A&A*, 365, L51
- Watson, M. G., Roberts, T. P., Akiyama, M., & Ueda, Y. 2005, *A&A*, 437, 899
- Watson, M. G., Schröder, A. C., Fyfe, D., et al. 2009, *A&A*, 493, 339
- Watson, M. G., Stanger, V., & Griffiths, R. E. 1984, *ApJ*, 286, 144
- Weedman, D. W., Feldman, F. R., Balzano, V. A., et al. 1981, *ApJ*, 248, 105

- Weisskopf, M. C., Tananbaum, H. D., Van Speybroeck, L. P., & O'Dell, S. L. 2000, in Society of Photo-Optical Instrumentation Engineers (SPIE) Conference Series, Vol. 4012, Society of Photo-Optical Instrumentation Engineers (SPIE) Conference Series, ed. J. E. Truemper & B. Aschenbach, 2–16
- White, R. L., Becker, R. H., Helfand, D. J., & Gregg, M. D. 1997, *ApJ*, 475, 479
- Wilkes, B. J. & Elvis, M. 1987, *ApJ*, 323, 243
- Worrall, D. M. 2009, *A&AR*, 17, 1
- Worthey, G. & Ottaviani, D. L. 1997, *ApJS*, 111, 377
- York, D. G., Adelman, J., Anderson, Jr., J. E., et al. 2000, *AJ*, 120, 1579
- Zimmermann, H.-U., Boller, T., Döbereiner, S., & Pietsch, W. 2001, *A&A*, 378, 30

Acronyms

1XMM	1 st XMM-Newton Serendipitous Source Catalogue
2dF	Two Degree Field
2XMM	2 nd XMM-Newton Serendipitous Source Catalogue
AGN	Active Galactic Nucleus
ALG	Absorption Line Galaxy
BLR	Broad Line Region
BLRG	Broad Line Radio Galaxy
FIRST	Faint Images of the Radio Sky at Twenty centimeters
HMXB	High Mass X-ray Binary
ISM	Interstellar Medium
JHU	Johns Hopkins University
K-S	Kolmogorov-Smirnov
LINER	Low Ionization Nuclear Emission Region
LLAGN	Low Luminosity AGN
LMXB	Low Mass X-ray Binary

MJ	MPA/JHU
MPA	Max-Planck-Institute for Astrophysics
NELG	Narrow Emission Line Galaxy
NLR	Narrow Line Region
NLRG	Narrow Line Radio Galaxy
NLS	Narrow Line Seyfert
QSO	Quasi-Stellar Object
SDSS	Sloan Digital Sky Survey
SF	Star-Forming
SFR	Star-Formation Rate
SNR	Supernova Remnant
SSC	Survey Science Centre
SSS	SuperCOSMOS Sky Survey
ULX	Ultraluminous X-ray source
XS	XMM-Newton/SDSS
XSSS	XMM-Newton/SDSS Serendipitous Survey
XWAS	XMM-Newton/2dF Wide Angle serendipitous Survey